Méthodologie pour génération de modèles réduits dynamiques multiphysiques : application aux open rotors

Hadrien Tournaire

NNT : 2017SACLC040

Thèse de doctorat de l'Université Paris-Saclay préparée à CentraleSupelec

Ecole doctorale n°579
Sciences mécaniques et énergétiques, matériaux et géosciences
Spécialité de doctorat : Mécanique

par

Hadrien Tournaire

Méthodologie pour génération de modèles réduits dynamiques multi-physiques : application aux open rotors

Thèse présentée et soutenue à SUPMÉCA, le 12 juillet 2017.

Composition du Jury :

M.	Régis Dufour	Professeur INSA Lyon	(Président du Jury)
M.	Etienne Balmès	Professeur associé SDTools - Arts et Métiers Paritech	(Rapporteur)
M.	Emmanuel Rigaud	Professeur associé École Centrale de Lyon	(Rapporteur)
M.	Cyril Touzé	Professeur ENSTA ParisTech	(Examinateur)
M.	Gabriel Delgado	Docteur IRT SystemX	(Examinateur)
M.	Jean-Luc Dion	Professeur Supméca	(Directeur de thèse)
M.	Franck Renaud	Maître de conférences Supméca	(Encadrant de thèse)

Remerciements

Je remercie Safran Aircraft Engines et tout particulièrement Bruno Mahieux et Antoine Millecamps pour leur intérêt dans mon sujet de thèse. Je tiens également à remercier l'IRT SystemX qui a accueilli et encadré cette thèse et notamment Eric Perrin-Pelletier et Paul Labrogère.

Je présente toute ma gratitude à mon directeur de thèse Jean-Luc Dion et mon encadrant Franck Renaud pour la confiance qu'ils m'ont accordé, leurs enseignements et leurs qualités humaines.

Ce travail de thèse a été pour moi l'occasion de rencontrer de nombreuses personnes qui m'ont aidé par leurs compétences techniques ou leurs amitiés, bien souvent les deux. Bien qu'il me soit impossible de tous les nommer, je tiens à citer les membres du laboratoire QWARTZ : Marco, Kamil, Karl, Adrien et enfin Adrien pour leur bonne humeur et leur humour; les membres de l'IRT SystemX : Romain, Gauthier, Mian, Laura, Anaïs, Emna, Paul avec lesquels nous avons tant de fois refait le monde; mes collègues Gabriel, Yves, Jean-Patrick et Fatima qui m'ont aidé à parfaire mes connaissances en espagnol et a compléter ma culture cinématographique.

Je remercie chaleureusement Luc, Keveen, Maxime, Guillaume, Florian et Lory pour leurs amitiées et leurs conseils avisés qui m'ont bien souvent aidé à prendre du recul et à faire descendre la pression. Enfin je souhaite remercier ma famille pour son soutien ainsi qu'Isabelle Passat et Frank De Nebehay.

Résumé substantiel

Le contexte économique et environnemental actuel amène un grand nombre d'industriels à optimiser leurs produits afin de réduire leurs consommations en énergie. Le domaine de l'aéronautique n'est pas épargné par cette tendance, l'entreprise Safran Aircraft Engines (SAE) a notamment marqué son engagement dans cette voie par son intention de développer un nouveau moteur d'avion de type open rotor.

Développé dans le cadre du projet de recherche européen Clean Sky, ce nouveau moteur est dénommé CROR (Counter Rotative Open Rotor). Une maquette numérique de ce moteur est montrée sur la figure Fig. 1. En 2017, les objectifs de SAE quant aux performances du CROR sont une réduction de 30% de la consommation de carburant et de 10dB sonores en comparaison avec le CFM56[1].

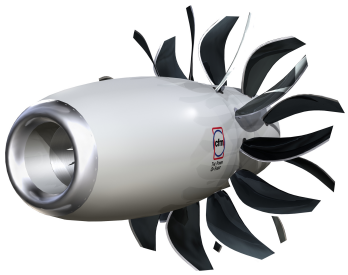

Figure 1 – Maquette numérique du CROR.

Par définition, un moteur de type open rotor est un turboréacteur composé d'un étage à hélices contrarotatives non carénées. L'étage amont correspond à un réacteur classique dont les gaz d'échappement sont injectés dans des tuyères et entrainent en rotation l'étage hélicé, en aval. Ces hélices sont montrées sur le schéma[2] Fig. 2, leur calage est piloté afin d'augmenter ou de réduire la poussée du moteur.

Fondé en 2012, l'IRT SystemX offre une infrastructure afin de faire coopérer des chercheurs de milieux académiques et industriels. En 2013, en vue d'accélérer la conception de l'open rotor, SAE a pris part au projet ROM (Réduction et Optimisation Multi-physique) mené par l'IRT SystemX. Le but du projet ROM est de proposer aux partenaires industriels, des méthodologies de conception et des algorithmes d'optimisation pour des systèmes de grande taille. Ce partenariat entre SAE, l'IRT SystemX et Supméca s'est concrétisé par le financement de la présente thèse en fin 2013.

[1] *Open rotor, le moteur du futur au banc d'essai. Disponible sur le site : <http://www.safran-group.com/fr/media/20140102_open-rotor-le-moteur-du-futur-au-banc-dessai>. (20.12.2016)*

[2] Schéma extrait du brevet : Danielson, David R. Carvalho, Paul A. Raes, Mark Perkinson, Robert H. *Counter-rotating open-rotor (CROR)*. 2011.

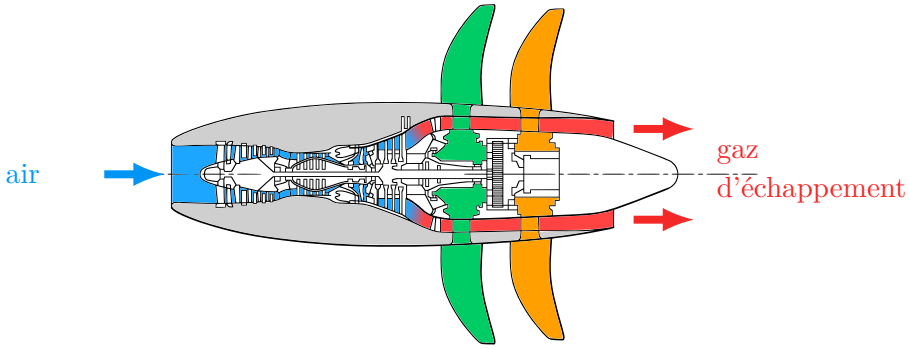

Figure 2 – Schéma du CROR. Le flux d'air circule de gauche à droite. L'air (en bleu) entre à gauche et est tout d'abord dirigé dans l'étage amont du moteur : le réacteur classique. Les gaz d'échappement (en rouge) traversent ensuite l'étage aval du réacteur, entrainant en rotation les hélices contrarotatives (en vert et en orange). Les parties grisées ne tournent pas.

Cas d'étude industriel : réduction de l'étage aval d'un open rotor

Le cas d'étude proposé par SAE concerne la réduction du modèle de l'étage aval du CROR (voir Fig. 4) dans le but d'accélérer la conception de ses pales. En effet, cette pièce possède un rôle important dans l'efficacité du moteur, sa conception et son optimisation sont donc des étapes critiques dans le développement de l'open rotor. Le profil de la pale est décidé conjointement par plusieurs services chez SAE, en vue d'optimiser à la fois la commande du moteur, ainsi que ses performances dynamiques et acoustiques. La géométrie complexe de la pale oblige les ingénieurs de SAE à concevoir cette pièce de manière itérative, à travers l'exploration de son espace de conception, voir Fig. 3.

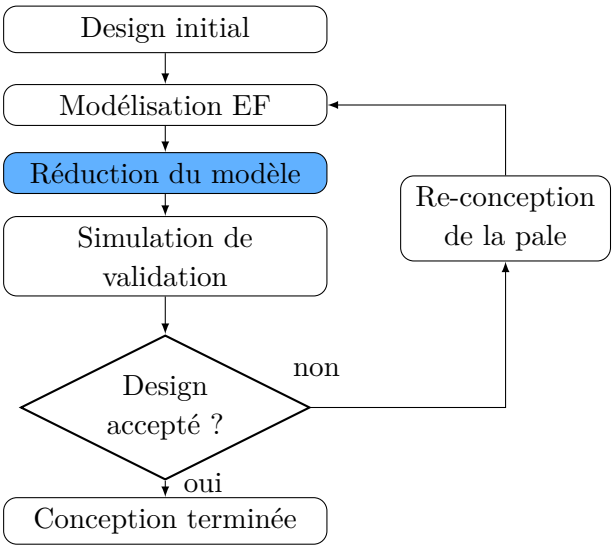

Figure 3 – Principe de la conception itérative. La pale est reconçue tant qu'un design satisfaisant n'est pas atteint.

La conception mécanique d'un système requiert de nombreuses études, notamment afin de caractériser et de valider son comportement dynamique sur sa plage de fonctionnement. En pratique, ce type d'analyse peut être réalisée numériquement à l'aide de la méthode des éléments finis. Cependant, dans ce contexte, la précision et le niveau de détail requis mènent à des modèles dont les tailles conséquentes et les temps de résolution ralentissent significativement le processus de conception.

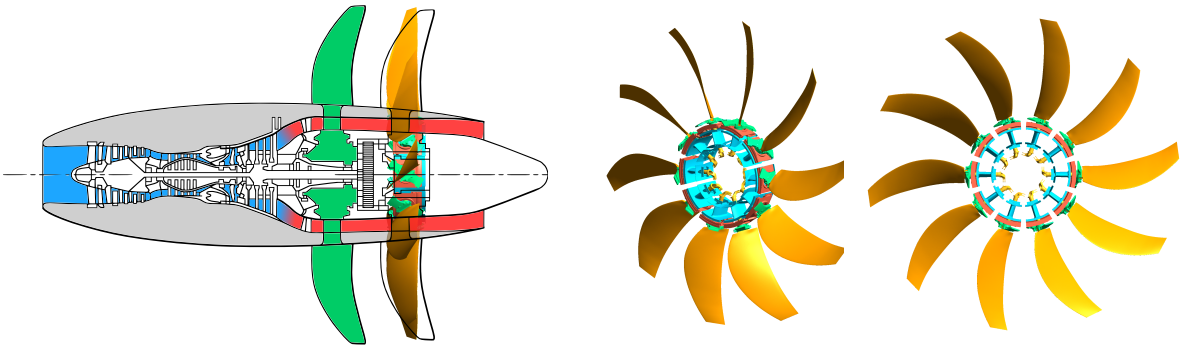

Figure 4 – Vue du maillage de l'étage aval du CROR fourni par SAE. Pour des raisons de visibilité, les arrêtes des éléments ne sont pas montrées. La localisation de ce modèle est donnée sur la figure de gauche.

Dans le cas de la pale, la validation d'un design nécessite l'évaluation des modes et fréquences propres du moteur, calculés pour différents calages de pale et vitesses de rotations. La réduction de ce temps de calcul possède un double impact pour SAE :

- accélérer la conception de la pale
- mieux explorer l'espace de conception de la pale

Afin d'assurer une précision standardisée lors de l'évaluation des propriétés modales du système, le maillage associé au modèle éléments finis de chaque conception de pale est obtenu à l'aide de technique de morphing. En dépit de cet aspect bénéfique cette méthodologie peut faire l'objet de critiques. En effet, en fonction de l'avancement de la conception, l'utilisation d'un maillage raffiné peut s'avérer inutile. Dans le cas présent, la méthodologie de travail adoptée par SAE impose l'exploitation d'un maillage fin.

Le principal besoin de SAE est une méthode de réduction dédiée à l'analyse modale. La prise en compte d'effets non linéaires est un but auxiliaire dont la mise en pratique est discutée en fin de thèse. Les contraintes imposées par SAE sur la méthodologie de réduction recherchée sont les suivantes :

- La méthode de réduction doit être compatible avec l'analyse modale linéaire.
- Le contexte de conception itérative doit être pris en considération.
- L'enrichissement d'un modèle réduit doit être possible.

D'autres contraintes trouvent leurs sources dans les outils de travail disponibles au sein du projet ROM. En effet, les modèles éléments finis de l'open rotor ont été construits à l'aide de codes industriels mais n'ont pas pu être exploité dans ce travail de thèse. Du fait de la volonté de l'IRT SystemX de ne travailler qu'avec des logiciels libres, la méthodologie de réduction a été développée sous le logiciel GNU Octave.

Description de l'open rotor et de sa dynamique

Les liaisons entre les composants de l'open rotor de SAE permettent de grands déplacements, ce qui donne un caractère non linéaire à la dynamique du système. La dynamique des multicorps flexibles propose des formulations adaptées au traitement de ce type de non-linéarités. Dans ce contexte industriel précis, l'approche dite "référentiel mobile" possède des propriétés particulièrement intéressantes pour la formulation de la dynamique de l'open rotor :

- elle permet d'exprimer la dynamique du système avec un nombre restreint d'équations non linéaires. En comparaison, une approche fondée sur l'utilisation d'un seul référentiel fixe mène à un modèle dont tous les degrés de liberté sont non linéaires.
- les opérateurs éléments finis non linéaires sont peu nombreux et relativement petits à l'échelle du modèle complet. En conséquence, la mise à jour de ces opérateurs est rapide.
- la distinction entre les contributions flexibles et rigides proposée par la formulation "référentiel mobile" offre l'opportunité de mieux analyser la dynamique du système. Les effets d'inertie liés aux accélérations des composants sont de même clairement identifiés grâce à cette formulation.

En dépit de ces avantages, un travail analytique conséquent peut être nécessaire afin de formaliser correctement la dynamique du système. Ce travail comprend notamment le paramétrage du système.

Bien que la mise à jour de certains opérateurs éléments finis soit nécessaire, il est possible d'alléger cette opération à l'aide de quelques stratégies de calcul. En effet, il est possible d'observer que certains des opérateurs éléments finis non linéaires peuvent être aisément paramétrés. Ainsi, la mise à jour de ces termes ne nécessite plus une intégration numérique mais une simple multiplication matricielle.

Bien que la plupart des liaisons entre les composants de l'open rotor soient ponctuelles, le contact entre la pale et son support s'effectue sur une importante surface (voir figure Fig. 5). Dans le domaine de la réduction de modèle, de telles interfaces ont tendance à réduire l'efficacité des méthodes de réduction. C'est pourquoi, le travail présenté dans cette thèse s'attache principalement à la réduction de ces interfaces.

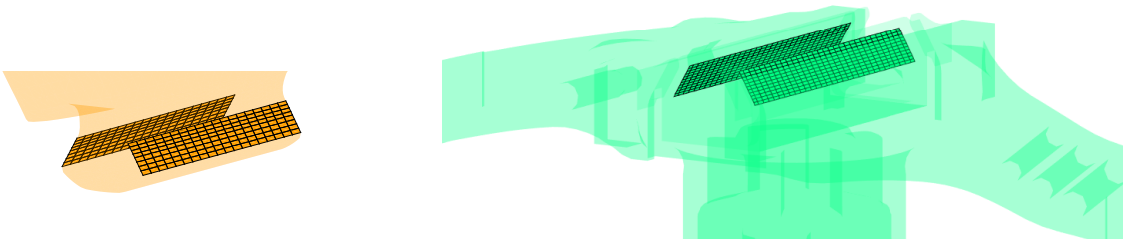

(a) La pale et son interface (b) La support et son interface

Figure 5 – Vue de la pale et de son support. Les interfaces sur lesquelles les deux composants sont en contact sont opaques et leurs maillages sont mis en évidence.

Réduction du modèle linéaire pale-support

La réduction des interfaces de contact est dans un premier temps étudiée en considérant les deux composants encastrés. La méthode de réduction développée s'appuie sur les techniques de sous-structuration dynamique déjà existantes. La stratégie de réduction de l'interface exploitée par la méthode proposée est la principale contribution de ce travail. Cette réduction de l'interface se base sur l'hypothèse que les modes propres libres des composants contiennent suffisamment d'informations pour décrire la cinématique de cette interface lorsque les deux composants sont assemblés. En résumé, les principales caractéristiques de la méthode de réduction proposée sont les suivantes :

- l'interface entre les composants est réduite à l'aide d'une technique basée sur la décomposition en valeurs singulières (SVD) des modes propres des composants.
- la méthode de réduction possède une précision équivalente à celle de la méthode de Craig-Bampton.
- la méthode proposée permet de construire des modèles réduit pour l'analyse modale dans un contexte de conception itérative.

La réduction de l'interface permet de générer des modèles réduis compact et précis. En termes de MAC et d'erreur relative sur les fréquences propres, la méthode proposée est équivalente à la méthode de Craig-Bampton, ce qui permet de considérer sa précision comme acceptable. En terme de compacité, on observe que :

- la méthode proposée est bien plus compacte que la méthode de Craig-Bampton car elle ne comprend pas de réduction d'interface.
- en comparaison avec une méthode exploitant la réduction d'interface (la méthode AMLS) la compacité de la méthode proposée n'est pas particulièrement remarquable.

Ces résultats sont résumé quantitativement dans le tableau Tab. 1.

Méthode	Craig et Bampton	Méthode AMLS	Méthode proposée
Taille du modèle réduit	1165	101	185
Moyenne de MAC	94.37%	98.90%	99.28%
Moyenne de l'erreur relative sur les fréquences propres	0.26%	0.09%	0.18%

Table 1 – Comparaison de la compacité et de la précision de la méthode proposée avec les méthode de Craig-Bampton et AMLS.

D'un point de vue re-conception, la modification de l'un des composants du système ne nécessite pas une reconstruction totale du modèle réduit. En effet, cette mise à jour peut être effectuée en ne recalculant uniquement que les sous-opérateurs impactés par ce changement, à l'aide de leurs expressions analytiques. La perspective majeure de ce travail est une formulation CMS de la méthode proposée, ce qui pourrait permettre de travailler sur des systèmes comprenant de nombreux composants.

Finalement, la qualité des résultats fournis par un modèle réduit est étudiée de manière *a priori*, sans connaissance des solutions HFM du problème. Couplée à un enrichissement basé sur la méthode de Krylov, cette estimation a permis de construire un algorithme d'enrichissement permettant d'affiner le modèle réduit jusqu'à obtenir la précision désirée.

Prise en compte du phénomène de contact-friction

Dans la dernière partie de ce travail de thèse le contact et la friction entre la pale et son support des deux composants est prise en compte. Ces deux phénomènes sont modélisés à l'aide des lois de Signorini et Coulomb. Une formulation bi-potentielle est adoptée pour l'expression de ces lois et l'utilisation de la méthode des différences centrées ont amené à la construction d'un algorithme pour la simulation du système.

De récents travaux s'attaquent à la réduction de modèles non linéaires. Cependant, les applications de ces travaux, sont encore restreintes à des modèles de petites tailles. Ainsi, en dernière partie, une méthode de réduction est proposée pour des simulations en temps. Cette méthode implique la réduction de l'interface de contact à l'aide d'une prédiction des efforts de contact-friction.

Contents

Table of acronyms

AMLS: Automated Multi-Level Solver
CMS: Component Mode Synthesis
CROR: Counter Rotating Open Rotor
DC: Direct Coupling
DCMS: Double Component Modes Synthesis
DoF: Degrees of Freedom
DS: Dynamic Substructuring
FE: Finite Element
FETI: Finite Element Tearing and Interconnecting
FMD: Flexible Multibody Dynamics
FMS: Flexible Multibody System
FRF: Frequency Response Function
HFM: High Fidelity Model
IRT: Institut de Recherche Technologique
KLD: Karhunen-Loève Decomposition
MAC: Modal Assurance Criterion
MTA: Modal Truncation Augmentation
NNM: Nonlinear Normal Mode
NSCD: Non-Smooth Contact Dynamics
PGR: PolyGonal Ring (constitutive part of the CROR)
POD: Proper Orthogonal Decomposition
ROM: Reduced Order Model
SAE: Safran Aircraft Engines
SVD: Singular Value Decomposition

Chapter 1

Introduction

The nowadays economic and environmental context has led a large number of manufacturers to optimize the energy consumption of their products. The aerospace has not been spared by this situation and Safran Aicraft Engine (SAE) is involved into an energy reduction logic that is notably marked by the development of a new engine based on open rotor architecture.

Developed in the frame of the European researched project Clean Sky, this new engine is referred to as CROR, that stands for Counter Rotating Open Rotor. A numerical mock-up of this engine is shown in Fig. 1.1. In 2017, the SAE's expectation about the CROR fuel consumption is a reduction of 30% compared to the current flying engines[1].

Figure 1.1 – Numerical mock up of SAE's CROR.

By definition, the open rotor is a turbine engine featuring contra rotating fan stages not enclosed within a casing. Its upstream stage corresponds to a classical turboreactor whose exhaust gases are sent to rotating ducts that drag the rotation of the engine external blade. Those blades are visible on the open rotor sketch[2] Fig. 1.2. The pitch angle of the blades is tunable, this allows to increase or decrease the engine thrust.

[1]Comparison made with the CFM56. SAFRAN. *Open rotor, le moteur du futur au banc d'essai. Available at: <http://www.safran-group.com/fr/media/20140102_open-rotor-le-moteur-du-futur-au-banc-dessai>. (20.12.2016)*

[2]Sketch from the patent: Danielson, David R. Carvalho, Paul A. Raes, Mark Perkinson, Robert H. *Counter-rotating open-rotor (CROR)*. 2011.

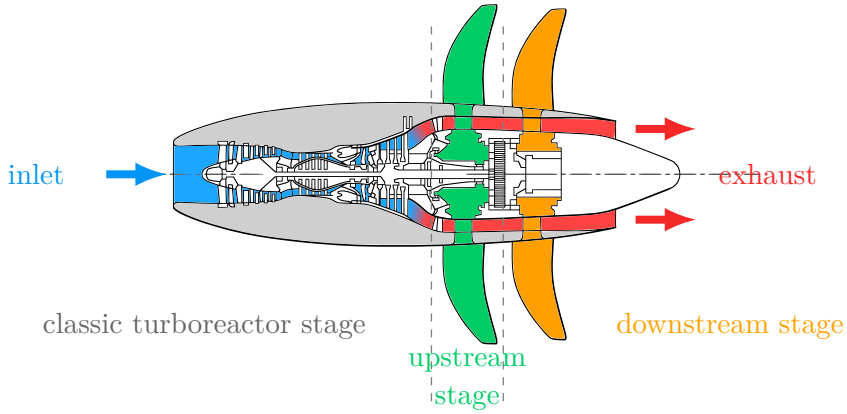

Figure 1.2 – CROR scheme. The air flows from the left to the right. The inlet gases (in blue) first go through the classical turboreactor stages. The exhaust gases (in red) cross the contra rotating blade stage in green and orange. The grey parts are not rotating. The CROR upstream stage is coloured in green while the downstream stage is in orange.

Established in 2012, the IRT SystemX provides a structure that promotes interactions and work between industrial and academic researchers. In 2013, with the wish to speed up the design process of the CROR and to share their industrial issues, SAE joined the ROM research project lead by IRT SystemX. The ROM project (Réduction et Optimisation Multi-physiques) aims at building and spreading modelling methodologies and optimization simulation algorithms for large scale systems into the industries. This partnership has resulted into the launch of the present PhD work, shared between SAE, the IRT SystemX and Supmeca.

Industrial case study: the downstream stage reduction

The case study brought by SAE deals with the model reduction of the CROR downstream system (see Fig. 1.3) in order to speed up the design of its external blades. The design and optimization of this part is indeed a key point of the engine development and is conjointly performed by different departments with regards to the system structural dynamics, acoustics and command system. The complex shape of the CROR's downstream blades has led engineers to adopt an iterative design strategy.

Mechanically, the dynamics of each new design is studied over the engine operating frequency range. In the present case, the validation of a blade design is checked by SAE through its modal analysis. This kind of study is performed numerically thanks to the finite element method, in this context however the accuracy and level of detail required involve models whose significant sizes lead to time consuming simulations. Moreover, the optimization process of the blade demand numerous validation computations that considerably slow down the design process. Nowadays, the validation of a blade design requires about 20 computation days, while only 2 days are necessary for the redesign of

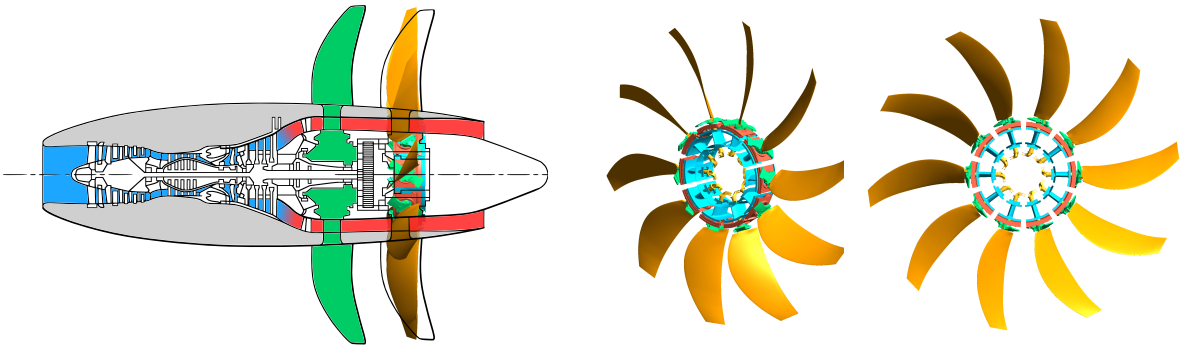

Figure 1.3 – View of the CROR dowstream stage mesh provided by SAE. For the sake of visibility, the numerous nodes and edges are not shown. The model location on the whole engine is shown on the left picture.

a new blade. For SAE, reducing the validation delay has a double impact on the system design and optimization since:

- The design of the blade is speeded up
- A better exploration of the design space is allowed

For each new design, the mesh of the blade is obtained from morphing technique, this working methodology ensure a standard and trustworthy spatial description of the blade's dynamics. Beyond this beneficial aspect, the quality of this imposed mesh might sometimes appear as uselessly high. Since no modification of the system mesh is permitted by the SAE's working procedure, investigations for the computational acceleration are oriented toward model reduction.

Industrial requirement on the reduction methodology

The main need of SAE is a reduction methodology for the system linear modal analysis, taking into account nonlinear effects is an auxiliary goal that is discussed all along this work. Strategies for including such effects are notably proposed in chapter 2 and chapter 4, but were not numerically tested on the case study. The requirements imposed by SAE about the searched reduction methodology for the modal analysis are the following ones:

- The reduction methodology should be suited for linear modal analysis
- The redesign context of the blade has to be taken into account
- The model enrichment has to be considered

Other requirements directly emerged from the available tools. Indeed, although the finite element operators were built and extracted from commercial codes, no FE code has been used for this work. Moreover, the requirement of the IRT SystemX to rely only on free softwares has led us to develop the proposed reduction methodology under Octave (GNU license).

Model characteristics & research directions

Physically, the dynamics of the open rotor is influenced by three kinds of nonlinear phenomena: the structural large displacements, the aerodynamics external loads and contact-friction phenomenon. Since the present work is mainly oriented toward modal analysis, thus the external aerodynamics loads are not taken into account.

The large displacements of the structure impact the mass finite element operator of the structure as highlighted in section 2.2.3. In spite of this, chapter 2 shows that appropriated finite element formulation can drastically reduce the number of nonlinear equations of the system and allows to consider constant flexible mass matrix M_{ff}. This justifies that the method proposed in chapter 3 and 4 that deal with constant mass matrix can be used for the reduction of a model facing large displacements nonlinearities.

The contact and friction of the CROR's constitutive parts are only considered between the blade and the hub. Indeed, the blade and the hub assembly is ensured by the engine centrifugal force. Whereas this nonlinearity remains very local, the contact between the blade and the hub occurs on a large interface and is thus not neglected.

Such interfaces lower the efficiency of most common reduction method, like the Craig-Bampton method. Being able to reduce those interfaces is then a mandatory requirement of the searched reduction methodology. A methodology involving the SAE's requirement previously highlighted and the reduction interface is proposed in chapter 3. This methodology deals with the reduction of model for the linear modal analysis and widely exploit dynamic substructuring techniques. Eventually, the a priori estimation of the solution provided by the reduced model is treated and a method for the model enrichment is proposed.

Lastly, the reduction is considered to speed up the evaluation of the damping induced by the contact and friction phenomenon. For this reason, chapter 4 points the reduction for time simulation including contact and friction behaviours.

Chapter 2

Finite element modelling of the open rotor

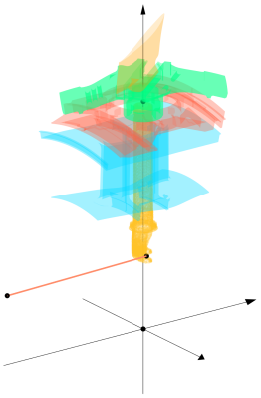

Abstract

This chapter introduces the kinematics of the open rotor and its modelling. The floating frame approach is adopted for the formulation of the current problem. Such an approach provides models with few nonlinear equations that is convenient for a subsequent model reduction.

Contents

The adjustment of the external blade pitch angle induces rotations and translations of the open rotor constitutive components. This kinematic is detailed in section 2.1. Thus, the behaviour of the system is ruled by two scale dynamics: the component large displacements and their deformations. Practically, the discipline describing the dynamics of flexible interconnected components is referred to as the flexible multibody dynamics [1].

In the field of mechanics, the finite element method is widely used to solve structural dynamics problems and can be used to solve the current problem. The large displacements induced by the component joints lead to numerous nonlinearities that modify the finite element operators of the model. In order to overcome this issue, the floating frame formulation has been developed by the flexible multibody dynamics community in the seventies. This formulation is presented in a general context in section 2.2.

The modelling of joints is a critical point in a flexible multibody dynamics model [1]. Indeed, linkages can be the source of components large displacements. Such displacement bring nonlinerities that are expected to deeply influence the system dynamics. This chapter ends with a brief discussion about the system joints and their modelling. Section 2.3 focuses on the contact interface between the blade and the hub and highlights the main concern of this work: **the reduction of large interface in structural dynamics.**

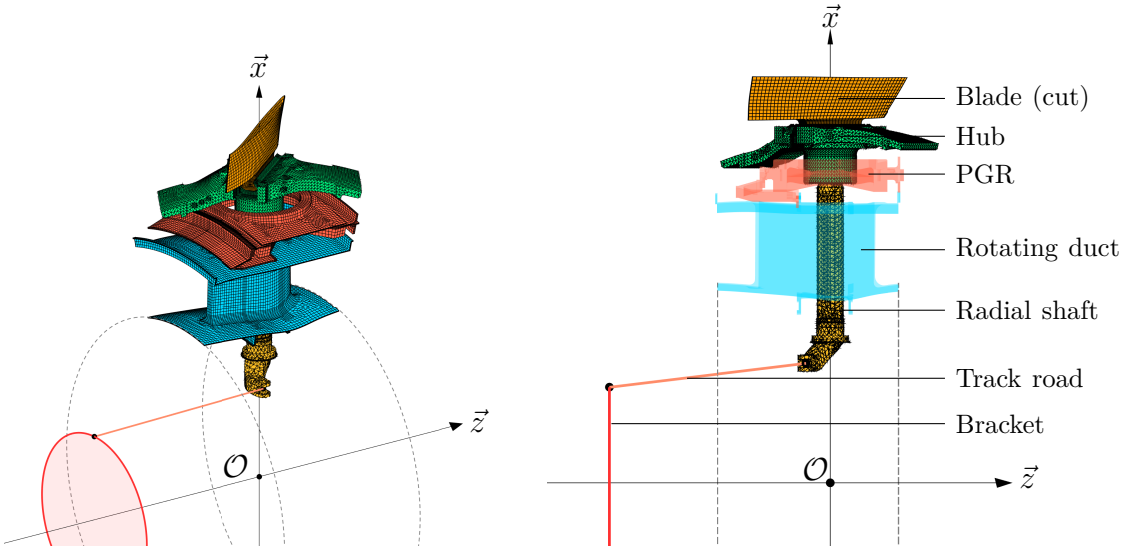

(a) Mesh associated to the assembled parts of an open rotor sector.

(b) A radial shaft allows the motion from the track road to the blade.

Figure 2.1 – View of the open rotor (downstream stage) sector mesh provided by SAE. The engine rotation axis is $\vec{z}$. The dashed lines delimit the rotating duct shape of the whole open rotor. The red disc symbolizes a bracket. As the blade is long, it has been cut on this scheme for the sake of visibility.

2.1 Open rotor kinematics

The open rotor downstream stage presents a cyclic symmetry along its rotation axis $\vec{z}$. This characteristic can notably be used to simplify the structural dynamics analysis of the system. The studied open rotor stage has 10 external blades (see Fig. 1.3) and is thus split into 10 sectors that are geometrically identical, one sector is depicted in Fig. 2.1a.

Under precise assumptions, the cyclic symmetry allows to reduce a mechanical problem by the number of identical sectors. This strategy is widely used for turbines study ([2], [3], [4]) and available in lots of industrial FE codes. Since this technique is already exploited by SAE thanks to the finite element code SAMCEF it is not investigated here.

The engine rotates around the $\vec{z}$ axis with a rotation speed $\Omega(t)$, its instantaneous angular position $\theta(t)$ (shown in Fig. 2.3) is given by $\theta(t) = \theta(t_0) + \int_{t_0}^{t} \Omega(t)dt$, this rotation axis $\vec{z}$ is shown in Fig. 2.1. Basically, the open rotor model is expressed in the fixed Galilean frame $\mathcal{R} = (\mathcal{O}, \vec{x}, \vec{y}, \vec{z})$, this frame is shown in Fig. 2.1b. The engine rotation leads to the definition of a second referential $\mathcal{R}_\theta = (\mathcal{O}_\theta, \vec{x}_\theta, \vec{y}_\theta, \vec{z}_\theta)$ (see Fig. 2.3), this frame follows the rotation of the studied sector around the $\vec{z}$ axis.

In this section, the open rotor model produced by SAE and its kinematics are first described, then a method for the evaluation of the system configuration is proposed. The six constitutive parts of each sectors are described below:

- **a blade** that enables to increase (or decrease) the engine thrust by blowing the air that flows out of the reactor, along the engine fuselage.

- **a hub** that maintains the blade on the rotor and grants its rotation on the radial axis. Depending on the analysis, this linkage is either modelled by the perfect bonding of the two parts (chapter 3) or by a simple contact (chapter 4) imposed by the centrifugal force.

- **a track road** that is used to set the blade pitch angle α thanks to a rigid bracket that is linked to one of its end. The track road is linked to the bracket and a radial shaft thanks to spherical joints and modelled as a flexible beam.

- **a radial shaft** that ensure the motion transmission from the bracket to the blade. The radial shaft is assembled with the hub through fluting. In practice, this linkage is modelled by the perfect bonding of the two parts. The radial shaft is linked to a polygonal ring through a ball bearing that is not modelled.

- **a polygonal ring** (PGR) at the interface between the engine interior and external

environment. The polygonal ring is fixed in the rotating frame $\mathcal{R}_\theta$. The PGR is linked to a rotating duct thanks to bolted joints.

- **a rotating duct**, this part both aims at driving the exhaust gases of the classical reactor level and sheltering the radial shaft from this gas flow (see Fig. 2.1b). The rotating duct is fixed in the rotating frame $\mathcal{R}_\theta$.

The components of the present system are connected in an open loop configuration. The tuning of the pitch angle α is performed thanks to the positioning $p(t)$ of a bracket on the rotation axis $\vec{z}$. The track road ends (respectively denoted $\mathcal{A}$ and $\mathcal{B}$) are linked to this bracket and to the radial shaft. The translation of the bracket along $\vec{z}$ tends to modify the pitch angle α.

Three main kinematic classes can be identified: the first class (1) is fixed in the rotating referential $\mathcal{R}_\theta$, it involves the rotating frame and the polygonal ring. The second kinematic class (2) contains the parts rotating both on the $\vec{z}$ and $\vec{x}_\theta$ axis: the blade, the hub and the shaft. A third kinematic class (3) contains the track road only. The linkage between the parts and their modelling are summed up in Fig. 2.2.

For a better comprehension of the system kinematics, let us define some points of interest. The point $\mathcal{A}$ corresponds to the center of the spherical linkage between the bracket and the track road. The point $\mathcal{B}$ is the center of the spherical joint between the track road and the radial shaft (see Fig. 2.3 and Fig. 2.4). The point $\mathcal{C}$ is located on the center of the hinge between the radial shaft and the polygonal ring. The center of the fixed and rotating referential $\mathcal{O}$ and $\mathcal{O}_\theta$ coincide. Those points are depicted in Fig. 2.3.

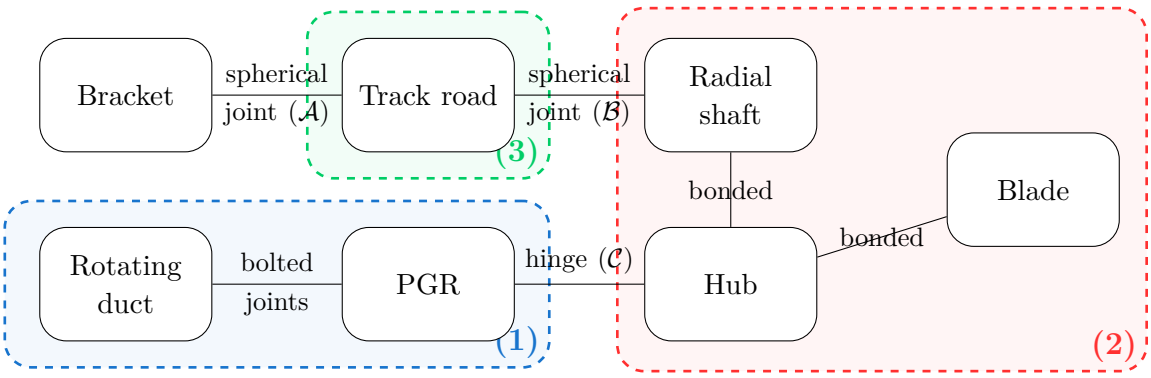

Figure 2.2 – Components of an open rotor sector and the modelling of their linkages. Kinematic classes are represented and numbered using coloured squares.

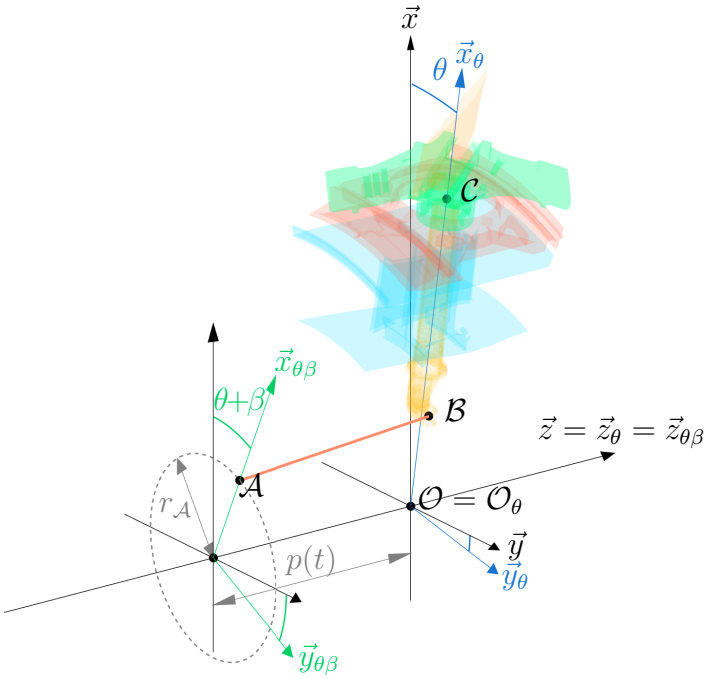

Figure 2.3 – View of the relative positioning of the referential $\mathcal{R}_\theta$ and $\mathcal{R}_{\theta\beta}$. The dashed circle corresponds to the bracket radius.

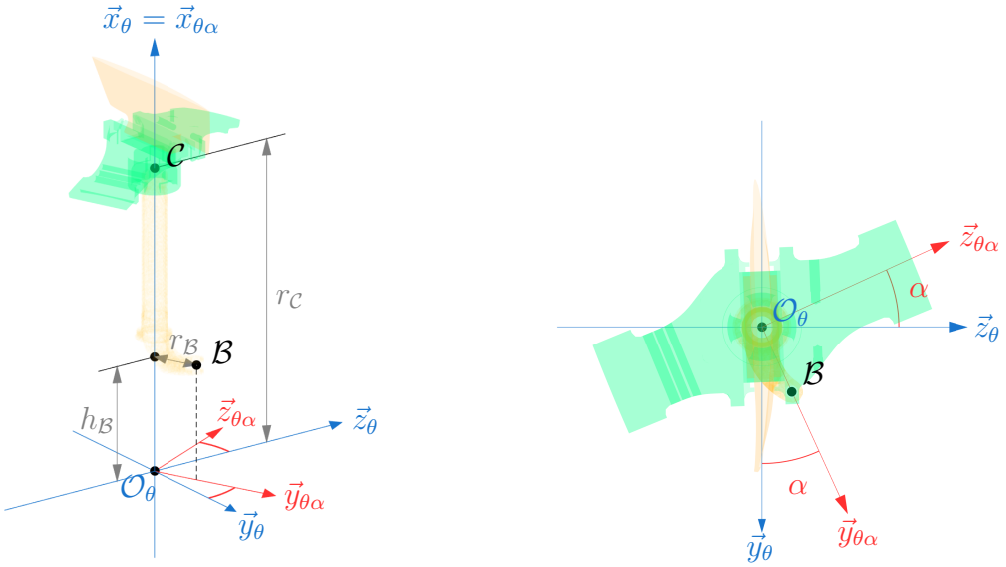

Figure 2.4 – View of the relative positioning of the referential $\mathcal{R}_\theta$ and $\mathcal{R}_{\theta\alpha}$.

The angular position of the engine in the fixed frame of reference $\mathcal{R} = (\mathcal{O}, \vec{x}, \vec{y}, \vec{z})$ is referred to as θ and shown in Fig. 2.3. The point $\mathcal{C}$ is defined as the theoretical center of the ball bearing between the hub and the radial shaft. This point is fixed in the rotating frame $\mathcal{R}_\theta = (\mathcal{O}_\theta, \vec{x}_\theta, \vec{y}_\theta, \vec{z}_\theta)$, the distance between $\mathcal{C}$ and the rotation axis $\vec{z}$ is $r_\mathcal{C}$ (see Fig. 2.3). The position of $\mathcal{C}$ can be simply express in the frame $\mathcal{R}_\theta$ as:

$$\mathcal{C}(t) = r_\mathcal{C}\vec{x}_\theta \quad \text{with} \quad \vec{x}_\theta = \cos(\theta)\vec{x} + \sin(\theta)\vec{y}.$$

The first end of the track road, that is linked to the bracket, is attached to the rotation frame $\mathcal{R}_{\theta\beta}$ in $\mathcal{A}$. The point $\mathcal{A}$ is also attached to the hinge (represented as a red circle) and follows the engine rotation θ on the axis $\vec{z}$ with an angular shift β. The radius of the bracket is $r_\mathcal{A}$ and its imposed position along $\vec{z}$ is $p(t)$ (see Fig. 2.3). Hence the position of the track road end can be described using three parameters, $r_\mathcal{A}$, β and $p(t)$ as follows:

$$\mathcal{A}(t) = p(t)\vec{z} + r_\mathcal{A}\vec{x}_{\theta\beta} \quad \text{with} \quad \vec{x}_{\theta\beta} = \cos(\theta+\beta)\vec{x} + \sin(\theta+\beta)\vec{y}. \tag{2.1}$$

The pitch angle α of the blade is defined in the rotating frame $\mathcal{R}_\theta = (\mathcal{O}_\theta, \vec{x}_\theta, \vec{y}_\theta, \vec{z}_\theta)$. It is used to locate the second track road end: $\mathcal{B}$. Indeed, the angle α is defined so that $\mathcal{B}$ is placed along $\vec{y}_\theta$ for a null pitch ($\alpha = 0$). The distance between $\mathcal{B}$ and its rotation axis $\vec{x}_\theta$ is $r_\mathcal{B}$ while $h_\mathcal{B}$ is its coordinate on $\vec{x}_\theta$ (see Fig. 2.4). The position of $\mathcal{B}$ is then defined thanks to three parameters α, $r_\mathcal{B}$ and $h_\mathcal{B}$ so that:

$$\mathcal{B}(t) = h_\mathcal{B}\vec{x}_\theta + r_\mathcal{B}\vec{y}_{\theta\alpha} \quad \text{with} \quad \vec{y}_{\theta\alpha} = \cos(\alpha)\vec{y}_\theta + \sin(\alpha)\vec{z}_\theta. \tag{2.2}$$

Geometrical evaluation of the system configuration

In the previous section, the kinematics of the open rotor has been presented, let us see now how the configuration of the system can be evaluated. In the present case, the system configuration is ruled by three variables: $p(t)$, β and α. Considering the parts as rigid and weightless, this matter can be answered using a geometrical approach. The track road length is constant and denoted L, this distance can be expressed in the rotating frame in function of the system parameters:

$$L = \|\overrightarrow{\mathcal{AB}}\| = \|\overrightarrow{\mathcal{O}_\theta\mathcal{B}} - \overrightarrow{\mathcal{O}_\theta\mathcal{A}}\|.$$

The vectors $\overrightarrow{\mathcal{O}_\theta\mathcal{A}}$ and $\overrightarrow{\mathcal{O}_\theta\mathcal{B}}$ give the positions of the nodes $\mathcal{A}$ and $\mathcal{B}$ in the rotating frame $\mathcal{R}_\theta$. Those positions are respectively expressed by Eq. (2.1) and Eq. (2.2). This allows to express the square of the track road length L^2 as a function of the time variables $p(t)$, $\alpha(t)$ and $\beta(t)$:

$$\overrightarrow{\mathcal{AB}} = \Big(h_\mathcal{B} - r_\mathcal{A}\cos(\beta)\Big)\vec{x}_\theta + \Big(r_\mathcal{B}\cos(\alpha) - r_\mathcal{A}\sin(\beta)\Big)\vec{y}_\theta + \Big(r_\mathcal{B}\sin(\alpha) - p(t)\Big)\vec{z}_\theta, \tag{2.3}$$

$$L^2 = \left\|\overrightarrow{\mathcal{AB}}\right\|^2 = \Big(h_\mathcal{B} - r_\mathcal{A}\cos(\beta)\Big)^2 + \Big(r_\mathcal{B}\cos(\alpha) - r_\mathcal{A}\sin(\beta)\Big)^2 + \Big(r_\mathcal{B}\sin(\alpha) - p(t)\Big)^2. \tag{2.4}$$

The expansion of the previous equation and the use of auxiliaries variables a, b and c leads to the following expressions:

$$\Big(r_{\mathcal{A}}\sin(\beta)\cos(\alpha)+p(t\sin(\alpha)\Big)=\frac{1}{2r_{\mathcal{B}}}\Big(h_{\mathcal{B}}^2+r_{\mathcal{A}}^2+r_{\mathcal{B}}^2+p(t)^2-L^2-2h_{\mathcal{B}}r_{\mathcal{A}}\cos(\beta)\Big). \quad (2.5)$$

An analytical expression of the pitch angle α can be established. The left term of Eq. (2.5) can be identified to the following equation

$$a\cos(\alpha)+b\sin(\alpha)=\frac{a}{\cos\left(\operatorname{atan}\left(\frac{b}{a}\right)\right)}\cos\left(\alpha-\operatorname{atan}\left(\frac{b}{a}\right)\right),\ \text{with}\ \begin{cases}a=r_{\mathcal{A}}\cos(\beta),\\ b=p(t).\end{cases} \quad (2.6)$$

For the sake of clarity, two auxiliary variables a and b are defined. Let us define a third variable ξ so that:

$$\xi=\operatorname{atan}\left(\frac{b}{a}\right). \quad (2.7)$$

From the relation established in Eq. (2.6) and the notation ξ previously defined in Eq. (2.7) it is possible to give an analytical expression of the pitch angle α in regard to the system parameters

$$\alpha=\xi+\operatorname{acos}\left(\frac{\cos(\xi)}{2r_{\mathcal{A}}r_{\mathcal{B}}}\left(h_{\mathcal{B}}^2+r_{\mathcal{A}}^2+r_{\mathcal{B}}^2+p(t)^2-L^2-2h_{\mathcal{B}}r_{\mathcal{A}}\cos(\beta)\right)\right). \quad (2.8)$$

This formula Eq. (2.8) allows then to build abacus of the system pitch angle for different hinge position $p(t)$ and shift angles β. Note that this formula is only true for non-null shift angle ($\beta \neq 0$). In order to bypass this issue it is possible to compute α from Eq. (2.4) thanks to a Newton-Raphson procedure.

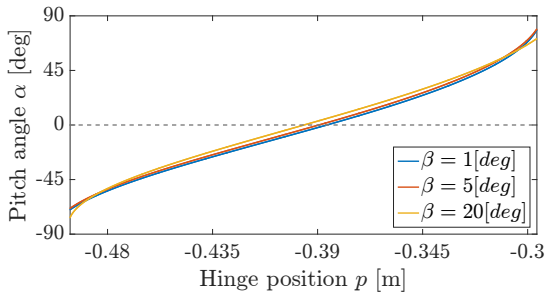

Figure 2.5 – Pitch angle α given for different bracket positions p and shift angles β.

2.2 Flexible multibody modelling approaches using the finite element method

In section 2.1, a method for the evaluation of the open rotor configuration with regards to the bracket position has been presented. Hence, it is possible to study the open rotor dynamics for a given working point (i.e. imposed track road position) using the finite element method.

The knowledge of the system configuration allows to build its finite element model for an imposed position of the bracket. In addition to that, the hypothesis of small deformations, that is assumed here, leads to a linear model of the system dynamics. Such a model provides accurate results when translations and rotations of the components remain negligible. This approach assumes that the structural dynamics can be described linearly by its flexible motion $\boldsymbol{u}$ and acceleration $\ddot{\boldsymbol{u}}$, in practice, this leads to finite element model involving the well known dynamic equation:

$$\mathrm{M}\ddot{\boldsymbol{u}}(t) + \mathrm{K}\boldsymbol{u}(t) = \boldsymbol{f}(t). \tag{2.9}$$

The matrices M and K respectively refer to mass and stiffness finite element operators. Because of its linearity, the structural analysis of such a model is convenient. From the position of the bracket, a straightforward algorithm can be established for the linear finite element analysis of the open rotor, see Fig. 2.6. The configuration is first computed with Eq. (2.8), then the finite element operators of the system are built with regards to the component configurations (i.e. p, β and α).

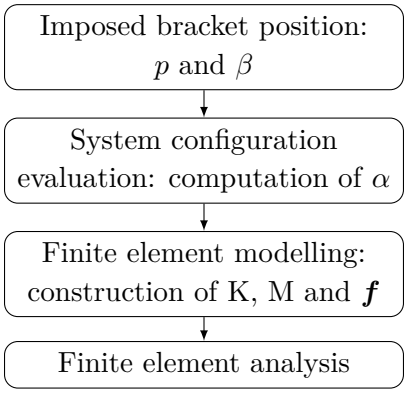

Figure 2.6 – Direct procedure for the open rotor dynamics analysis, considering an imposed working configuration. The system is studied using the finite element model whose configuration has been previously evaluated.

The procedure presented in Fig. 2.6 can be used to give a quick approximation of a system dynamics. However, it can not be used to treat the open rotor dynamics since rotations and translation of the system are nonnegligible. Moreover, the strategy presented in Fig.

2.6 requires the update of the finite element operators when the system configuration changes. Practically, the construction of the finite element operator is a consequent task associated to nonnegligible computational cost. Indeed, these operators are computed through several numerical integrations over the numerous element of the model mesh. Furthermore, the approach described in Fig. 2.6 assumes a decoupling between the rigid motions of the parts (rotations and translations) and their elastic deformations.

In order to tackle these issues, it is possible to consider conjointly the flexibility and large displacements of the components. The strategies used to solve such a problem match with the definition of flexible multibody dynamics (FMD) given by Wasfy and Noor in [5]. The flexible multibody systems (FMS) have been studied from the 1970's and still feed a large number of publications and conferences [5].

The more natural way to describe the dynamics of a FMS is to use a fixed frame. This formulation is refereed in the literature as inertial frame approach and provides fully nonlinear models. The main advantage of this technique is that the rigid and flexible motions are described with a high precision in any configuration. Note that the rigid and flexible motions are expressed by the same DoF. The formulation of such a problem is complex and its construction might be time consuming. Moreover, the resolution and reduction of this model are rather complicated due to its numerous nonlinear equations.

Over the years, methods involving intermediate reference frames attached to the flexible components have been developed. Those methods allow to appropriately take into account the effects induced by the large displacements. Such methods directly distinguish the rigid and flexible motions of a structure, that is not straightforward with a fully nonlinear approach. Two main approaches can be cited for the study of flexible multibody dynamics:

- the corotational frame approach has been developed by Belytschko and Hsieh [6]. This formulation uses a local referential attached to each element and the global system referential (inertial frame) to express the motion of the structure. This approach is useful for the study of nonlinear system undergoing small deformations and large displacements. This method is however hardly compatible with linear model reduction as a large number of equations remain nonlinear.

- the floating frame approach [7] is the natural way to extend rigid multibody dynamics to flexible multibody system. This method consists in using a floating frame attached to each part or kinematic class. Hence, in the present case, this leads to a small number of nonlinear equations (as the current system own only 3 kinematic objects). Consequently, linear model reduction can be reasonably considered.

The floating frame approach appears to be the best choice to treat the current FMD

(flexible multibody dynamics) problem since it provides model with a restrained number a nonlinear equations and allows further model reduction.

In this section, the floating frame formulation is described in a general way. First, the Ritz approximation and Hamilton principle are reminded in section 2.2.1. The displacement quantity, velocity and acceleration of a point are then described in section 2.2.2. Next, section 2.2.3 highlights the construction of the finite element operator associated to the floating frame formulation. Eventually, assumptions and strategies for a quick update of these finite element operators are presented in section 2.2.4.

2.2.1 Hamilton principle and Ritz discretization

According to the principle of least action, the evolution of a system state minimizes its action. Since this action is characterized by its position u and velocity $\dot{u}$, the system state is the one that satisfies:

$$\min_{\dot{u},u} \int_t \big(\mathcal{W}_a - \mathcal{W}_e - \mathcal{W}_f\big)\mathrm{d}t = \min_{\dot{u},u} \int_t \mathcal{J}(\dot{u},u)\mathrm{d}t. \tag{2.10}$$

$\mathcal{W}_a$, $\mathcal{W}_e$ and $\mathcal{W}_f$ are respectively the energies of the system brought by its acceleration, elastic deformations and external load. The functional $\mathcal{J}$ corresponds to the system energy. Since this energy $\mathcal{J}$ is defined and positive, the solution of Eq. (2.10) is also solution of the algebraic equation:

$$\delta\mathcal{J} = \delta\mathcal{W}_a - \delta\mathcal{W}_e - \delta\mathcal{W}_f = 0. \tag{2.11}$$

The Ritz method, developed in 1909, enables to discretize a functional using an approximation of the fields u, $\dot{u}$, $\ddot{u}$. Each field is approximated as a sum of n functions N_i, all the functions N_i are associated to a degree of freedom u_i, $\dot{u}_i$ or $\ddot{u}_i$ (DoF) so that:

$$u = \sum_{i=1}^{n} \mathrm{N}_i u_i = \mathrm{N}\boldsymbol{u} \quad , \quad \dot{u} = \sum_{i=1}^{n} \mathrm{N}_i \dot{u}_i = \mathrm{N}\dot{\boldsymbol{u}} \quad \text{and} \quad \ddot{u} = \sum_{i=1}^{n} \mathrm{N}_i \ddot{u}_i = \mathrm{N}\ddot{\boldsymbol{u}}. \tag{2.12}$$

The work quantities $\delta\mathcal{W}_a$, $\delta\mathcal{W}_e$ and $\delta\mathcal{W}_f$ can then be expressed in a matrix way thanks to the finite element operators M, K and $\boldsymbol{f}$ so that:

$$\delta\mathcal{W}_a = \delta\boldsymbol{u}^\top \mathrm{M}\ddot{\boldsymbol{u}} \quad , \quad \delta\mathcal{W}_e = \delta\boldsymbol{u}^\top \mathrm{K}\boldsymbol{u} \quad \text{and} \quad \delta\mathcal{W}_f = \delta\boldsymbol{u}^\top \boldsymbol{f}. \tag{2.13}$$

The construction of the operators M, K and $\boldsymbol{f}$ is highlighted in section 2.2.3. The finite element method use nodal basis for the discretization of the fields u, $\dot{u}$, $\ddot{u}$. Whereas the Ritz solution is not exact its accuracy increases with the number of degrees of freedom (i.e. the number of nodes of the associated mesh).

2.2.2 Floating frame formulation

The floating frame formulation splits the model coordinate into a flexible and a rigid part. Consequently, the system configuration doesn't bind to an entire update of the operators M and K (unlike the fully nonlinear approach or the method presented in Fig. 2.6). This feature is the main advantage of the floating frame formulation.

In this section, the position $\boldsymbol{u}_{\mathcal{P}}^{\mathcal{R}}$ of a point $\mathcal{P}$ of a structure Σ whose mesh is defined in a Galilean frame $\mathcal{R}$ is studied. A floating frame $\mathcal{R}^\star$ is attached to the mesh of the considered part, so that the position of $\mathcal{P}$ in the local frame $\mathcal{R}^\star$ is noted $\boldsymbol{u}_{\mathcal{P}}^{\mathcal{R}^\star}$, see Fig. 2.7.

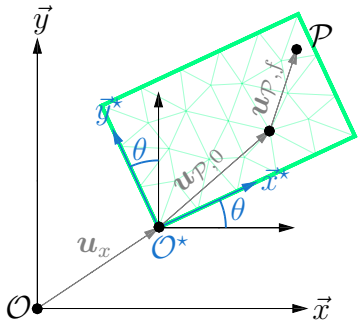

Figure 2.7 – Structure undergoing deformation associated to large displacement. The frame $\mathcal{R} = (\mathcal{O}, \vec{x}, \vec{y})$ is fixed while $\mathcal{R}^\star = (\mathcal{O}^\star, \vec{x}^\star, \vec{y}^\star)$ is attached to the mesh of the component Σ.

The relative positioning of the two referentials $\mathcal{R}$ and $\mathcal{R}^\star$ is expressed thanks to two set of parameters: the vector $\boldsymbol{u}_x = \overrightarrow{\mathcal{O}\mathcal{O}^\star}$ and the vector $\boldsymbol{u}_\theta$ that contains the angular position of $\mathcal{R}^\star$ in $\mathcal{R}$.

In the local referential $\mathcal{R}^\star$, the position $\boldsymbol{u}_{\mathcal{P}}^{\mathcal{R}^\star}$ of $\mathcal{P}$ is split into two parts: $\boldsymbol{u}_{\mathcal{P},0}$ and $\boldsymbol{u}_{\mathcal{P},f}$. The notation $\boldsymbol{u}_{\mathcal{P},0}$ denotes the position of the $\mathcal{P}$ in $\mathcal{R}^\star$, when no deformation is assumed. The term $\boldsymbol{u}_{\mathcal{P},f}$ corresponds to the displacement of the point $\mathcal{P}$ due to the structure deformation. Hence, the position of $\mathcal{P}$ can be expressed in $\mathcal{R}$ as:

$$\boldsymbol{u}_{\mathcal{P}}^{\mathcal{R}} = \boldsymbol{u}_x + \mathrm{R}(\boldsymbol{u}_\theta) \underbrace{\left(\boldsymbol{u}_{\mathcal{P},0} + \boldsymbol{u}_{\mathcal{P},f}\right)}_{\boldsymbol{u}_{\mathcal{P}}^{\mathcal{R}^\star}}.$$

While $\boldsymbol{u}_\theta$ is a vector that contains all the angular parameters of the system, the term $\mathrm{R}(\boldsymbol{u}_\theta)$ corresponds to a rotation matrix. The variables $\boldsymbol{u}_{\mathcal{P},0}$ and $\boldsymbol{u}_{\mathcal{P},f}$ are defined in the floating frame $\mathcal{R}^\star$. In a more general way, let the notation $\boldsymbol{u}_0$ and $\boldsymbol{u}_f$ refer to vectors containing the initial positions and displacements of all the nodes of the considered

finite element model. The position $\boldsymbol{u}_{\mathcal{P}}^{\mathcal{R}}$ can be rewritten thanks to the use of a constant interpolation matrix $\mathrm{N}_{\mathcal{P}}$ as:

$$\boldsymbol{u}_{\mathcal{P}}^{\mathcal{R}} = \boldsymbol{u}_x + \mathrm{R}(\boldsymbol{u}_\theta) \underbrace{\mathrm{N}_{\mathcal{P}}\Big(\boldsymbol{u}_0 + \boldsymbol{u}_f\Big)}_{\boldsymbol{u}_{\mathcal{P}}^{\mathcal{R}^\star}}. \tag{2.14}$$

It is worth noticing that the formulation Eq. (2.14) is only valid if the shape function matrix $\mathrm{N}_{\mathcal{P}}$ does not admit rigid body motions in the floating frame [7]. Otherwise, the large displacements of a structure would be both described by the rigid coordinates $\boldsymbol{u}_x$, $\boldsymbol{u}_\theta$ and by the rigid body motions defined in the local referential $\mathcal{R}^\star$.

The position of the local frame $\mathcal{R}^\star$ (see Fig. 2.7) is part of the floating frame formulation unknown as well as the structure flexible motions $\boldsymbol{u}_f$. Since the position of $\mathcal{R}^\star$ is characterized by the variables $\boldsymbol{u}_x$ and $\boldsymbol{u}_\theta$, the problem coordinate vector $\boldsymbol{u}$ is organized as follows:

$$\boldsymbol{u} = \begin{Bmatrix} \boldsymbol{u}_x \\ \boldsymbol{u}_\theta \\ \boldsymbol{u}_f \end{Bmatrix}.$$

The main principle of the floating frame formulation has been introduced in this section: it consists in splitting the rigid and flexible motions of a structure. Now let us see how to describe the rotation $\mathrm{R}(\boldsymbol{u}_\theta)$ between the intermediate frame $\mathcal{R}^\star$ and the reference frame $\mathcal{R}$.

Spherical motion description

Among the well-known rotation descriptions used in the flexible multibody dynamics field, Bryan (nautical) and Euler angles can be cited. Although Bryant angles have been adopted by the flight mechanics engineers, the present work relies on the use of the Euler angles to express the angular position of the floating frame. Indeed, Euler angles provide the most intuitive kinematic description of rotating systems [1]. Moreover, Euler angles are defined relatively to themselves, this is depicted in Fig. 2.8.

Such an angular description allows us to express the global rotation matrix $\mathrm{R}(\boldsymbol{u}_\theta)$ of the structure Σ as the multiplication of elementary rotation matrix $\mathrm{R}_{\theta_\mathrm{i}}$. In a three dimensional space, the rotation matrix $\mathrm{R}(\boldsymbol{u}_\theta)$ is then defined as the product:

$$\mathrm{R}(\boldsymbol{u}_\theta) = \mathrm{R}_{\theta_1}(u_{\theta_1}) \times \mathrm{R}_{\theta_2}(u_{\theta_2}) \times \mathrm{R}_{\theta_3}(u_{\theta_3}). \tag{2.15}$$

It has to be noticed that in practice, geometric parameters have a serious drawback since rotation matrix becomes singular for critical angles. Moreover, the evaluation of sine and cosine functions involved in the rotation matrix R_{θ_i} lead to numerical imprecision [8].

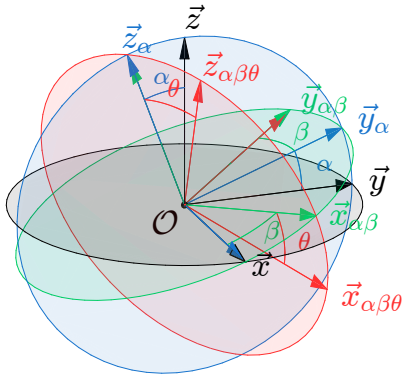

Figure 2.8 – Example of the Euler description of a rotation. The referential $\mathcal{R}_\alpha = (\mathcal{O}, \vec{x}_\alpha, \vec{y}_\alpha, \vec{z}_\alpha)$ is defined as the rotation α around the axis $\vec{x}$ of $\mathcal{R} = (\mathcal{O}, \vec{x}, \vec{y}, \vec{z})$. The referential $\mathcal{R}_{\alpha\beta} = (\mathcal{O}, \vec{x}_{\alpha\beta}, \vec{y}_{\alpha\beta}, \vec{z}_{\alpha\beta})$ is defined as the rotation β around the axis $\vec{z}_\alpha$ of $\mathcal{R}_\alpha$. The referential $\mathcal{R}_{\alpha\beta\theta} = (\mathcal{O}, \vec{x}_{\alpha\beta\theta}, \vec{y}_{\alpha\beta\theta}, \vec{z}_{\alpha\beta\theta})$ is defined as the rotation θ around the axis $\vec{y}_{\alpha\beta}$ of $\mathcal{R}_{\alpha\beta}$.

In order to later study the kinematics and dynamics of any point $\mathcal{P}$, the quantity and derivation of the rotation matrix are now presented. The quantity $\delta\mathrm{R}$ and the derivative $d\mathrm{R}$ of the rotation matrix R are rather analogous:

$$\delta\mathrm{R} = \sum_{i=1}^{n_\theta} \frac{\partial \mathrm{R}}{\partial u_{\theta_i}} \delta u_{\theta_i} \quad \text{and} \quad d\mathrm{R} = \sum_{i=1}^{n_\theta} \frac{\partial \mathrm{R}}{\partial u_{\theta_i}} du_{\theta_i}. \tag{2.16}$$

The tensor notation can provide a more compact expression of Eq. (2.16) in which the sums are implicitly performed through the contracted product denoted $\cdot$. Furthermore, using the tensor product $\otimes$ enables to express $\delta\mathrm{R}$ and $\frac{d\mathrm{R}}{dt}$ as:

$$\delta\mathrm{R} = (\nabla_{\boldsymbol{u}_\theta} \otimes \mathrm{R}) \cdot \delta \boldsymbol{u}_\theta \quad \text{and} \quad \frac{d\mathrm{R}}{dt} = (\nabla_{\boldsymbol{u}_\theta} \otimes \mathrm{R}) \cdot \dot{\boldsymbol{u}}_\theta. \tag{2.17}$$

The gradient denoted $\nabla_{\boldsymbol{u}_\theta}$ is used for the derivation with regards to angular coordinates u_{θ_i}. Thus, the tensor resulting from the product $(\nabla_{\boldsymbol{u}_\theta} \otimes \mathrm{R})$ is of third order and its elements are defined as:

$$[\nabla_{\boldsymbol{u}_\theta} \otimes \mathrm{R}]_{(k,i,j)} = \frac{\partial [\mathrm{R}]_{(i,j)}}{\partial u_{\theta_k}}.$$

The operator $[\bullet]_{(k,i,j)}$ returns the indexed term (k, i, j) of a tensor. When multiplied by any vector $\boldsymbol{v}$, the associativity of the tensor contraction, coupled to its commutativity for vectors (tensor of order one) allow to write:

$$\delta\mathrm{R}\boldsymbol{v} = \Big((\nabla_{\boldsymbol{u}_\theta} \otimes \mathrm{R}) \cdot \boldsymbol{v}\Big)\delta \boldsymbol{u}_\theta, \tag{2.18}$$

$$\frac{d\mathrm{R}}{dt}\boldsymbol{v} = \Big((\nabla_{\boldsymbol{u}_\theta} \otimes \mathrm{R}) \cdot \boldsymbol{v}\Big)\dot{\boldsymbol{u}}_\theta. \tag{2.19}$$

Let us express now the second time derivative of the rotation matrix R. This derivation can be written thanks to the relation established previously in Eq. (2.17):

$$\frac{d^2\mathrm{R}}{dt^2} = \frac{d}{dt}\Big((\nabla_{\boldsymbol{u}_\theta} \otimes \mathrm{R}) \cdot \dot{\boldsymbol{u}}_\theta\Big) = (\nabla_{\boldsymbol{u}_\theta} \otimes \mathrm{R}) \cdot \ddot{\boldsymbol{u}}_\theta + \Big(\nabla_{\boldsymbol{u}_\theta} \otimes (\nabla_{\boldsymbol{u}_\theta} \otimes \mathrm{R}) \cdot \dot{\boldsymbol{u}}_\theta\Big) \cdot \dot{\boldsymbol{u}}_\theta. \tag{2.20}$$

Considering a structure undergoing three rotations the term $\Big(\nabla_{\boldsymbol{u}_\theta} \otimes (\nabla_{\boldsymbol{u}_\theta} \otimes \mathrm{R}) \cdot \dot{\boldsymbol{u}}_\theta\Big) \cdot \dot{\boldsymbol{u}}_\theta$ of Eq. (2.20) can be expanded as:

$$\Big(\nabla_{\boldsymbol{u}_\theta} \otimes (\nabla_{\boldsymbol{u}_\theta} \otimes \mathrm{R}) \cdot \dot{\boldsymbol{u}}_\theta\Big) \cdot \dot{\boldsymbol{u}}_\theta = \begin{pmatrix} \frac{\partial^2}{\partial u_{\theta_1}^2}\mathrm{R}\dot{u}_{\theta_1} + \frac{\partial^2}{\partial u_{\theta_1}\partial u_{\theta_2}}\mathrm{R}\dot{u}_{\theta_2} + \frac{\partial^2}{\partial u_{\theta_2}\partial u_{\theta_3}}\mathrm{R}\dot{u}_{\theta_3} \\ \frac{\partial^2}{\partial u_{\theta_1}\partial u_{\theta_2}}\mathrm{R}\dot{u}_{\theta_1} + \frac{\partial^2}{\partial u_{\theta_2}^2}\mathrm{R}\dot{u}_{\theta_2} + \frac{\partial^2}{\partial u_{\theta_2}\partial u_{\theta_3}}\mathrm{R}\dot{u}_{\theta_3} \\ \frac{\partial^2}{\partial u_{\theta_1}\partial u_{\theta_3}}\mathrm{R}\dot{u}_{\theta_1} + \frac{\partial^2}{\partial u_{\theta_2}\partial u_{\theta_3}}\mathrm{R}\dot{u}_{\theta_2} + \frac{\partial^2}{\partial u_{\theta_3}^2}\mathrm{R}\dot{u}_{\theta_3} \end{pmatrix} \cdot \begin{pmatrix} \dot{u}_{\theta_1} \\ \dot{u}_{\theta_2} \\ \dot{u}_{\theta_3} \end{pmatrix}$$

$$= \frac{\partial^2\mathrm{R}}{\partial u_{\theta_1}^2}\dot{u}_{\theta_1}^2 + \frac{\partial^2\mathrm{R}}{\partial u_{\theta_2}^2}\dot{u}_{\theta_2}^2 + \frac{\partial^2\mathrm{R}}{\partial u_{\theta_3}^2}\dot{u}_{\theta_3}^2 + 2\frac{\partial^2\mathrm{R}}{\partial u_{\theta_1}\partial u_{\theta_2}}\dot{u}_{\theta_1}\dot{u}_{\theta_2} + 2\frac{\partial^2\mathrm{R}}{\partial u_{\theta_2}\partial u_{\theta_3}}\dot{u}_{\theta_2}\dot{u}_{\theta_3} + 2\frac{\partial^2\mathrm{R}}{\partial u_{\theta_3}\partial u_{\theta_1}}\dot{u}_{\theta_3}\dot{u}_{\theta_1}.$$

The definition of new coordinates $\dot{\boldsymbol{u}}_\theta^2$ and a new gradient $\nabla_{\boldsymbol{u}_\theta^2}$ allow a more interesting expression of Eq. (2.20). Assuming three rotations we define the variables $\dot{\boldsymbol{u}}_\theta^2$ and $\nabla_{\boldsymbol{u}_\theta^2}$ as

$$\dot{\boldsymbol{u}}_\theta^2 = \begin{bmatrix} \dot{u}_{\theta_1}^2 & \dot{u}_{\theta_2}^2 & \dot{u}_{\theta_3}^2 & \dot{u}_{\theta_1}\dot{u}_{\theta_2} & \dot{u}_{\theta_2}\dot{u}_{\theta_3} & \dot{u}_{\theta_3}\dot{u}_{\theta_1} \end{bmatrix}^\top \tag{2.21}$$

$$\nabla_{\boldsymbol{u}_\theta^2} = \begin{bmatrix} \frac{\partial^2}{\partial u_{\theta_1}^2} & \frac{\partial^2}{\partial u_{\theta_2}^2} & \frac{\partial^2}{\partial u_{\theta_3}^2} & 2\frac{\partial^2}{\partial u_{\theta_1}\partial u_{\theta_2}} & 2\frac{\partial^2}{\partial u_{\theta_2}\partial u_{\theta_3}} & 2\frac{\partial^2}{\partial u_{\theta_3}\partial u_{\theta_1}} \end{bmatrix}^\top. \tag{2.22}$$

Hence, Eq. (2.20) can be written in a more convenient way as:

$$\frac{d^2\mathrm{R}}{dt^2} = (\nabla_{\boldsymbol{u}_\theta} \otimes \mathrm{R}) \cdot \ddot{\boldsymbol{u}}_\theta + \Big(\nabla_{\boldsymbol{u}_\theta} \otimes (\nabla_{\boldsymbol{u}_\theta} \otimes \mathrm{R}) \cdot \dot{\boldsymbol{u}}_\theta\Big) \cdot \dot{\boldsymbol{u}}_\theta \tag{2.23}$$

$$= (\nabla_{\boldsymbol{u}_\theta} \otimes \mathrm{R}) \cdot \ddot{\boldsymbol{u}}_\theta + (\nabla_{\boldsymbol{u}_\theta^2} \otimes \mathrm{R}) \cdot \dot{\boldsymbol{u}}_\theta^2. \tag{2.24}$$

Analogously to Eq. (2.19), tensor properties enables to express the vector $\frac{d^2\mathrm{R}}{dt^2}\boldsymbol{v}$ as:

$$\frac{d^2\mathrm{R}}{dt^2}\boldsymbol{v} = \Big((\nabla_{\boldsymbol{u}_\theta} \otimes \mathrm{R}) \cdot \boldsymbol{v}\Big)\ddot{\boldsymbol{u}}_\theta + \Big((\nabla_{\boldsymbol{u}_\theta^2} \otimes \mathrm{R}) \cdot \boldsymbol{v}\Big)\dot{\boldsymbol{u}}_\theta^2. \tag{2.25}$$

The coupled coordinates $\dot{\boldsymbol{u}}_\theta^2$ that appeared during the second time derivation of the rotation matrix (see Eq. (2.24)) have paramount importance in the problem nonlinearity, they notably induce inertial forces.

Velocity and position

The term $\boldsymbol{u}_0$ corresponds to the positions of the structure nodes when no deformation is assumed. Consequently, these positions are constant and $\delta\boldsymbol{u}_0$ is null. Expressed in the

fixed referential $\mathcal{R}$, the position quantity $\delta\boldsymbol{u}^{\mathcal{R}}$ of the mesh nodes are then given by the formula:

$$\begin{aligned}\delta\boldsymbol{u}^{\mathcal{R}} &= \delta\boldsymbol{u}_x + \delta\mathrm{RN}(\boldsymbol{u}_0+\boldsymbol{u}_f) + \mathrm{RN}\delta\boldsymbol{u}_f \\ &= \delta\boldsymbol{u}_x + \underbrace{\Big((\nabla_{\boldsymbol{u}_\theta}\otimes\mathrm{R})\cdot\mathrm{N}(\boldsymbol{u}_0+\boldsymbol{u}_f)\Big)}_{\mathrm{H}}\delta\boldsymbol{u}_\theta + \mathrm{RN}\delta\boldsymbol{u}_f.\end{aligned}$$

The relation Eq. (2.16) allows a matrix expression of the position quantity $\delta\boldsymbol{u}^{\mathcal{R}}$. In order to lighten this expression we use the matrix H so that $\mathrm{H} = (\nabla_{\boldsymbol{u}_\theta}\otimes\mathrm{R})\cdot\mathrm{N}(\boldsymbol{u}_0+\boldsymbol{u}_f)$. Thus, the position quantity can now be expressed as the following matrix product:

$$\delta\boldsymbol{u}^{\mathcal{R}} = \begin{bmatrix}\mathrm{I} & \mathrm{H} & \mathrm{RN}\end{bmatrix}\begin{Bmatrix}\delta\boldsymbol{u}_x\\ \delta\boldsymbol{u}_\theta\\ \delta\boldsymbol{u}_f\end{Bmatrix} \quad \text{with} \quad \mathrm{H} = (\nabla_{\boldsymbol{u}_\theta}\otimes\mathrm{R})\cdot\mathrm{N}(\boldsymbol{u}_0+\boldsymbol{u}_f). \tag{2.26}$$

In the context of Eq. (2.26), the matrix I corresponds to the identity of size $n_x \times n_x$. Analogously to Eq. (2.26), the velocity $\dot{\boldsymbol{u}}^{\mathcal{R}}$ can be written as a matrix product thanks to the use of Eq. (2.16):

$$\dot{\boldsymbol{u}}^{\mathcal{R}} = \dot{\boldsymbol{u}}_x + \frac{d\mathrm{R}}{dt}\mathrm{N}(\boldsymbol{u}_0+\boldsymbol{u}_f) + \mathrm{RN}\dot{\boldsymbol{u}}_f = \begin{bmatrix}\mathrm{I} & \mathrm{H} & \mathrm{RN}\end{bmatrix}\begin{Bmatrix}\dot{\boldsymbol{u}}_x\\ \dot{\boldsymbol{u}}_\theta\\ \dot{\boldsymbol{u}}_f\end{Bmatrix}. \tag{2.27}$$

In this section, matrix expressions of the displacement quantity $\delta\boldsymbol{u}^{\mathcal{R}}$ and velocity $\dot{\boldsymbol{u}}^{\mathcal{R}}$ have been presented thanks to the use of tensor notations. Although the term H has been introduced to lighten Eq. (2.26) and Eq. (2.27), it is important to keep in mind that $\delta\boldsymbol{u}^{\mathcal{R}}$ and $\dot{\boldsymbol{u}}^{\mathcal{R}}$ nonlinearly depends on $\boldsymbol{u}_\theta$ and $\boldsymbol{u}_f$.

Acceleration

The acceleration is deduced by time-derivating the velocity $\dot{\boldsymbol{u}}^{\mathcal{R}}$ (see Eq. (2.27)). This leads to the following expression:

$$\ddot{\boldsymbol{u}}^{\mathcal{R}} = \ddot{\boldsymbol{u}}_x + \frac{d^2\mathrm{R}}{dt^2}\mathrm{N}(\boldsymbol{u}_0+\boldsymbol{u}_f) + 2\frac{d\mathrm{R}}{dt}\mathrm{N}\dot{\boldsymbol{u}}_f + \mathrm{RN}\ddot{\boldsymbol{u}}_f.$$

Although $\ddot{\boldsymbol{u}}^{\mathcal{R}}$ is nonlinear, the use of the expression Eq. (2.19) and Eq. (2.25) can be used to split the acceleration $\ddot{\boldsymbol{u}}^{\mathcal{R}}$ into a pseudo-linear $\ddot{\boldsymbol{u}}^{\mathcal{R}}_{pl}$ and a nonlinear $\ddot{\boldsymbol{u}}^{\mathcal{R}}_{nl}$ term as follows:

$$\ddot{\boldsymbol{u}}^{\mathcal{R}} = \underbrace{\begin{bmatrix}\mathrm{I} & \mathrm{H} & \mathrm{RN}\end{bmatrix}\begin{Bmatrix}\ddot{\boldsymbol{u}}_x\\ \ddot{\boldsymbol{u}}_\theta\\ \ddot{\boldsymbol{u}}_f\end{Bmatrix}}_{\ddot{\boldsymbol{u}}^{\mathcal{R}}_{pl}} + \underbrace{2\Big((\nabla_{u_\theta}\otimes\mathrm{R})\cdot\mathrm{N}\dot{\boldsymbol{u}}_f\Big)\dot{\boldsymbol{u}}_\theta + \Big((\nabla_{\boldsymbol{u}_\theta^2}\otimes\mathrm{R})\cdot\mathrm{N}(\boldsymbol{u}_0+\boldsymbol{u}_f)\Big)\dot{\boldsymbol{u}}_\theta^2}_{\ddot{\boldsymbol{u}}^{\mathcal{R}}_{nl}}. \tag{2.28}$$

Let us have a look on the different acceleration terms and their meanings. In Eq. (2.28), five terms can be identified, three of them are found in the pseudo-linear acceleration $\ddot{\boldsymbol{u}}_{pl}^{\mathcal{R}}$ and involve the acceleration coordinates $\ddot{\boldsymbol{u}}_x$, $\ddot{\boldsymbol{u}}_\theta$ and $\ddot{\boldsymbol{u}}_f$. The two other terms belong to the so called nonlinear acceleration $\ddot{\boldsymbol{u}}_{nl}^{\mathcal{R}}$ and refer to:

- the Coriolis acceleration that is purely tangential $2\Big((\nabla_{u_\theta} \otimes \mathrm{R}) \cdot \mathrm{N}\dot{\boldsymbol{u}}_f\Big)\dot{\boldsymbol{u}}_\theta$.
- the centrifugal acceleration that is radial $\Big((\nabla_{\boldsymbol{u}_\theta^2} \otimes \mathrm{R}) \cdot \mathrm{N}(\boldsymbol{u}_0 + \boldsymbol{u}_f)\Big)\dot{\boldsymbol{u}}_\theta^2$.

The nonlinear term of acceleration $\ddot{\boldsymbol{u}}_{nl}^{\mathcal{R}}$ can be managed in different ways. Since this terms involve angular positions and velocities $\dot{\boldsymbol{u}}_\theta$ and $\dot{\boldsymbol{u}}_f$ it can be treated as a damping. This acceleration can also be handled as a load applied on the structure that is updated at each time step.

2.2.3 Matrix expression of the work quantities

In order to apply the Hamilton principle reminded in 2.2.1, the work quantities $\mathcal{W}_a$, $\mathcal{W}_e$ and $\mathcal{W}_f$ are sought. The expression of the acceleration work quantity $\delta\mathcal{W}_a$ is first given and detailed, then the work $\delta\mathcal{W}_e$ linked to the deformation (linear elasticity) of a structure is reminded. Eventually the work quantity $\delta\mathcal{W}_f$ brought by the external load is studied.

Work of the acceleration

The expression of the acceleration in the floating frame coordinate has been established in Eq. (2.28), the work quantity of the structure acceleration $\delta\mathcal{W}_a(\delta u, \ddot{u})$ is now searched. The computation of this work is performed thanks to the following integration over the spatial domain of the considered mesh Σ:

$$\delta\mathcal{W}_a = \int_\Sigma \delta u^{\mathcal{R}}(\mathrm{x}) \times \rho(\mathrm{x}) \times \ddot{u}^{\mathcal{R}}(\mathrm{x}) d\Sigma = \int_\Sigma \left(\delta\boldsymbol{u}^{\mathcal{R}}\right)^\top \times \rho(\mathrm{x}) \times \ddot{\boldsymbol{u}}^{\mathcal{R}} d\Sigma.$$

As the acceleration has been split, the work acceleration quantity $\delta\mathcal{W}_a$ is decomposed into a pseudo-linear $\delta\mathcal{W}_{a,pl}$ and a nonlinear part $\delta\mathcal{W}_{a,nl}$ so that:

$$\delta\mathcal{W}_a = \int_\Sigma \rho(\mathrm{x}) \left(\delta\boldsymbol{u}^{\mathcal{R}}\right)^\top \ddot{\boldsymbol{u}}^{\mathcal{R}} d\Sigma = \underbrace{\int_\Sigma \rho(\mathrm{x}) \left(\delta\boldsymbol{u}^{\mathcal{R}}\right)^\top \ddot{\boldsymbol{u}}_{pl}^{\mathcal{R}} \, d\Sigma}_{\delta\mathcal{W}_{a,pl}} + \underbrace{\int_\Sigma \rho(\mathrm{x}) \left(\delta\boldsymbol{u}^{\mathcal{R}}\right)^\top \ddot{\boldsymbol{u}}_{nl}^{\mathcal{R}} \, d\Sigma}_{\delta\mathcal{W}_{a,nl}}.$$

Thanks to the displacement quantity Eq. (2.26) and the expression of the pseudo-linear acceleration $\ddot{\boldsymbol{u}}_{pl}^{\mathcal{R}}$ defined in Eq. (2.28) we are now able to establish the expression the work

quantity $\delta\mathcal{W}_{a,pl}$:

$$\delta\mathcal{W}_{a,pl} = \int_\Sigma \rho(\mathrm{x})\left(\delta\boldsymbol{u}^{\mathcal{R}}\right)^\top \ddot{\boldsymbol{u}}^{\mathcal{R}}_{pl}\, d\Sigma = \delta\boldsymbol{u}^\top \underbrace{\left(\int_\Sigma \rho(\mathrm{x})\begin{bmatrix}\mathrm{I} & \mathrm{H} & \mathrm{RN}\end{bmatrix}^\top \begin{bmatrix}\mathrm{I} & \mathrm{H} & \mathrm{RN}\end{bmatrix} d\Sigma\right)}_{\mathrm{M}} \ddot{\boldsymbol{u}}. \tag{2.29}$$

Let us highlight the mass operator M and its constitutive sub-matrix, reminding that the rotation matrix R is orthogonal (then $\mathrm{R}^\top\mathrm{R} = \mathrm{I}$) leads to:

$$\mathrm{M} = \int_\Sigma \rho(\mathrm{x}) \begin{bmatrix} \mathrm{I} & \mathrm{H} & \mathrm{RN} \\ \mathrm{H}^\top & \mathrm{H}^\top\mathrm{H} & \mathrm{H}^\top\mathrm{RN} \\ (\mathrm{RN})^\top & (\mathrm{RN})^\top\mathrm{H} & \mathrm{N}^\top\mathrm{N} \end{bmatrix} d\Sigma = \begin{bmatrix} \mathrm{M}_{xx} & \mathrm{M}_{x\theta} & \mathrm{M}_{xf} \\ \text{sym.} & \mathrm{M}_{\theta\theta} & \mathrm{M}_{\theta f} \\ \text{sym.} & \text{sym.} & \mathrm{M}_{ff} \end{bmatrix}. \tag{2.30}$$

The matrix M is symmetric, moreover the sub-matrix M_{xx} and M_{ff} terms do not depend on the system configuration. Indeed, while the matrix M_{ff} correspond to the classical mass matrix of the finite element model in the floating frame, the matrix M_{xx} correspond to the identity multiplied by the component mass m_Σ.

Seeing the nonlinear acceleration $\ddot{\boldsymbol{u}}^{\mathcal{R}}_{nl}$ as the source of inertial external load leads to the definition of the quadratic velocity operator $\boldsymbol{h}$ so that:

$$\delta\mathcal{W}_{a,nl} = \int_\Sigma \rho(\mathrm{x})\left(\delta\boldsymbol{u}^{\mathcal{R}}\right)^\top \ddot{\boldsymbol{u}}^{\mathcal{R}}_{nl}\, d\Sigma = \delta\boldsymbol{u}^\top \underbrace{\int_\Sigma \rho(\mathrm{x})\begin{bmatrix}\mathrm{I} & \mathrm{H} & \mathrm{RN}\end{bmatrix}^\top \ddot{\boldsymbol{u}}^{\mathcal{R}}_{nl}\, d\Sigma}_{\boldsymbol{h}}. \tag{2.31}$$

In the present work, the operator $\boldsymbol{h}$ is used to regroup the Coriolis and centrifugal force and is treated as an external force $-\boldsymbol{h}$ that is applied on the structure Σ.

Work induced by the elastic deformations

The work quantity induced by the elastic deformations corresponds to the integral [8]:

$$\delta\mathcal{W}_e = -\int_\Sigma \delta\boldsymbol{\varepsilon}^\top \times \boldsymbol{\sigma}\, d\Sigma. \tag{2.32}$$

Where $\boldsymbol{\sigma}$ is the stress of the structure, this stress is linked to the deformation $\boldsymbol{\varepsilon}$ of the structure thanks to the Hooke tensor so that: $\boldsymbol{\sigma} = \mathrm{L}\boldsymbol{\varepsilon}$. Moreover, the hypothesis of small deformation leads to a relation between the deformation $\boldsymbol{\varepsilon}$ and the flexible displacements of the structure $\boldsymbol{u}_f$.

$$\begin{cases} \boldsymbol{\sigma} = \mathrm{L}\boldsymbol{\varepsilon} & \text{Hooke's law} \\ \boldsymbol{\varepsilon} = \dfrac{1}{2}\left((\nabla_\mathrm{x} \otimes \boldsymbol{u}_f) + (\nabla_\mathrm{x} \otimes \boldsymbol{u}_f)^\top\right) = \mathrm{D}\boldsymbol{u}_f & \text{Small deformation} \end{cases}. \tag{2.33}$$

Hence, the law and assumption formulated in Eq. (2.33) allow to give an expression of the work quantity $\delta\mathcal{W}_e$ thanks to the flexible coordinates $\boldsymbol{u}_f$ only. The stiffness matrix K is then defined as follows:

$$\begin{aligned}\delta\mathcal{W}_e &= -\int_\Sigma \delta\boldsymbol{\varepsilon}^\top \mathrm{L}\boldsymbol{\varepsilon}\ d\Sigma = -\int_\Sigma \delta\boldsymbol{u}_f^\top \mathrm{D}^\top \mathrm{L}\mathrm{D}\boldsymbol{u}_f\ d\Sigma \\ &= -\delta\boldsymbol{u}^\top \underbrace{\left(\int_\Sigma \begin{bmatrix}0 & 0 & \mathrm{I}\end{bmatrix}^\top \mathrm{D}^\top \mathrm{L}\mathrm{D} \begin{bmatrix}0 & 0 & \mathrm{I}\end{bmatrix} d\Sigma\right)}_{\mathrm{K}} \boldsymbol{u}.\end{aligned}$$

$$\text{thus}\quad \delta\mathcal{W}_e = -\delta\boldsymbol{u}^\top \mathrm{K}\boldsymbol{u} = -\delta\boldsymbol{u}_f^\top \mathrm{K}_{ff}\boldsymbol{u}_f \quad \text{with}\quad \mathrm{K} = \begin{bmatrix}0 & 0 & 0\\ 0 & 0 & 0\\ 0 & 0 & \mathrm{K}_{ff}\end{bmatrix}. \tag{2.34}$$

The term K_{ff} corresponds to a classic stiffness matrix computed in the local frame $\mathcal{R}^\star$, under the assumption of small deformations. More precise highlights about the construction of K_{ff} and small deformation assumption can be found in the reference [9].

Work of the external forces

If the external load is defined in the fixed frame $\mathcal{R}$, it is convenient to compute the work $\delta\mathcal{W}_f$ it induces. Indeed, in such a case, this work is directly given by the relation:

$$\delta\mathcal{W}_f = \delta\boldsymbol{u}^\top \underbrace{\int_\Sigma \begin{bmatrix}\mathrm{I} & \mathrm{H} & \mathrm{RN}\end{bmatrix}^\top \boldsymbol{f}^{\mathcal{R}} d\Sigma}_{\boldsymbol{f}} = \delta\boldsymbol{u}^\top \boldsymbol{f}.$$

The finite element operator $\boldsymbol{f}$ corresponds here to a vector that depends on the external force $\boldsymbol{f}^{\mathcal{R}}$ applied on the structure Σ and the coordinates $\boldsymbol{u}$. Hence, this vector should be frequently updated during time simulation.

2.2.4 Computational strategies for the evaluation of the floating frame operators

In this section, strategies for the re-evaluation of the finite element operators are presented. First of all, invariant terms of the mass matrix are identified. Then negligible terms are looked for. Eventually the parametrization of the mass sub-matrix is investigated

Invariant rigid matrix

As highlighted in section 2.2.3, M_{ff} and K_{ff} are invariant. Indeed, the built of these matrices is based on interpolation functions N that are defined in a floating frame $\mathcal{R}^\star$.

The rigid/rigid term M_{xx} is another example of invariant matrix:

$$\mathrm{M}_{xx} = \int_\Sigma \rho(\mathrm{x})\ d\Sigma = \begin{pmatrix} m_\Sigma & & \\ & m_\Sigma & \\ & & m_\Sigma \end{pmatrix}.$$

Where m_Σ refers to the mass of the considered structure. Indeed, no matter how the position of the structure, the kinetic energy required to move it in any direction u_{x_i} is always equal to $\frac{1}{2} m_\Sigma \|\dot{\boldsymbol{u}}_x\|^2$ in the global frame of reference $\mathcal{R}$.

Formulation simplifications

Another approach for the simplification of the floating frame model consists in searching and deleting the negligible terms that may exist. A first interesting and often pertinent hypothesis is to assume that the flexible motions of the structure $\boldsymbol{u}_f$ do not dramatically modify the node position in the mesh. Mechanically this means that the inertial effects undergone by the structure are mostly due to the initial structure geometry:

$$\boldsymbol{u}_0 + \boldsymbol{u}_f \simeq \boldsymbol{u}_0. \tag{2.35}$$

This assumption automatically turns the pseudo-linear acceleration and work into rigorously linear terms. Assuming the velocity of some rotations as negligible is another way to simplify the floating frame model. In the present case the pitch angle α is targeted by this assumption since its velocity is expected to be negligible as compared to the engine speed ($\dot{\alpha} \ll \dot{\theta}$). Such an assumption directly impacts the nonlinear acceleration $\ddot{\boldsymbol{u}}_{nl}^{\mathcal{R}}$ and simplifies the construction and update of the inertial load $\boldsymbol{h}$.

Parametrization of the mass sub-matrix

In the present work, the so called parametrization of the mass sub-operators is the extraction of the system variables out of the integral. In this way, the re-computation of some mass sub-matrix is not anymore performed thanks to a numerical integration but through a simple matrix product.

Translation-deformation mass matrix M_{xf}: The parametrization of the translation-deformation mass matrix gives:

$$\mathrm{M}_{xf} = \int_\Sigma \rho(\mathrm{x})\mathrm{R}\mathrm{N} d\Sigma = \mathrm{R} \times \underbrace{\left(\int_\Sigma \rho(\mathrm{x})\mathrm{N}\ d\Sigma \right)}_{\text{constant matrix}}. \tag{2.36}$$

Since the integral term $\int_\Sigma \rho(\mathrm{x})\mathrm{N}\ d\Sigma$ is constant, it can be saved an re-used for the update of M_{xf} thanks to the matrix product of Eq. (2.36).

Translation-rotation mass matrix $\mathrm{M}_{x\theta}$**:** The translation-rotation mass sub-matrix is expressed as:

$$\mathrm{M}_{x\theta} = \int_\Sigma \rho(\mathrm{x})\mathrm{H}d\Sigma = \left(\nabla_{\boldsymbol{u}_\theta} \otimes \mathrm{R}\right) \int_\Sigma \rho(\mathrm{x})\mathrm{N}(\boldsymbol{u}_0 + \boldsymbol{u}_f)d\Sigma \tag{2.37}$$

$$= \left(\nabla_{\boldsymbol{u}_\theta} \otimes \mathrm{R}\right) \times \underbrace{\left(\int_\Sigma \rho(\mathrm{x})\mathrm{N}d\Sigma\right)}_{\text{constant matrix}} \times \underbrace{(\boldsymbol{u}_0 + \boldsymbol{u}_f)}_{\simeq \boldsymbol{u}_0}. \tag{2.38}$$

The integration $\int_\Sigma \rho(\mathrm{x})\mathrm{N}\ d\Sigma$ return a constant matrix, if this matrix is known than the re-computation of $\mathrm{M}_{x\theta}$ can be obtained by the simple matrix product Eq. (2.38).

2.3 Modelling of the joints and system kinematic constraints

In the previous sections the floating frame formulation for flexible multibody dynamics has been introduced. The modelling of the joints is now discussed. In the field of the FMD, the modelling of the joints plays a central role since it enables to describe the relative motions of the components. Indeed, the large displacement allowed by these joints induce nonlinearities that are expected to significantly influence the dynamics of the system.

2.3.1 Joint constraint formulations

A linkage can be expressed as a constraint set $\boldsymbol{\Phi}$ that rules the motions $\boldsymbol{\mu} = (\ddot{\boldsymbol{u}}, \dot{\boldsymbol{u}}, \boldsymbol{u})$ of one or more component. Constraints can be classified into two groups: holonomic and nonholonomic.

- Holonomic refers to constraints that can be written as an algebraic equation. This is notably the case of prismatic, cylindrical, spherical joints. The perfect bonding, that avoids rigid motions between two structures is a typical example of holonomic constraint and is detailed in chapter 3.

- Nonholonomic constraints are used for the description of rolling, sliding motion or for unilateral behaviours. This is the case of the contact and friction phenomenon whose modelling and resolution are treated in chapter 4.

It has been seen in Fig. 2.2 that five different types of linkages are involved in the SAE's CROR sector modelling. Four of those constraints are holonomic: bonding, spherical joint, hinge and bolted joint. Those constraints can then be written thanks to the algebraic equation:

$$\boldsymbol{\Phi}(\boldsymbol{\mu}) = \mathbf{0} \quad \text{with} \quad \boldsymbol{\mu} = (\ddot{\boldsymbol{u}}, \dot{\boldsymbol{u}}, \boldsymbol{u}) \tag{2.39}$$

Hence, considering linkages, the solution of the finite element problem is not anymore solution of Eq. (2.10) only but should also respect Eq. (2.39). In such a case the solution $\boldsymbol{\mu}$ of the finite element problem satisfies:

$$\min_{\boldsymbol{\mu}} \mathcal{J}(\boldsymbol{\mu}) = \min_{\boldsymbol{\mu}} \left(\mathcal{W}_a + \mathcal{W}_e - \mathcal{W}_f \right) \tag{2.40}$$

$$\text{knowing that} \quad \boldsymbol{\Phi}(\boldsymbol{\mu}) = \mathbf{0} \tag{2.41}$$

Among the methods allowing to solve such a problem we can cite the penalization and Lagrangian multipliers based methods. Those methods are reminded and detailed in [1], [10]. This section aim not at reminding the modelling of the classic holonomic linkage cited below. The kinematics of those linkages and their modelling can be found in the book of Géradin and Cardonna [1]. The modelling of the bolted joints is detailed in the PhD thesis of Hammami [11].

2.3.2 Blade-hub interface description

While most of the CROR linkages are modelled in a pointwise fashion by SAE (like the spherical joints in $\mathcal{A}$, $\mathcal{B}$ and the cylindrical joint in $\mathcal{C}$), the contact between the blade and the hub is spread on a surface and involves a consequent set of constraints $\boldsymbol{\Phi}$. This linkage is central to the present work and **the reduction of the blade and hub interfaces is the main goal targeted in this thesis**.

(a) The blade and its interface (b) The hub and its interface

Figure 2.9 – View of the blade and hub, the contact interface are opaque.

The blade interface has 360 nodes (1080 DoF) while the hub interface owns 768 nodes (2304 DoF). The superposition of those two interfaces is shown in Fig. 2.10. In chapter 3, this linkage is modelled as a perfect bonding while contact and friction phenomenon are assumed in chapter 4.

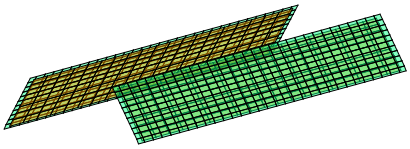

Figure 2.10 – Superposition of the blade and hub interfaces.

Chapter conclusion

Although the present thesis does not focus on flexible multibody dynamics (FMD) it investigates the reduction of the finite element operators M_{ff} and K_{ff} presented in Eq. (2.30) and Eq. (2.34). This preliminary study of the open rotor dynamics formulation justifies the coherence between the reduction method proposed in the next chapters with the FMS nature of the studied system. Indeed, the reduced operators produced in chapters 3 and 4 can be used conjointly to a FMD formulation of the open rotor dynamics.

In the present chapter, the floating frame formulation has been chosen for the description of the open rotor dynamics. The floating frame formulation has multiple advantages:

- it allows to produce finite element models of FMS with a small number of nonlinear equations. Indeed, classical fixed frame approach provides fully nonlinear model.

- the nonlinear finite element operators are not numerous and rather small in regards to the flexible mass M_{ff}. Consequently, their quick update is not expected to significantly impact the computational cost of the simulation process.

- the rigid and flexible motions of the system dynamics are basically distinguished which may help to analyse the behaviour of the system. Moreover, the effects brought by the rotation inertia are clearly identified in Eq. (2.28).

In spite of this, the floating frame formulation requires a consequent analytical work. Moreover the system parametrization using geometrical parameters (Euler parameters in the present case) might bring numerical imprecision [1]. According to [1], this issue can be bypassed by the use of quaternions for the system parametrization.

Whereas the evolution of the system configuration requires an update of some of the mass matrix sub-operator, assumptions and strategies have been presented in section 2.2.4 to speed up their re-computation.

The constraints spread on surfaces, like the perfect bonding of component can be ex-

pressed thanks to constraints sets $\mathbf{\Phi}$ (see section 2.3). Depending on the contacting interface meshes, those constraint might be numerous. The linkage between the blade and the hub encounter this issue as their contact interface is large. In order to resolve this issue, the reduction of the contacting interface is tackled in the two next chapters. The interface reduction is first studied in chapter 3 and assumes the perfect bonding of the two component. Secondly, chapter 4, the reduction of the contacting interface is investigated while considering the contact-friction phenomenon.

Bibliography

[1] M. Géradin and A. Cardona, *Flexible Multibody Dynamics - A Finite Element Approach*. john wiley ed., 2001.

[2] D.-M. Tran, "Component mode synthesis methods using interface modes: Application to structures with cyclic symmetry," *Computers & Structures*, vol. 87, no. 17-18, pp. 1141–1153, 2001.

[3] A. Sternchüss, *Multi-Level Parametric Reduced Models of Rotating Bladed Disk Assemblies*. PhD thesis, École Centrale Paris, 2009.

[4] D. D. Quinn, "Modal analysis of jointed structures," *Journal of Sound and Vibration*, vol. 331, no. 1, pp. 81–93, 2012.

[5] T. M. Wasfy and A. K. Noor, "Computational strategies for flexible multibody systems," *Applied Mechanics Reviews*, vol. 56, no. 6, pp. 553–613, 2003.

[6] T. Belytschko and B. J. Hsieh, "Non-linear transient finite element analysis with convected co-ordinates," *International Journal for Numerical Methods in Engineering*, vol. 7, no. 3, pp. 255–271, 1973.

[7] A. A. Shabana and R. Schwertassek, "Equivalence of the Floating Frame of Reference Approach and Finite Element Formulations," *International Journal of Non-Linear Mechanics*, vol. 33, no. 3, pp. 417–432, 1998.

[8] D. D. Dekker, *Efficient Modeling of Rotational Effects for Wind Turbine Structural Dynamic Analysis*. PhD thesis, Delft University of Technology, 2010.

[9] G. Dhatt, G. Touzot, and E. Lefrançois, *Méthode des éléments finis*. Hermes Science, 2007.

[10] B. Simeon, "On Lagrange multipliers in flexible multibody dynamics," *Computer Methods in Applied Mechanics and Engineering*, vol. 195, no. 50-51, pp. 6993–7005, 2006.

[11] C. Hammami, *Intégration de modèles de jonctions dissipatives dans la conception vibratoire de structures amorties*. PhD thesis, Ecole National Supérieure des Arts et Métiers - ENSAM, 2014.

Chapter 3

Reduction of assemblies for modal analysis

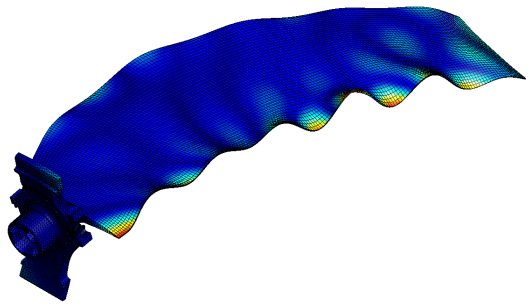

Abstract

An interface oriented reduction method for the modal analysis is proposed. The contribution of this work is the use of component eigenmodes to build an interface reduction basis. Estimators are built to evaluate the accuracy of the searched solutions and to enrich the reduced order model with Arnoldi vectors.

Contents

The mechanical design of a system involves numerous investigations, notably the validation of its dynamics over its operating frequency range. This kind of analysis can be performed numerically using the FE (finite element) method, however in this context, the required accuracy and level of details involve models whose significant sizes lead to time-consuming validation process in the frame of an optimization loop. Indeed, such an optimization process may demand numerous validation computations that considerably slows down the design process.

Nowadays, the blade of the CROR (Counter Rotative Open Rotor) developed by Safran Aircraft Engines is iteratively developed. Starting from an initial design, the engine constitutive components are modelled using the FE (finite element) method, then the dynamics of the assembled system is studied. Eventually, the results of those simulations are used to validate the design of the blade. When rejected, the blade is redesigned and its dynamics is retested. This procedure is performed until a satisfying design is reached, this approach is summarized in Fig. 3.1.

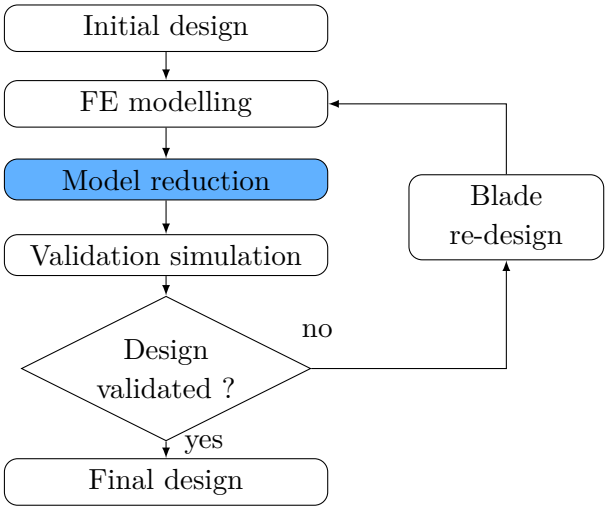

Figure 3.1 – Iterative design process. The work presented in this chapter focus on the coloured box: Model reduction.

This chapter focuses on the modal validation. In practice, this study is performed through the computation of the system natural frequencies for different rotation speeds and angular configurations. Ten different configurations are tested. In this chapter, the modal analysis is only performed on the assembled blade and hub. This case study is of a humble size by nowadays standards (189888 nodes) but handled using basic laptop.

SAE's wish is to exploit the model reduction in order to speed-up its design process. The reduction context presented here allows to formulate requirements on the sought reduction method:

- In the frame of a design context, data about the modal influence of each component

into the overall response of the assembled system is of interest. Hence, the model reduction should involve free component eigenmodes (see section 3.1.1).

- The contacting interfaces between components are refined and should be reduced in order to increase the reduced order model compactness (see section 3.5).

- The redesign of the blade should not lead to a whole reduction of the assembled system. In other words, the reduced order model has to be updatable (see section 3.5.3).

- The method's accuracy must be acceptable. This will be validated by comparing it with the Craig-Bampton and the AMLS method.

In order to fulfil those requirements, a kinematic reduction methodology that relies on primal direct coupling (DC) is proposed in this chapter. The modal properties of a structure are recovered using a Ritz subspace spanned by component free eigenmodes and additional vectors. Those additional vectors are obtained from the dynamic condensation of the components with regards to specific interface modes. Classically, reduction methods like the Craig-Bampton method are limited by interface number of DoF. The main idea of the present work is to reduce the interface using the component free eigenmodes. The displacement allowed on the interface are chosen using the singular value decomposition (SVD) of the component eigenmodes interface motions. This approach enables building a reduced order model using component free eigenmodes whose size and accuracy can be tuned by selecting SVD-interface modes.

The proposed reduction methodology has four mains steps (see Fig. 3.2): the structure assembly, the description of the interface motions, the reduction of the assembled system and eventually its enrichment if required.

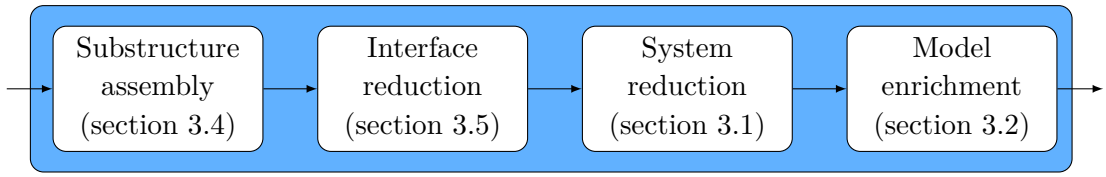

Figure 3.2 – The four steps of the model reduction process that is coloured in Fig. 3.1.

First of all, the basics of the model reduction using a projection on a Ritz subspace are introduced in section 3.1. Section 3.4 highlights the concept of dynamic substructuring and presents some widespread methods like the Craig-Bampton and Mac-Neal methods. The contribution of this work - a reduction method for the modal analysis, using component free eigenmodes and interface reduction - is then proposed in section 3.5.

3.1 Projection of a finite element model on a Ritz subspace

The reduction using the projection into a Ritz subspace consists in searching the problem solution into a subspace whose dimension p is smaller than n, the number of DoF of the finite element model in which it was initially expressed. Once projected, the number p of coordinates of the reduced order model (ROM) is equal to the dimension of the projection subspace. Hence, the stake of the model reduction is to recover as best as possible the response of a finite element model with a small number of DoF. The non-reduced finite element model is commonly referred to as high fidelity model (HFM).

Considering a finite element model involving n degrees of freedom (DoF), its projection on a Ritz subspace of dimension p is performed thanks to the projection matrix $\mathrm{T} \subset \mathbb{R}^{n,p}$. The link between the displacement solution $\boldsymbol{u}$ in the nodal space and its projection $\boldsymbol{q}$ on the displacement subspace is defined by:

$$\boldsymbol{u}_{n\times 1} = \mathrm{T}_{n\times p}\boldsymbol{q}_{p\times 1}. \tag{3.1}$$

Considering an orthogonal reduction basis T, a pseudo inverse T^+ of T can be defined. Thus the inverse formula of Eq. (3.1) is deduced in the following manner:

$$\mathrm{T}^+\mathrm{T} = \mathrm{I}_p \quad \text{thus, from Eq. (3.1):} \quad \mathrm{T}^+\boldsymbol{u} = \mathrm{T}^+\mathrm{T}\boldsymbol{q} = \boldsymbol{q}.$$

The projection of the time dynamic equation onto the subspace spanned by the orthogonal basis T is obtained by multiplying Eq. (2.9) by T^+ on the left and using the relation Eq. (3.1):

$$\underbrace{\mathrm{T}^+\mathrm{M}\mathrm{T}}_{\tilde{\mathrm{M}}_{p\times p}}\ddot{\boldsymbol{q}}(t) + \underbrace{\mathrm{T}^+\mathrm{K}\mathrm{T}}_{\tilde{\mathrm{K}}_{p\times p}}\boldsymbol{q}(t) = \underbrace{\mathrm{T}^+\boldsymbol{f}(t)}_{\tilde{\boldsymbol{f}}_{p\times 1}}. \tag{3.2}$$

As the solutions of the finite element problem Eq. (2.9) are now searched in the subspace spanned by T, the computed solutions $\boldsymbol{u}$ are now limited to linear combinations of the p vectors expressed by the columns of T (see Eq. (3.1)). In the frequency domain, the Fourier transform of the reduced dynamic equation is expressed as:

$$\tilde{\mathrm{Z}}\hat{\boldsymbol{q}} = \left(-\omega^2\tilde{\mathrm{M}} + \tilde{\mathrm{K}}\right)_{p\times p}\hat{\boldsymbol{q}}_{p\times 1} = \hat{\tilde{\boldsymbol{f}}}_{p\times 1} \tag{3.3}$$

$$\text{with} \quad \tilde{\mathrm{Z}} = \mathrm{T}^\top\left(-\omega^2\mathrm{M} + \mathrm{K}\right)\mathrm{T} = -\omega^2\tilde{\mathrm{M}} + \tilde{\mathrm{K}}. \tag{3.4}$$

Where the operator Z is commonly referred to as the dynamic stiffness. In order to lighten Eq. (3.3), from now the hat will be omitted, the notations $\boldsymbol{u}$ and $\boldsymbol{f}$ will refer to the Fourier transform of the time variables $\boldsymbol{u}(t)$ and $\boldsymbol{f}(t)$.

3.1.1 Eigenvectors basis for the model reduction

The eigenmodes $\boldsymbol{\phi}$ associated to a finite element model are defined as the solution of the frequency equation Eq. (3.3) with null external load $\boldsymbol{f}$:

$$\mathrm{Z}\boldsymbol{\phi}_i = \left(-\omega_i^2\mathrm{M} + \mathrm{K}\right)_{n\times n}\boldsymbol{\phi}_i = \mathbf{0}_{n\times 1} \quad \text{with the notation} \quad f_i = \frac{1}{2\pi}\omega_i. \tag{3.5}$$

Such a problem has n solution couples $(\omega_i^2, \boldsymbol{\phi}_i)$, where ω_i refers to the natural frequency associated to the eigenmode $\boldsymbol{\phi}_i$. In structural dynamics, the projection of a problem on a modal basis Φ (truncated to n_Φ normal modes $\boldsymbol{\phi}_i$ only) has interesting properties. First of all, the reduction of a FE model into its modal space allows evaluating the contribution of each mode into the dynamics of the structure. Moreover, a mass-normalized modal basis Φ leads to a convenient expression of the reduced finite element operators:

$$\tilde{\mathrm{M}} = \Phi^\top\mathrm{M}\Phi = \mathrm{I}_{n_\Phi} \quad \text{and} \quad \tilde{\mathrm{K}} = \Phi^\top\mathrm{K}\Phi = \begin{bmatrix} \omega_1^2 & & \\ & \ddots & \\ & & \omega_{n_\Phi}^2 \end{bmatrix} = \Lambda. \tag{3.6}$$

Where I_{n_Φ} is the identity of size n_Φ and Λ is a spectral matrix containing the n_Φ natural frequencies ω_i^2 associated to the mass-normalized eigenvectors in Φ. A mass-normalized eigenmode $\boldsymbol{\phi}_i$ (i.e. $\boldsymbol{\phi}_i$ is M-orthogonal) has a unitary kinetic energy. Throughout the rest of this work, the eigenmodes are always mass-normalized. Consequently, the pseudo inverse Φ^+ of Φ can be defined starting from its basic property:

$$\Phi^+\Phi = \Phi^\top\mathrm{M}\Phi = \mathrm{I}_{n_\Phi} \quad \text{thus} \quad \Phi^+ = \Phi^\top\mathrm{M}.$$

The free structures (with no tied DoF) admit rigid eigenmodes. Those modes express pure translations and rotations of the structure, their associated natural frequencies are always null.

Using the properties of Eq. (3.6) it is possible to write the dynamic flexibility Z^{-1} of a finite element model as the sum of n terms:

$$\mathrm{Z}^{-1} = \sum_{i=1}^{n} \frac{\boldsymbol{\phi}_i{\boldsymbol{\phi}_i}^\top}{\omega_i^2 - \omega^2}. \tag{3.7}$$

Eq. (3.7) expresses that each eigenmodes $\boldsymbol{\phi}_i$ can be used to describe the structural behaviour of a structure in the vicinity of ω_i. Let us consider the academic 2D structure Fig. 3.3 with tied foot nodes (in black) and excited with an harmonic force that is applied on the blue node and whose direction is given by the blue arrow. The structure has te properties of a common steel ($\rho = 7800\mathrm{kg.m}^{-3}$, $E = 210000\mathrm{MPa}$ and $\nu = 0.3$).

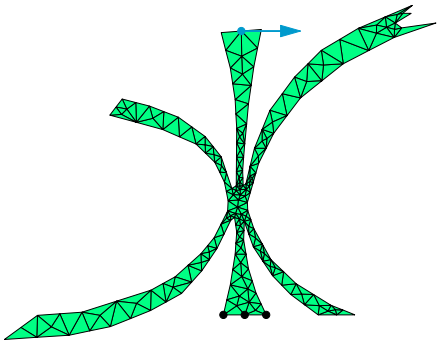

Figure 3.3 – Presentation of a simple 2D academic structure

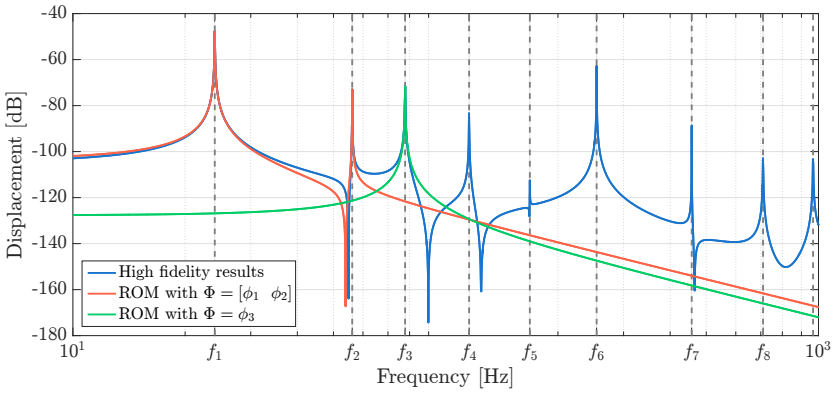

Figure 3.4 – Comparison of the frequency response function computed with reduced and HFM model. The ROM models allow to well recover the FRF in the vicinity of the frequencies $f_i = \frac{1}{2\pi}\omega_i$ associated to the eigenmodes $\boldsymbol{\phi}_i$ involved in the reduction basis.

A comparison of the frequency response function (FRF) obtained with the high fidelity model (HFM) and with ROM using different eigenmodes $\boldsymbol{\phi}$ is presented in Fig. 3.4.

A reduced order model built from truncated modal basis neglects the contribution of certain modes. In practice, the truncation should filter the modes out of the frequency band $\Delta f = [f_{\min}\ ;\ f_{\max}]$ of interest. It is a common practice to keep only the mode located over $[0\ ;\ 1,5 \times f_{\max}]$, this truncation is referred to as Rubin's criterion [1].

The modal projection is widely used in reduction methods and allows to perform forced response computations. However, the modal superposition may be subjected to two kinds of errors [**?**]:

- The spectral convergence deals with the approximation done using a modal truncation. Indeed, a good response prediction requires to build a reduced model whose modal bandwidth is larger than the studied bandwidth. This issue is generally by

passed by verifying that the modal basis respect the Rubin's criterion:

$$\forall \boldsymbol{\phi}_i \in \Phi, \quad f_i \in [0; 1.5 \times f_{\max}]. \tag{3.8}$$

- The spatial convergence is linked to the orthogonality that may exist between the external loads applied on the structure and the eigenmodes chosen for the reduction. A simple way to check the spatial convergence consist in verifying that the L^2 norm of the force not recovered by the M−orthonormal reduction basis Φ is smaller than the norm of $\boldsymbol{f}$ itself:

$$\left\| \left(\mathrm{I}_n - \Phi \Phi^\top \mathrm{M} \right) \boldsymbol{f} \right\| \ll \|\boldsymbol{f}\|. \tag{3.9}$$

In order to tackle those issues, the modal balanced technique [2] has been developed and enable to sort and select eigenmodes with regard to the significance of their contributions into the exact dynamics of a system. This allows to increase the spatial convergence of a reduced model while reducing its dimension. In 2014, Holzwarth *et al.* [2] notably improved the accuracy of the Craig-Bampton method trough a smart selection of the tied interface eigenmodes in a flexible multi-body context.

3.1.2 Singular Value Decomposition

Let us give a quick presentation of the singular value decomposition that will be used later to briefly highlight the proposed method and the interface reduction and its properties. The Singular Value Decomposition can be seen as a generalisation of the eigen-decomposition problem for rectangular matrix. This method considers the decomposition of a rectangular matrix U as the product:

$$\mathrm{U}_{n\times m} = \Phi_{n\times n} \Sigma_{n\times m} {\Psi^\top}_{m\times m} \quad \text{with} \quad \Phi = \begin{bmatrix} \boldsymbol{\varphi}_1 & \boldsymbol{\varphi}_2 & \dots & \boldsymbol{\varphi}_n \end{bmatrix}. \tag{3.10}$$

While Ψ is commonly referred to as the right singular vectors, the matrix Σ is diagonal and contains the singular values σ_i associated to each element $\boldsymbol{\varphi}_i$. The SVD based reduction methods are commonly referred to as *a posteriori* reduction methods as the construction of the reduction basis Φ relies on the knowledge of some snapshots $\mathrm{u}(\mathrm{x}, \omega)$ (i.e. HFM solutions). A more detailed presentation of the SVD is made in the appendix A.1.

3.1.3 Correction of the reduced order model dynamic behaviour

In the frame of the present work, the reduced order model (ROM) aims at recovering as best as possible the properties of the non-reduced finite element model. Hence, the non-reduced model is referred to as high fidelity model (HFM) in the sense that its solutions are considered as references that should be recovered by the ROM.

In order to bypass the spectral and spatial convergence issues presented in section 3.1.1 methods have been developed. Some common techniques are presented below: the enrichment using harmonic solution, the Krylov method, the modal truncation augmentation and the use of the residual flexibility.

Enrichment using harmonic solutions

In terms of FRF, the use of eigenmodes $\boldsymbol{\phi}_i$ allows to accurately recover the structural dynamics of a structure in the vicinity of ω_i. However, this might not be sufficient to get an accurate representation of the FRF all over the studied frequency band. This can be notably observed in Fig. 3.4: the results of the reduced order model using $\boldsymbol{\phi}_1$ and $\boldsymbol{\phi}_2$ appear as inaccurate between ω_1 and ω_2. In order to improve the ROM it is a common practice to use the results $\boldsymbol{\theta}_f$ of the dynamic equation Eq. (3.3) to enrich the reduction basis:

$$\boldsymbol{\theta}_f = \left(-\omega^2 \mathrm{M} + \mathrm{K}\right)^{-1} \boldsymbol{f}. \tag{3.11}$$

The result $\boldsymbol{\theta}_f$ is associated to external the load $\boldsymbol{f}$ and a given circular frequency ω. This vector $\boldsymbol{\theta}_f$ is classically orthogonalized to Φ before enriching the reduction basis. Such a procedure can be used to increase the accuracy of the reduced order model for low frequencies that are deeply impacted by the modal truncation of high frequency modes. This last method is common and referred to as static correction [3] when $\boldsymbol{\theta}_f$ is built with $\omega = 0$.

Krylov-subspace based method for the model enrichment [4]

Starting from an approximated solution $\tilde{\boldsymbol{u}} = \mathrm{T}^\top \mathrm{M} \boldsymbol{q}$ (see section 3.1), the principle of the Krylov method is to build a space $\mathcal{K}_p$ that spans the exact solution $\boldsymbol{u}$:

$$\mathcal{K}_p = \mathrm{Vect}\left\{\tilde{\boldsymbol{u}} \ , \ \boldsymbol{v}^1 \ , \ \boldsymbol{v}^2 \ , \ \dots \ , \ \boldsymbol{v}^{p-1}\right\} \quad \text{with} \quad \boldsymbol{v}^j = (\mathrm{K}^{-1}\mathrm{M})^j \tilde{\boldsymbol{u}}.$$

The index p corresponds to the smaller value for which the Krylov vector $\boldsymbol{v}_p$ is linearly dependent to the preceding vectors $\mathrm{V} = \{\tilde{\boldsymbol{u}}, \boldsymbol{v}^1 \ , \dots \ , \ \boldsymbol{v}^{p-1}\}$. Practically, the Krylov subspace used for the enrichment are truncated and p is arbitrary imposed. Basically, the collinearity of the Krylov vectors is high that prevent its practical use because of numerical issues. This problem is tackled by the Arnoldi and Lanczos methods that use an orthogonalization of the vectors $\boldsymbol{v}^i$ by themselves. The only difference between the Arnoldi and Krylov methods relies on their orthogonalization procedure.

In the present work, the Arnoldi vectors are obtained using a Gram-Schmidt procedure [5] for the orthogonalisation of the vectors $\boldsymbol{v}^i$. Hence the basis V is built as:

$$\mathrm{V} = \mathrm{GramSchmidt}\Big(\begin{bmatrix} \tilde{\boldsymbol{u}} & \boldsymbol{v}^1 & \dots & \boldsymbol{v}^{p-1} \end{bmatrix} \Big). \tag{3.12}$$

Modal truncation augmentation

The modal truncation augmentation (MTA) can be seen as an extension of the static correction method using its expansion. In time simulation, this method allows capturing the spatial part of the force response that is not represented because of the modal truncation. When facing sinusoidal external load, the modal truncation augmentation technique leads to:

$$\boldsymbol{u} = \Phi\boldsymbol{q} + \left[\sum_{k=0}^{p-1}\left((-\omega^2)^k\left(-\mathrm{MK}^{-1}\right)^k\mathrm{K}^{-1}\right)\right]\boldsymbol{f}. \tag{3.13}$$

Note that this technique is close to the moment matching technique, this link is not detailed here but is highlighted in [6] and [3]. Moreover, the vectors $(-\mathrm{MK}^{-1})^k\,\mathrm{K}^{-1}\boldsymbol{f}$ can be seen as k^{th} order Krylov vectors computed from the displacement generated by $\mathrm{K}^{-1}\boldsymbol{f}$ [7].

Dynamic residual flexibility

The spectral convergence issues due to the modal truncation (see section 3.1.1) can be bypassed using the residual flexibility R of the truncated modal basis Φ. In a general way, considering an orthogonal reduction basis Φ, the exact solution $\boldsymbol{u}$ can be expressed as the sum of the solution spanned by Φ and a displacement residue $\boldsymbol{r}$ so that:

$$\boldsymbol{u} = \Phi\boldsymbol{q} + \boldsymbol{r}. \tag{3.14}$$

Where $\boldsymbol{q}$ corresponds to purely modal coordinates. The residue $\boldsymbol{r}$ itself can be written as the multiplication of a matrix R called dynamic residual flexibility and the external load $\boldsymbol{f}$ for a given circular frequency ω. Knowing the expressions of $\boldsymbol{u}$ and $\Phi\boldsymbol{q}$ (see A.3 for a detailed demonstration), it is possible to express the residue $\boldsymbol{r}$ in the following way:

$$\boldsymbol{r} = \boldsymbol{u} - \Phi\boldsymbol{q} = \underbrace{\left(\mathrm{Z}^{-1} - \Phi\tilde{\mathrm{Z}}^{-1}\Phi^\top\right)}_{\mathrm{R}}\boldsymbol{f} \tag{3.15}$$

$$\text{with}\quad \mathrm{R} = \mathrm{Z}^{-1} - \Phi\tilde{\mathrm{Z}}^{-1}\Phi^\top. \tag{3.16}$$

The decomposition Eq. (3.14) is notably exploited by the Craig-Martinez [8] (see appendix A.4) and Mac-Neal [9] (see appendix A.5) methods. Those methods involve a static residual flexibility $\mathrm{R}(\omega = 0)$ and propose a reduction basis [10] for the statement given in Eq. (3.14).

3.2 Accuracy and enrichment of a reduced order model for modal analysis

The reduction of a model can be seen as a simplification of its dynamics. Consequently, the solutions of a ROM are easier to found but might inacurately approximate the HFM solutions. This kind of error is difficult to avoid, however its quantification is crucial and it would be hazardous to exploit a ROM without this information.

In this section, few *a posteriori* and *a priori* estimators (without any knowledge of the exact solutions) of a solution accuracy are presented. Next, the Krylov-subspace method for model enrichment is introduced, eventually a closed-loop enrichment algorithm using both error estimators and Krylov enrichment is proposed.

3.2.1 The modal assurance criterion (MAC)

The mass modal assurance criterion (mass-MAC) is a reference method [11] that allows comparing the orthogonality of modes using the mass matrix of a given finite element model. More precisely, the mass-MAC of two vectors $\boldsymbol{u}$ and $\boldsymbol{v}$ is defined as:

$$\mathrm{MAC}(\boldsymbol{u},\boldsymbol{v}) = \frac{(\boldsymbol{u}^\top \mathrm{M}\boldsymbol{v})^2}{(\boldsymbol{u}^\top \mathrm{M}\boldsymbol{u}) \times (\boldsymbol{v}^\top \mathrm{M}\boldsymbol{v})}. \tag{3.17}$$

3.2.2 *A priori* error estimation on approximated solution

In the frame of this work, the aim of the reduction is to recover the modal behaviour of a structure without any knowledge of the system assembled modes. The approximation $\tilde{\boldsymbol{\phi}}_i$ of the HFM eigenmode $\boldsymbol{\phi}_i$ is computed as follows:

$$\tilde{\boldsymbol{\phi}}_i = \mathrm{T}\boldsymbol{\psi}_i \quad \text{with} \quad \left(-\tilde{\omega}_i^2 \tilde{\mathrm{K}} + \tilde{\mathrm{K}}\right) \boldsymbol{\psi}_i = \mathbf{0}. \tag{3.18}$$

Since the ROM solutions are computed in a reduced space, with modified finite element operators, they might not exactly match with the HFM eigensolution $\boldsymbol{\phi}_i$, and then:

$$\left(-\tilde{\omega}_i^2 \mathrm{M} + \mathrm{K}\right) \tilde{\boldsymbol{\phi}}_i = \boldsymbol{r}(\tilde{\boldsymbol{\phi}}_i) \simeq \mathbf{0}. \tag{3.19}$$

The vector $\boldsymbol{r}$ corresponds to a residual load that is null when $(\tilde{\omega}_i, \tilde{\boldsymbol{\phi}}_i)$ is equal to the HFM eigensolutions. A displacement $\boldsymbol{r}_u$ associated to this residue $\boldsymbol{r}$ can be computed as:

$$\boldsymbol{r}_u(\tilde{\boldsymbol{\phi}}_i) = \mathrm{K}^{-1}\boldsymbol{r}(\tilde{\boldsymbol{\phi}}_i). \tag{3.20}$$

In practice, when rigid body motions are taken into account, the inverse of the stifness K can not be computed but can however be approximated using a pseudo inverse K^+.

Practically, such an inverse K^+ can be computed thanks a mass shift α follows:

$$\mathrm{K}^+ = (\mathrm{K} + \alpha \mathrm{M})^{-1}. \tag{3.21}$$

The choice of the coefficient α has a significant impact on the approximation of the pseudo inverse K^+. A positive coefficient α will provide a positive and definite term $\mathrm{K} + \alpha\mathrm{M}$ that can then be inverted. For negative values of α, the pseudo inverse K^+ corresponds to the following mechanical flexibility (see Eq. (3.7)):

$$\mathrm{K}^+ = \sum_{i=1}^{n} \frac{\boldsymbol{\phi}_i \boldsymbol{\phi}_i^\top}{\omega_i^2 + \alpha}.$$

In such a case, it is important to avoid the correspondence of the shift value α with any $-\omega_i^2$. In his work, Bobillot [12] used a negative shift α, taken in the range $]-\tilde{\omega}_f^2\ ;\ -\tilde{\omega}_f^2/10[$, with $\tilde{\omega}_f$ corresponding to the approximated eigenvalue associated to the first flexible eigenmode.

The ratio between the energy of the residual displacement $\boldsymbol{r}_u(\tilde{\boldsymbol{\phi}}_i)$ and the energy of the approximated eigenmode $\tilde{\boldsymbol{\phi}}_i$ gives an estimation of the solution inaccuracy. Such an estimator can be either computed using the mass or the stiffness matrix as scalar product.

$$\varepsilon(\tilde{\boldsymbol{\phi}}_i) = \frac{\left\|\boldsymbol{r}_u(\tilde{\boldsymbol{\phi}}_i)\right\|_{\mathrm{K}}^2}{\left\|\tilde{\boldsymbol{\phi}}_i\right\|_{\mathrm{K}}^2} \quad \text{or} \quad \varepsilon(\tilde{\boldsymbol{\phi}}_i) = \frac{\left\|\boldsymbol{r}_u(\tilde{\boldsymbol{\phi}}_i)\right\|_{\mathrm{M}}^2}{\left\|\tilde{\boldsymbol{\phi}}_i\right\|_{\mathrm{M}}^2} \tag{3.22}$$

$$\text{moreover, we define } \boldsymbol{\varepsilon} \text{ so that: } \quad \boldsymbol{\varepsilon} = \left[\varepsilon\left(\tilde{\boldsymbol{\phi}}_1\right) \quad \varepsilon\left(\tilde{\boldsymbol{\phi}}_2\right) \quad \dots \quad \varepsilon\left(\tilde{\boldsymbol{\phi}}_m\right)\right]. \tag{3.23}$$

When using the mass matrix the energies computed refer to kinetic energies while the stiffness matrix allows computing potential deformation energies. In this work, the error estimator ε is computed using the stiffness matrix.

3.2.3 Enrichment algorithm

In the last sections, enrichment methods and *a priori* quality estimators for ROM solutions were introduced. The present section deals with the association of those last techniques in order to provide an automatic procedure for the model enrichment.

Let $\mathrm{T}^{(0)}$ be the initial reduction basis that enable the computation of the ROM eigenvectors $\tilde{\Phi}^{(0)}$. Each vector $\tilde{\boldsymbol{\phi}}_i^{(0)}$ is said to be "inaccurately approximated" when its associated error estimator $\varepsilon(\tilde{\boldsymbol{\phi}}_i^{(0)})$ is bigger than a given threshold $\varepsilon_{\max}$. Let $\tilde{\Phi}_{\mathrm{bad}}^{(0)}$ denote the inaccurate solutions $\tilde{\Phi}^{(0)}$, such solutions can be improved thanks to the use of Arnoldi vectors $\mathrm{V}^{(0)}$ (see section 3.1.3):

$$\mathrm{V}^{(0)} = \mathrm{GramSchmidt}\Big(\left[\tilde{\Phi}_{\mathrm{bad}}^{(0)} \quad \mathrm{K}^{-1}\mathrm{M}\tilde{\Phi}_{\mathrm{bad}}^{(0)} \quad \dots \quad (\mathrm{K}^{-1}\mathrm{M})^{p-1}\tilde{\Phi}_{\mathrm{bad}}^{(0)}\right] \Big). \tag{3.24}$$

Hence, a reduction basis $\mathrm{T}^{(1)}$ can be built from the initial basis $\mathrm{T}^{(0)}$ and all the set of Arnoldi vectors $\mathrm{V}^{(0)}$. Repeating this operation leads to the definition of a reduction basis $\mathrm{T}^{(2)}$. The $k+1$ iteration leads to reduction basis $\mathrm{T}^{(\mathrm{k}+1)}$ defined as:

$$\mathrm{T}^{(\mathrm{k}+1)} = \mathrm{GramSchmidt}\Big(\begin{bmatrix} \mathrm{T}^{(\mathrm{k})} & \mathrm{V}^{(k)} \end{bmatrix} \Big). \tag{3.25}$$

Algorithm 3.2.1: Enrichment algorithm

input : K, M, T, $\tilde{\Phi}$, p, $\varepsilon_{\max}$

Initialization

$\mathrm{T}^{(0)} = \mathrm{T}$;

$\tilde{\Phi}^{(0)} = \tilde{\Phi}$;

$k = 0$;

Estimation of the error level of the approximated solutions $\tilde{\Phi}^{(k=0)}$ (Eq. (3.22) and Eq. (3.23))

$$\boldsymbol{\varepsilon} := \begin{bmatrix} \varepsilon(\tilde{\boldsymbol{\phi}}_1^{(k)}) & \varepsilon(\tilde{\boldsymbol{\phi}}_2^{(k)}) & \dots & \varepsilon(\tilde{\boldsymbol{\phi}}_m^{(k)}) \end{bmatrix} \quad \text{with} \quad \varepsilon(\tilde{\boldsymbol{\phi}}_i^{(k)}) = \frac{\left\| \boldsymbol{r}_u(\tilde{\boldsymbol{\phi}}_i^{(k)}) \right\|_{\mathrm{K}}^2}{\left\| \tilde{\boldsymbol{\phi}}_i^{(k)} \right\|_{\mathrm{K}}^2};$$

While badly approximated solutions are detected

while $\mathrm{find}(\boldsymbol{\varepsilon} > \varepsilon_{\max})$ **do**

Find the badly approximated solution $\tilde{\Phi}_{bad}^{(k)}$

$$\tilde{\Phi}_{\mathrm{bad}}^{(k)} = \left\{ \tilde{\boldsymbol{\phi}}_i^{(k)} \in \tilde{\Phi}^{(k)} \ \text{ such that } \ \varepsilon(\tilde{\boldsymbol{\phi}}_i^{(k)}) > \varepsilon_{\max} \right\}$$

Compute the set of Arnoldi vectors that enrich the badly approximated solutions $\tilde{\Phi}_{bad}^{(k)}$ (Eq. (3.24))

$$\mathrm{V}^{(k)} = \mathrm{GramSchmidt}\Big(\begin{bmatrix} \tilde{\Phi}_{\mathrm{bad}}^{(k)} & \mathrm{K}^{-1}\mathrm{M}\tilde{\Phi}_{\mathrm{bad}}^{(k)} & \dots & (\mathrm{K}^{-1}\mathrm{M})^{p-1}\tilde{\Phi}_{\mathrm{bad}}^{(k)} \end{bmatrix} \Big);$$

Update the reduction basis (Eq. (3.25))

$$\mathrm{T}^{(\mathrm{k}+1)} = \mathrm{GramSchmidt}\Big(\begin{bmatrix} \mathrm{T}^{(\mathrm{k})} & \mathrm{V}^{(k)} \end{bmatrix} \Big);$$

$k := k + 1$;

Model reduction (Eq. (3.2))

$\tilde{\mathrm{K}} := {\mathrm{T}^{(\mathrm{k})}}^{\top} \mathrm{K} \mathrm{T}^{(\mathrm{k})}$;

$\tilde{\mathrm{M}} := {\mathrm{T}^{(\mathrm{k})}}^{\top} \mathrm{M} \mathrm{T}^{(\mathrm{k})}$;

Computation of the desired eigensolutions $\tilde{\phi}^{(k)}$ (Eq. (3.18))

$$\tilde{\Phi}^{(k)} = \begin{bmatrix} \tilde{\boldsymbol{\phi}}_1^{(k)} & \tilde{\boldsymbol{\phi}}_2^{(k)} & \dots & \tilde{\boldsymbol{\phi}}_m^{(k)} \end{bmatrix} \quad \text{with} \quad \tilde{\boldsymbol{\phi}}_i^{(k)} = \mathrm{T}^{(\mathrm{k})} \boldsymbol{\psi}_i \quad \text{and} \quad \left(-\tilde{\omega}_i^2 \tilde{\mathrm{M}} + \tilde{\mathrm{K}} \right) \boldsymbol{\psi}_i = \mathbf{0}$$

Estimation of the error level of the approximated solutions $\tilde{\phi}^{(k)}$ (Eq. (3.22) and Eq. (3.23))

$$\boldsymbol{\varepsilon} := \begin{bmatrix} \varepsilon(\tilde{\boldsymbol{\phi}}_1^{(k)}) & \varepsilon(\tilde{\boldsymbol{\phi}}_2^{(k)}) & \dots & \varepsilon(\tilde{\boldsymbol{\phi}}_m^{(k)}) \end{bmatrix} \quad \text{with} \quad \varepsilon(\tilde{\boldsymbol{\phi}}_i^{(k)}) = \frac{\left\| \boldsymbol{r}_u(\tilde{\boldsymbol{\phi}}_i^{(k)}) \right\|_{\mathrm{K}}^2}{\left\| \tilde{\boldsymbol{\phi}}_i^{(k)} \right\|_{\mathrm{K}}^2};$$

end

In practice however, such a procedure leads to reduction basis $\mathrm{T}^{(\mathrm{k}+1)}$ that quickly becomes very large. This can be bypassed using restart strategies. A simple restart method consists

in using the set of approximated eigensolution $\tilde{\Phi}^{(k)}$ to replace the reduction basis $\mathrm{T}^{(k)}$ in Eq. (3.25):

$$\mathrm{T}^{(\mathrm{k+1})} = \mathrm{GramSchmidt}\Big(\begin{bmatrix} \tilde{\Phi}^{(k)} & \mathrm{V}^{(k)} \end{bmatrix} \Big). \tag{3.26}$$

Such a restart is referred to as explicit, more efficient strategies like the IRA restart method exist [12] but are not presented in this work. The enrichment algorithm 3.2.1 is based on the procedure described above. It should be noticed that in practice it is more interesting to build a consequent but precise reduced order model rather than using algorithm 3.2.1 to enrich a compact but inaccurate reduced order model.

3.3 Handling substructures with non-conforming interface meshes

In the previous section, the model reduction has been presented in a general frame. Let us introduce in this section how managing the displacement and force interactions between components with non-conforming interfaces meshes.

3.3.1 Dynamic equilibrium of contacting substructures

Let us consider a structure Σ made of two components Σ_1 and Σ_2, involving n_1 and n_2 DoF, respectively. The two substructures are tied together through the contacting interface denoted Γ called transfer interface (see Fig. 3.5).

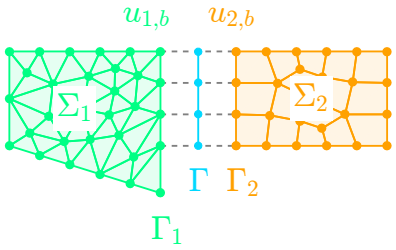

Figure 3.5 – Example of two contacting finite element models with conforming meshes on their contacting surfaces Γ_1 and Γ_2.

The notations M_k and K_k refers to the mass and stifness matrices of the k^{th} component. For each component, the superscripts b, refers to boundary (contacting) DoF, while i will refer to interior DoF, respectively. At a substructure scale, the dynamic equilibrium of each component Σ_k is ruled by the equation:

$$\mathrm{Z}_k \boldsymbol{u}_k = \left(-\omega^2 \mathrm{M}_k + \mathrm{K}_k\right) \boldsymbol{u}_k = \boldsymbol{f}_k + \boldsymbol{p}_k, \tag{3.27}$$

$$\text{with} \quad \mathrm{Z}_k = -\omega^2 \mathrm{M}_k + \mathrm{K}_k. \tag{3.28}$$

The external load $\boldsymbol{p}_k$ corresponds to the connecting force that keeps the substructures bonded, thus, this force only occurs on the contacting nodes. The finite element operators of each component Σ_k can be partitioned into several sub-operators:

$$\left(-\omega^2 \begin{bmatrix} \mathrm{M}_{k,ii} & \mathrm{M}_{k,bi} \\ \mathrm{M}_{k,ib} & \mathrm{M}_{k,bb} \end{bmatrix} + \begin{bmatrix} \mathrm{K}_{k,ii} & \mathrm{K}_{k,bi} \\ \mathrm{K}_{k,ib} & \mathrm{K}_{k,bb} \end{bmatrix}\right) \begin{Bmatrix} \boldsymbol{u}_{k,i} \\ \boldsymbol{u}_{k,b} \end{Bmatrix} = \begin{Bmatrix} \boldsymbol{f}_{k,i} \\ \boldsymbol{f}_{k,b} \end{Bmatrix} + \begin{Bmatrix} \boldsymbol{0} \\ \boldsymbol{p}_{k,b} \end{Bmatrix}. \tag{3.29}$$

In the model substructuring, the physical contacting interface is discretized twice by Γ_1 and Γ_2. In the same way, the force vectors $\boldsymbol{f}_{1,b}$ and $\boldsymbol{f}_{2,b}$ are used to represent the same force. Thus, when the interface meshes are conforming, these two vectors are the same. At the structure scale, the uncoupled model of the whole assembly is expressed using the notation:

$$\mathrm{M} = \begin{bmatrix} \mathrm{M}_1 & \\ & \mathrm{M}_2 \end{bmatrix}, \quad \mathrm{K} = \begin{bmatrix} \mathrm{K}_1 & \\ & \mathrm{K}_2 \end{bmatrix}, \; \boldsymbol{u} = \begin{Bmatrix} \boldsymbol{u}_1 \\ \boldsymbol{u}_2 \end{Bmatrix}, \; \boldsymbol{f} = \begin{Bmatrix} \boldsymbol{f}_1 \\ \boldsymbol{f}_2 \end{Bmatrix} \text{ and } \boldsymbol{p} = \begin{Bmatrix} \boldsymbol{p}_1 \\ \boldsymbol{p}_2 \end{Bmatrix}. \tag{3.30}$$

The model coupling is ensured by the interaction forces $\boldsymbol{p}$, that are only defined on the contacting interface. The perfect bonding of two structures is characterized by the respect of two conditions: the displacement continuity and the force equilibrium sum on the contacting interfaces. Those conditions ensure a continuity of the displacement and force field through the contacting interface. Moreover, this also prevents the energy dissipation in this contact that is theoretically perfect.

The primal coupling condition consists in maintaining the displacement (Dirichlet) boundary condition on the contacting interfaces. In other words, the chosen coupling strategy has to ensure that the displacement fields on the contacting interface are equal. Thus, the displacement gap $g_\Gamma(\mathrm{x})$ is expected to be null over the contacting interface Γ, that can be expressed as follow:

$$g_\Gamma(\mathrm{x}) = u_{1,\Gamma}(\mathrm{x}) - u_{2,\Gamma}(\mathrm{x}) = 0 \quad \forall \mathrm{x} \in \Gamma. \tag{3.31}$$

Where $u_{1,\Gamma}(\mathrm{x})$ and $u_{2,\Gamma}(\mathrm{x})$ are respectively the displacements of the components Σ_1 and Σ_2 at the coordinate x of the contacting interface Γ. The Neumann (dual) condition is expressed as:

$$p_{1,\Gamma}(\mathrm{x}) + p_{2,\Gamma}(\mathrm{x}) = 0 \quad \forall \mathrm{x} \in \Gamma. \tag{3.32}$$

The coupling conditions (primal, dual or hybrid) associated with dynamic substructuring methods have a significant impact on the performance of the reduced order model. The dual coupling formulation is based on the Neumann condition so that the displacement condition Eq. (3.31) is weakly enforced. However, this last feature allows a certain level of non-conformity with regards to the coupling constraint that negatively affects the accuracy of the displacement field.

It has to be noticed that hybrid methods can provide a good trade-off between the respect of both primal (Eq. (3.31)) and dual (Eq. (3.32)) coupling constraints.

3.3.2 Interface regularization

One non negligible advantage of the dynamic substructuring in a design context, is that it allows combining structures independently designed and modelled. Hence it is possible to perform numerical simulations on assemblies whose components were designed separately without any considerations for the neighbouring substructures. Such a procedure may lead to non-conforming substructure interfaces meshes. This means that the interface nodes of a couple of components are not located at the same geometric position, see Fig. 3.6.

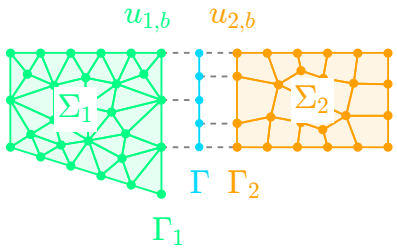

Figure 3.6 – Example of two finite element models with non-conforming meshes on their contacting surfaces Γ_1 and Γ_2.

The vectors $\boldsymbol{u}_1$ and $\boldsymbol{u}_2$ respectively refer to the DoF of the components Σ_1 and Σ_2. Analogously, the vectors $\boldsymbol{u}_{1,b}$ and $\boldsymbol{u}_{2,b}$ refer to the interface DoF of component interfaces respectively denoted Γ_1 and Γ_2.

Re-meshing the contacting interfaces Γ_1 and Γ_2 could bypass the non-conformity (Fig. 3.6) issue but appears as laborious, time consuming and might modify the element nature. Moreover, the meshing provided by the different engineering teams should not be changed as their modifications might influence the convergence of the FE method results [**?**].

Another solution consists in interpolating the interface displacement and force field and to enforce the coupling condition on a transfer interface Γ, such methods are referred to as three-field [13] approach. In this case, the matrix expression of the coupling conditions Eq. (3.31) and Eq. (3.32) is not direct but nevertheless possible thanks to the finite element interpolation function. Practically, this interpolation is performed thanks to interpolation matrix denoted $[\mathrm{L}_{\Gamma\leftarrow\Gamma_1}]$ and $[\mathrm{L}_{\Gamma\leftarrow\Gamma_2}]$ defined so that:

$$\boldsymbol{u}_{1,\Gamma} = [\mathrm{L}_{\Gamma\leftarrow\Gamma_1}]\,\boldsymbol{u}_{1,b} \quad \text{and} \quad \boldsymbol{u}_{2,\Gamma} = [\mathrm{L}_{\Gamma\leftarrow\Gamma_2}]\,\boldsymbol{u}_{2,b}. \tag{3.33}$$

Among the regularization techniques one can cite two main approaches, the first is based on the definition of a master interface that imposes its displacement (and/or force) to the other. In such a case, the transfer interface Γ is defined as the interface of the master

component. In practice, the master interface is commonly chosen as the stiffer one.

The second family of methods relies on the minimisation of the displacement (and/or force) gap. Practically, such methods use a projection of the interface operators into a basis of compatible fields. This compatibility can be characterized by the least square of the gap in terms of displacement (or force).

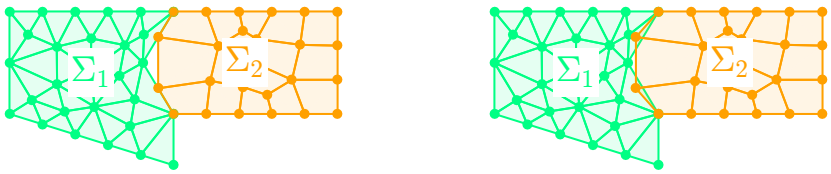

(a) Master/slave interface regularization, the gap due to the mesh non-conformity appears to be very local.

(b) Regularization technique based on the minimization of the gap mean square. The residual gap is spread on the interface.

Figure 3.7 – Comparison of the methods using a master/slave approach (a) and a mean square minimization of the interface gap (b) for the interface regularization.

Whereas this section mainly highlights the regularization from a kinematic point of view, it has to be noticed that hybrid formulations calling for the use of Lagrangian multipliers are also suggested in [14] and [15]. In practice, the choice of a regularization method should be done with regards to the goal targeted by the simulation.

A simple way to build a regularization interface may consist in performing a triangulation over the covering nodes of the interfaces Γ_1 and Γ_2. Let's take an academic example dealing with two simple non-conforming contacting interfaces Γ_1 and Γ_2 to illustrate this method. The transfer interfaces Γ involves all the nodes that belong to the surface intersection $\Gamma_1 \cap \Gamma_2$. An illustration is given in Fig. 3.8.

The regularization of the contacting interfaces leads to modifications of the structural dynamic equations Eq. (3.29) of the boundary DoF. This operation generates new sub-operators that emanate from the interpolations over Γ (see Eq. (3.33)):

$$\begin{aligned}
&\underbrace{[\mathrm{L}_{\Gamma\leftarrow\Gamma_1}]\,\mathrm{Z}_{1,bi}}_{\mathrm{Z}_{1,\Gamma i}}\boldsymbol{u}_{1,i} + \underbrace{[\mathrm{L}_{\Gamma\leftarrow\Gamma_1}]\,\mathrm{Z}_{1,bb}[\mathrm{L}_{\Gamma\leftarrow\Gamma_1}]^\top}_{\mathrm{Z}_{1,\Gamma\Gamma}}\boldsymbol{u}_{1,\Gamma} = \boldsymbol{f}_{1,\Gamma} + \boldsymbol{p}_{1,\Gamma},\\
&\underbrace{[\mathrm{L}_{\Gamma\leftarrow\Gamma_2}]\,\mathrm{Z}_{2,bi}}_{\mathrm{Z}_{2,\Gamma i}}\boldsymbol{u}_{2,i} + \underbrace{[\mathrm{L}_{\Gamma\leftarrow\Gamma_2}]\,\mathrm{Z}_{2,bb}[\mathrm{L}_{\Gamma\leftarrow\Gamma_2}]^\top}_{\mathrm{Z}_{2,\Gamma\Gamma}}\boldsymbol{u}_{2,\Gamma} = \boldsymbol{f}_{2,\Gamma} + \boldsymbol{p}_{2,\Gamma}.
\end{aligned}$$

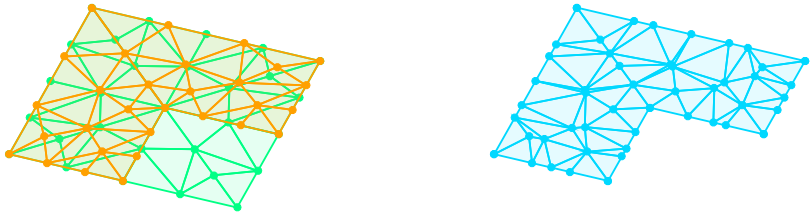

(a) Superposition of the component contacting interfaces Γ_1 and Γ_2.

(b) Transfer interface Γ built from a Delaunay triangulation on the nodes of $\Gamma_1 \cap \Gamma_2$.

Figure 3.8 – Example of two non-conforming meshes with partial covering (a) and built of a transfer interface (b).

$$\text{with} \quad \mathrm{Z}_{1,bi} = -\omega^2 \mathrm{M}_{1,bi} + \mathrm{K}_{1,bi}, \quad \mathrm{Z}_{1,bb} = -\omega^2 \mathrm{M}_{1,bb} + \mathrm{K}_{1,bb}, \tag{3.34}$$

$$\text{and} \quad \mathrm{Z}_{2,bi} = -\omega^2 \mathrm{M}_{2,bi} + \mathrm{K}_{2,bi}, \quad \mathrm{Z}_{2,bb} = -\omega^2 \mathrm{M}_{2,bb} + \mathrm{K}_{2,bb}. \tag{3.35}$$

It has to be noticed that when the transfer interface Γ has more DoF than the contacting interface Γ_k (i.e. $n_{\Gamma_k} < n_\Gamma$), the new sub-operator $\mathrm{Z}_{k,\Gamma\Gamma}$ becomes singular. Indeed, in such a case the operator $\mathrm{Z}_{k,\Gamma\Gamma}$ allows to express the motions of Γ_k in a n_Γ dimension space while only n_{Γ_k} independent equations coming from the initial operator $\mathrm{Z}_{k,bb}$ are available.

This explains why the use of a nodal regularization basis is hardly possible. In order to avoid generating singular sub-operator the motions of the interface Γ can be projected into a reduced basis of dimension $\min(n_{\Gamma_1}\ ,\ n_{\Gamma_2})$.

Regularization using compatible displacements

In their work [16], Vermot des Roches *et al.* looked for an interface regularization basis made of $(1-\epsilon)$ compatible displacements of the contacting interface Γ_1 and Γ_2. The principle of this approach is to define a strain energy functional $\mathcal{W}_{g_\Gamma}$ that penalizes the gap $g_\Gamma(\mathrm{x})$ using a stiffness k and then to find an orthogonal displacement basis $\mathrm{T}_{(1-\epsilon)}$ in which the gap energy is small:

$$\mathcal{W}_{g_\Gamma} = \int_\Gamma k g_\Gamma^2(\mathrm{x}) dS. \tag{3.36}$$

This integral can be numerically approximated using a Gaussian quadrature. Hence, using the notation γ_i for the i^{th} gauss point, ω_i for its associated weight and J_i as the determinant of its interpolation function Jacobian matrix, the strain energy $\mathcal{W}_{g_\Gamma}$ is ap-

proximated by:

$$\mathcal{W}_{g_\Gamma} = \int_\Gamma k g_\Gamma^2(\mathrm{x}) dS \simeq \sum_{i=1}^{n_\mathrm{x}} k\omega_i J_i g_{\gamma_i} = \boldsymbol{g}_\gamma{}^\top \begin{bmatrix} \ddots & & \\ & k\omega_i J_i & \\ & & \ddots \end{bmatrix} \boldsymbol{g}_\gamma. \tag{3.37}$$

Analytic expressions of the interpolation function determinant J_i can be found in the book of Touzot, Dhatt and Lefrançois [17]. Let us define the interpolation matrix $[\mathrm{L}_{\gamma\leftarrow\Gamma}]$ that allows to interpolate a field from the transfer interface Γ to the Gauss points γ. The interpolation of the k$^{\text{th}}$ component interface displacement $\boldsymbol{u}_{k,b}$ on the Gauss points leads to a motion $\boldsymbol{u}_{k,\gamma}$ that is expressed as:

$$\boldsymbol{u}_{k,\gamma} = [\mathrm{L}_{\gamma\leftarrow\Gamma}] \underbrace{[\mathrm{L}_{\Gamma\leftarrow\Gamma_k}]\, \boldsymbol{u}_{k,b}}_{\boldsymbol{u}_{k,\Gamma}}. \tag{3.38}$$

Hence, the gap can be evaluated on the Gauss points g_{γ_i} in a matrix way $\boldsymbol{g}_\gamma$:

$$\boldsymbol{g}_\gamma = [\mathrm{L}_{\gamma\leftarrow\Gamma}]\, \boldsymbol{g}_\Gamma = [\mathrm{L}_{\gamma\leftarrow\Gamma}] \underbrace{\begin{bmatrix} 0 & [\mathrm{L}_{\Gamma\leftarrow\Gamma_1}] & 0 & -[\mathrm{L}_{\Gamma\leftarrow\Gamma_2}] \end{bmatrix}}_{\mathrm{B}} \underbrace{\begin{Bmatrix} \boldsymbol{u}_{1,i} \\ \boldsymbol{u}_{1,b} \\ \boldsymbol{u}_{2,i} \\ \boldsymbol{u}_{2,b} \end{Bmatrix}}_{\boldsymbol{u}} = \mathrm{B}\boldsymbol{u} \tag{3.39}$$

$$\text{with} \quad \mathrm{B} = \begin{bmatrix} 0 & [\mathrm{L}_{\Gamma\leftarrow\Gamma_1}] & 0 & -[\mathrm{L}_{\Gamma\leftarrow\Gamma_2}] \end{bmatrix} \quad \text{and} \quad \boldsymbol{u} = \begin{Bmatrix} \boldsymbol{u}_{1,i} \\ \boldsymbol{u}_{1,b} \\ \boldsymbol{u}_{2,i} \\ \boldsymbol{u}_{2,b} \end{Bmatrix}. \tag{3.40}$$

Consequently, the strain energy $\mathcal{W}_{g_\Gamma}$ can be written as a matrix product

$$\mathcal{W}_{g_\Gamma} = \boldsymbol{u}^\top \mathrm{B}^\top [\mathrm{L}_{\gamma\leftarrow\Gamma}]^\top \begin{bmatrix} \ddots & & \\ & k\omega_i J_i & \\ & & \ddots \end{bmatrix} [\mathrm{L}_{\gamma\leftarrow\Gamma}]\, \mathrm{B}\boldsymbol{u} = \boldsymbol{u}^\top \mathrm{E}\boldsymbol{u} \tag{3.41}$$

$$\text{with} \quad \mathrm{E} = \mathrm{B}^\top [\mathrm{L}_{\gamma\leftarrow\Gamma}]^\top \begin{bmatrix} \ddots & & \\ & k\omega_i J_i & \\ & & \ddots \end{bmatrix} [\mathrm{L}_{\gamma\leftarrow\Gamma}]\, \mathrm{B}. \tag{3.42}$$

The singular value decomposition of the operator E is used to find an orthogonal displacement basis Φ associated to singular values σ. These singular values σ denotes the gap strain energy $\mathcal{W}_{g_\Gamma}$ associated to each element $\boldsymbol{\varphi}_i$ of Φ:

$$\mathrm{E} = \Phi\Sigma\Psi^\top \quad \text{with} \quad \Phi = \begin{Bmatrix} \Phi_{1,b} \\ \Phi_{2,b} \end{Bmatrix}. \tag{3.43}$$

Thus, the compatible vectors are those associated to small values σ (i.e. small gap energy $\mathcal{W}_{g_\Gamma}$). Each vector of the basis Φ can be split into two parts: an interface displacement associated to Γ_1 and one other associated to Γ_2. In their work, Vermot des Roches *et al.* use those displacement to define the $(1-\epsilon)$ compatible interface displacements basis $\mathrm{T}_{(1-\epsilon)}$ as:

$$\mathrm{T}_{(1-\epsilon)} = \left\{ \boldsymbol{\varphi}_i \in \Phi \quad \text{with} \quad i \quad \text{so that} \quad \frac{\sigma_i}{\max \sigma_i} \leq \epsilon \right\}. \tag{3.44}$$

This regularization method has been notably used by Vermot des Roches to treat the contact-friction problem in [18]. This application led him to consider dual compatible interface shapes in order to avoid the locking due to stress concentration.

Regularization of the blade and hub interfaces

The perfect bonding of the blade and hub assumes that the gap $\boldsymbol{g}_\Gamma$ between the two components is null. For this reason, the $(1-\epsilon)$ compatibility technique proposed in [16] is used. The transfer interface Γ is built using a Delaunay triangulation over the nodes of the interfaces $\Gamma_1 \cap \Gamma_2$ (see Fig. 3.8 for a simpler example). This interface is shown in Fig. 3.9b.

(a) Superposition of the blade and hub interfaces Γ_1 and Γ_2

(b) Transfer interface Γ built from the blade and hub interfaces

Figure 3.9 – Construction of the blade-hub transfer interface

The evolution of the ϵ value is given in Fig. 3.10. The $(1-\epsilon)$ compatibility clearly decrease around the 100^{th} interface mode. In order to keep an accurate description of the interface motions and to avoid the singularity of the interface operator $\mathrm{Z}_{k,\Gamma\Gamma}$ discussed above, the truncation of the basis $\mathrm{T}_{(1-\epsilon)}$ is made at $\min(n_{\Gamma_1}, n_{\Gamma_2}) = 1080$. Otherwise the interface operators $\mathrm{Z}_{k,bb}$ (Eq. (3.34) and Eq. (3.35)) would become singular.

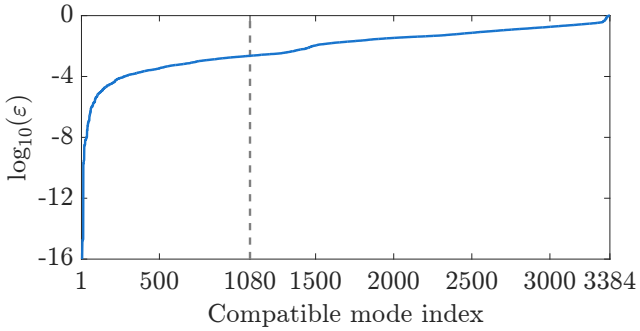

Figure 3.10 – Evolution of the variable ϵ. The motions associated to the smaller values are the most compatible.

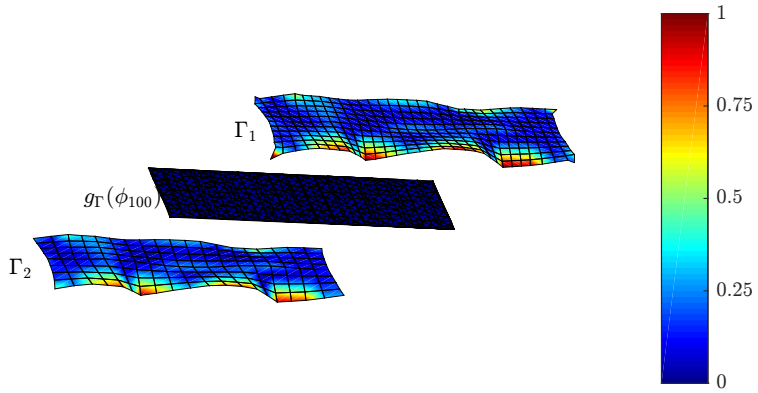

(a) Compatible motion $\boldsymbol{\phi}_{100}$, $\epsilon_{100} = 4.89 \times 10^{-6}$

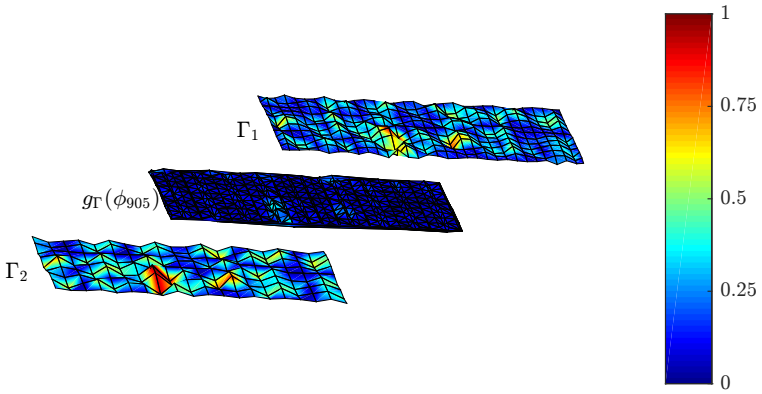

(b) Compatible motion $\boldsymbol{\phi}_{905}$, $\epsilon_{905} = 1.60 \times 10^{-3}$

Figure 3.11 – $1 - \epsilon$ compatible displacements and their associated gap $\boldsymbol{g}_\Gamma$. For the sake of clarity, interfaces Γ_1 and Γ_2 are not entirely shown. The compatible motions of Γ_1 and Γ_2 are shown on the upper and lower interfaces. The middle interface is Γ and is used to the gap $\boldsymbol{g}_\Gamma$.

Two examples of $(1-\epsilon)$ compatible motions are given in Fig. 3.11. The compatibility is more important for small values of ϵ. Indeed, while the gap $\boldsymbol{g}_\Gamma$ is hardly visible in Fig. 3.11a (for $\boldsymbol{\phi}_{100}$) it can be clearly seen in Fig. 3.11b for the mode $\boldsymbol{\phi}_{904}$.

From now we consider that all the components are regularized or that their interfaces are basically conforming. Consequently, the dynamic equation of a component Σ_k is now defined as:

$$\left(-\omega^2 \begin{bmatrix} \mathrm{M}_{k,ii} & \mathrm{M}_{k,\Gamma i} \\ \mathrm{M}_{k,i\Gamma} & \mathrm{M}_{k,\Gamma\Gamma} \end{bmatrix} + \begin{bmatrix} \mathrm{K}_{k,ii} & \mathrm{K}_{k,\Gamma i} \\ \mathrm{K}_{k,i\Gamma} & \mathrm{K}_{k,\Gamma\Gamma} \end{bmatrix}\right) \begin{Bmatrix} \boldsymbol{u}_{k,i} \\ \boldsymbol{u}_{k,\Gamma} \end{Bmatrix} = \begin{Bmatrix} \boldsymbol{f}_{k,i} \\ \boldsymbol{f}_{k,\Gamma} \end{Bmatrix} + \begin{Bmatrix} \boldsymbol{0} \\ \boldsymbol{p}_{k,\Gamma} \end{Bmatrix}. \tag{3.45}$$

Moreover, for the sake of simplicity, we assume that the DoF $\boldsymbol{u}_{1,\Gamma}$ and $\boldsymbol{u}_{2,\Gamma}$ are similarly sorted. Note that the topology of the finite element operators M, K, $\boldsymbol{u}$, $\boldsymbol{f}$ and $\boldsymbol{p}$ remain unchanged:

$$\mathrm{M} = \begin{bmatrix} \mathrm{M}_1 & \\ & \mathrm{M}_2 \end{bmatrix}, \quad \mathrm{K} = \begin{bmatrix} \mathrm{K}_1 & \\ & \mathrm{K}_2 \end{bmatrix}, \boldsymbol{u} = \begin{Bmatrix} \boldsymbol{u}_1 \\ \boldsymbol{u}_2 \end{Bmatrix}, \quad \boldsymbol{f} = \begin{Bmatrix} \boldsymbol{f}_1 \\ \boldsymbol{f}_2 \end{Bmatrix} \text{ and } \boldsymbol{p} = \begin{Bmatrix} \boldsymbol{p}_1 \\ \boldsymbol{p}_2 \end{Bmatrix}. \tag{3.46}$$

3.4 Model dynamic substructuring

Recent reviews of reduction methods were carried out by [3] and [4]. These kinds of methods are used to evaluate the behaviour of models (sometime in real-time [19]) incorporating several million degrees of freedom (DoF), see for example [20], [21] and [22]. The dynamic substructuring technique (DS), first initiated by Hurty in the early 60s, was of paramount importance in this progress. Indeed, the basic idea of this technique is to consider a large model as an assembly of smaller models that are easier to handle. Two main families can be identified [23] among these DS-based methods: Direct Coupling (DC) and Component Mode Synthesis (CMS). Whereas direct coupling deals with the enforcement of the Dirichlet and/or Neumann conditions on the contacting interfaces in the nodal space, the CMS method imposes these conditions in the reduced space through the choice of the reduction vectors [24]. Indeed, CMS methods consider the reduction of independent component finite element models whose interactions are described with modes.

The advantages provided by dynamic substructuring methods to structural dynamics are numerous [23]. They allow evaluating the dynamics of a structure that is too large or too complex to be analysed as a whole [20]. Indeed, since the nonlinearity of the matrix inversion and eigensolution algorithm leads to computational cost, the beneficial aspect of breaking down a large problem into a set of small ones is immediate. Moreover, as substructuring involves independent computations on the components, the parallelism achieved is widely used in classical methods such as the Craig-Bampton, MacNeal, FETI (Finite Element Tearing and Interconnecting) [22] and AMLS (Automated Multi-Level Solver) [25] [26] methods as well as in more recent methods [20].

Another feature provided by substructuring is that the contribution of each component to the overall response of the assembled structure becomes apparent. This investigation can be achieved using the free-free eigenmodes of components as reduction vectors. From the design point of view, this type of analysis provides access to information that can be used to guide the redesign of components independently. Dual CMS methods like those of Mac-Neal [9], and more recently the dual Craig-Bampton method developed by Rixen [27] and [28], [29], and [30] use component eigenmodes. Nevertheless these methods are based on maintaining continuous force at the contacting interface. Such an approach may not be well-adapted when the displacement field is of primary importance.

Another great advantage provided by dynamic substructuring is linked to its capacity to enrich the assembled model with experimental measurements and to combine them with other models. It is thus possible to evolve from an initial model as the product design progresses, i.e. using experimental data from physical parts of the assembly and increasing its level of detail by combining it with other substructures. In other words, the assembled model of a system can be progressively enriched by taking into account the contribution of an increasing number of components.

3.4.1 Direct component coupling

The direct coupling is a branch of the dynamic substructuring method that considers the component coupling in the physical domain. The FETI method provides typical examples of how direct coupling can be involved in reduction methods. In this section, the component models are already regularized using the transfer interface Γ and their interface DoF are similarly sorted. Consequently, the expression of the Dirichlet Eq. (3.31) and Neumann Eq. (3.32) coupling conditions are written in matrix form as follows (see FE operators partitioning in Eq. (3.29)):

$$\boldsymbol{u}_{1,\Gamma} - \boldsymbol{u}_{2,\Gamma} = \begin{bmatrix} 0 & \mathrm{I}_\Gamma & 0 & -\mathrm{I}_\Gamma \end{bmatrix} \boldsymbol{u} = \mathrm{B}\boldsymbol{u} = \boldsymbol{0} \tag{3.47}$$

$$\boldsymbol{p}_{1,\Gamma} + \boldsymbol{p}_{2,\Gamma} = \begin{bmatrix} 0 & \mathrm{I}_\Gamma & 0 & \mathrm{I}_\Gamma \end{bmatrix} \boldsymbol{p} = \boldsymbol{0}. \tag{3.48}$$

Primal direct component coupling

The direct primal coupling of two structures can be established starting from the force equilibrium equation at the interface. In section 3.3.1, the structural dynamic equations of the uncoupled components Σ_1 and Σ_2 are given in Eq. (3.45), respectively. Once coupled, the interface force equilibrium of the two structures can be written as follows:

$$\begin{cases} \mathrm{Z}_{1,\Gamma i}\boldsymbol{u}_{1,i} + \mathrm{Z}_{1,\Gamma\Gamma}\boldsymbol{u}_{1,\Gamma} = \boldsymbol{f}_{1,\Gamma} + \boldsymbol{p}_{1,\Gamma} \\ \mathrm{Z}_{2,\Gamma i}\boldsymbol{u}_{2,i} + \mathrm{Z}_{2,\Gamma\Gamma}\boldsymbol{u}_{2,\Gamma} = \boldsymbol{f}_{2,\Gamma} + \boldsymbol{p}_{2,\Gamma}. \end{cases} \tag{3.49}$$

Vectors $\boldsymbol{p}_1$ and $\boldsymbol{p}_2$ denote the interaction forces that ensure the contact of the two substructures. It is important to note that the interaction forces exist only on the contacting interfaces. In order to guarantee conformity with the Dirichlet boundary conditions we assume

$$\boldsymbol{u}_{1,\Gamma} = \boldsymbol{u}_{2,\Gamma} = \boldsymbol{u}_{\Gamma}. \tag{3.50}$$

Thus the force equilibrium at the interface is expressed as:

$$\mathrm{Z}_{1,\Gamma i}\boldsymbol{u}_{1,i} + \left(\mathrm{Z}_{1,\Gamma\Gamma} + \mathrm{Z}_{2,\Gamma\Gamma}\right)\boldsymbol{u}_{\Gamma} + \mathrm{Z}_{2,\Gamma i}\boldsymbol{u}_{2,i} = \boldsymbol{f}_{1,\Gamma} + \boldsymbol{f}_{2,\Gamma} + \underbrace{\boldsymbol{p}_{1,\Gamma} + \boldsymbol{p}_{2,\Gamma}}_{\mathbf{0}}. \tag{3.51}$$

In primal methods Eq. (3.50) is assumed and the force equilibrium $\boldsymbol{p}_{1,\Gamma} + \boldsymbol{p}_{2,\Gamma} = \mathbf{0}$ is targeted [23]. Hence the dynamic stiffness of the assembled model can be written as:

$$\mathrm{Z}_p(\omega) = \begin{bmatrix} \mathrm{Z}_{1,ii} & \mathrm{Z}_{1,i\Gamma} & 0 \\ \mathrm{Z}_{1,\Gamma i} & \mathrm{Z}_{1,\Gamma\Gamma} + \mathrm{Z}_{2,\Gamma\Gamma} & \mathrm{Z}_{2,\Gamma i} \\ 0 & \mathrm{Z}_{2,i\Gamma} & \mathrm{Z}_{2,ii} \end{bmatrix}, \text{ with } \boldsymbol{u} = \begin{Bmatrix} \boldsymbol{u}_{1,i} \\ \boldsymbol{u}_{\Gamma} \\ \boldsymbol{u}_{2,i} \end{Bmatrix}, \text{ and } \mathrm{Z}_p = -\omega^2\mathrm{M}_p + \mathrm{K}_p. \tag{3.52}$$

Here, the superscript p given to Z_p, M_p and K_p refers to the coupling method ans is used to distinguished these matrix from M, K and Z defined in Eq. (3.46). The second block row and columns are referred to as interface block. An interesting property of this assembled model Eq. (3.52) is that the symmetry of the primarily assembled matrix is kept. This allows using efficient numerical methods to manage them such as the Cholesky decomposition method.

Dual direct component coupling

Based on the Neumann condition, the popularity of the dual formulation rose in the 1990's. Indeed, the capacity to use this formulation as a way to implement efficient solvers on parallel processing computers [4] has notably led to the development of the FETI family method (also known as dual Schur complement methods). Analogously to Eq. (3.50), the Neumann condition Eq. (3.32) can be expressed in a matrix way using interpolation matrix and a single interface connecting force $\boldsymbol{p}_{\Gamma}$:

$$\boldsymbol{p}_{2,\Gamma} = -\boldsymbol{p}_{1,\Gamma} = \boldsymbol{p}_{\Gamma} \quad \text{thus} \quad \boldsymbol{p}_1 = \begin{Bmatrix} \mathbf{0} \\ \boldsymbol{p}_{1,\Gamma} \end{Bmatrix} = \begin{bmatrix} \mathbf{0} \\ -\mathrm{I}_{\Gamma} \end{bmatrix}\boldsymbol{p}_{\Gamma} \quad \text{and} \quad \boldsymbol{p}_2 = \begin{Bmatrix} \mathbf{0} \\ \boldsymbol{p}_{2,\Gamma} \end{Bmatrix} = \begin{bmatrix} \mathbf{0} \\ \mathrm{I}_{\Gamma} \end{bmatrix}\boldsymbol{p}_{\Gamma} \tag{3.53}$$

$$\text{then} \quad \boldsymbol{p} = \begin{Bmatrix} \boldsymbol{p}_1 \\ \boldsymbol{p}_2 \end{Bmatrix} = -\begin{bmatrix} 0 \\ \mathrm{I}_{\Gamma} \\ 0 \\ -\mathrm{I}_{\Gamma} \end{bmatrix}\boldsymbol{p}_{\Gamma} = \begin{bmatrix} 0 & \mathrm{I}_{\Gamma} & 0 & -\mathrm{I}_{\Gamma} \end{bmatrix}^{\top}\boldsymbol{p}_{\Gamma} = \mathrm{B}^{\top}\boldsymbol{p}_{\Gamma}. \tag{3.54}$$

The matrix B (see Eq. (3.47)) is referred to a constraint matrix. The dual direct coupling of a model is ruled by combined equations: Eq. (3.47) and Eq. (3.54). This leads to the

following matrix system:

$$\begin{bmatrix} \mathrm{Z}_1 & 0 \\ 0 & \mathrm{Z}_2 \end{bmatrix} \begin{Bmatrix} \boldsymbol{u}_1 \\ \boldsymbol{u}_2 \end{Bmatrix} + \mathrm{B}^\top \boldsymbol{p}_\Gamma = \begin{Bmatrix} \boldsymbol{f}_1 \\ \boldsymbol{f}_2 \end{Bmatrix} \quad \text{and} \quad \mathrm{B}\boldsymbol{u} = \boldsymbol{0}. \tag{3.55}$$

The connecting force $\boldsymbol{p}_\Gamma$ can be seen as a Lagrangian multiplier (2.3). Such a formulation is also sometimes referred to a penalization since the term $\mathrm{B}\boldsymbol{u} = \boldsymbol{0}$ can be seen as a primal condition that increases the energy $\delta\mathcal{J}$ (see Eq. (2.11)) when not respected. For this reason it is possible to introduce a coefficient k, that amplifies the gap penalization:

$$\begin{bmatrix} \mathrm{Z} & k\mathrm{B}^\top \\ k\mathrm{B} & 0 \end{bmatrix} \begin{Bmatrix} \boldsymbol{u} \\ \boldsymbol{p}_\Gamma \end{Bmatrix} = \begin{Bmatrix} \boldsymbol{f} \\ \boldsymbol{0} \end{Bmatrix}. \tag{3.56}$$

The greater the coefficient k, the best the Dirichlet Eq. (3.31) condition is enforced. However, consequent penalization might also deteriorate the problem conditioning. The constraint matrix only involve the position $\boldsymbol{u}$, hence the time equation of a dually assembled model is deduced as being:

$$\begin{bmatrix} \mathrm{M} & 0 \\ 0 & 0 \end{bmatrix} \begin{Bmatrix} \ddot{\boldsymbol{u}} \\ \ddot{\boldsymbol{p}}_\Gamma \end{Bmatrix} + \begin{bmatrix} \mathrm{K} & k\mathrm{B}^\top \\ k\mathrm{B} & 0 \end{bmatrix} \begin{Bmatrix} \boldsymbol{u} \\ \boldsymbol{p}_\Gamma \end{Bmatrix} = \begin{Bmatrix} \boldsymbol{f} \\ \boldsymbol{0} \end{Bmatrix}. \tag{3.57}$$

Such a problem can be solved using Newmark integration scheme as presented later in chapter 4, introducing the time simulation of system facing the contact-friction phenomenon.

3.4.2 Component Mode Synthesis

The component mode synthesis (CMS) is a family of methods belonging to the dynamic substructuring, involving the modal recombination at a component level. Main CMS development were performed around the 1960's, notably by Craig, Guyan, Mac-Neal and Rubin. Nowadays, those methods are widely implemented in industrial FE codes and are still improved [27].

Those methods characterize the dynamics of each component Σ_k thanks to a set of reduction vectors that can be independently computed. Hence, the particularity of component mode synthesis is that the coupling of the components is performed through a reduction basis T. Starting from a block diagonal matrix containing the component dynamic stiffness, the coupling of the two components is only raised by the Ritz vectors contained in the reduction basis T [23].

$$\tilde{\mathrm{Z}} = \mathrm{T}^\top \begin{bmatrix} \mathrm{Z}_1 & 0 \\ 0 & \mathrm{Z}_2 \end{bmatrix} \mathrm{T} \quad \text{with } \mathrm{T} = \begin{bmatrix} \mathrm{T}_1 \\ \mathrm{T}_2 \end{bmatrix} \quad \text{and} \quad \mathrm{T}_k = \begin{bmatrix} \mathrm{T}_{k,i} \\ \mathrm{T}_{k,\Gamma} \end{bmatrix}.$$

The description of a substructure dynamics can be done using various data. Classical reduction methods commonly involve component eigenmodes and quasi-static structure response that enable to respectively represent the substructures dynamics and their coupling.

Primal CMS methods

Starting from a set of reduced coordinates $\boldsymbol{q}$, the primal coupling condition Eq. (3.31) that expresses the interface displacement continuity can be written thanks to the interpolation matrix previously introduced:

$$\boldsymbol{g}_\Gamma = \mathrm{B}\mathrm{T}\boldsymbol{q} = \boldsymbol{0} \text{ where } \boldsymbol{q} \neq \boldsymbol{0}. \tag{3.58}$$

Knowing that the reduced coordinates are basically not trivial (i.e. $\boldsymbol{q} \neq \boldsymbol{0}$), a sufficient but not necessary condition on the reduction basis T can be assessed for the respect of the Eq. (3.58).

$$\mathrm{T}_{1,\Gamma} - \mathrm{T}_{2,\Gamma} = 0 \quad \text{with } \mathrm{T}_{k,\Gamma} = \begin{bmatrix} 0 & \mathrm{I}_\Gamma \end{bmatrix} \mathrm{T}_k. \tag{3.59}$$

This means that the restriction of the reduction basis $\mathrm{T}_{1,\Gamma}$ and $\mathrm{T}_{2,\Gamma}$ on the interface are equal. The interior displacement $\boldsymbol{u}_{k,i}$ of each component can be expressed in function of the load $\boldsymbol{f}_k$ and boundary displacement $\boldsymbol{u}_{k,\Gamma}$ thanks to the condensation:

$$\boldsymbol{u}_{k,i} = \mathrm{Z}_{k,ii}^{-1}\Big(\boldsymbol{f}_{k,i} - \mathrm{Z}_{k,i\Gamma}\boldsymbol{u}_{k,\Gamma}\Big). \tag{3.60}$$

For a null circular frequency and assuming that no external force is applied on the interior DoF (i.e. $\boldsymbol{f}_{k,i} = \boldsymbol{0}$), this is referred to as Guyan's condensation and allows the definition of a transformation matrix Θ_k that express the coordinate $\boldsymbol{u}_k$ as:

$$\Theta_k = \begin{bmatrix} -\mathrm{K}_{k,ii}^{-1}\mathrm{K}_{k,i\Gamma} \\ \mathrm{I}_\Gamma \end{bmatrix}. \tag{3.61}$$

In order to improve the description of the interior DoF dynamics, Craig-Bampton added modal data using eigenmode Ψ computed with fixed boundary DoF in order to respect Eq. (3.59).

$$\mathrm{T} = \begin{bmatrix} \Psi_{1,i} & 0 & \begin{bmatrix} -\mathrm{K}_{1,ii}^{-1}\mathrm{K}_{1,i\Gamma} \\ \mathrm{I}_\Gamma \end{bmatrix} \\ 0 & 0 & \\ 0 & \Psi_{2,i} & \begin{bmatrix} -\mathrm{K}_{2,ii}^{-1}\mathrm{K}_{2,i\Gamma} \\ \mathrm{I}_\Gamma \end{bmatrix} \\ 0 & 0 & \end{bmatrix} = \begin{bmatrix} \mathrm{T}_{1,i} \\ \mathrm{T}_{1,\Gamma} \\ \mathrm{T}_{2,i} \\ \mathrm{T}_{2,\Gamma} \end{bmatrix}.$$

The Craig-Bampton method is a widely implemented component mode synthesis method based on a primal coupling approach. This method is known to be applicable for dynamic model evaluation in a frequency range closely linked to the truncation of the component

modes. The Guyan's vector allow taking into account the interactions between the component and the modal contributions neglected by the modal truncation.

In practice this approach can be criticized since the number of Guyan condensed vectors Θ_1 and Θ_2 relies on the number of interface DoF n_Γ. The compactness of the Craig-Bampton based reduced order model then decreases as the number of interface DoF n_Γ increases.

Dual CMS methods

The dual component mode synthesis methods relies on the enforcement of the Neumann condition into a reduced space. Hence, the force equilibrium relies on a variant of the matrix condition Eq. (3.54) dealing with reduced coordinates:

$$\tilde{\boldsymbol{p}} = -\mathrm{T}^\top \mathrm{B}^\top \boldsymbol{p}_\Gamma = -\tilde{\mathrm{B}}^\top \boldsymbol{p}_\Gamma \quad \text{with} \quad \tilde{\mathrm{B}} = \mathrm{BT}$$
$$\text{reminding} \quad \mathrm{B} = \begin{bmatrix} 0 & \mathrm{I}_\Gamma & 0 & -\mathrm{I}_\Gamma \end{bmatrix}.$$

The displacement reduction using a basis T of the dual direct coupling equation Eq. (3.55) leads to the dual CMS equation:

$$\begin{cases} \mathrm{T}^\top \mathrm{Z} \mathrm{T} \boldsymbol{q} + \mathrm{T}^\top \mathrm{B}^\top \boldsymbol{p} = \mathrm{T}^\top \boldsymbol{f} \\ \mathrm{BT}\boldsymbol{q} = \boldsymbol{0} \end{cases} \quad \text{leads to} \quad \begin{bmatrix} \tilde{\mathrm{Z}} & \tilde{\mathrm{B}}^\top \\ \tilde{\mathrm{B}} & 0 \end{bmatrix} \begin{Bmatrix} \boldsymbol{q} \\ \boldsymbol{p}_\Gamma \end{Bmatrix} = \begin{Bmatrix} \tilde{\boldsymbol{f}} \\ \boldsymbol{0} \end{Bmatrix}. \tag{3.62}$$

Eq. (3.62) is analogous to Eq. (3.55). The Mac-Neal and Rubin's method are typical examples of dual CMS methods and are highlighted in appendix A.5.

Multi-level reduction for eigencomputation - The AMLS method [26]

The reduction of a model can results from several successive reductions, this is commonly referred to as multi-level reduction. Each reduction decrease the system size using a reduction matrix computed at the previous stage. Whereas those methods can be used to build very compact reduced order model, they also require a rigorous management of the successive reduction basis.

The Algebraic Multi-Level Sub-structuring method (AMLS) has been initiated by Kaplan *et al.* [25] and corresponds to a multi-level extension of the CMS method. This method allows solving eigenvalue and forced response of large problems in structural dynamics and acoustics. The AMLS method for modal analysis is presented in the appendix A.6 and is later compared to the proposed method.

3.5 Interface reduction using component eigenmodes

The aim of this section is to describe the development of a reduced order model for modal analysis in a design context. The design process of most industrial systems is based on the reuse of certain components. Thus a reduction method involving component eigenmodes is proposed in this section. More specifically, this method introduces a SVD-basis for the interface reduction. Two different situations might be faced:

- When the interface mesh is coarse and the interface is large as compared to the substructures volume. Thus a large number of interface vectors are required as compared to the number of interface DoFs. In that case, our method provides no advantages in comparison to Craig-like methods, but it has more or less the same accuracy.

- When the interface mesh is fine and the interface is small as compared to the volume. Thus few interface vectors are required compared to the number of interface DoFs. This leads to a very small reduced order model compared to Craig-like models and, once again, to more or less the same accuracy. In this case the advantage of our method is obvious.

The proposed reduction method is well suited to the design context as it allows building updatable reduced order models. Indeed, the modification of one component does not require the total reconstruction of the reduced order model.

Lastly, the proposed reduction methodology is compared to the Craig-Bampton method and the AMLS method proposed by Gao *et al.* [26] through their application on two cases study, one of them is the SAE's open rotor.

3.5.1 Primal reduction using free component eigenmodes

Let us use the FE operators (defined in Eq. (3.52)) of the two components assembled in the physical domain thanks to the Dirichlet equation Eq. (3.50). The reduction of such an assembled model Eq. (3.52) with component free eigenmodes is possible thanks to the use of the reduction basis T:

$$\mathrm{T} = \Phi_l = \begin{bmatrix} \Phi_{1,i} & 0 \\ \Phi_{1,\Gamma} & \Phi_{2,\Gamma} \\ 0 & \Phi_{2,i} \end{bmatrix}. \tag{3.63}$$

Where Φ_1 and Φ_2 denote the truncated modal basis of the component Σ_1 and Σ_2. Let us consider the finite element model whose mesh is presented in Fig. 3.12 to highlight our purpose.

(a) Mesh of the assembled case study

(b) Contact interface Γ between Σ_1 and Σ_2

Figure 3.12 – The case study is made of two parts: Σ_1, in green with 3747 DoF and Σ_2 in orange with 3933 DoF.

Reference [18] explains that the use of free-free components eigenmode allows recovering the interface dynamics for low frequency behaviour only. Indeed, unlike the fixed-interface eigenmodes used in the Craig-Bampton method, the interface motions of the free component eigenmodes are rather incompatible. Although the description of the component motion on their internal DoF is accurate, the interface displacements are represented poorly. In practice this results in eigensolutions with displacement step around the interface (Fig. 3.13b) or modes with only one component involved (Fig. 3.13a).

Furthermore, Vermot Des Roches [18] showed that the number of component eigenmodes required to enlarge the validity bandwidth of the ROM rapidly becomes large. Therefore the use of additional vectors is required to increase the accuracy of the reduced model and enforce the Dirichlet constraint Eq. (3.47).

3.5.2 Additional vectors and interface reduction

Additional vectors are required to improve the accuracy of our reduced order model. Those vectors are subjected to the following criteria:

- The additional vectors must involve the component interior DoF and correct the problem observed in Fig. 3.13.

- The contacting interface must be reduced. Indeed, one of the main criticisms of the classical primal CMS method is that the description of the interface motion is performed using a nodal displacement basis that may lead to large reduced order model. For this reason, a reduced basis of the interface displacements is sought. A review of the main interface reduction methods was written by Tran in [1].

(a) On mode #16 we can see that displacement are mainly located on one of the substructure (Σ_2) only.

(b) The mode #23 provides a typical example of displacement step in the vicinity of the interface.

Figure 3.13 – Problems occurring when using component eigenmodes only for the model reduction as suggested in Eq. (3.63).

In [18] the eigenmodes Φ of the assembled system were orthogonalized to the component modes and used as additional vectors:

$$\mathrm{T} = \left[\Phi_l \quad \Phi\right]_{\text{orth.}}. \tag{3.64}$$

In this way, it is possible to build a very accurate reduced order model with few assembled system modes. However, in the present case the modes Φ are sought, thus they are not available.

Other more accessible interface reduction techniques using restrained eigenmodes were proposed in [20], [31], [32] and [33]. In the work of Aoyama and Yagawa [20] the additional vectors are defined as the eigensolution of the problem of components assembled two-by-two. In the present case this corresponds to the assembled eigensolutions Φ. Recently, Jezequel and Garambois [34] proposed and compared several DCMS (Double Component Modes Synthesis) for the Hellinger-Reissner (displacement-stress) formulation in structural dynamics. The DCMS methods studied in [34] used various combinations of fixed, free and branch modes for the modal analysis of two components tied to each other.

The main contribution of this work is the build of a compact interface motions basis Υ. This basis Υ is built from the interface motions $\Phi_{1,\Gamma}$ and $\Phi_{2,\Gamma}$ found in the component free eigenmodes of the substructures. To achieve this goal, a singular value decomposition (SVD) of the eigenmodes interface motions is used.

The desired basis Υ is expected to recover all the interface motions $\Phi_{1,\Gamma}$ and $\Phi_{2,\Gamma}$. In order to ensure that all the interface motions will be accurately represented by the singular value decomposition it is important to normalize $\left[\Phi_{1,\Gamma} \quad \Phi_{2,\Gamma}\right]$. Here this normalization is

performed with regards to the interface mass matrix $\mathrm{M}_{1,\Gamma\Gamma} + \mathrm{M}_{2,\Gamma\Gamma}$ so that the following equation is respected:

$$\begin{bmatrix}\Phi_{1,\Gamma} & \Phi_{2,\Gamma}\end{bmatrix}^\top \left[\mathrm{M}_{1,\Gamma\Gamma} + \mathrm{M}_{2,\Gamma\Gamma}\right] \begin{bmatrix}\Phi_{1,\Gamma} & \Phi_{2,\Gamma}\end{bmatrix} = \mathrm{I}_{n_{\Phi_1}+n_{\Phi_2}} \tag{3.65}$$

$$\text{thanks to the procedure: } \forall \boldsymbol{\phi}_i \in \begin{bmatrix}\Phi_{1,\Gamma} & \Phi_{2,\Gamma}\end{bmatrix}, \boldsymbol{\phi}_i := \frac{1}{\|\boldsymbol{\phi}_i\|} \times \boldsymbol{\phi}_i. \tag{3.66}$$

The singular value decomposition allows the decomposition of the interface displacement matrix $\begin{bmatrix}\Phi_{1,\Gamma} & \Phi_{2,\Gamma}\end{bmatrix}$ into left singular vectors Υ, a singular value matrix $\Lambda = \mathrm{diag}(\lambda_1, \ldots, \lambda_n)$ and right singular vectors V as follows:

$$\begin{bmatrix}\Phi_{1,\Gamma} & \Phi_{2,\Gamma}\end{bmatrix} = \Upsilon \Lambda \mathrm{V}^\top \quad \text{with} \quad \Lambda = \begin{bmatrix}\lambda_1 & & \\ & \lambda_2 & \\ & & \ddots\end{bmatrix}. \tag{3.67}$$

In this decomposition the matrix Υ is an orthogonal basis of interface motions sorted according to their associated singular values λ. Using this basis Υ for interface reduction is the main contribution of this work.

The SVD-basis Υ is built from the 51 component eigenmodes found on the frequency range $[0; 3000]$ Hz, once normalized (Eq. (3.65)), the singular value decomposition of the interface displacements provide the basis Υ (Eq. (3.67)). In Fig. 3.14, the logarithmic evolution of the singular values λ shows that a truncation at the 45^{th} vector of Υ make sense.

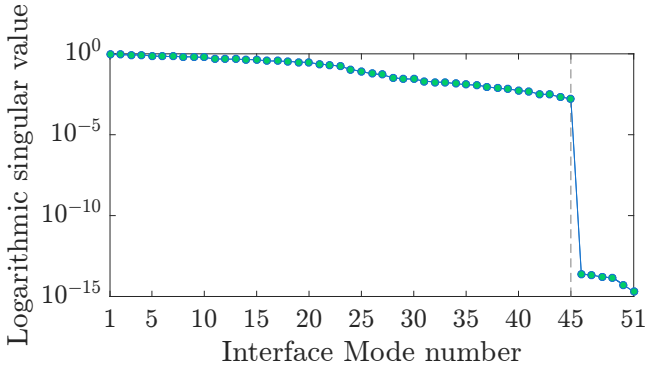

Figure 3.14 – Singular values associated with the motions contained in the basis Υ.

In Fig. 3.14, a clear decrease can be observed for the 45^{th} singular value λ. The small singular values traduce the high colinearity of some interface displacement found in $\Phi_{1,\Gamma}$ and $\Phi_{2,\Gamma}$. In this example, the 6 small singular values (from 46 to 51) are generated by the interface motions associated to component rigid body motions. Indeed, such displacements are similar for the structures Σ_1 and Σ_2.

It is possible to make a truncation of Υ so that the interface motions are efficiently described in a compact manner. The vectors $\boldsymbol{\upsilon}_i$ associated with the largest singular values λ_i are the most significant for the recovery of the interface displacement observed. This means that the size of the basis Υ can be optimized with regards to the singular value λ.

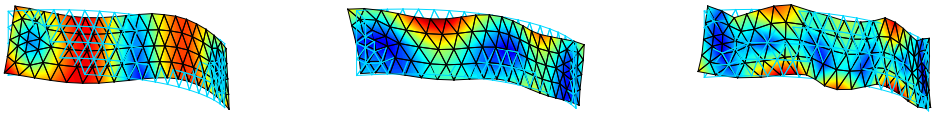

(a) Interface motion υ_9, $\lambda_9 = 0.64$ (b) Interface motion υ_{17}, $\lambda_{17} = 0.36$ (c) Interface motion υ_{25}, $\lambda_{25} = 0.08$

Figure 3.15 – Example of interface motions obtained from the SVD of the interface eigenmode restriction

The displacements in Υ are common to both components so that we define Θ_Υ (see Eq. (3.68)) as the uplift of the component interior DoF associated to the interface displacement of the basis Υ. Since all the interface motions Υ can be recovered by the component eigenmodes Φ_l (Eq. (3.63)), it is unnecessary to include Υ in Θ_Υ:

$$\Theta_\Upsilon = \begin{bmatrix} -\mathrm{Z}_{1,ii}^{-1}\,\mathrm{Z}_{1,i\Gamma}\Upsilon & 0 \\ 0 & 0 \\ 0 & -\mathrm{Z}_{2,ii}^{-1}\,\mathrm{Z}_{2,i\Gamma}\Upsilon \end{bmatrix}. \tag{3.68}$$

The condensations are often implicitly performed for a null circular frequency like the Guyan condensation. In order to increase the amount of information in the reduction basis, the additional vectors Θ_Υ are computed for different circular frequencies. Naturally, these operations are time consuming since they require the inversion of $\mathrm{Z}_{1,ii}$ and $\mathrm{Z}_{2,ii}$. Moreover, the larger the reduction basis, the lower the reduction efficiency. In this work we arbitrarily choose to calculate only the additional vectors for ω_{min}, ω_{max} and $\omega_{mid} = \frac{1}{2}(\omega_{max} + \omega_{min})$ of the studied frequency band $\Delta\omega$. This leads to the following reduction:

$$\mathrm{T} = \begin{bmatrix} \Phi_l & \Theta_\Upsilon(\omega_{min}) & \Theta_\Upsilon(\omega_{mid}) & \Theta_\Upsilon(\omega_{max}) \end{bmatrix}. \tag{3.69}$$

The thinking behind the choice of the condensation circular frequency is that using frequencies regularly spread over the bandwidth of interest Δf will help recovering the dynamics of the system over Δf. Indeed, the condensation tends to neglect the contributions of the modes whose natural frequency are distant from the condensation frequency. The choice of the condensation frequency is strategic choice and should be made with regards to the case study considered and the targeted goal.

This procedure leads to the reduction basis T of size $n_T = n_{\Phi_1} + n_{\Phi_2} + 6n_\Upsilon$, indeed 3 circular frequencies are used, one for each component. In order to improve the numerical

conditioning of the reduced order model produced by the proposed reduction methodology an orthonormalization of the reduction basis T (see Eq. (3.69)) with regards to the assembled mass matrix M is performed, thus:

$$\mathrm{T}^{\top}\mathrm{M}\mathrm{T} = \mathrm{I}_{n_{\mathrm{T}}}. \tag{3.70}$$

The reduction methodology proposed in this section enables to building a model whose accuracy and size are tunable thanks to the truncation of the basis Υ. The SVD interface modes Υ allow describing the interface motions of the component free eigenmodes with the desired accuracy.

In order to study the impact of the Υ truncation on the quality of the results, the mass-MAC average [11] is evaluated for several truncations. In Fig. 3.16 it can be seen that, the impact of the truncation is significant around 45 vectors. Indeed, using more than 45 interface motions does not significantly improve the quality of the results.

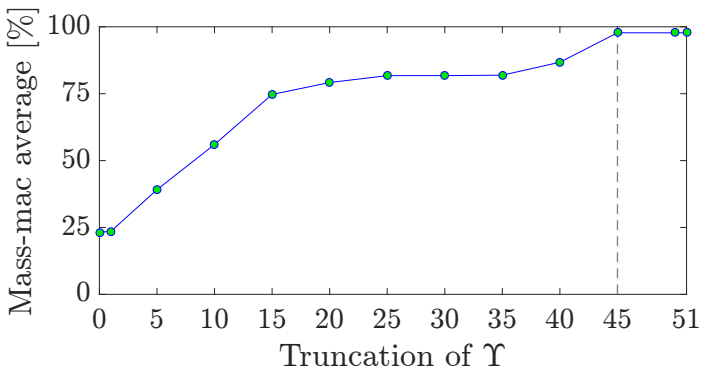

Figure 3.16 – MAC average of ROM built with different truncations of Υ

The choice of using several additional vectors Θ_{Υ} with different circular frequencies is justified since it increase the ROM accuracy over the frequency band of interest, let us verify this assertion. The Fig. 3.17 gives the mass-MAC results obtained using different condensation circular frequencies.

As it can be seen in Fig. 3.17, the additional vectors Θ_{Υ} computed for 1500 Hertz and 3000 Hertz improves the solutions of the highest frequencies. Let us compare the results obtained using the proposed method and the Craig-Bampton method.

For this specific application we conclude that the Craig-Bampton method provides better results than the proposed method, although its associated reduced order model is less compact.

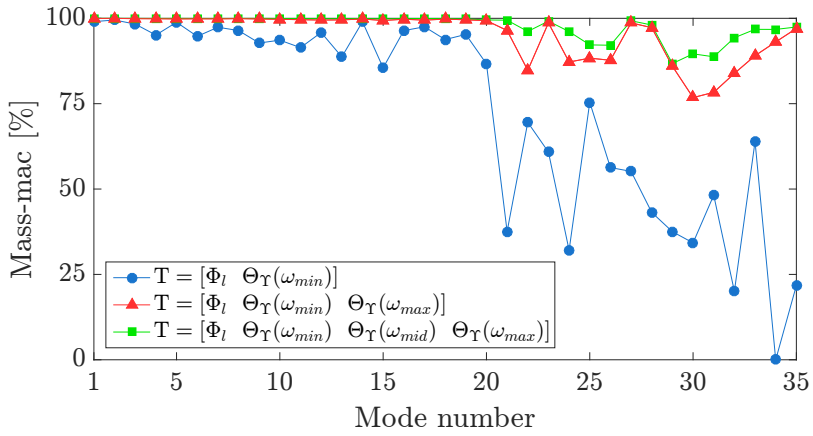

Figure 3.17 – Comparison of the mass-MAC obtained with different reduced order models. The basis Υ is truncated at its 45^{th} element and the additional vectors Θ_Υ are computed for different frequencies: $f_{min} = 0\text{Hz}$, $f_{mid} = 1500\text{Hz}$, $f_{max} = 3000\text{Hz}$

Method	Craig-Bampton method	Proposed methodology using the first 45 vectors of Υ
Basis size	393	321
MAC average	98.59%	97.76%
Frequency error average	0.35%	0.52%

Table 3.1 – Comparison of the compactness and accuracy of the proposed and Craig-Bampton method for modal analysis: application to the academic cast study presented in Fig. 3.12.

3.5.3 Reduced order model update

In the context of an iterative design of the CROR's blade, the reduced order model of the hub-blade assembly considerably changes. Although the frequent redesign of the blade leads to modifications of its FE model, the hub remains unchanged. Thus, instead of entirely rebuilding the assembly ROM at each design iteration, it is interesting to identify whichs term have to be updated. In this section, the system considered has only two components (the hub and the blade), however the results presented can be extended to an assembly with more components.

When regrouping the component condensation in the reduction basis Eq. (3.69) it is

possible to express T as follows:

$$\mathrm{T} = \begin{bmatrix} \Phi_l & \Theta_\Upsilon \end{bmatrix} = \begin{bmatrix} \Phi_{1,i} & 0 & \Theta_{1,\Upsilon} & 0 \\ \Phi_{1,\Gamma} & \Phi_{2,\Gamma} & 0 & 0 \\ 0 & \Phi_{2,i} & 0 & \Theta_{2,\Upsilon} \end{bmatrix}. \tag{3.71}$$

The ROM $\tilde{\mathrm{Z}}$ obtained by the reduction of the assembled matrix Eq. (3.52) with the reduction basis Eq. (3.71) has the following symmetric topology:

$$\tilde{\mathrm{Z}} = \begin{bmatrix} \tilde{\mathrm{Z}}_{11} & \tilde{\mathrm{Z}}_{12} & \tilde{\mathrm{Z}}_{13} & \tilde{\mathrm{Z}}_{14} \\ \text{sym.} & \tilde{\mathrm{Z}}_{22} & \tilde{\mathrm{Z}}_{23} & \tilde{\mathrm{Z}}_{24} \\ \text{sym.} & \text{sym.} & \tilde{\mathrm{Z}}_{33} & 0 \\ \text{sym.} & \text{sym.} & \text{sym.} & \tilde{\mathrm{Z}}_{44} \end{bmatrix}. \tag{3.72}$$

The terms of the reduced matrix Eq. (3.72) are given below:

$$\begin{aligned}
\tilde{\mathrm{Z}}_{11} &= \Big(-\omega^2 \mathrm{I}_{n_{\Phi_1}} + \Lambda_1 \Big) + \Phi_{1,\Gamma}^\top \mathrm{Z}_{2,\Gamma\Gamma} \Phi_{1,\Gamma} \\
\tilde{\mathrm{Z}}_{12} &= \Big(\Phi_{1i}^\top \mathrm{Z}_{1,i\Gamma} + \Phi_{1,\Gamma}^\top (\mathrm{Z}_{1,\Gamma} + \mathrm{Z}_{2,\Gamma}) + \Phi_{1,\Gamma}^\top \mathrm{Z}_{2,i\Gamma} \Big) \Phi_{2,\Gamma} \\
\tilde{\mathrm{Z}}_{22} &= \Big(-\omega^2 \mathrm{I}_{n_{\Phi_2}} + \Lambda_2 \Big) + \Phi_{2,\Gamma}^\top \mathrm{Z}_{1,\Gamma\Gamma} \Phi_{2,\Gamma} \\
\tilde{\mathrm{Z}}_{13} &= \Big(\Phi_{1,\Gamma}^\top \mathrm{Z}_{1,\Gamma i} + \Phi_{1,i}^\top \mathrm{Z}_{1,ii} \Big) \Theta_{1,\Upsilon} \\
\tilde{\mathrm{Z}}_{33} &= \Theta_{1,\Upsilon}^\top \mathrm{Z}_{1,ii} \Theta_{1,\Upsilon} \\
\tilde{\mathrm{Z}}_{14} &= \Phi_{1,\Gamma}^\top \mathrm{Z}_{2,\Gamma i} \Theta_{2,\Upsilon} \\
\tilde{\mathrm{Z}}_{44} &= \Theta_{2,\Upsilon}^\top \mathrm{Z}_{2,ii} \Theta_{2,\Upsilon} \\
\tilde{\mathrm{Z}}_{23} &= \Phi_{2,\Gamma}^\top \mathrm{Z}_{1,\Gamma i} \Theta_{1,\Upsilon} \\
\tilde{\mathrm{Z}}_{24} &= \Big(\Phi_{2,\Gamma}^\top \mathrm{Z}_{2,\Gamma i} + \Phi_{2,i}^\top \mathrm{Z}_{2,ii} \Big) \Theta_{2,\Upsilon}
\end{aligned}$$

The modification of one component (Σ_1 or Σ_2) impacts all the terms of $\tilde{\mathrm{Z}}$. Let us consider the modification of the component Σ_2, which alters Φ_2, $\Theta_{2,\Upsilon}$ and $\Theta_{1,\Upsilon}$. Theoretically, such a modification of Σ_2 requires an update of all the terms $\tilde{\mathrm{Z}}$.

Nevertheless, it is possible to consider that the modification of Σ_2 does not significantly impact Υ. This can be measured by verifying that the interface basis Υ allows accurately recovering the displacements expressed by the modified term $\Phi_{2,\Gamma}$. In practice, this can be done by checking that for each vector $\boldsymbol{\phi}_{2,\Gamma}$ of $\Phi_{2,\Gamma}$:

$$\left\| \left(\mathrm{I} - \Upsilon^\top \Upsilon \right) \boldsymbol{\phi}_{2,\Gamma} \right\| \ll \left\| \boldsymbol{\phi}_{2,\Gamma} \right\|. \tag{3.73}$$

Note that here, the basis Υ is normalized with the identity matrix since it results from the singular value decomposition (Eq. (3.67)).

If no update of the interface basis Υ is necessary, then the terms $\tilde{Z}_{13}$ and $\tilde{Z}_{33}$ are no longer dependent on the modifications applied to Σ_2. Consequently, the modification of Σ_2 leads only to the re-computation of 7 of the 16 terms of $\tilde{Z}$: $\tilde{Z}_{11}$, $\tilde{Z}_{22}$, $\tilde{Z}_{44}$, $\tilde{Z}_{12}$, $\tilde{Z}_{14}$, $\tilde{Z}_{23}$ and $\tilde{Z}_{24}$.

Starting from a reduced model $\tilde{Z}$, the update of the reduced matrix due to a modification of Σ_2 should be managed as follow:

1. parallel re-computation of Φ_2 and $\Theta_{2,\Upsilon}$.
2. orthogonalisation $\Theta_{2,\Upsilon}$ to Φ_{2i}.
3. parallel re-computation of $\tilde{Z}_{11}$, $\tilde{Z}_{22}$, $\tilde{Z}_{44}$, $\tilde{Z}_{12}$, $\tilde{Z}_{14}$, $\tilde{Z}_{23}$ and $\tilde{Z}_{24}$.
4. re-assembly of $\tilde{Z}$ using the term previously re-computed.

3.5.4 Application of the proposed reduction method to an industrial case study

To validate our premise, the methodology described previously is applied to the blade of the CROR when tied to the hub. The assembly (see Fig. 3.18b) contains 189888 DoF and is studied over a frequency bandwidth Δf between 0 and 2000 Hz. Over this range, the system assembled has 53 flexible eigenmodes that should all be recovered by the proposed reduced order model. The dynamics of both parts is assumed to be linear.

The results of this industrial case study reduction are compared with those obtained with the Craig-Bampton method. The accuracy of the two methods are compared using the mass-MAC (see section 3.2.1) computed in the nodal space (HFM). In the following, the hub will be denoted Σ_1 while Σ_2 refers to the blade model in the next section.

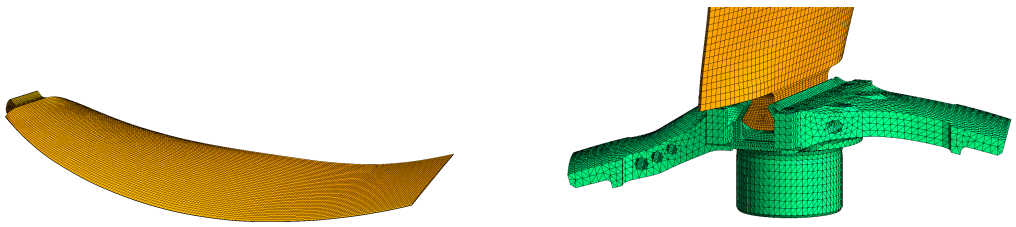

(a) Mesh of the whole blade Σ_2.

(b) The hub Σ_1 is assembled with the blade Σ_2.

Figure 3.18 – The mesh of the blade Σ_2 is composed of 39724 nodes ($n_2 = 119172$ DoF) while 24370 nodes ($n_1 = 70716$ DoF) are used for the hub mesh Σ_1

Moreover, the proposed reduction technique is tested but the reduced order model update described in section 3.5.3 is not applied.

Application of the Craig-Bampton method

The component fixed-interface eigenmodes are truncated using Rubin's criterion over the frequency range $[0, 1.5 \times f_{max}] = [0, 3000]$ Hertz, which corresponds to 85 reduction vectors. Indeed, on this bandwidth, the blade owns 78 tied interface modes while the hub owns 7.

The size of the reduced order model obtained using the fixed-interface mode and the component static condensation is 1165×1165. This reduced order model has an average relative frequency error of 0.26% (see Fig. 3.22) while its average MAC reaches more than 94% (see Fig. 3.23a).

As the first 6^{th} eigensolutions are identified as rigid body motions, their associated eigenvalues vanish, thus the associated relative frequency error tends to infinity. This is why these 6 relative frequency errors are not plotted in Fig. 3.22. As it can be seen in Fig. 3.23a, 2 eigensolutions have an MAC below 60%.

Application of the AMLS method for eigenvalue problem

The compactness issues of the Craig-Bampton method due to the interface size are well known in dynamic substructuring. Hence, in order to balance the comparison of the proposed method with other existing and more recent methods, the AMLS method presented in section 3.4.2 is applied.

In the present application, the substructures are defined as the components: the blade and the hub. The separator is arbitrary forced to be interface between those two components. Moreover, the matrices K_p and M_p (see Eq. (A.18)) correspond to matrix Eq. (3.52) after a proper reorganization. Adapted to a two components problem, the expressions of the stiffness operator $\hat{\mathrm{K}}$ then becomes:

$$\mathrm{K}_p = \mathrm{L}\mathrm{D}\mathrm{L}^\top \quad \text{with} \quad \mathrm{L} = \begin{bmatrix} \mathrm{I}_1 & 0 & 0 \\ 0 & \mathrm{I}_2 & 0 \\ \mathrm{K}_{31}\mathrm{K}_{11}^{-1} & \mathrm{K}_{32}\mathrm{K}_{22}^{-1} & \mathrm{I}_3 \end{bmatrix}$$

$$\hat{\mathrm{K}} = \mathrm{D} = \begin{bmatrix} \hat{\mathrm{K}}_{11} & 0 & 0 \\ 0 & \hat{\mathrm{K}}_{22} & 0 \\ 0 & 0 & \hat{\mathrm{K}}_{33} \end{bmatrix} \quad \text{knowing} \quad \begin{cases} \hat{\mathrm{K}}_{11} = \mathrm{K}_{11} \\ \hat{\mathrm{K}}_{22} = \mathrm{K}_{22} \\ \hat{\mathrm{K}}_{33} = \mathrm{K}_{33} - \mathrm{K}_{31}\mathrm{K}_{11}^{-1}\mathrm{K}_{13} - \mathrm{K}_{21}\mathrm{K}_{22}^{-1}\mathrm{K}_{12} \end{cases} .$$

The topology of the mass matrix $\hat{\mathrm{M}}$ can be observed in this example. The constitutive

matrix $\hat{\mathrm{M}}_{ij}$ of $\hat{\mathrm{M}}$ are given by the following relations:

$$\hat{\mathrm{M}} = \mathrm{L}^{-1}\mathrm{M}_p\mathrm{L}^{-\top} = \begin{bmatrix} \mathrm{M}_{11} & 0 & \hat{\mathrm{M}}_{13} \\ 0 & \mathrm{M}_{22} & \hat{\mathrm{M}}_{23} \\ \hat{\mathrm{M}}_{13}^\top & \hat{\mathrm{M}}_{23}^\top & \hat{\mathrm{M}}_{33} \end{bmatrix}.$$

$$\text{knowing} \quad \begin{cases} \hat{\mathrm{M}}_{13}^\top &= \mathrm{M}_{13} - \mathrm{M}_{11}^{-1}\mathrm{K}_{13} \\ \hat{\mathrm{M}}_{23}^\top &= \mathrm{M}_{23} - \mathrm{M}_{22}^{-1}\mathrm{K}_{23} \\ \hat{\mathrm{M}}_{33}^\top &= \mathrm{M}_{33} - \left(\hat{\mathrm{K}}_{13}^\top\mathrm{K}_{11}^{-1}\mathrm{M}_{13} + \hat{\mathrm{M}}_{13}^\top\mathrm{K}_{11}^{-1}\mathrm{K}_{13} - \hat{\mathrm{K}}_{13}^\top\mathrm{K}_{11}^{-1}\mathrm{M}_{11}\mathrm{K}_{11}^{-1}\hat{\mathrm{K}}_{13}\right) \\ & \quad - \left(\hat{\mathrm{K}}_{23}^\top\mathrm{K}_{22}^{-2}\mathrm{M}_{23} + \hat{\mathrm{M}}_{23}^\top\mathrm{K}_{22}^{-2}\mathrm{K}_{23} - \hat{\mathrm{K}}_{23}^\top\mathrm{K}_{22}^{-2}\mathrm{M}_{22}\mathrm{K}_{22}^{-2}\hat{\mathrm{K}}_{23}\right) \end{cases}.$$

The modes associated to the substructures are truncated using the same Rubin's criterion than for the Craig-Bampton method previously presented. Thus, the truncation is performed at $1.5 \times f_{\max} = 3000$ Hertz, that leads to 7 modes for $\hat{\Phi}_1$ and 78 modes for $\hat{\Phi}_2$.

$$\tilde{\hat{\mathrm{Z}}} = \hat{\Phi}^\top \underbrace{\left(\mathrm{L}^{-1}\mathrm{Z}_p\mathrm{L}^{-\top}\right)}_{\hat{\mathrm{Z}}} \hat{\Phi} \quad \text{with} \quad \hat{\Phi} = \begin{bmatrix} \hat{\Phi}_1 & 0 & 0 \\ 0 & \hat{\Phi}_2 & 0 \\ 0 & 0 & \hat{\Phi}_3 \end{bmatrix}. \tag{3.74}$$

The convergence of this AMLS method is studied through the selection of separator modes $\hat{\Phi}_3$. This grants the compactness comparison of both AMLS and proposed method. It is visible in Fig. 3.19 that the AMLS method requires around 15 separator modes to provide accurate results, this lead to a reduced order model carrying around hundred modes: $n_{\hat{\Phi}_1} + n_{\hat{\Phi}_2} + n_{\hat{\Phi}_3} = 7 + 78 + 15 = 100$.

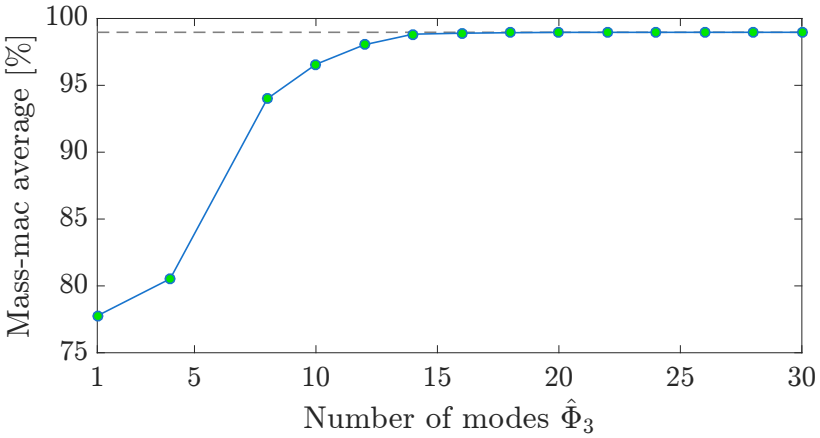

Figure 3.19 – Convergence of the AMLS method with regards to the selected number of seperator modes $\hat{\Phi}_3$. When converging, the method reach 98.97% of mass-mac.

The AMLS method allows to build compact and accurate reduced order model (mass-max $\simeq$ 99%). Using 16 modes $\hat{\Phi}_3$ lead to a reduced order model with 101 DoF, a mass

mac of 98.90 % and a relative error frequency of 0.09 %. It is worth noticing that the AMLS method does not use free component eigenmodes, unlike the proposed method.

Application of the proposed method

The first step of the proposed method is the computation of the component free eigenmodes. The selection of the component eigenmodes is a key point of the modal truncation that can be treated in various ways. In the present case we decided to use only the component eigenmodes over the frequency range $[0, 2000]$ Hz which gives $n_{\Phi_1} = 9$ modes for the hub and $n_{\Phi_2} = 56$ modes for the blade.

The singular value decomposition of the component interface motions leads to the truncated basis Υ of the interface motion which has $n_{\Phi_1} + n_{\Phi_2} = 65$ modes. From the singular values λ_i associated with these displacements υ_i (Fig. 3.20) it can be seen that the interface displacement ($\Phi_{1,\Gamma}$ and $\Phi_{2,\Gamma}$) of the component eigenmodes can be mostly recovered using a restricted displacement SVD-basis.

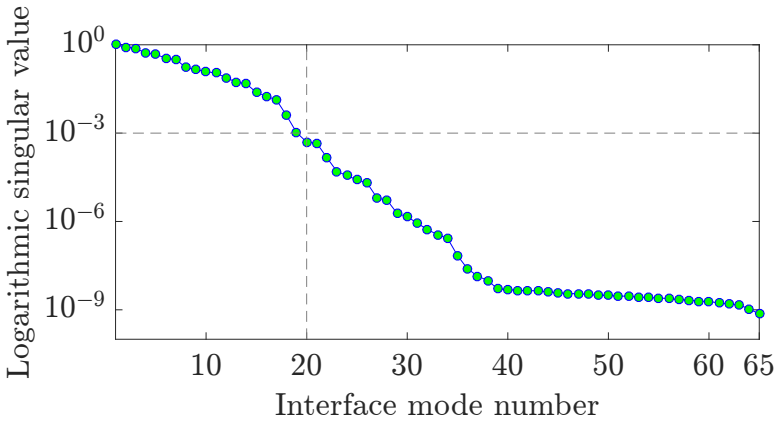

Figure 3.20 – Singular values λ_i associated with the vectors Υ_i of the basis Υ.

The fall of the singular value is slower than that obtained in the first case study Fig. 3.14. In that case the threshold was set by considering one thousand of the first eigenvalue. Using this criterion, the description of the interface motion over $[0,\ 2000]$ Hz is assumed using 20 DoF whereas the interface owns 1080 DoF (see Fig. 3.10).

Several interface motions of Υ are given as examples in Fig. 3.21. The first 12 displacements correspond to rigid modes; indeed the interface is split into two parts, each having 6 rigid modes.

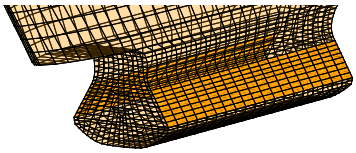

(a) Contacting interface between the blade and the hub

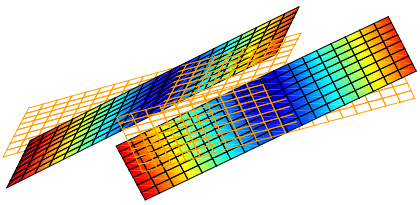

(b) Interface displacement υ_5, $\lambda_5 = 5.36$

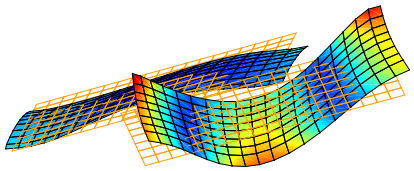

(c) Interface displacement υ_{15}, $\lambda_{15} = 1.48 \times 10^{-2}$

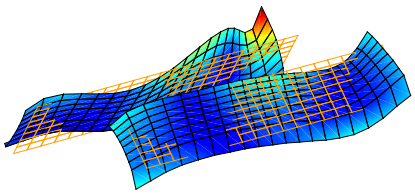

(d) Interface displacement υ_{22}, $\lambda_{22} = 4.29 \times 10^{-4}$

Figure 3.21 – Examples of interface displacements obtained from the singular value decomposition of the component eigenmodes interface restriction. On the current plot, those displacement are evaluated on the blade interface.

In order to build a compact reduced order model, we use only the first 20 elements of Υ as their associated singular values are much higher than the others (see Fig. 3.20). The vectors Θ_Υ (Eq. (3.68)) are computed for $f_{\text{min}} = 0$Hz, $f_{\text{mid}} = 1000$Hz and $f_{\text{max}} = 2000$ Hz. Thus, once built, the reduced order model has only $n = 185$ DoF (while the high fidelity model has 189888 DoF), indeed $n = n_{\Phi_1} + n_{\Phi_2} + 6 \times 20$.

As it can be seen in Fig. 3.22, the reduced order model provides good results in terms of MAC and relative frequency error. Indeed the averages of the relative frequency (0.18%, see Fig. 3.22) and the MAC (98.16, see Fig. 3.23b) are better than those obtained using the Craig-Bampton method.

The Fig. 3.23b indicates that the solution #38 and #39 are inaccurate since their mass-MAC are below 70%. In fact, this phenomenon is due to the eigenproblem solver. Indeed, whereas the MAC between the ROM and HFM solutions is small, $\tilde{\boldsymbol{\phi}}_{38}$ and $\tilde{\boldsymbol{\phi}}_{39}$ describe a 2D space that is able to accurately span $\boldsymbol{\phi}_{38}$ and $\boldsymbol{\phi}_{39}$. In other words, the solutions $\tilde{\boldsymbol{\phi}}_{38}$ and $\tilde{\boldsymbol{\phi}}_{39}$ can be used to recover $\boldsymbol{\phi}_{38}$ and $\boldsymbol{\phi}_{39}$, these new approximations are noted $\boldsymbol{\psi}_{38}$ and $\boldsymbol{\psi}_{39}$:

$$\begin{cases} \boldsymbol{\psi}_{38} = \left(\boldsymbol{\phi}_{38}^\top \mathrm{M} \tilde{\boldsymbol{\phi}}_{38}\right) \tilde{\boldsymbol{\phi}}_{38} + \left(\boldsymbol{\phi}_{38}^\top \mathrm{M} \tilde{\boldsymbol{\phi}}_{39}\right) \tilde{\boldsymbol{\phi}}_{39} \\ \boldsymbol{\psi}_{39} = \left(\boldsymbol{\phi}_{39}^\top \mathrm{M} \tilde{\boldsymbol{\phi}}_{38}\right) \tilde{\boldsymbol{\phi}}_{38} + \left(\boldsymbol{\phi}_{39}^\top \mathrm{M} \tilde{\boldsymbol{\phi}}_{39}\right) \tilde{\boldsymbol{\phi}}_{39} \end{cases} .$$

This recombination of the vectors $\tilde{\boldsymbol{\phi}}_{38}$ and $\tilde{\boldsymbol{\phi}}_{39}$ is efficient since it allows to recover the HFM modes $\boldsymbol{\phi}_{38}$ and $\boldsymbol{\phi}_{39}$ with respectively 96.49% and 98.58% of mass-MAC. Hence, the

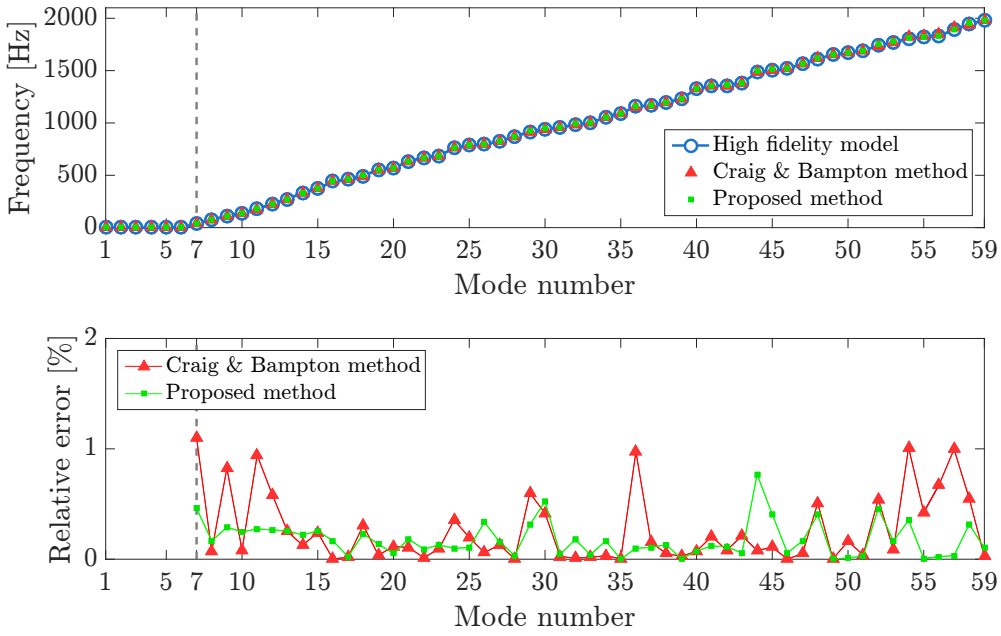

Figure 3.22 – Comparison of the natural frequencies computed with the Craig-Bampton and the proposed method.

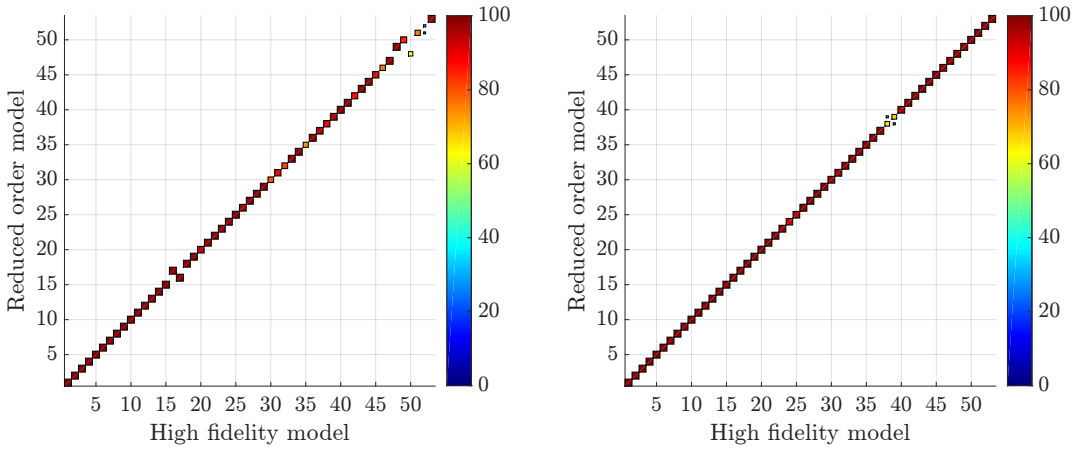

(a) Craig-Bampton method:number of DoF: 1165, MAC average: 94.37% (min.: 32.30%)

(b) Proposed method method: number of DoF: 185, MAC average: 98.16% (min.: 67.07%)

Figure 3.23 – Mass-MAC of the Craig-Bampton and proposed method.

results of the proposed methods are better than the ones shown in Fig. 3.23. The results obtained with this modal recombination are given in Fig. 3.24.

The results of the previous experiments are summarized in the table Tab. 3.2.

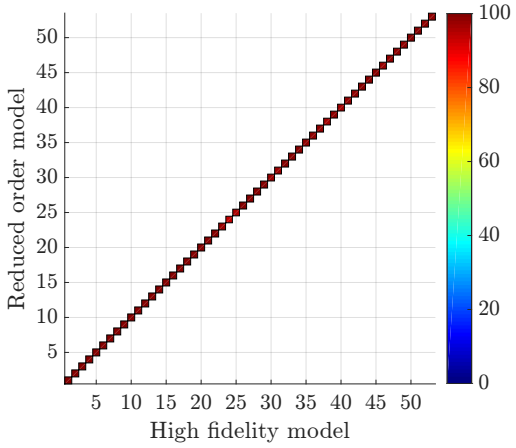

(a) Proposed method method with corrected MAC: number of DoF: 185, MAC average: 99.28% (min.: 93.75%)

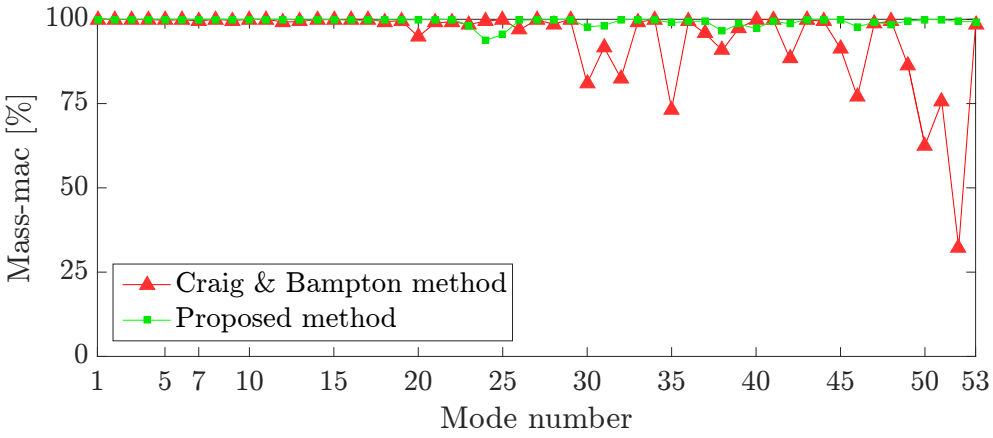

(b) Comparison of the mass-MAC obtained with Craig-Bampton and the proposed method

Figure 3.24 – Results of the proposed methods after the recombination of the modes $\tilde{\boldsymbol{\phi}}_{38}$ and $\tilde{\boldsymbol{\phi}}_{39}$.

3.5.5 Improvement of the proposed method

It has been seen in 3.5.1 that the use of component eigenmodes Φ_l only is not sufficient to well recover the assembled eigenmodes. This is notably due to the incompatibility of the component interface motions found in the eigenmodes $\Phi_{1,\Gamma}$ and $\Phi_{2,\Gamma}$. In order to tackle this issue, additional displacements Θ_Υ have been proposed in section 3.5.2. Basically, some of the component interface displacements might be compatible, although they are not expected to be numerous.

The SVD-basis Υ should be built from incompatible component interface motions only.

Method	Craig-Bampton method	AMLS method	Proposed methodology using the first 20^{th} vectors of $\boldsymbol{\Upsilon}$
Basis size	1165	101	185
MAC average	94.37%	98.90%	99.28%
Frequency error average	0.26%	0.09%	0.18%

Table 3.2 – Compactness and accuracy comparison between the Craig-Bampton, AMLS and proposed method.

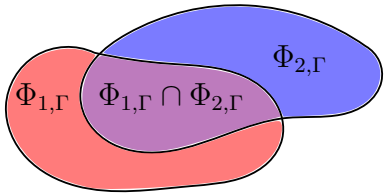

Figure 3.25 – Representation of the subspaces spanned by $\Phi_{1,\Gamma}$ and $\Phi_{2,\Gamma}$.

Indeed, the free eigenmodes with compatible interface motions ($\Phi_{1,\Gamma} \cap \Phi_{2,\Gamma}$) are not likely to generate displacement step. The incompatible interface motions can be defined using the difference between the union ($\Phi_{1,\Gamma} \cup \Phi_{2,\Gamma}$) and the compatible interface motions ($\Phi_{1,\Gamma} \cap \Phi_{2,\Gamma}$). Mathematically, the non-compatible interface motions can be written using the difference operator $\setminus$ as: $(\Phi_{1,\Gamma} \cup \Phi_{2,\Gamma}) \setminus (\Phi_{1,\Gamma} \cap \Phi_{2\Gamma})$. Let us note $\Psi_{1,\Gamma}$ and $\Psi_{2,\Gamma}$, the incompatible interface displacement of the component Σ_1 and Σ_2. Those motions are defined as:

$$\begin{cases} \Psi_{1,\Gamma} = \Phi_{1,\Gamma} \setminus \Phi_{2,\Gamma} \\ \Psi_{2,\Gamma} = \Phi_{2,\Gamma} \setminus \Phi_{1,\Gamma} \end{cases} \quad \text{so that} \quad \begin{cases} \Phi_{1,\Gamma} = \Psi_{1,\Gamma} \cup \left(\Phi_{1,\Gamma} \cap \Phi_{2,\Gamma}\right) \\ \Phi_{2,\Gamma} = \Psi_{2,\Gamma} \cup \left(\Phi_{1,\Gamma} \cap \Phi_{2,\Gamma}\right) \end{cases} .$$

In order to filter the plausible compatible interface motions it is possible to perform the SVD (Eq. (3.67)) on the non-compatible interface motions ($\Psi_{1,\Gamma} \cup \Psi_{2,\Gamma}$). Practically, the non-compatible interface motions $\Psi_{1,\Gamma}$ and $\Psi_{2,\Gamma}$ are computed using a Gram-Schmidt based procedure. The SVD basis is now computed as:

$$\begin{bmatrix} \Psi_{1,\Gamma} & \Psi_{2,\Gamma} \end{bmatrix} = \Upsilon \Lambda \mathrm{V}^{\top}. \tag{3.75}$$

The application of this new procedure has been performed on the blade-hub interface. The evolution of the singular values λ_i associated to the improved proposed method are given in Fig. 3.26.

A noticeable drop of the singular values λ_i has been brought by this improvement of the proposed method we can see it in Fig. 3.26. In section 3.5.4 the truncation of the basis

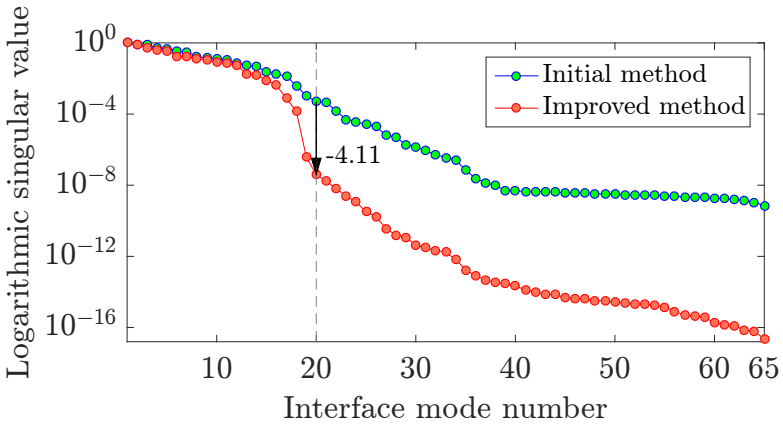

Figure 3.26 – Comparison of the singular value decrease with the SVD proposed in Eq. (3.67) and Eq. (3.75).

Υ has been performed at the 20^{th} vector with a singular value $\lambda_{20} = 5 \times 10^{-4}$, with this improvement this value has been reduced to 3.12×10^{-8}. As a conclusion, the proposed improvement can be used to build more compact interface basis Υ.

Chapter conclusion

In this chapter, a modal analysis oriented reduction methodology has been proposed. The proposed method is a powerful tool in dynamics for building reduced order models of assembled structures with free component eigenmodes and without any dynamic simulation of the complete structure. Good compactness can be provided by the interface reduction method proposed in section 3.5, and it is the central contribution of this work. In section 3.5.1 we showed that the matrix of the reduced order model is suited for tuning. Indeed, model tuning can be considered through the direct modification of the component eigenvalues that appear in the terms $\tilde{Z}_{11}$ and $\tilde{Z}_{22}$ highlighted in section 3.5.3.

The main approach set out in this chapter, i.e. interface reduction using the SVD of the component free-free eigenmodes, is efficient and has several advantages. It is a simple and powerful technique that allows recovering most of the interface motions of the assembled system. Moreover, the singular values can be used to select the interface motions and then to manage the compactness and the precision of a reduced order model. Contrary to the Craig-Bampton method, the number of interface DoF is no longer linked to its mesh but to its dynamics. The efficiency of this method increases as the interface dynamics decreases, which can be seen when comparing the compactness of the reduced order model obtained for the different case studies.

Once applied it can be clearly seen that the proposed method enabled to obtain an ac-

curate and compact reduction basis in terms of MAC (average: 99.28%, see Fig. 3.24) and relative frequency error (average: 0.18%, see Fig. 3.22). The number of degrees of freedom plummeted from 189888 to 185 with our reduction method while the Craig-Bampton method required 1147 DoF and provided less accurate results: MAC average 94.37%, relative frequency error 0.26%. Although it is possible to find more compact reduction methods (like the AMLS method), the performance of the proposed method appears to be clearly good. Note that the proposed method uses free component eigenmodes whereas the tested methods (Craig-Bampton and the AMLS) involve eigenmodes with tied DoF.

The efficiency of the proposed method is better for case studies with low interface dynamics. This was visible in particular for the first case study, for which the proposed method was roughly equivalent to the Craig-Bampton method in terms of accuracy and compactness.

In conclusion, the work presented a reduction method inspired from the dynamic substructuring technique and characterized by the three following features:

- the interface is reduced using a basis Υ built from component eigenmodes.
- the method accuracy is about equivalent to the Craig-Bampton method but produces smaller reduced order models thanks to the interface reduction.
- the reduction targets the modal analysis in a redesign context.

In section 3.2, the quality of the eigensolutions obtained from a ROM are evaluated through appropriated estimators. Eventually, those estimators are used conjointly to Arnoldi vectors in order to enrich the ROM. This enrichment algorithm is given in 3.2.1.

Bibliography

[1] D.-M. Tran, "Component mode synthesis methods using partial interface modes: Application to tuned and mistuned structures with cyclic symmetry," *Computers & Structures*, vol. 87, no. 17-18, pp. 1141–1153, 2009.

[2] P. Holzwarth and P. Eberhard, "Input-output based model reduction for interconnected systems," in *11th World Congress on Computational Mechanics (WCCM XI)*, pp. 20–25, 2014.

[3] B. Besselink, U. Tabak, A. Lutowska, N. van de Wouw, H. Nijmeijer, D. J. Rixen, M. E. Hochstenbach, and W. H. A. Schilders, "A comparison of model reduction techniques from structural dynamics, numerical mathematics and systems and control," *Journal of Sound and Vibration*, vol. 332, no. 19, pp. 4403–4422, 2013.

[4] U. Hetmaniuk, R. Tezaur, and C. Farhat, "Review and assessment of interpolatory model order reduction methods for frequency response structural dynamics and acoustics problems," *International Journal for Numerical Methods in Engineering*, vol. 90, no. 13, pp. 1636–1662, 2011.

[5] M. H. Gutknecht, "A Brief Introduction to Krylov Space Methods for Solving Linear Systems," *Frontiers of Computational Science*, pp. 53–62, 2007.

[6] D. J. Rixen, "Modal Truncation Augmentation and Moment Matching : two faces of the same coin." 2009.

[7] É. Balmès, *Modèles analytiques réduits et modèles expérimentaux complets en dynamique des structures*. Habilitation à diriger des recherches, 1997.

[8] D. Martinez, A. Miller, and T. Carne, "Combined experimental/analytical modeling of shell/payload structures." 1985.

[9] R. H. MacNeal, "A hybrid method of component mode synthesis," *Computers & Structures*, vol. 1, no. 4, pp. 581–601, 1971.

[10] A. Batailly and M. Legrand, "Technical note: another presentation of Craig-Martinez method." 2011.

[11] R. J. Allemang, "The Modal Assurance Criterion - Twenty Years of Use and Abuse," *Sound and Vibration*, vol. 37, no. 8, pp. 14–20, 2003.

[12] A. Bobillot, *Méthodes de réduction pour le recalage. Application au cas d'Ariane 5.* PhD thesis, Ecole Centrale Paris, 2002.

[13] P. Gosselet, C. Rey, and D. J. Rixen, "On the initial estimate of interface forces in FETI methods," *Computer Methods in Applied Mechanics and Engineering*, vol. 192, no. 25, pp. 2749–2764, 2003.

[14] É. Balmès, "Use of Generalized Interface Degrees of Freedom in Component Mode Synthesis," *Proceedings of the 14th International Modal Analysis Conference*, pp. 1–7, 1996.

[15] C. Farhat and M. Géradin, "On a component mode synthesis method and its application to incompatible substructures," *Computers & Structures*, vol. 51, no. 5, pp. 459–473, 1994.

[16] G. Vermot Des Roches, É. Balmès, H. Ben Dhia, R. Lemaire, and T. Pasquet, "Compatibility measure and penalized contact resolution for incompatible interfaces," *European Journal of Computational Mechanics*, vol. 19, no. 3, pp. 317–328, 2010.

[17] G. Dhatt, G. Touzot, and E. Lefrançois, *Méthode des éléments finis.* Hermes Science, 2007.

[18] G. Vermot des Roches, *Frequency and time simulation of squeal instabilities. Application to the design of industrial automotive brakes.* PhD thesis, Ecole Centrale Paris, 2011.

[19] J. V. Aguado, A. Huerta, F. Chinesta, and E. Cueto, "Real-time monitoring of thermal processes by reduced order modeling," *International Journal for Numerical Methods in Engineering*, vol. 102, no. 5, pp. 991–1017, 2015.

[20] Y. Aoyama and G. Yagawa, "Component mode synthesis for large-scale structural eigenanalysis," *Computers & Structures*, vol. 79, no. 6, pp. 605–615, 2001.

[21] R. Shioya and G. Yagawa, "Parallel finite elements of ten-million dofs based on domain decomposition method." 2004.

[22] C. Farhat, J. Li, and P. Avery, "A FETI-DP method for the parallel iterative solution of indefinite and complex-valued solid and shell vibration problems," *International Journal for Numerical Methods in Engineering*, vol. 63, no. 3, pp. 398–427, 2005.

[23] D. De Klerk, D. J. Rixen, and S. N. Voormeeren, "General Framework for Dynamic Substructuring: History, Review and Classification of Techniques," *AIAA Journal*, vol. 46, no. 5, pp. 1169–1181, 2008.

[24] A. L. Hale and L. Meirovitch, "A general substructure synthesis method for the dynamic simulation of complex structures," *Journal of Sound and Vibration*, vol. 69, no. 2, pp. 309–326, 1980.

[25] M. F. Kaplan, *Implementation of automated multilevel substructuring for frequency response analysis of structures*. PhD thesis, The University of Texas at Austin, 2001.

[26] W. Gao, X. S. Li, C. Yang, and Z. Bai, "An Implementation and Evaluation of the AMLS Method for Sparse Eigenvalue Problems," *ACM Transactions on Mathematical Software (TOMS)*, vol. 34, no. 4, p. 20, 2008.

[27] D. J. Rixen, "A dual Craig-Bampton method for dynamic substructuring," *Journal of Computational and Applied Mathematics*, vol. 168, no. 1-2, pp. 383–391, 2004.

[28] A. Shanmugam and C. Padmanabhan, "A fixed-free interface component mode synthesis method for rotordynamic analysis," *Journal of Sound and Vibration*, vol. 297, no. 3-5, pp. 664–679, 2006.

[29] N. Bouhaddi and J. P. Lombard, "Improved free-interface substructures representation method," *Computers and Structures*, vol. 77, no. 3, pp. 269–283, 2000.

[30] C. U. A. Bucher, "A modal synthesis method employing physical coordinates, free component modes, and residual flexibilities," *Computers & Structures*, vol. 22, no. 4, pp. 559–564, 1986.

[31] K. Brahmi, N. Bouhaddi, and R. Fillod, "Reduction of Junction Degrees of Freedom in Certain Methods of Dynamic Substructure Synthesis," in *IMAC-XIII-13th*, pp. 1763 – 1769, 1995.

[32] H. Hassis, "Proposition of a New Approach for the Substructure Method," *Journal of Sound and Vibration*, vol. 232, no. 4, pp. 659–668, 2000.

[33] D.-M. Tran, "Component mode synthesis methods using interface modes: Application to structures with cyclic symmetry," *Computers & Structures*, vol. 87, no. 17-18, pp. 1141–1153, 2001.

[34] P. Garambois, S. Besset, and L. Jézéquel, "Various double component mode synthesis and sub-structuring methods for dynamic mixed FEM," *European Journal of Mechanics, A/Solids*, vol. 53, pp. 196–219, 2015.

Chapter 4

Modelling and reduction of the contact-friction problem

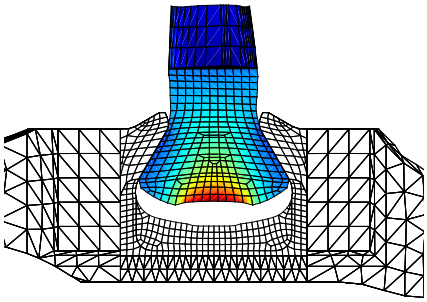

Abstract

The present chapter introduces the contact-friction modelling and time-resolution using Signorini and Coulomb laws. In the last section, reduction techniques and ideas for the reduction of the model and its contacting interface are presented.

Contents

The numerical study of the contact and friction in large assembled structure has risen in the middle of the 70's [1] [1] and still feed a large number of international congresses and research projects. The effects of the contact and friction on assembled structures are known to bring damping and nonlinear behaviour. These phenomena are modelled and studied for various reasons in different fields like the evaluation of equivalent contact-friction damping [2], the prediction of squeal instabilities in vehicles brakes [3], the validation of bolted structure dynamics in aircraft manufacturing [4] or the haptic rendering for surgery training [5].

The open rotor is a multibody system and the contact between some of its constitutional parts is expected to dramatically influence the damping behaviour of the assembled structure. In order to quantify this influence, the damping brought by the contact and the friction effects are sought. This information can be obtained through time simulation considering forced excitations [6]. Thus, in this section the targeted goal is to provide a numerical methodology allowing to perform quick time simulations of contacting reduced structures with friction effects.

In the present case, the studied system is the open rotor blade contacting with its hub, Fig. 4.1a. Simulations performed at SAE consists in analysing the blade behaviour facing acceleration forces $\boldsymbol{f}_{\text{rot.}}$ due to the motor angular speed $\omega_{\text{rot.}}$. This force $\boldsymbol{f}_{\text{rot.}}$ has two parts, both depends on $\omega_{\text{rot.}}$: a tangential part that tends to bend the blade and a radial part that keeps the blade tied in the hub. In practice, the rotor speed of interest is increasingly reached so that the force $\boldsymbol{f}_{\text{rot.}}$ progressively raises while the preload force $\boldsymbol{f}_{\text{pl.}}$ progressively decreases.

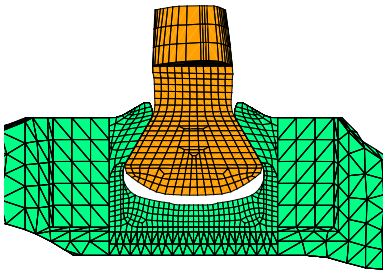

(a) View of the blade Σ_2 tied in the groove of the hub Σ_1 (3D model).

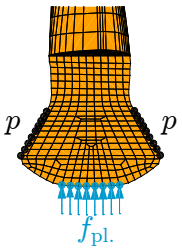

(b) Locations of the contact-friction $\boldsymbol{p}$ and preload forces $\boldsymbol{f}_{\text{pl.}}$.

Figure 4.1 – Illustration of the preload $\boldsymbol{f}_{\text{pl.}}$ applied on the bottom blade. The load $\boldsymbol{f}_{\text{rot.}}$ induced by the blade rotation is applied on all the DoF of the structure. While the contact-friction forces $\boldsymbol{p}$ occurs on the black nodes, forces $\boldsymbol{f}_{\text{pl.}}$ are applied on the bottom of the blade to keep its contact with the hub. The preload force is applied on 160 nodes.

In order to ensure the contact of the blade in its hub at the beginning of the simulation,

when $\omega_{\text{rot.}}$ and $\boldsymbol{f}_{\text{rot.}}$ are null, a preload force $\boldsymbol{f}_{\text{pl.}}$ is imposed on the bottom of the blade. This force is shown in Fig. 4.1b. Hence, although local detachment of the two part are allowed, a constant contact of the two part is assumed. Moreover, the direction of the rotational load $\boldsymbol{f}_{\text{rot.}}$ let us suggest that tangential motions of the blade in the hub groove will be rather small.

The present chapter is organized as follows, in 4.1, contact-friction law are first selected, then different formulations of those laws are proposed in 4.2. Numerical operators for the resolution of the contact-friction problem are proposed in section 4.3. After that, in section 4.4, integration scheme are proposed for the time resolution of the contact-friction problem. Eventually, ideas for the reduction of the current problem are proposed in section 4.5.

4.1 Constitutive laws for the unilateral contact problems with friction

In this section the contact-friction is first introduced, the contact-friction laws used in this studies are highlighted and described. Secondly, different classical formulations of this problem are presented and selected. Eventually, this section ends with the presentation of the operators required to solve a contact friction problem in a three dimensional space.

4.1.1 Framework and notations

Let us consider two undamped and linear elastic bodies Σ_1 and Σ_2 that are free to contact each other on their interfaces Γ_1 and Γ_2. Starting from the discretized mass and stiffness finite element operators M and K of the Σ_1 and Σ_2, the equilibrium between the two structures is ruled by the matrix equations:

$$\begin{bmatrix} \mathrm{M}_1 & \\ & \mathrm{M}_2 \end{bmatrix} \begin{Bmatrix} \ddot{\boldsymbol{u}}_1 \\ \ddot{\boldsymbol{u}}_2 \end{Bmatrix} + \begin{bmatrix} \mathrm{C}_1 & \\ & \mathrm{C}_2 \end{bmatrix} \begin{Bmatrix} \dot{\boldsymbol{u}}_1 \\ \dot{\boldsymbol{u}}_2 \end{Bmatrix} + \begin{bmatrix} \mathrm{K}_1 & \\ & \mathrm{K}_2 \end{bmatrix} \begin{Bmatrix} \boldsymbol{u}_1 \\ \boldsymbol{u}_2 \end{Bmatrix} = \begin{Bmatrix} \boldsymbol{f}_1 \\ \boldsymbol{f}_2 \end{Bmatrix} + \begin{Bmatrix} \boldsymbol{p}_1(\boldsymbol{u}_1, \dot{\boldsymbol{u}}_1, \boldsymbol{u}_2, \dot{\boldsymbol{u}}_2) \\ \boldsymbol{p}_2(\boldsymbol{u}_1, \dot{\boldsymbol{u}}_1, \boldsymbol{u}_2, \dot{\boldsymbol{u}}_2) \end{Bmatrix}.$$

$$\text{more concisely written: } \mathrm{M}\ddot{\boldsymbol{u}}(t) + \mathrm{C}\dot{\boldsymbol{u}}(t) + \mathrm{K}\boldsymbol{u}(t) = \boldsymbol{f}(t) + \boldsymbol{p}(\boldsymbol{u}, \dot{\boldsymbol{u}}). \tag{4.1}$$

Where $\boldsymbol{f}_1$ and $\boldsymbol{f}_2$ are the external loads applied on the structures and $\boldsymbol{p}$ are reacting forces that emerge from the contact of the bodies. The reacting force $\boldsymbol{p}_1$ and $\boldsymbol{p}_2$ are nonlinear contact forces that rule the friction and sliding between the two bodies. These nonlinear forces depend on the chosen contact rules.

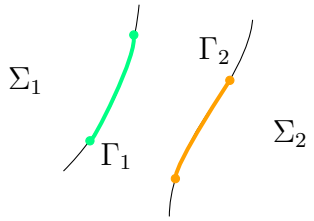

Figure 4.2 – Two components Σ_1 and Σ_2 and their potential contacting surfaces Γ_1 and Γ_2.

The contact forces $\boldsymbol{p}_1$ and $\boldsymbol{p}_2$ rule the friction and sliding between the two bodies and depends on the law used to describe this phenomenon. This contact forces $\boldsymbol{p}_1$ and $\boldsymbol{p}_2$ are only defined on the interface DoF b (boundary) of the bodies so that $\boldsymbol{p}_{1,i}$ and $\boldsymbol{p}_{2,i}$ are null (interior).

The following equilibrium condition has to be verified on the contacting surfaces: $\boldsymbol{p}_{1,b} + \boldsymbol{p}_{2,b} = \boldsymbol{0}$. For the sake of simplicity let us denote $\boldsymbol{p} = \boldsymbol{p}_{1,b} = -\boldsymbol{p}_{2,b}$. Moreover, we assume that the contacting meshes Γ_1 and Γ_2 are conforming or already regularized.

While the variables n_{Σ_1} and n_{Σ_2} respectively denote the number of nodes of the structures Σ_1 and Σ_2. The two structures own $n_\Sigma = n_{\Sigma_1} + n_{\Sigma_2}$ nodes.

4.1.2 Contact law and gap definition

A very simple and common law used to model the contact is the Signorini model [7]. Indeed, this law specifies that the two bodies Σ_1 and Σ_2 can not interpenetrate and that in case of contact a normal reacting force appears to avoid the interpenetration.

In this work, a unilateral contact is considered, thus the normal contacting force can only be oriented in direction of the normal $\vec{\boldsymbol{n}}$, this direction point the surface that is called "slave". The "master" surface often corresponds to the most stiff surface, in this work Γ_1 is considered as the master surface.

A definition of the gap $\boldsymbol{g}$ between the two components is required to give a mathematical representation of this law. This gap is computed as the distance between a given point of the master surface to the other contacting surface (slave surface) and is used to detect the interpenetration and the sliding of the structure.

All along the master surface, a local orthogonal referential $\mathcal{R}(\mathrm{x})$ is defined at each coordinate x. This local referential is made of the local normal $\vec{\boldsymbol{n}}$ and tangential directions $\vec{\boldsymbol{t}}$ of the master surface in the following way: $\mathcal{R}(\mathrm{x}) = (\vec{\boldsymbol{n}}, \vec{\boldsymbol{t}})$.

(a) Definition of the gap $\boldsymbol{g}$, orthogonal to the grey dashed line that is tangent to Γ_1.

(b) Example of a local referential $\mathcal{R}(\mathrm{x})$ that is defined regarding to Γ_1.

Figure 4.3 – Definition of the gap $\boldsymbol{g}$ and the local referential R(x).

This referential is used to locally split the gap $\boldsymbol{g}$ into a normal $\boldsymbol{g}_{\vec{n}}$ and tangential $\boldsymbol{g}_{\vec{t}}$ part:

$$\boldsymbol{g} = \boldsymbol{g}_{\vec{n}} + \boldsymbol{g}_{\vec{t}} = g_{\vec{n}}\vec{\boldsymbol{n}} + g_{\vec{t}}\,\vec{\boldsymbol{t}}.$$

The interpenetration between the component Σ_1 and Σ_2 is then numerically detected when the normal gap $\boldsymbol{g}_{\vec{n}}$ becomes strictly negative while a strictly positive normal gap corresponds to a surface detachment. In the same manner, the contacting force $\boldsymbol{p}$ can also be decomposed into a normal and a tangential part:

$$\boldsymbol{p} = \boldsymbol{p}_{\vec{n}} + \boldsymbol{p}_{\vec{t}} = p_{\vec{n}}\vec{\boldsymbol{n}} + p_{\vec{t}}\,\vec{\boldsymbol{t}}.$$

The normal directions and the unilateral Signorini reacting force $\boldsymbol{p}_{\vec{n}}$ were previously defined as oriented in the direction of the slave surface. The gap and reaction-forces ruled by the Signorini law can be sumed up by the plot given in Fig. 4.4.

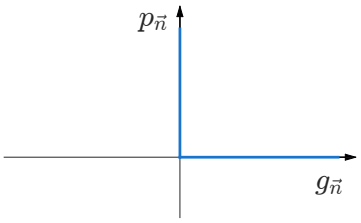

Figure 4.4 – Signorini contact-force law

The dual equilibrium of Eq. (4.1) is respected when the contacting forces $\boldsymbol{p}_{1,b}$ and $\boldsymbol{p}_{2,b}$ cancel each other. From Fig. 4.4 it is possible to summarize the Signorini law as the following linear complementarity problem (LCP):

$$g_{\vec{n}} \geq 0 \quad , \quad p_{\vec{n}} \geq 0 \quad \text{and} \quad g_{\vec{n}} \times p_{\vec{n}} = 0$$
$$\text{sometimes written as:} \quad 0 \leq g_{\vec{n}} \perp p_{\vec{n}} \geq 0$$

In theory, this law is infinitely steep and may generate acceleration nonregularities.

4.1.3 Friction modelling

In reference [8], the friction models are classified into three mains families. The first one are the Coulomb based laws that emerged from the rigid multibody dynamic mechanics and allow a macroscopic description of the interface. The second class is referred to as interface constitutive laws and takes into account elastic and plastic modifications of the contacting surfaces rheology due to the grinding that occurs during the friction. Eventually a third kind of laws families enables to feature more details like the asperity-lubricant model as an example.

A first approximation of the frictional effect is given by the Tresca law. This law describes the link between the sliding and a tangential contact force reaching a threshold $p_{sliding}$. This law also expresses the fact that the sliding direction is oriented oppositely to the tangential contact force $\boldsymbol{p}_{\vec{t}}$ and λ-proportional ($\lambda > 0$). This law can be mathematically expressed as:

$$\text{Tresca law: } \begin{cases} \text{stuck if} & \|\boldsymbol{p}_{\vec{t}}\| < p_{sliding} \text{ , thus } \dot{\boldsymbol{g}}_{\vec{t}} = \boldsymbol{0} \\ \text{sliding if} & \|\boldsymbol{p}_{\vec{t}}\| = p_{sliding} \text{ , thus } \dot{\boldsymbol{g}}_{\vec{t}} = -\lambda \boldsymbol{p}_{\vec{t}} \end{cases}. \tag{4.2}$$

Using such a model, the friction force of each contacting point is defined in a cylinder of radius $p_{sliding}$. The state of the contact is considered as sliding when the contacting force reaches the surface of the cylinder and stuck when the force stays inside the cylinder. A major drawback linked to this law is that the normal contacting force is not involved. Indeed, one would easily imagine than the state of a body placed on a inclined surface depends on the body mass, this phenomenon is not featured by the Tresca law.

In this work the Coulomb law is adopted to describe the interface friction behaviour. This law is commonly referred to as static since the interface rheology is not supposed to evolve. Practically, this modelling is very convenient to give a first approximation of the contact-friction effect on the system as it only requires a single rheological parameter μ. Moreover, tables giving general values of the parameter μ for different material associations are available in the literature while the use of more complex model would require parametric identification from experimentation measurement or joint simulations results.

The Coulomb law [9] developed in the end of the XVIII$^{\text{th}}$ century relies on the fact that the tangential displacement $\boldsymbol{g}$ is only possible if the tangential force $p_{\vec{t}}$ reaches a variable threshold that is directly linked to normal force $p_{\vec{n}}$ and the parameter μ. Like the Tresca law, this model considers two possible states of the contact: stuck or sliding

$$\text{Coulomb law: } \begin{cases} \text{stuck if} & \|\boldsymbol{p}_{\vec{t}}\| < \mu \|\boldsymbol{p}_{\vec{n}}\| \text{ , thus } \dot{\boldsymbol{g}}_{\vec{t}} = \boldsymbol{0} \\ \text{sliding if} & \|\boldsymbol{p}_{\vec{t}}\| = \mu \|\boldsymbol{p}_{\vec{n}}\| \text{ , thus } \boldsymbol{p}_{\vec{t}} = -\mu p_{\vec{n}} \frac{\dot{\boldsymbol{g}}_{\vec{t}}}{\|\dot{\boldsymbol{g}}_{\vec{t}}\|} \end{cases}. \tag{4.3}$$

Contrary to the Tresca law, the friction force of each contacting point is here defined in a cone $\mathscr{C}_\mu = \{\boldsymbol{p} \in \mathbb{R}^3,\ p_{\vec{n}} \geq 0,\ \|\boldsymbol{p}_{\vec{t}}\| \leq \mu p_{\vec{n}}\}$ with a rate μ. The state of the contact is

considered as sliding when the contacting force reaches the surface of the cone and stuck when the force stays inside the cone.

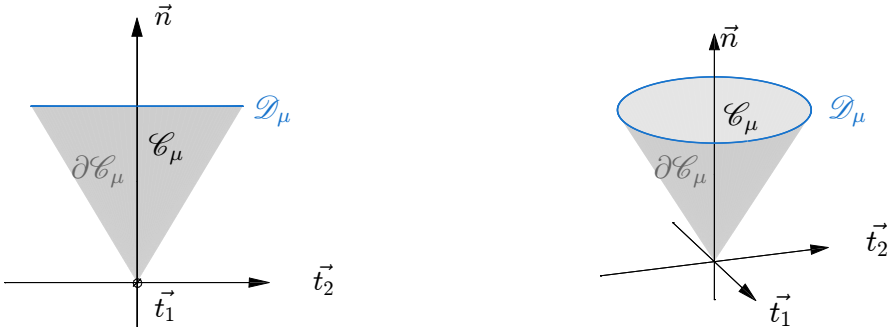

Figure 4.5 – Representation of the friction cone $\mathscr{C}_\mu$ with its surface $\partial\mathscr{C}_\mu$ and the friction disc $\mathscr{D}_\mu(\vec{p}_n)$ that depends on the friction rate μ and the normal force $\vec{p}_n$.

The contact is considered as sliding when the friction force is placed on the cone external surface $\partial\mathscr{C}_\mu = \{\boldsymbol{p} \in \mathbb{R}^3,\ p_{\vec{n}} \geq 0,\ \|\boldsymbol{p}_{\vec{t}}\| = \mu p_{\vec{n}}\}$. For a given normal force $p_{\vec{n}}$, the friction force $p_{\vec{t}}$ is defined into a friction disc $\mathscr{D}_\mu(p_{\vec{n}})$ whose border is noted $\partial\mathscr{D}_\mu(p_{\vec{n}})$.

4.2 Contact-friction formulations

Over the years, a large number of contact-friction formulations were developed. The major difficulty of the contact-friction problem resolution raises from its non-smooth nature. Thus the choice of a contact-friction formulation is closely linked to the choice of a resolution algorithm.

Basically, finding a solution that strictly verifies the contact-friction law like the Lagrangian method [10] might be time consuming. In order to bypass this drawback, some formulations provide a regularization of the contact-friction law [11]. This approach opens the way to iterative Newton based algorithm in which a gradient (or pseudo gradient) indicates the "direction" toward the solution. The more regular the problem is, the faster algorithm converges. However, regularizing the contact-friction law implies to approximate them and then the quality of the solutions found are lowered.

In 1976, the works performed by Rockfellar and Fortin extended the classical Lagrangian so that the formulation and resolution of frictionless contact and pure friction problem became possible. From this point numerous authors worked on the formulation of the contact-friction using the augmented Lagrangian method, we can notably cite, Hasslinger

[12], Alart and Curnier [13], Saxcé and Feng [14], Bussetta et al. [15]. It has to be noticed that variants of the lagrangian method, like perturbed Lagrangian have also been studied, notably by Simo, Wriggers and Taylor in [16] to treat the contact problem.

This section highlights the principle of the three main contact-friction formulations: using penalty function, Lagrangian formulation and eventually the augmented Lagrangian method.

4.2.1 The penalty function method

According to Brusseta, Marceau and Ponthot in [15], the penalty method is the most widespread to solve the contact-friction problem. This call for the use of two parameters $\rho_{\vec{n}} > 0$ and $\rho_{\vec{t}} > 0$ respectively playing the role of a normal stiffness and a tangential damping that ensure a continuous link between the gap and the contact-friction force.

Using this formulation, the contact force $p_{\vec{n}}$ is defined as $-\rho_{\vec{n}} g_{\vec{n}}$, that means that when interpenetration occurs ($g_{\vec{n}} < 0$) a reaction force ($p_{\vec{n}}$) oriented to the slave surface appears. To make sure that the normal reacting force is positive and to avoid the penalization of detachment, $-\rho_{\vec{n}} g_{\vec{n}}$ is projected in $\mathbb{R}^+$:

$$p_{\vec{n}} = \text{proj}_{\mathbb{R}^+}(-\rho_{\vec{n}} g_{\vec{n}}). \tag{4.4}$$

The tangential penalization is applied to the tangential velocity $\boldsymbol{g}_{\vec{t}}$. In this way, if sliding ($g_{\vec{t}} > 0$) is detected, then an opposite tangential force $\boldsymbol{p}_{\vec{t}}$ appears to express the dissipative nature of the friction. This tangential force $\boldsymbol{p}_{\vec{t}}$ is then projected into the friction disc $\mathscr{D}_\mu(p_{\vec{n}})$ in order to enforce the Coulomb's law:

$$\boldsymbol{p}_{\vec{t}} = \text{proj}_{\mathscr{D}_\mu(p_{\vec{n}})}(-\rho_{\vec{t}}\, \dot{\boldsymbol{g}}_{\vec{t}}). \tag{4.5}$$

In this method, $\rho_{\vec{n}}$ is homogeneous to a stiffness and $\rho_{\vec{t}}$ to a damping. Such a method provides a regularization of the contact-friction law. The higher these values are, the best the contact-friction law are approximated, see Fig. 4.6.

It should be noticed that the regularization presented on Eq. (4.4) and Eq. (4.5) correspond to linear penalization. Other functions can be used for the penalization, like the exponential for the contact law and the arctangent for the friction law. A penalization of the normal gap velocity [5] can be added in Eq. (4.4) with the use of a coefficient ρ_b:

$$p_{\vec{n}} = \text{proj}_{\mathbb{R}^+}(-\rho_{\vec{n}} g_{\vec{n}} - \rho_b \dot{g}_{\vec{n}}).$$

The functions used for the regularization have a significant impact on the accuracy of the results. As an example, the exponential regularization of the Signorini law presented in

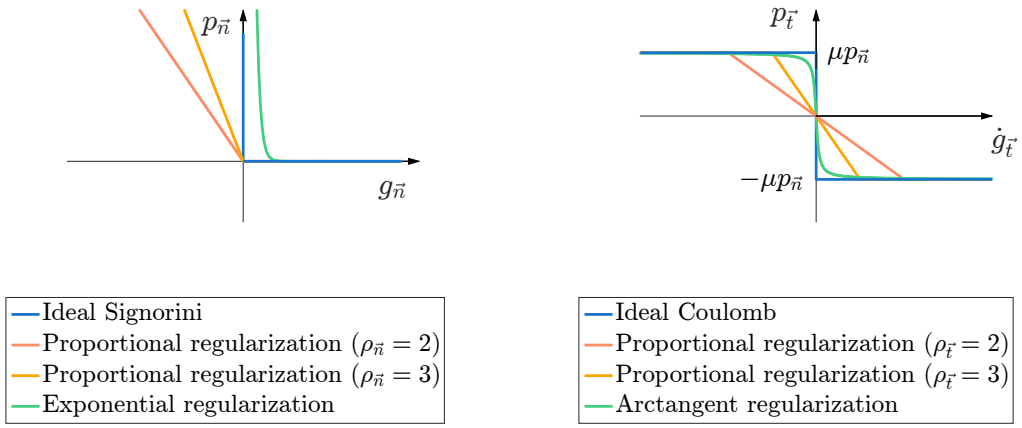

(a) Example of regularization functions for the Signorini law.

(b) Example of regularization functions for the Coulomb law.

Figure 4.6 – Regularization of the Signorini-Coulomb laws.

Fig. 4.6a tends to numerically increase the system energy as both gap and contact force can be simultaneously positive and non-null.

The choice of the penalty coefficients however remains a critical point of this class of methods. Indeed, penalization coefficients play a significant role in the efficiency of those methods. For proportional regularizations, the smaller this coefficient is, the more important the interpenetration is. Moreover small coefficient provides reversible tangential displacement at the contact interface. Indeed, the weak penalizations tend to smooth the motions as constraint violation may occurs. In the other hand, large values of these coefficient provides bad conditioning issues, numerical oscillations and prevent the algorithm convergence [15]. It has to be noticed that large coefficient also slow the convergence. According to De Saxcé and Feng in [14], this method is not well suited for stiff problems in a general way.

To tackle the problem of the coefficient choice, an adapted penalty method (referred to as APM) has been proposed by Chamoret in [17] and [18], in which the contact penalty coefficient $\rho_{\vec{n}}$ is automatically updated. This method however ask for an initialisation of the $\rho_{\vec{n}}$ and may suffer from non-convergence in the case where important variation of this coefficient occurs.

In a general way, the penalization methods allow to solve the contact-friction using an approximation of their laws. Thus, depending on the penalization coefficient, the solutions may be quickly found but not necessarily accurate since its value rules the approximation of the friction law.

4.2.2 The Lagrangian method

The classic Lagrangian method consists in computing the force $\boldsymbol{\lambda}$ that would keep the contacting node as stuck: $g_{\vec{n}} = 0$ and $\dot{g}_{\vec{t}} = 0$. Once known, the force $\boldsymbol{\lambda}$ is split into a normal and a tangential part $\lambda_{\vec{n}}\vec{\boldsymbol{n}}$ and $\boldsymbol{\lambda}_{\vec{t}}$. The contact and friction force are then deduced from $\lambda_{\vec{n}}$ and $\lambda_{\vec{t}}$ using their projection into the contact and friction force domain so that:

$$p_{\vec{n}} = \text{proj}_{\mathbb{R}^+}(\lambda_{\vec{n}}) \quad \text{and} \quad \boldsymbol{p}_{\vec{t}} = \text{proj}_{\mathscr{D}_\mu(p_{\vec{n}})}(\boldsymbol{\lambda}_{\vec{t}}). \tag{4.6}$$

Another more stable approach consists in only considering the contacting nodes as stuck on the normal (that can be performed by stating $g_{\vec{n}} = 0$) direction and then deducing the normal force $\lambda_{\vec{n}}$. The normal contacting forces $p_{\vec{n}}$ are computed as the projection in the domain $\mathbb{R}^+$ of the Lagrangian multiplier $\lambda_{\vec{n}}$ like in Eq. (4.6).

In this approach (see [10] for example), the tangential motions of the nodes are basically considered as sliding so that the tangential forces $\boldsymbol{g}_{\vec{t}}$ are expected to be located on the border of the frictional cone, and are computed using the relation:

$$\boldsymbol{p}_{\vec{t}} = -\mu p_{\vec{n}} \frac{\dot{\boldsymbol{g}}_{\vec{t}}}{\|\dot{\boldsymbol{g}}_{\vec{t}}\|}.$$

This second method is more stable than the first one since the dissipation is granted by the fact that the friction forces are defined as opposed to the tangential displacements.

Unlike the penalization, the Lagrangian method strictly respects the contact-friction law with no approximation. However, it can be noticed that this formulation is non-smooth, so that it is not possible to use Newton-Raphson based method to solve it. In conclusion, the Lagrangian methods allows finding precise solutions of the contact-friction problem to the detriment of the computational time.

4.2.3 The augmented Lagrangian method

The augmented Lagrangian method combines the advantages of the penalty and Lagrangian method. Indeed, the Lagrangian multipliers are combined to penalization terms so that it smoothes the problem while keeping a high precision level. In 1992, Jean and Moreau developed a formulation of the contact friction in which the contact and friction laws are seen as two non-differentiable convex potential functions called "pseudo-potential functions". Later, in 1998, De Saxé and Feng proposed, in [14] a formulation referred to as "bipotential" in which the contact and friction laws are summarized into a single pseudo-potential function.

The respect of those laws are verified on the extremum of those pseudo-potential functions, thus several resolution techniques were developed over the years. For instance, in

1982, Haslinger [12] used the least square method to resolve the contact-friction problem. In the work of Acary et al. [19] the contact-friction problem is also treated as an optimization problem. In 1991, Alart and Curnier [13] proposed an augmented Lagrangian formation, smooth enough to allow them to use the Newton method. In this case a pseudo-jacobian of the contact friction operator is defined.

Pseudo-potential associated to the Signorini's law

Let $p^\star_{\vec{n}}$ denote the normal part of any virtual contact force that belongs to $\mathbb{R}^+$. The Signorini law can be expressed as $(p^\star_{\vec{n}} - p_{\vec{n}}) \cdot g_{\vec{n}} \geq 0$. Indeed, the two possible configurations of $p_{\vec{n}}$ are:

- $p_{\vec{n}} = 0$ then $p^\star_{\vec{n}} \cdot g_{\vec{n}} \geq 0$, thus $g_{\vec{n}} \geq 0$ since $p^\star_{\vec{n}} \geq 0$. This mathematical assertion can be understood as: if no contact is detected ($p_{\vec{n}} = 0$), then the surfaces of the two bodies are not in contact or just brushing ($g_{\vec{n}} \geq 0$).

- $p_{\vec{n}} > 0$ then the sign of the term $(p^\star_{\vec{n}} - p_{\vec{n}})$ can be either positive or negative. Thus, the inequality $(p^\star_{\vec{n}} - p_{\vec{n}}) \cdot g_{\vec{n}} \geq 0$ is only respected if $g_{\vec{n}} = 0$. Indeed, non null contacting force ($p_{\vec{n}} > 0$) only appears when contact occurs ($g_{\vec{n}} = 0$).

Let $\tau_{\vec{n}} = p_{\vec{n}} - \rho g_{\vec{n}}$ denote the augmented contact force, the following equivalence can be established:

$$(p^\star_{\vec{n}} - p_{\vec{n}}) \cdot g_{\vec{n}} \geq 0 \Longleftrightarrow (p^\star_{\vec{n}} - p_{\vec{n}}) \cdot \Big(p_{\vec{n}} - \underbrace{(p_{\vec{n}} - \rho g_{\vec{n}})}_{\tau_{\vec{n}}}\Big) \geq 0 \text{ with } \rho > 0.$$

If $p_{\vec{n}}$ is null, then $-p^\star_{\vec{n}} \tau_{\vec{n}} \geq 0$ thus $\tau_{\vec{n}} \leq 0$. If the contact force $p_{\vec{n}}$ belongs to $\mathbb{R}^+$ then sign of the term $(p^\star_{\vec{n}} - p_{\vec{n}})$ is not defined. In such a case, the inequality is verified if $p_{\vec{n}} = \tau_{\vec{n}}$. From this two observations, it is possible to see the contact force $p_{\vec{n}}$ as the projection of the augmented lagrangian $\tau_{\vec{n}}$ on $\mathbb{R}^+$:

$$p_{\vec{n}} = \text{proj}_{\mathbb{R}^+}(\tau_{\vec{n}}) = \text{proj}_{\mathbb{R}^+}(p_{\vec{n}} - \rho_{\vec{n}} g_{\vec{n}}).$$

Pseudo-potential associated to the Coulomb's law

Let $\boldsymbol{p}^\star_{\vec{t}}$ denotes any virtual friction force belonging to the friction disc $\mathscr{D}_\mu(p_{\vec{n}})$ and oriented on the direction $\vec{\boldsymbol{t}}$. The Coulomb's law can be expressed in an analogue way to the Signorini law using the scalar product $(\boldsymbol{p}^\star_{\vec{t}} - \boldsymbol{p}_{\vec{t}}) \cdot \dot{\boldsymbol{g}}_{\vec{t}} \geq 0$.

- if $\boldsymbol{p}_{\vec{t}}$ is in the inner part of $\mathscr{D}_\mu(p_{\vec{n}})$ (i.e. $\boldsymbol{p}_{\vec{t}}$ belongs to $\mathscr{D}_\mu(p_{\vec{n}}) \setminus \partial\mathscr{D}_\mu(p_{\vec{n}})$) then the vector $(\boldsymbol{p}^\star_{\vec{t}} - \boldsymbol{p}_{\vec{t}})$ is non null and can be oriented anywhere in the plan $(\vec{\boldsymbol{t}}_1, \vec{\boldsymbol{t}}_2)$ so that $\dot{g}_{\vec{t}} = 0$. Indeed, if the friction force stays in the friction disc, no sliding is allowed

(see Fig. 4.7a).

- if $\boldsymbol{p}_{\vec{t}} \in \partial\mathscr{D}_\mu(p_{\vec{n}})$ then the sliding occurs, also as it is visible in Fig. 4.7b, $(\boldsymbol{p}^\star_{\vec{t}} - \boldsymbol{p}_{\vec{t}})$ can only be oriented inward the disc $\mathscr{D}_\mu(p_{\vec{n}})$. Furthermore, the only direction of $\dot{\boldsymbol{g}}_{\vec{t}}$ so that $(\boldsymbol{p}^\star_{\vec{t}} - \boldsymbol{p}_{\vec{t}}) \cdot \dot{\boldsymbol{g}}_{\vec{t}} \geq 0 \ \forall \boldsymbol{p}^\star_{\vec{t}} \in \mathscr{D}_\mu(p_{\vec{n}})$ is the one opposite to $\boldsymbol{p}_{\vec{t}}$.

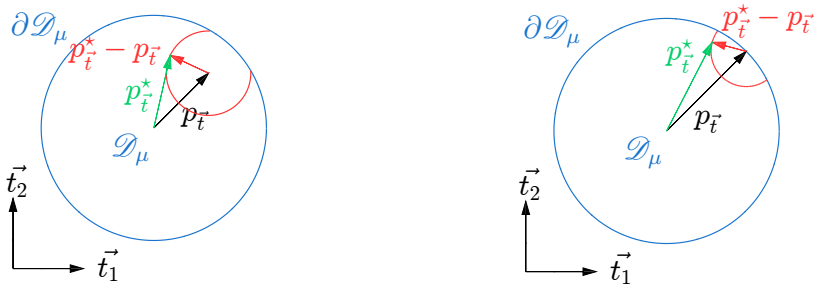

(a) Friction disc $\partial\mathscr{D}_\mu(p_{\vec{n}})$ in the stuck configuration. The vector $(\boldsymbol{p}^\star_{\vec{t}} - \boldsymbol{p}_{\vec{t}})$ can be oriented anywhere in the plan $\vec{\boldsymbol{t}}$.

(b) Friction disc $\partial\mathscr{D}_\mu(p_{\vec{n}})$ in the sliding configuration. The force $(\boldsymbol{p}^\star_{\vec{t}} - \boldsymbol{p}_{\vec{t}})$ is only oriented inward the disc $\partial\mathscr{D}_\mu(p_{\vec{n}})$.

Figure 4.7 – Potential configuration of the variables $\boldsymbol{p}_{\vec{t}}$ and $\boldsymbol{p}^\star_{\vec{t}}$ in a stuck and sliding state. The red circle describe the plausible orientation of the iso-norm vectors $(\boldsymbol{p}^\star_{\vec{t}} - \boldsymbol{p}_{\vec{t}})$.

Like previously, an augmented force $\boldsymbol{\tau}_{\vec{t}} = \boldsymbol{p}_{\vec{t}} - \rho\dot{\boldsymbol{g}}_{\vec{t}}$ is defined. This force is used to write the equivalence:

$$\left(\boldsymbol{p}^\star_{\vec{t}} - \boldsymbol{p}_{\vec{t}}\right) \cdot \dot{\boldsymbol{g}}_{\vec{t}} \geq 0 \iff \left(\boldsymbol{p}^\star_{\vec{t}} - \boldsymbol{p}_{\vec{t}}\right) \cdot \Big(\boldsymbol{p}_{\vec{t}} - \underbrace{(\boldsymbol{p}_{\vec{t}} - \rho\dot{\boldsymbol{g}}_{\vec{t}})}_{\boldsymbol{\tau}_{\vec{t}}}\Big) \geq 0 \text{ with } \rho > 0$$

When the friction force is inner the friction disc $\mathscr{D}_\mu(p_{\vec{n}})$ then the inequality is only true if $\boldsymbol{\tau}_{\vec{t}} = \boldsymbol{p}_{\vec{t}}$. When $\boldsymbol{p}_{\vec{t}}$ belongs to the disc border $\partial\mathscr{D}_\mu(p_{\vec{n}})$ then $(\boldsymbol{p}_{\vec{t}} - \boldsymbol{\tau}_{\vec{t}})$ follows the internal normal of the disc. Thus, in the previous demonstration, the friction force $\boldsymbol{p}_{\vec{t}}$ can be seen as the projected augmented force $\boldsymbol{\tau}_{\vec{t}}$:

$$\boldsymbol{p}_{\vec{t}} = \text{proj}_{\mathscr{D}_\mu(p_{\vec{n}})}(\boldsymbol{\tau}_{\vec{t}}) = \text{proj}_{\mathscr{D}_\mu(p_{\vec{n}})}(\boldsymbol{p}_{\vec{t}} - \rho_{\vec{t}}\dot{\boldsymbol{g}}_{\vec{t}}).$$

Bipotential formulation

In 1998, De Saxé and Feng proposed, in [14], a method called the Bipotential method, that sums up the contact and friction law into a single potential. In this formulation, the Signorini and Coulomb laws are expressed into a single potential function, defined as:

$$(\boldsymbol{p}^\star - \boldsymbol{p}) \cdot \underbrace{\left((\mu\|\dot{\boldsymbol{g}}_{\vec{t}}\| + g_{\vec{n}})\vec{\boldsymbol{n}} + \dot{\boldsymbol{g}}_{\vec{t}}\right)}_{\boldsymbol{v}} \geq 0. \tag{4.7}$$

Let us demonstrate that this formulation Eq. (4.7) enables to describe the three possible states of the Signorini-Coulomb contact-friction model: adherence, sliding and detached.

Adherence. When the contact-friction force $\boldsymbol{p}$ is inside the cone $\mathscr{C}_\mu$, the virtual force $(\boldsymbol{p}^\star - \boldsymbol{p})$ might be oriented in any direction and $\boldsymbol{v}$ cancels:

$$\boldsymbol{v} = \left((\mu\|\dot{\boldsymbol{g}}_{\vec{t}}\| + g_{\vec{n}})\vec{\boldsymbol{n}} + \dot{\boldsymbol{g}}_{\vec{t}}\right) = \boldsymbol{0} \quad \text{implies that} \quad \begin{cases} (\mu\|\dot{\boldsymbol{g}}_{\vec{t}}\| + g_{\vec{n}}) = 0 \\ \dot{\boldsymbol{g}}_{\vec{t}} = \boldsymbol{0} \end{cases} \quad \text{then} \quad \begin{cases} g_{\vec{n}} = 0 \\ \dot{g}_{\vec{t}} = 0 \end{cases} .$$

In conclusion, if the contact-friction force $\boldsymbol{p}$ belongs to $\mathscr{C}_\mu \setminus \left(\partial\mathscr{C}_\mu \cup \{0\}\right)$, then no inter-penetration $g_{\vec{n}}$ and tangential sliding $\dot{g}_{\vec{t}}$ are possible, this correspond to a stuck state.

Sliding. When the force $\boldsymbol{p}$ belongs to the cone border $\partial\mathscr{C}_\mu \setminus \{0\}$, then the term $(\boldsymbol{p}^\star - \boldsymbol{p})$ can only be oriented inward the cone. This can only be satisfied if the vector $\boldsymbol{v}$ is perpendicular to the cone surface $\partial\mathscr{C}_\mu$, this is shown in Fig. 4.8. In such a configuration, the vector $\boldsymbol{v}$ can be seen as belonging to the surface of a dual cone $\mathscr{C}_\mu^\star$ of rate $1/\mu$, referred to as polar of $\mathscr{C}_\mu$ in the literature [14], see Fig. 4.9.

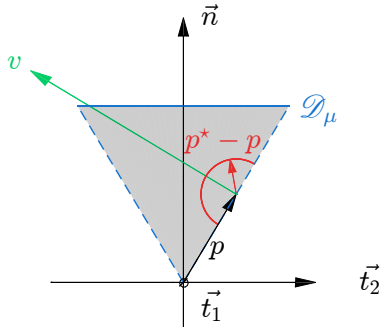

Figure 4.8 – Potential configuration of the variables $\boldsymbol{p}$, $\boldsymbol{p}^\star$ and $\boldsymbol{v}$ in a sliding state. The red circle describes the plausible orientations of the iso-norm vectors $(\boldsymbol{p}^\star - \boldsymbol{p})$

When belonging to the border of the cone $\partial\mathscr{C}_\mu$, the contact-friction force $\boldsymbol{p}$ can be split into a normal and a tangential part as follow:

$$\boldsymbol{p} = p_{\vec{n}}\vec{\boldsymbol{n}} + p_{\vec{t}}\vec{\boldsymbol{t}} = p_{\vec{n}}\left(\vec{\boldsymbol{n}} + \mu\vec{\boldsymbol{t}}\right).$$

In the same way, it is possible to split the term $\boldsymbol{v}$ that belongs to the border of the dual cone $\partial\mathscr{C}_\mu^\star$, that allows then to identify the terms $g_{\vec{n}}$ and $\|\dot{\boldsymbol{g}}_{\vec{t}}\|$:

$$\boldsymbol{v} = (\mu\|\dot{\boldsymbol{g}}_{\vec{t}}\| + g_{\vec{n}})\vec{\boldsymbol{n}} + \dot{\boldsymbol{g}}_{\vec{t}} = \alpha\left(\vec{\boldsymbol{n}} + \frac{1}{\mu}\vec{\boldsymbol{t}}\right).$$

$$\text{from which we deduce} \quad \begin{cases} \frac{\alpha}{\mu}\vec{\boldsymbol{t}} = \dot{\boldsymbol{g}}_{\vec{t}} \\ \alpha = \mu\|\dot{\boldsymbol{g}}_{\vec{t}}\| + g_{\vec{n}} \end{cases} \quad \text{then} \quad \begin{cases} \dot{g}_{\vec{t}} = \frac{\alpha}{\mu} \\ g_{\vec{n}} = 0 \end{cases} .$$

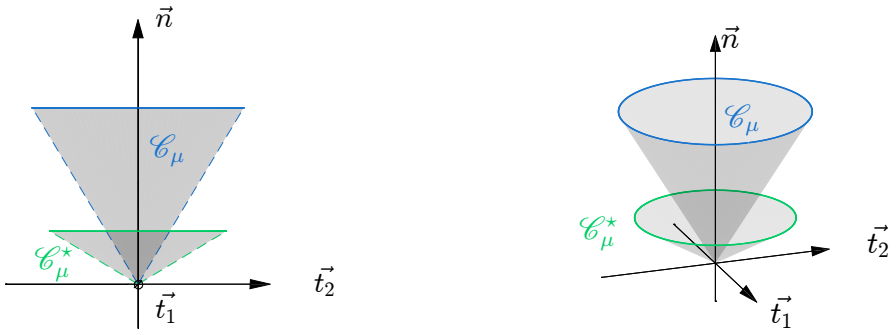

Figure 4.9 – Representation of the friction cone $\mathscr{C}_\mu$ with its polar cone $\mathscr{C}_\mu^\star$. The dual cone $\mathscr{C}_\mu^\star$ is defined by $\mathscr{C}_\mu^\star = \mathscr{C}_{1/\mu} = \left\{\boldsymbol{p} \in \mathbb{R}^3,\ p_{\vec{n}} \geq 0,\ \|\boldsymbol{p}_{\vec{t}}\| \leq \frac{1}{\mu} p_{\vec{n}}\right\}$. It can be observed on the left plot that the border of the two cones (in dashed lines) are perpendicular.

In conclusion, when the contact-friction force $\boldsymbol{p}$ belongs to the cone border, the sliding occurs since tangential motions $\dot{g}_{\vec{t}} \neq 0$ and contact $g_{\vec{n}} = 0$.

Detachment. When the contact-friction force $\boldsymbol{p}$ is null, then $\boldsymbol{p}^\star \cdot \boldsymbol{v} \geq 0$ that implies that $\boldsymbol{v}$ belongs to the boundary of the dual cone $\partial\mathscr{C}_\mu^\star$:

$$\mu\|\dot{\boldsymbol{g}}_{\vec{t}}\| \leq g_{\vec{n}} \Rightarrow g_{\vec{n}} \geq 0.$$

This last assertion allows to recover the expected behaviour in a detachment state: no contact $g_{\vec{n}} \geq 0$.

In an analogous way to the two pseudo-potential formulations previously presented, the augmented contact-friction force $\boldsymbol{p}$ is defined as $\boldsymbol{\tau} = \boldsymbol{p} - \rho\boldsymbol{v}$ and:

$$(\boldsymbol{p}^\star - \boldsymbol{p}) \cdot \boldsymbol{v} \geq 0 \Longleftrightarrow (\boldsymbol{p}^\star - \boldsymbol{p}) \cdot (\boldsymbol{p} - \boldsymbol{\tau}) \geq 0 \text{ with } \rho > 0. \tag{4.8}$$

According to DeSaxcé and Feng [14], this formulation Eq. (4.8) defines $\boldsymbol{p}$ as the projection of $\boldsymbol{\tau}$ in the friction cone:

$$\boldsymbol{p} = \mathrm{proj}_{\mathscr{C}_\mu}\Big(\boldsymbol{p} - \rho \underbrace{\big((\mu\|\dot{\boldsymbol{g}}_{\vec{t}}\| + g_{\vec{n}})\vec{\boldsymbol{n}} + \dot{\boldsymbol{g}}_{\vec{t}}\big)}_{\boldsymbol{v}}\Big) = \mathrm{proj}_{\mathscr{C}_\mu}(\boldsymbol{\tau})\,. \tag{4.9}$$

Let us give a quick verification of this assertion Eq. (4.9):

- if $\boldsymbol{p} \in \mathscr{C}_\mu \setminus \big(\partial\mathscr{C}_\mu \cup \{0\}\big)$, $(\boldsymbol{p}^\star - \boldsymbol{p})$ can be oriented anywhere in the friction cone, so the bipotential formulation Eq. (4.7) is only verified if $\boldsymbol{\tau} = \boldsymbol{p}$.

- if $\boldsymbol{p} \in \partial\mathscr{C}_\mu$, $\rho\boldsymbol{v}$ belongs to $\partial\mathscr{C}_\mu^\star$ and is then necessarily perpendicular to the border of the cone $\partial\mathscr{C}_\mu$ (see Fig. 4.9). It becomes then obvious that:

$$\underbrace{\boldsymbol{p}}_{\in\partial\mathscr{C}_\mu} = \mathrm{proj}_{\mathscr{C}_\mu}(\boldsymbol{\tau}) = \mathrm{proj}_{\mathscr{C}_\mu}\Big(\underbrace{\boldsymbol{p}}_{\in\partial\mathscr{C}_\mu} - \underbrace{\rho\boldsymbol{v}}_{\perp\partial\mathscr{C}_\mu}\Big).$$

Different formulations have been presented for the Signorini and Coulomb laws. In the present work, an augmented Lagrangian formulation is adopted as it provides both a fast convergence and a good accuracy of the resolution algorithm. Furthermore, the bipotential formulation is retained since it only requires the definition of a single operator for the augmentation of the Lagrangian whereas using the pseudo Signorini and Coulomb law would requires two numerical operators. Eventually, Talbi showed in her PhD thesis that the bipotential fomulation was more robust than the pseudo potential formulations [20].

4.3 Numerical operators for the contact friction

This section highlights the required operators for the resolution of the contact-friction problem. We assume now that the considered contact-friction problem takes place in a three dimensional space. In the previous section, the contact-friction laws were written for a single contacting node. In this section, numerical operators for the resolution of the contact-friction problem are presented.

Assumptions for the computation of the gap are made and presented in section 4.3.1. In a second time, a conewise projection operator is given in 4.3.2. Eventually, methods for the computation of the parameter ρ are succinctly presented and an algorithm for the Lagrangian augmentation is given in 4.3.3.

4.3.1 Contact detection and gap computation

In contact-friction problem, the contact detection is often time consuming so the method used for this task has a paramount importance in the efficiency of the algorithm. In this work the method used to detect the contact is referred to as 'stepping' which means that the contacts are detected at the end of a time step. On the contrary, it is also possible to use 'event-driven' methods that stop and restart the integration steps every time that a new contact is detected. The 'event-driven' method are widespread in the robotic fields, notably in haptic applications [5].

Here the studied joint is a perfect bonding (between the blade and its hub), so that the sliding is assumed to be small with regards to the element size. Thus, the gap $\boldsymbol{g}$ involve couples of node that are not evolving with the time. This approach is commonly referred

to as node-to-node (Fig. 4.10a), more precise methods consider node-to-surface gap (Fig. 4.10b). Node-to-surface procedures consider that the nodes are directly contacting an element of the front surface.

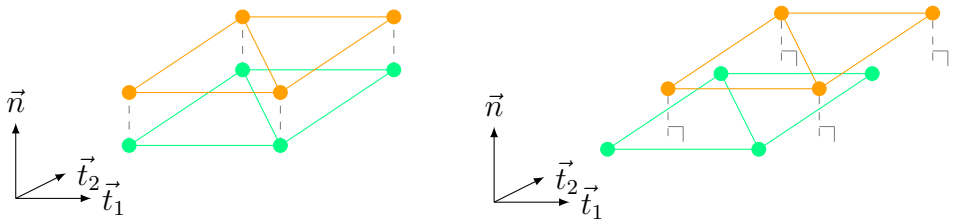

(a) Node to node assumption. The node are always considered as exactly facing each other that only involve boolean localisation matrix for the computation of the gap.

(b) Node to surface assumption. It is assumed that the nodes are facing element surface, it is then necessary to use interpolation matrix for the gap evaluation.

Figure 4.10 – Illustration of the node-to-node and node-to-surface assumption for the gap computation in contact-friction problems.

While the node-to-node assumption is more comfortable than the node-to-surface approach from an algorithmic point of view, this approxiation might lower the model's fidelity. In practice, the gap between the master (Γ_1) and slave (Γ_2) surface is computed as a vector $\boldsymbol{g}$, the node-to-node approach leads to the following formula:

$$\boldsymbol{g} = \boldsymbol{u}_{\Gamma_1} - \boldsymbol{u}_{\Gamma_2} = \begin{bmatrix} \mathrm{L}_{\Gamma_1} & -\mathrm{L}_{\Gamma_2} \end{bmatrix} \boldsymbol{u} = \mathrm{B}\boldsymbol{u}$$

The matrix L_{Γ_1} and L_{Γ_2} are referred to as localisation matrix, such matrix are boolean and allows to localize the DoF of the contacting interface Γ_1 and Γ_2. Thus, the vector $\boldsymbol{g}$ contains all the gap between the couples of facing nodes expressed in the global referential of the structure. In a three-dimensional space, considering n_Γ contacting nodes leads to matrix size as follows: $\mathrm{B}_{3n_\Gamma \times 3n_\Sigma}$

The split of the gap and contact-friction force into the local referential is performed using projection matrix P. In a three dimension space, the matrix $\mathrm{P}_{\vec{n}}$ that projects the motion or force on the direction $\vec{n}$ of the n_Γ local referentials is expressed as:

$$\mathrm{P}_{\vec{n}} = \mathrm{diag}\left(\vec{n}_1^\top,\ \vec{n}_2^\top,\ \ldots,\ \vec{n}_{n_\Gamma}^\top\right) = \begin{bmatrix} \vec{n}_1^\top & & \\ & \ldots & \\ & & \vec{n}_{n_\Gamma}^\top \end{bmatrix}_{n_\Gamma \times 3n_\Gamma}$$

Thus, the decomposition of the gap into the normal directions is done using the normal constraint matrix $\mathrm{B}_{\vec{n}}$ while the tangential part of the gap is defined as the complementary

part of $\boldsymbol{g}_{\vec{n}}$:

$$\boldsymbol{g}_{\vec{n}} = \mathrm{P}_{\vec{n}}\boldsymbol{g} = \mathrm{P}_{\vec{n}}\mathrm{B}\boldsymbol{u} = \mathrm{B}_{\vec{n}}\boldsymbol{u} = \left\langle g_{\vec{n}}^1 \;\; g_{\vec{n}}^2 \;\; \dots \;\; g_{\vec{n}}^{n_\Gamma} \right\rangle^\top \tag{4.10}$$

$$\boldsymbol{g}_{\vec{t}} = \boldsymbol{g} - \mathrm{P}_{\vec{n}}{}^\top \boldsymbol{g}_{\vec{n}} = \underbrace{\left(\mathrm{I}_{n_\Gamma} - \mathrm{P}_{\vec{n}}{}^\top \mathrm{P}_{\vec{n}}\right)}_{\mathrm{P}_{\vec{t}}} \mathrm{B}\boldsymbol{u} = \mathrm{B}_{\vec{t}}\boldsymbol{u} = \left\langle \boldsymbol{g}_{\vec{t}}^1 \;\; \boldsymbol{g}_{\vec{t}}^2 \;\; \dots \;\; \boldsymbol{g}_{\vec{t}}^{n_\Gamma} \right\rangle^\top \tag{4.11}$$

Where the superscript refers to the contacting node index. In the present case, the regularization of the contacting surface is performed using a master/slave approach where the stiffer surface is considered as the master.

4.3.2 Conewise projection operator

The projection of the contact-friction force $\boldsymbol{p}^k$ associated to k$^{\text{th}}$ node of the master surface on the friction cone $\mathscr{C}_\mu$ can be split into three cases. When the normal part of contact-friction force is negative, then the contact is no more ensured and the detachment is assumed. In such a case, the force $\boldsymbol{p}^k$ is considered as null. For adherence, $\boldsymbol{p}^k$ is still inside the cone so it remains unchanged, however, when sliding $\boldsymbol{p}^k$ should belong to the cone border $\partial\mathscr{C}_\mu$ (see Fig. 4.11).

$$\mathrm{proj}_{\mathscr{C}_\mu}(\boldsymbol{p}^k) = \begin{cases} \boldsymbol{p}^k \quad \text{for the adherence} & \left(\|\boldsymbol{p}_{\vec{t}}^k\| < \mu \boldsymbol{p}_{\vec{n}}^k\right) \\ \dfrac{1}{1+\mu^2}\left(\mu\|\boldsymbol{p}_{\vec{t}}^k\| + \boldsymbol{p}_{\vec{n}}^k\right)\left(\mu\dfrac{\boldsymbol{p}_{\vec{t}}^k}{\|\boldsymbol{p}_{\vec{t}}^k\|} + \vec{\boldsymbol{n}}\right) \quad \text{when sliding} & \left(\|\boldsymbol{p}_{\vec{t}}^k\| = \mu \boldsymbol{p}_{\vec{n}}^k\right) \\ \mathbf{0} \quad \text{when} \quad \boldsymbol{p}_{\vec{n}}^k < \mathbf{0} \end{cases} \tag{4.12}$$

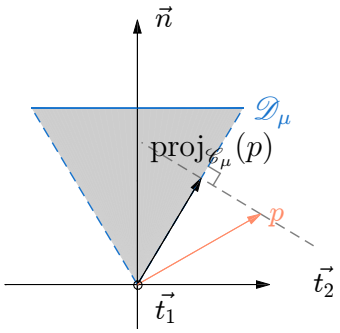

Figure 4.11 – Projection of $\boldsymbol{p}$, outside of the friction cone $\mathscr{C}_\mu$, on the border $\partial\mathscr{C}_\mu$.

4.3.3 Bipotential augmentation

The selection of the parameter ρ for the Lagrangian augmentation has a key role in the convergence speed. However, while small values of ρ provides slow convergence, larges

values might lead to non-convergence issues. In order to tackle the previously cited problems and avoid arbitrary selection of ρ, methods were developed to find values that ensure the convergence of the algorithm.

In the publication [14], Feng and de Saxcé defined a global stiffness ρ that avoid numerical instabilities. This stiffness is defined as:

$$\rho = \min\left(\frac{1}{\operatorname{diag}(\mathrm{W})}\right) \quad \text{where} \quad \mathrm{W} = \begin{bmatrix} \mathrm{P}_{\vec{n}} \\ \mathrm{P}_{\vec{t}} \end{bmatrix} \mathrm{K}^{-1} \begin{bmatrix} \mathrm{P}_{\vec{n}}{}^{\top} & \mathrm{P}_{\vec{t}}{}^{\top} \end{bmatrix}$$

In the literature, W is referred to as the Delassus matrix. In [21], Jean developed a method based on the use of local stiffness, computed for each contacting node k and for the directions $\vec{n}$ and $\vec{t}$. In the present work, a constant value of ρ is empirically chosen. This value is set to $5 \times 10^9 \mathrm{N.m}^{-1}$.

Function BipotentialAugmentation($\dot{\boldsymbol{u}}_{n+1}, \boldsymbol{u}_{n+1}, \boldsymbol{p}_{n+1}$)

output: $\boldsymbol{p}_{n+1}$

Gap computation

$\boldsymbol{g}_{\vec{n}} = \mathrm{B}_{\vec{n}} \boldsymbol{u}_{n+1}$; *Normal gap Eq. (4.10)*

$\dot{\boldsymbol{g}}_{\vec{t}} = \mathrm{B}_{\vec{t}} \dot{\boldsymbol{u}}_{n+1}$; *Tangential gap velocity Eq. (4.11)*

For each node of the contacting interface (n_Γ nodes)

for $k = 1 : n_\Gamma$ **do**

Computation of the variable $\boldsymbol{\tau}^k$

$\boldsymbol{v}^k = \left((\mu \|\dot{\boldsymbol{g}}_{\vec{t}}^k\| + g_{\vec{n}}^k)\vec{\boldsymbol{n}}_k + \dot{\boldsymbol{g}}_{\vec{t}}^k\right)$; *Eq. (4.7)*

$\boldsymbol{\tau}^k = \boldsymbol{p}_{n+1}^k - \rho^k \boldsymbol{v}^k$; *Eq. (4.8)*

Projection of $\boldsymbol{\tau}^k$ into the contact-friction cone $\mathscr{C}_\mu$

$\boldsymbol{p}_{n+1}^k := \mathrm{proj}_{\mathscr{C}_\mu}\left(\boldsymbol{\tau}^k\right)$; *Eq. (4.9)*

end

As a conclusion of this section, a function for the bipotential Lagrangian augmentation "BipotentialAugmentation" is given. This algorithm will be used later by the different time integration algorithms.

4.4 Time integration scheme and resolution methods

In the previous section, different formulations of the contact and friction laws were given. Now, popular methods for the resolution of the Signorini-Coulomb problem are given. The choice of a resolution method can be driven by the smoothness of the problem formulation, precision required or expected convergence speed. In this sections, three

resolution methods are highlighted: the Non Smooth Contact Dynamic method, the non-linear Newmark algorithm with Newton-Raphson iterations and eventually the central difference scheme coupled with an Uzawa procedure.

Each presented method involves a time-scheme and an iteration procedure. The Non Smooth Contact Dynamic method presented in section 4.4.1 rely on a $\theta-$integration scheme coupled to Newton-Raphson iteration. The Newmark method is then presented in section 4.4.2 and coupled with a Newton-Raphson procedure is given in algorithm 4.4.2. Eventually, the central difference method is presented in section 4.4.3 and applied with an Uzawa iteration procedure (see 4.4.3).

4.4.1 Non Smooth Contact Dynamic method

Developed by Jean and Moreau, the Non Smooth Dynamic Contact method (NSCD) aimed at solving the contact-friction problem when the formulation of the Signorini-Coulomb laws are not regularized.

This method was notably used by Acary and Jean [10] to compute the displacement of monuments using augmented an lagrangian formulation. In this example, the blocks (stones) are considered as rigid and not glued together by mortar [22].

Non-smooth formulations (like pure Lagrangian formulation) tend to lower the regularity of the acceleration $\ddot{\boldsymbol{u}}(t)$. Indeed, from a time step n to $n+1$, an impact may generate velocity $\dot{\boldsymbol{u}}(t)$ discontinuities that lead to undefined accelerations. Consequently, the acceleration $\ddot{\boldsymbol{u}}(t)$ may become undefined for certain time steps.

Thus, instead of working on an instantaneous expression, the NSCD method considers the integral of the system dynamic equation Eq. (4.1) over a time step $]t_n, t_{n+1}]$:

$$\mathcal{E} = \int_{t_n}^{t_{n+1}} \Big(\mathrm{M}\ddot{\boldsymbol{u}}(t) + \mathrm{C}\dot{\boldsymbol{u}}(t) + \mathrm{K}\boldsymbol{u}(t) - \boldsymbol{f}(t) - \boldsymbol{p}(t)\Big)\mathrm{d}t = \ \ldots$$
$$\int_{t_n}^{t_{n+1}} \mathrm{M}\ddot{\boldsymbol{u}}(t)\mathrm{d}t + \int_{t_n}^{t_{n+1}} \Big(\mathrm{C}\dot{\boldsymbol{u}}(t) + \mathrm{K}\boldsymbol{u}(t) - \boldsymbol{f}(t)\Big)\mathrm{d}t - \int_{t_n}^{t_{n+1}} \boldsymbol{p}(t)\mathrm{d}t, \tag{4.13}$$

where the vector term $\mathcal{E}$ is a residue that appears when the solutions are inaccurately approximated. Here, the acceleration $\ddot{\boldsymbol{u}}(t)$ is not a time function (because of its regularity issues), but rather a time distribution. Under such an assumption, considering φ as a test time-function (with compact time-support and of class C^∞), the integral $\mathcal{I}(\varphi)$ does exist by definition:

$$\mathcal{I}(\varphi) = \int_\tau \Big(\ddot{\boldsymbol{u}}(t) \cdot \varphi(t)\Big)\mathrm{d}t \ , \ \varphi(t) \in C^\infty.$$

As the velocity $\dot{\boldsymbol{u}}(t)$ is always time-defined (at least $\dot{\boldsymbol{u}}(t) \in C^0$), the integral of the acceleration $\int_{t_n}^{t_{n+1}} \mathrm{M}\ddot{\boldsymbol{u}}(t)\mathrm{d}t$ over a time step can be approximated as follow:

$$\int_{t_n}^{t_{n+1}} \mathrm{M}\ddot{\boldsymbol{u}}(t)\mathrm{d}t = \mathrm{M}\int_{t_n}^{t_{n+1}} \ddot{\boldsymbol{u}}(t)\mathrm{d}t = \mathrm{M}\Big[\dot{\boldsymbol{u}}(t)\Big]_{t_n}^{t_{n+1}} = \mathrm{M}\left(\dot{\boldsymbol{u}}_{n+1} - \dot{\boldsymbol{u}}_n\right). \tag{4.14}$$

The NSCD method also use a numerical quadrature involving a parameter θ to approximate the position at time t_{n+1}. For this reason, the Non Smooth Contact Dynamic method belongs to a more general family referred to as θ-method.

$$\boldsymbol{u}_{n+1} = \boldsymbol{u}_n + \int_{t_n}^{t_{n+1}} \dot{\boldsymbol{u}}(\tau)d\tau = \boldsymbol{u}_n + h\Big((1-\theta)\dot{\boldsymbol{u}}_n + \theta\dot{\boldsymbol{u}}_{n+1}\Big)\ ,\ \theta \in [0;1]. \tag{4.15}$$

Using the same quadrature, it is possible to also approximate the integral of the position $\boldsymbol{u}(t)$ and external force $\boldsymbol{f}(t)$ as:

$$\begin{aligned}
\int_{t_n}^{t_{n+1}} \boldsymbol{u}(\tau)\mathrm{d}t &= h\Big((1-\theta)\boldsymbol{u}_n + \theta\boldsymbol{u}_{n+1}\Big)\\
\int_{t_n}^{t_{n+1}} \dot{\boldsymbol{u}}(\tau)\mathrm{d}t &= h\Big((1-\theta)\dot{\boldsymbol{u}}_n + \theta\dot{\boldsymbol{u}}_{n+1}\Big)\\
\int_{t_n}^{t_{n+1}} \boldsymbol{f}(\tau)\mathrm{d}t &= h\Big((1-\theta)\boldsymbol{f}_n + \theta\boldsymbol{f}_{n+1}\Big).
\end{aligned}$$

In [21], Jean computed the integral of the nonlinear force $\boldsymbol{p}$ thanks to an implicit quadrature as follow:

$$\frac{1}{h}\int_{t_n}^{t_{n+1}} \boldsymbol{p}(\tau)\mathrm{d}t = \boldsymbol{p}_{n+1}.$$

Eventually, all those approximations allow to rewrite the integral Eq. (4.13) as:

$$\begin{aligned}
\mathcal{E}_{n+1} = \Big(\mathrm{M} + h\theta\mathrm{C} + (h\theta)^2\mathrm{K}\Big)\dot{\boldsymbol{u}}_{n+1} - \mathrm{M}\dot{\boldsymbol{u}}_n - h\boldsymbol{p}_{n+1}\\
-h\theta\Big(\mathrm{K}\Big(\boldsymbol{u}_n + h(1-\theta)\dot{\boldsymbol{u}}_n\Big) - \boldsymbol{f}_{n+1}\Big) - h(1-\theta)\Big(\mathrm{C}\dot{\boldsymbol{u}}_n + \mathrm{K}\boldsymbol{u}_n - \boldsymbol{f}_n\Big).
\end{aligned} \tag{4.16}$$

The θ-formalism coupled with Newton-Raphson procedure

This approximation of the contact-friction problem can be solved at t_{n+1} using a Newton-Rapshon procedure, in order to find the solution that cancels the integral residue $\mathcal{E}_{n+1}$. Note that due to the term $\boldsymbol{p}$, equation Eq. (4.16) remains nonlinear. Let $\dot{\boldsymbol{u}}_{n+1}^k$ denote the k^{th} approximation of the velocity:

$$\begin{aligned}
\mathcal{E}_{n+1} = \mathcal{E}(\dot{\boldsymbol{u}}_{n+1}^{k+1}) = \mathcal{E}(\dot{\boldsymbol{u}}_{n+1}^{k}) + \frac{\partial\mathcal{E}_{n+1}}{\partial\dot{\boldsymbol{u}}_{n+1}}(\dot{\boldsymbol{u}}_{n+1}^{k+1} - \dot{\boldsymbol{u}}_{n+1}^{k})\\
\frac{\partial\mathcal{E}_{n+1}}{\partial\dot{\boldsymbol{u}}_{n+1}} = \Big(\mathrm{M} + h\theta\mathrm{C} + (h\theta)^2\mathrm{K}\Big) = \mathrm{C}_T.
\end{aligned}$$

The convergence of the velocity $\dot{\boldsymbol{u}}_{n+1}^{k+1}$ is reached when the residual $\mathcal{E}(\dot{\boldsymbol{u}}_{n+1}^{k+1})$ becomes small with respect to the external load $\boldsymbol{f}_{n+1}$, the convergence is reached when:

$$\|\mathcal{E}_{n+1}\| \leq \varepsilon \boldsymbol{f}_{n+1}. \tag{4.17}$$

Since the integral of the residue cancels when the exact velocity is reached, the corrected velocity $\dot{\boldsymbol{u}}_{n+1}^{k+1}$ can be computed as:

$$\dot{\boldsymbol{u}}_{n+1}^{k+1} = \dot{\boldsymbol{u}}_{n+1}^{k} - \mathrm{C}_T^{-1}\mathcal{E}(\dot{\boldsymbol{u}}_{n+1}^{k}). \tag{4.18}$$

Algorithm 4.4.1: θ-method coupled with Newton-Raphson for the non-smooth contact-friction resolution

input: M, $\boldsymbol{f}_0$, $\boldsymbol{p}_0$, $\boldsymbol{u}_0$, $\dot{\boldsymbol{u}}_0$, h, $n = 0$

Initial acceleration computation

$\ddot{\boldsymbol{u}}_0 = \mathrm{M}^{-1}(\boldsymbol{f}_0 + \boldsymbol{p}_0 - \mathrm{C}\dot{\boldsymbol{u}}_0 - \mathrm{K}\boldsymbol{u}_0)$; *Dynamic equation Eq. (4.1)*

Until the end the simulation at time t_f

while $t_n < t_f$ **do**

Time incrementation to t_{n+1}

$t_{n+1} = t_n + h$;

First prediction of the system state at t_{n+1}

$\dot{\boldsymbol{u}}_{n+1}^{k=0} = \dot{\boldsymbol{u}}_n$; *Velocity initialisation*

$\boldsymbol{u}_{n+1}^{k=0} = \boldsymbol{u}_n + h(1-\theta)\dot{\boldsymbol{u}}_n$; *Eq. (4.15)*

$\boldsymbol{p}_{n+1}^{k=0} = \mathrm{BipotentialAugmentation}\big(\boldsymbol{u}_{n+1}^{k=0}, \dot{\boldsymbol{u}}_{n+1}^{k=0}, \boldsymbol{p}_n\big)$;

$\mathcal{E}_{n+1} = \mathcal{E}\big(\boldsymbol{u}_n, \dot{\boldsymbol{u}}_n, \boldsymbol{u}_{n+1}^{k=0}, \dot{\boldsymbol{u}}_{n+1}^{k=0}, \boldsymbol{p}_{n+1}^{k=0}\big)$; *Eq. (4.16)*

While the residue $\mathcal{E}_{n+1}$ is nonnegligible: Eq. (4.17)

while $\|\mathcal{E}_{n+1}\| > \varepsilon \boldsymbol{f}_{n+1}$ **do**

Velocity correction

$\dot{\boldsymbol{u}}_{n+1}^{k+1} = \dot{\boldsymbol{u}}_{n+1}^{k} - \mathrm{C}_T^{-1}\mathcal{E}_{n+1}$; *Eq. (4.18)*

Position correction

$\boldsymbol{u}_{n+1}^{k+1} = \boldsymbol{u}_n + h\big((1-\theta)\dot{\boldsymbol{u}}_n + \theta\dot{\boldsymbol{u}}_{n+1}^{k+1}\big)$; *Eq. (4.15)*

Integral residue $\mathcal{E}_{n+1}$ update

$\boldsymbol{p}_{n+1}^{k+1} = \mathrm{BipotentialAugmentation}\big(\boldsymbol{u}_{n+1}^{k+1}, \dot{\boldsymbol{u}}_{n+1}^{k+1}, \boldsymbol{p}_{n+1}^{k}\big)$;

$\mathcal{E}_{n+1} := \mathcal{E}\big(\boldsymbol{u}_n, \dot{\boldsymbol{u}}_n, \boldsymbol{u}_{n+1}^{k+1}, \dot{\boldsymbol{u}}_{n+1}^{k+1}, \boldsymbol{p}_{n+1}^{k+1}\big)$; *Eq. (4.16)*

Iteration index incrementation

$k := k + 1$;

end

Save the computed variables for t_{n+1}

$\dot{\boldsymbol{u}}_{n+1} = \dot{\boldsymbol{u}}_{n+1}^{k+1}$;

$\boldsymbol{u}_{n+1} = \boldsymbol{u}_{n+1}^{k+1}$;

Time index incrementation

$n := n + 1$;

end

At a first sight, such a procedure seems convenient as the gradient C_T is constant. A possible way to implement the θ-method with Newton-Raphson procedure is given in algorithm 4.4.1.

It has to be noticed that the θ-method is unconditionally stable for $\theta \geq 1/2$ [21]. The scheme using $\theta = 1/2$ is referred to as Crank-Nicholson scheme. In the present work however, this method is not convenient. Indeed, the NSCD method does not grant the access to the acceleration variable $\ddot{\boldsymbol{u}}$ that is required for the system instantaneous energy evaluation.

4.4.2 Newmark's family method

The Newmark method is a single step integration formula. It relies on the following Taylor series expansion of the system velocity $\dot{\boldsymbol{u}}_{n+1}$ and position $\boldsymbol{u}_{n+1}$, [23]:

$$\dot{\boldsymbol{u}}_{n+1} = \dot{\boldsymbol{u}}_n + h\Big((1-\gamma)\ddot{\boldsymbol{u}}_n + \gamma\ddot{\boldsymbol{u}}_{n+1}\Big) \qquad , \gamma \in [0;1] \tag{4.19}$$

$$\boldsymbol{u}_{n+1} = \boldsymbol{u}_n + h\dot{\boldsymbol{u}}_n + \frac{1}{2}h^2\Big((1-2\beta)\ddot{\boldsymbol{u}}_n + 2\beta\ddot{\boldsymbol{u}}_{n+1}\Big) \qquad , \beta \in \left[0;\frac{1}{2}\right] \tag{4.20}$$

Consequently, unlike the θ-method previously introduced, the problem treated is supposed to be regular. Indeed, this expression assume that the acceleration is defined at the times t_n and t_{n+1}. In the present case this requires the regularization of the contact-friction laws that might be provided by the use of penalization or augmented Lagrangian formulation.

Newmark's parameters tuning

The choice of the parameters couple (γ, β) is a key point that plays both on the speed and stability of algorithm. The demonstrations highlighting the different stability area of the Newmark scheme are not detailed here but can be found in the literature, they are notably remembered in the book by Géradin and Rixen [23].

Considering the second order differential equation $\ddot{\eta} + \omega^2\eta = 0$, the resolution stability such as the periodicity error of the computed solution η depends on (γ, β).

Iterative resolution of nonlinear problems using Newmark scheme

Nevertheless, in the present case the contact-friction forces $\boldsymbol{p}$ are nonnull and depend on the position and velocity of the system. The nonlinear nature of the problem leads to an iterative resolution of the problem where corrections are performed on the displacements

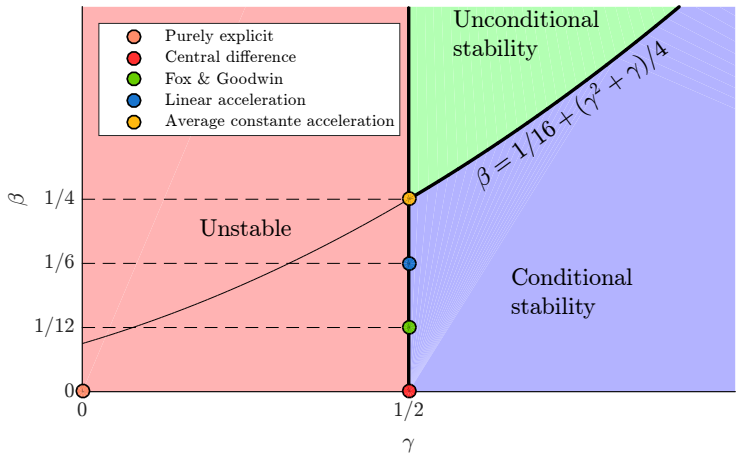

Figure 4.12 – Stability regions for the Newmark algorithm

Algorithm	γ	β	Stability limit ωh	Periodicity error
Purely explicit	0	0	0	-
Central difference	$\frac{1}{2}$	0	2	$-\frac{\omega^2 h^2}{24}$
Fox & Goodwin	$\frac{1}{2}$	$\frac{1}{12}$	2.45	$\mathcal{O}(h^3)$
Linear acceleration	$\frac{1}{2}$	$\frac{1}{6}$	3.46	$\frac{\omega^2 h^2}{24}$
Average constant acceleration	$\frac{1}{2}$	$\frac{1}{4}$	∞	$\frac{\omega^2 h^2}{12}$

Table 4.1 – Common Newmark parameters configuration and their properties when solving the linear second order differential equation $\ddot{\eta} + \omega^2 \eta = 0$ with a fixed time step h.

$\boldsymbol{u}_{n+1}$ and tend to cancel the instantaneous residue $\boldsymbol{r}_{n+1}$. The vector $\boldsymbol{r}_{n+1}$ is homogeneous to a residual force that appears in the equation of the system dynamics:

$$\boldsymbol{r}_{n+1} = \boldsymbol{r}(\boldsymbol{u}_{n+1}, \dot{\boldsymbol{u}}_{n+1}, \ddot{\boldsymbol{u}}_{n+1}) \tag{4.21}$$

$$= \mathrm{M}\ddot{\boldsymbol{u}}_{n+1} + \mathrm{C}\dot{\boldsymbol{u}}_{n+1} + \mathrm{K}\boldsymbol{u}_{n+1} - \boldsymbol{f}_{n+1} - \boldsymbol{p}_{n+1} \tag{4.22}$$

A classical iterative method enabling to achieve this goal is based on the Newton-Raphson principle and requires the stiffness tangent matrix K_T, see algorithm 4.4.2.

Let $\Delta\boldsymbol{u}^k_{n+1}$ denote the k$^{\text{th}}$ correction of the prediction $\boldsymbol{u}^k_{n+1}$ at time t_{n+1}, the corrected solution $\boldsymbol{u}^{k+1}_{n+1}$ is defined as $\boldsymbol{u}^{k+1}_{n+1} = \boldsymbol{u}^k_{n+1} + \Delta\boldsymbol{u}^k_{n+1}$. The Newton-Raphson procedure consist here to iterate on the displacement correction to minimise the residual force $\boldsymbol{r}_{n+1}$.

Using a first order approximation of the residue $\boldsymbol{r}_{n+1}$ it is possible to write

$$\boldsymbol{r}(\boldsymbol{u}_{n+1}^{k+1}) = \boldsymbol{r}(\boldsymbol{u}_{n+1}^{k}) + \frac{\partial \boldsymbol{r}_{n+1}}{\partial \boldsymbol{u}_{n+1}} \Delta \boldsymbol{u}_{n+1}^{k} \tag{4.23}$$

$$\text{knowing that: } \Delta \boldsymbol{u}_{n+1}^{k} = \boldsymbol{u}_{n+1}^{k+1} - \boldsymbol{u}_{n+1}^{k} \tag{4.24}$$

In practice, the convergence is reached when the norm of the residual load $\boldsymbol{r}_{n+1}$ become small with regards to the norm of the external load $\boldsymbol{f}_{n+1}$. A tolerance threshold $\varepsilon_{\boldsymbol{r}}$ is used to check this constraint. The convergence of the position is reached when

$$\|\boldsymbol{r}_{n+1}\| \leq \varepsilon_{\boldsymbol{r}} \|\boldsymbol{f}_{n+1}\| \tag{4.25}$$

In Eq. (4.23) a tangent stiffness matrix K_T that corresponds to the Jacobian operator of the residual force $\boldsymbol{r}_{n+1}$ regarding to the position $\boldsymbol{u}_{n+1}$ is required.

$$\mathrm{K}_T = \frac{\partial \boldsymbol{r}_{n+1}}{\partial \boldsymbol{u}_{n+1}} = \frac{\partial}{\partial \boldsymbol{u}_{n+1}} \Big(\mathrm{M}\ddot{\boldsymbol{u}}_{n+1} + \mathrm{C}\dot{\boldsymbol{u}}_{n+1} + \mathrm{K}\boldsymbol{u}_{n+1} - \boldsymbol{f}_{n+1} - \boldsymbol{p}_{n+1} \Big)$$

If the corrected position $\boldsymbol{u}_{n+1}^{k+1}$ is well approximated in Eq. (4.23) then the residue $\boldsymbol{r}(\boldsymbol{u}_{n+1})$ vanishes, so it is possible to express the correction $\Delta \boldsymbol{u}_{n+1}^{k}$ in function of the tangent matrix K_T and the residual force $\boldsymbol{r}_{n+1}^{k}$:

$$\Delta \boldsymbol{u}_{n+1}^{k} = -\mathrm{K}_T^{-1} \boldsymbol{r}_{n+1}^{k} \tag{4.26}$$

The acceleration and velocity can be expressed with the correction $\Delta \boldsymbol{u}_{n+1}$ by respectively substituting the Newmark quadratures Eq. (4.19) and Eq. (4.20) at the iterations $k+1$ and k lead to the following relations:

$$\ddot{\boldsymbol{u}}_{n+1}^{k+1} = \ddot{\boldsymbol{u}}_{n+1}^{k} + \frac{1}{h^2 \beta} \Delta \boldsymbol{u}_{n+1}^{k} \tag{4.27}$$

$$\dot{\boldsymbol{u}}_{n+1}^{k+1} = \dot{\boldsymbol{u}}_{n+1}^{k} + \frac{\gamma}{h \beta} \Delta \boldsymbol{u}_{n+1}^{k} \tag{4.28}$$

The equations Eq. (4.27) and Eq. (4.28) highlight the link between the residual force $\boldsymbol{r}_{n+1}$ and position correction $\Delta \boldsymbol{u}_{n+1}$. This allows to find an expression of the tangent stiffness matrix K_T.

$$\boldsymbol{r}_{n+1} = \mathrm{M} \left(\ddot{\boldsymbol{u}}_{n+1}^{k} + \frac{1}{h^2 \beta} \Delta \boldsymbol{u}_{n+1}^{k} \right) + \mathrm{C} \left(\dot{\boldsymbol{u}}_{n+1}^{k} + \frac{\gamma}{h \beta} \Delta \boldsymbol{u}_{n+1}^{k} \right) + \mathrm{K}\boldsymbol{u}_{n+1} - \boldsymbol{f}_{n+1} - \boldsymbol{p}_{n+1}$$

The predicted variables at the k^{th} iteration and the external load $\boldsymbol{f}_{n+1}$ are not impacted by the displacement iterations, for this reason the tangent matrix K_T is express as:

$$\mathrm{K}_T = \frac{1}{h^2 \beta} \mathrm{M} + \frac{\gamma}{h \beta} \mathrm{C} + \mathrm{K} - \frac{\partial \boldsymbol{p}_{n+1}}{\partial \boldsymbol{u}_{n+1}} \tag{4.29}$$

Algorithm 4.4.2: Displacement based Newmark-Newton-Raphson algorithm for the contact-friction resolution

input: M, $\boldsymbol{f}_0$, $\boldsymbol{p}_0$, $\boldsymbol{u}_0$, $\dot{\boldsymbol{u}}_0$, h, $n = 0$

Initial acceleration computation

$\ddot{\boldsymbol{u}}_0 = \mathrm{M}^{-1}(\boldsymbol{f}_0 + \boldsymbol{p}_0 - \mathrm{C}\dot{\boldsymbol{u}}_0 - \mathrm{K}\boldsymbol{u}_0)$; *Dynamic equation Eq. (4.1)*

While end time of the simulation t_f is not reached

while $t_n < t_f$ **do**

Time incrementation to t_{n+1}

$t_{n+1} = t_n + h$;

Prediction of the system state at t_{n+1}

$\ddot{\boldsymbol{u}}_{n+1}^{k=0} = \boldsymbol{0}$; *Acceleration initialisation*

$\dot{\boldsymbol{u}}_{n+1}^{k=0} = \dot{\boldsymbol{u}}_n + h(1-\gamma)\ddot{\boldsymbol{u}}_n$; *Eq. (4.19)*

$\boldsymbol{u}_{n+1}^{k=0} = \boldsymbol{u}_n + h\dot{\boldsymbol{u}}_n + \frac{1}{2}h^2(1-2\beta)\ddot{\boldsymbol{u}}_n$; *Eq. (4.20)*

$\boldsymbol{p}_{n+1}^{k=0} = \text{BipotentialAugmentation}\big(\boldsymbol{u}_{n+1}^{k=0}, \dot{\boldsymbol{u}}_{n+1}^{k=0}, \boldsymbol{p}_n\big)$;

$\boldsymbol{r}_{n+1} = \mathrm{M}\ddot{\boldsymbol{u}}_{n+1}^{k=0} + \mathrm{C}\dot{\boldsymbol{u}}_{n+1}^{k=0} + \mathrm{K}\boldsymbol{u}_{n+1}^{k=0} - \boldsymbol{f}_{n+1} - \boldsymbol{p}_{n+1}^{k=0}$; *Eq. (4.22)*

While the residue $\boldsymbol{r}_{n+1}$ is nonnegligible: Eq. (4.25)

while $||\boldsymbol{r}_{n+1}|| > \varepsilon||\boldsymbol{f}_{n+1}||$ **do**

Displacement correction computation $\Delta\boldsymbol{u}_{n+1}$

$\mathrm{K}_T = \frac{\partial \boldsymbol{r}_{n+1}}{\partial \boldsymbol{u}_{n+1}}$; *Eq. (4.29)*

$\Delta\boldsymbol{u}_{n+1}^{k} = -\mathrm{K}_T^{-1}\boldsymbol{r}_{n+1}$; *Eq. (4.26)*

Correction of the prediction state at t_{n+1}

$\ddot{\boldsymbol{u}}_{n+1}^{k+1} = \ddot{\boldsymbol{u}}_{n+1}^{k} + \frac{1}{\beta h^2}\Delta\boldsymbol{u}_{n+1}^{k}$; *Eq. (4.27)*

$\dot{\boldsymbol{u}}_{n+1}^{k+1} = \dot{\boldsymbol{u}}_{n+1}^{k} + \frac{\gamma}{\beta h}\Delta\boldsymbol{u}_{n+1}^{k}$; *Eq. (4.28)*

$\boldsymbol{u}_{n+1}^{k+1} = \boldsymbol{u}_{n+1}^{k} + \Delta\boldsymbol{u}_{n+1}^{k}$; *Eq. (4.24)*

$\boldsymbol{p}_{n+1}^{k+1} = \text{BipotentialAugmentation}\big(\boldsymbol{u}_{n+1}^{k+1}, \dot{\boldsymbol{u}}_{n+1}^{k+1}, \boldsymbol{p}_{n+1}^{k}\big)$;

$\boldsymbol{r}_{n+1} := \mathrm{M}\ddot{\boldsymbol{u}}_{n+1}^{k+1} + \mathrm{C}\dot{\boldsymbol{u}}_{n+1}^{k+1} + \mathrm{K}\boldsymbol{u}_{n+1}^{k+1} - \boldsymbol{f}_{n+1} - \boldsymbol{p}_{n+1}^{k+1}$; *Eq. (4.22)*

Iteration index incrementation

$k := k + 1$;

end

Save the last correction of the system state at t_{n+1}

$\ddot{\boldsymbol{u}}_{n+1} = \ddot{\boldsymbol{u}}_{n+1}^{k+1}$;

$\dot{\boldsymbol{u}}_{n+1} = \dot{\boldsymbol{u}}_{n+1}^{k+1}$;

$\boldsymbol{u}_{n+1} = \boldsymbol{u}_{n+1}^{k+1}$;

Time index incrementation

$n = n + 1$;

end

In this work, this method is referred to as Newmark-Newton-Rapshon procedure (see 4.4.2). The difficulty of this method is the evaluation of the term $\frac{\partial \boldsymbol{p}_{n+1}}{\partial \boldsymbol{u}_{n+1}}$. Moreover, the computation of this last term is only possible if the associated contact-friction laws are smooth enough. Details about the practical implementation of this methods are given in

the thesis of Vermot des Roches [24].

4.4.3 Central difference method

Using an explicit integration scheme allows to avoid the use of Newton-Raphson procedure and linearisation [8]. Unfortunately, in practice, the purely explicit scheme can not be used because of its instability (see table 4.1).

In this section we show how the central difference algorithm iterates on the nonlinear force $\boldsymbol{p}_n$ to respect the Signorini-Coulomb law in terms of velocity and position at the next time step $n+1$. This approach is referred to as Uzawa iteration [23] and has two main advantages:

- Unlike the Newton-Raphson procedure previously presented, no definition of a gradient or pseudo-gradient is needed, this deeply simplifies the resolution of the problem.

- The regularization of the Signorini-Coulomb laws is no longer required and the augmented Lagrangian formulation can be used, providing an accurate resolution of the problem.

The central difference method ($\gamma = 1/2, \beta = 0$) provides a good compromise between explicit formulation and stability. Indeed, this numerical scheme does not suppress the dependency of the velocity $\dot{\boldsymbol{u}}_{n+1}$ on the implicit acceleration $\ddot{\boldsymbol{u}}_{n+1}$ and its stability can be reached using an appropriated integration time step h.

$$\dot{\boldsymbol{u}}_{n+1} = \dot{\boldsymbol{u}}_n + \frac{1}{2}h\left(\ddot{\boldsymbol{u}}_n + \ddot{\boldsymbol{u}}_{n+1}\right), \tag{4.30}$$

$$\boldsymbol{u}_{n+1} = \boldsymbol{u}_n + h\dot{\boldsymbol{u}}_n + \frac{1}{2}h^2\ddot{\boldsymbol{u}}_n. \tag{4.31}$$

The evaluation of the velocity at t_{n+1} is more efficient than Eq. (4.30) from an algorithmic point of view [23]. The central difference algorithm use Newmark equation Eq. (4.30) for the evaluation of the intermediate velocity $\dot{\boldsymbol{u}}_{n+\frac{1}{2}}$ between the time step t_n and t_{n+1}:

$$\dot{\boldsymbol{u}}_{n+\frac{1}{2}} = \dot{\boldsymbol{u}}_{n-\frac{1}{2}} + h\ddot{\boldsymbol{u}}_n. \tag{4.32}$$

Initially, the first approximation of the velocity $\dot{\boldsymbol{u}}_{\frac{1}{2}}$ at a centred time step is performed using an incomplete Newmark scheme since the acceleration $\ddot{\boldsymbol{u}}_1$ is not known, thus:

$$\dot{\boldsymbol{u}}_{\frac{1}{2}} = \dot{\boldsymbol{u}}_0 + \frac{1}{2}h\ddot{\boldsymbol{u}}_0. \tag{4.33}$$

The stability of the central difference method is given by $\omega h \leq 2$ where ω is associated to the largest natural frequency of the considered finite element model. This stability criterion is remembered in Tab. 4.1.

Central difference integration scheme coupled with Uzawa iterations

At the beginning of the simulation at time step n, neither the acceleration $\ddot{\boldsymbol{u}}_n$ nor the contact-friction force $\boldsymbol{p}_n$ are known. However, knowing the position $\boldsymbol{u}_n$, velocity $\dot{\boldsymbol{u}}_n$ and assessing the contact-friction force $\boldsymbol{p}_n^{k=0}$ as null the acceleration $\ddot{\boldsymbol{u}}_n$ can be estimated.

Knowing the system state at t_n, it is possible to predict the future velocity and position at t_{n+1}. The acceleration $\ddot{\boldsymbol{u}}_n$ is first evaluated using the velocity $\dot{\boldsymbol{u}}_n$, position $\boldsymbol{u}_n$, external force $\boldsymbol{f}_n$ and an estimated contact-friction force $\boldsymbol{p}_n^k$. Those predictions at t_{n+1} might not respect the Signorini-Coulomb laws at t_{n+1}. Practically, this is expressed by a nonnull Lagrangian augmentation so that:

$$\boldsymbol{p}_n^k - \text{BipotentialAugmentation}\left(\dot{\boldsymbol{u}}_{n+\frac{1}{2}}, \boldsymbol{u}_{n+1}, \boldsymbol{p}_n^k\right) \neq \boldsymbol{0}.$$

In the present case, the Uzawa procedure iterates on the contact-friction force $\boldsymbol{p}_n^k$ until its convergence. For this reason, the convergence test used to check the stabilisation of $\boldsymbol{p}_n$ is defined as follows:

$$\boldsymbol{p}_n^{k+1} = \text{BipotentialAugmentation}\left(\dot{\boldsymbol{u}}_{n+\frac{1}{2}}, \boldsymbol{u}_{n+1}, \boldsymbol{p}_n^k\right) \tag{4.34}$$

$$\text{the convergence of } \boldsymbol{p}_n \text{ is } \begin{cases} \text{reached if } \|\boldsymbol{p}_n^{k+1} - \boldsymbol{p}_n^k\| \leq \varepsilon_{\boldsymbol{p}} \\ \text{not reached if } \|\boldsymbol{p}_n^{k+1} - \boldsymbol{p}_n^k\| > \varepsilon_{\boldsymbol{p}} \end{cases}. \tag{4.35}$$

The new estimation $\boldsymbol{p}_n^{k+1}$ it then used to refresh the acceleration estimation at time $\ddot{\boldsymbol{u}}_n$. This new acceleration is used to update the prediction of the system state at time t_{n+1}. The Uzawa iteration is presented in the function Evolution.

Function Evolution($\dot{\boldsymbol{u}}_{n-\frac{1}{2}}, \boldsymbol{u}_n, \boldsymbol{p}_n^k$)

output: $\ddot{\boldsymbol{u}}_n, \dot{\boldsymbol{u}}_{n+\frac{1}{2}}, \boldsymbol{u}_{n+1}, \boldsymbol{p}_n^{k+1}$

Computation of the acceleration $\ddot{\boldsymbol{u}}_n$

$\ddot{\boldsymbol{u}}_n = \mathrm{M}^{-1}\left(\boldsymbol{f}_n + \boldsymbol{p}_n^k - \mathrm{C}\dot{\boldsymbol{u}}_{n-\frac{1}{2}} - \mathrm{K}\boldsymbol{u}_n\right)$; *Eq. (4.1)*

Estimation of the velocity at $t_{n+\frac{1}{2}}$

$\dot{\boldsymbol{u}}_{n+\frac{1}{2}} = \dot{\boldsymbol{u}}_{n-\frac{1}{2}} + h\ddot{\boldsymbol{u}}_n$; *Eq. (4.32)*

Estimation of the position at t_{n+1}

$\boldsymbol{u}_{n+1} = \boldsymbol{u}_n + h\dot{\boldsymbol{u}}_{n+\frac{1}{2}}$; *Eq. (4.31)*

Lagrangian augmentation

$\boldsymbol{p}_n^{k+1} = \text{BipotentialAugmentation}\left(\dot{\boldsymbol{u}}_{n+\frac{1}{2}}, \boldsymbol{u}_{n+1}, \boldsymbol{p}_n^k\right)$; *Eq. (4.34)*

In 4.4.3, the convergence is reached trough the iterative augmentation of the bipotential formulation of $\boldsymbol{p}_n$, thus this algorithm is referred to as Uzawa-Bipotential. Although this kind of algorithm provides highly accurate solutions, reaching the convergence of the contact-friction force $\boldsymbol{p}_n$ might be time consuming [17].

Algorithm 4.4.3: Central difference algorithm for the contact-friction problem

input : M, K, C, $\boldsymbol{u}_0$, $\dot{\boldsymbol{u}}_0$, $n = 0$

Initial acceleration computation $\ddot{\boldsymbol{u}}_0$

$\ddot{\boldsymbol{u}}_0 = \mathrm{M}^{-1}\left(\boldsymbol{f}_0 - \mathrm{C}\dot{\boldsymbol{u}}_0 - \mathrm{K}\boldsymbol{u}_0\right)$; *Eq. (4.1)*

Prediction of the velocity at $t_{\frac{1}{2}}$

$\dot{\boldsymbol{u}}_{n+\frac{1}{2}} = \dot{\boldsymbol{u}}_{\frac{1}{2}} = \dot{\boldsymbol{u}}_0 + \frac{1}{2}h\ddot{\boldsymbol{u}}_0$; $(+\frac{1}{2}h\ddot{\boldsymbol{u}}_1 = \boldsymbol{0})$ *Eq. (4.33)*

While end time of the simulation t_f *is not reached*

while $t_n < t_f$ **do**

Time incrementation to t_{n+1}

$t_{n+1} = t_n + h$;

First iteration on the contact-friction force $\boldsymbol{p}_n$

$\boldsymbol{p}_n^{k=0} = \boldsymbol{0}$; *Initialisation of* $\boldsymbol{p}_n$

$\left[\ddot{\boldsymbol{u}}_n^1, \dot{\boldsymbol{u}}_{n+\frac{1}{2}}^1, \boldsymbol{u}_{n+1}^1, \boldsymbol{p}_n^1\right] :=$ Evolution $\left(\dot{\boldsymbol{u}}_{n-\frac{1}{2}}, \boldsymbol{u}_n, \boldsymbol{p}_n^{k=0}\right)$;

While the value of $\boldsymbol{p}_n$ *has not converged Eq. (4.35)*

while $\|\boldsymbol{p}_n^{k+1} - \boldsymbol{p}_n^k\| > \varepsilon_{\boldsymbol{p}}$ **do**

Iteration on the contact-friction force $\boldsymbol{p}_n$

$k := k + 1$;

$\left[\ddot{\boldsymbol{u}}_n^{k+1}, \dot{\boldsymbol{u}}_{n+\frac{1}{2}}^{k+1}, \boldsymbol{u}_{n+1}^{k+1}, \boldsymbol{p}_n^{k+1}\right] :=$ Evolution $\left(\dot{\boldsymbol{u}}_{n-\frac{1}{2}}, \boldsymbol{u}_n, \boldsymbol{p}_n^k\right)$;

end

Save the converged solutions and reset k

$\ddot{\boldsymbol{u}}_n = \ddot{\boldsymbol{u}}_n^{k+1}$ $\dot{\boldsymbol{u}}_{n+\frac{1}{2}} = \dot{\boldsymbol{u}}_{n+\frac{1}{2}}^{k+1}$ $\boldsymbol{u}_{n+1} = \boldsymbol{u}_{n+1}^{k+1}$ $k = 0$;

Time index incrementation

$n = n + 1$;

end

Application with rigid hub assumption

In order to highlight our purpose, a time simulation of the preload $\boldsymbol{f}_{\text{pl.}}$ rise is performed. In this simulation the hub is consider as a rigid body, the preload force rises in 5×10^{-5} seconds. The position of the blade during this rise, at $t = 3 \times 10^{-5}$ is given in Fig. 4.13b. The time evolution of the preload $\boldsymbol{f}_{\text{pl.}}$ imposed on the bottom of the blade is given in Fig. 4.13a.

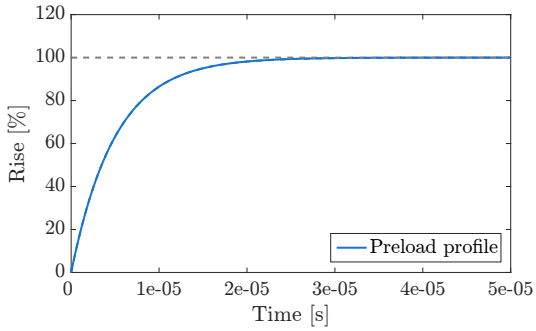

(a) Rise of the force $\boldsymbol{f}_{\text{pl.}}$, the nominal load is reached around 3×10^{-5} seconds.

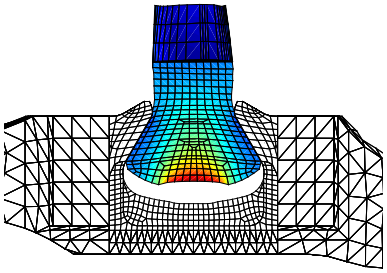

(b) Position of the blade during the preload $\boldsymbol{f}_{\text{pl.}}$ raise, at $t = 3 \times 10^{-5}$ seconds.

Figure 4.13 – Application of the Uzawa algorithm (4.4.3) with central difference scheme for the resolution of the first simulation step that correspond to the preload of the blade (3D model) in order to keep parts contacting.

At each new time step, the iteration of the contact-friction force $\boldsymbol{p}_n$ leads approximately to a logarithmic decrease of the convergence variable $(\boldsymbol{p}_n^{k+1} - \boldsymbol{p}_n^k)$ (highlighted in Eq. (4.35)). This decrease can be seen in Fig. 4.14. In this example, the error threshold $\varepsilon_{\boldsymbol{p}}$ is set as 10^{-8}.

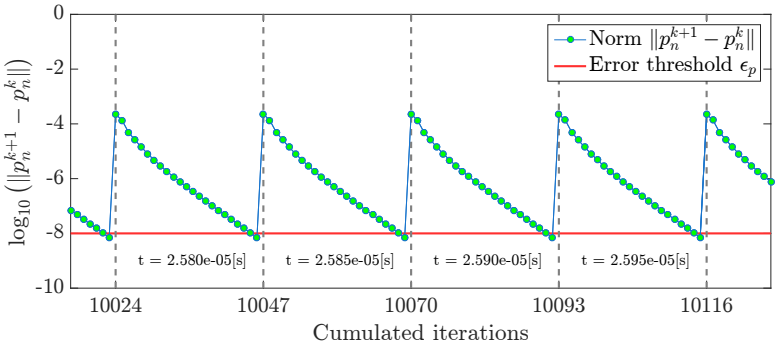

Figure 4.14 – Evolution of the error criterion $\|\boldsymbol{p}_n^{k+1} - \boldsymbol{p}_n^k\|$, proposed in Eq. (4.35) for $t \in [2.58\ ;\ 2.59] \times 10^{-5}$ seconds. The dashed lines are used to highlight the time step change, that occur as soon as the error indicator $\|\boldsymbol{p}_n^{k+1} - \boldsymbol{p}_n^k\|$ drops under the convergence threshold $\varepsilon_{\boldsymbol{p}}$.

In the present application, sliding is hardly observable because of the excitation nature. However, the enforcement of the Signorini law can be studied, accordingly to Fig. 4.15 this seems to be well respected as the interpenetration (i.e. negative gap) remain very small with respect to the displacement of the interior DoF.

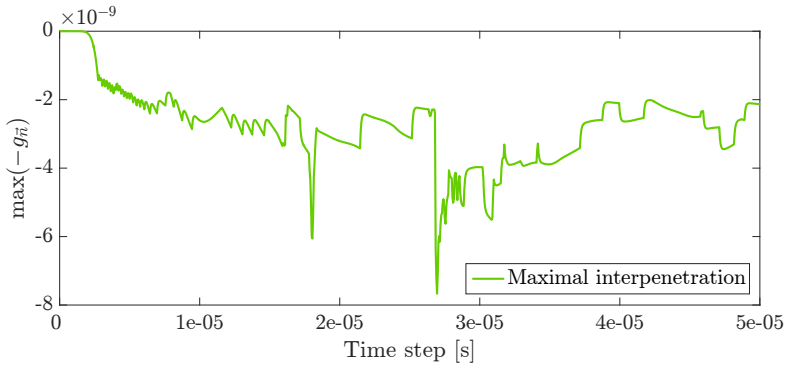

Figure 4.15 – Maximal interpenetration $\max(-\boldsymbol{g}_{\vec{n}})$ detected for each converged time step.

Fig. 4.14 suggests that the number of iteration nedded to reach the convergence of each time step is relatively constant. Having a look at the number of iteration performed at each time step (see Fig. 4.16), we note some variation of the needed iteration. Although those iterations number varies in the transient state ($t < 3.5 \times 10^{-5}$ s), they becomes rather constant during the steady state ($t \geq 3.5 \times 10^{-5}$ s).

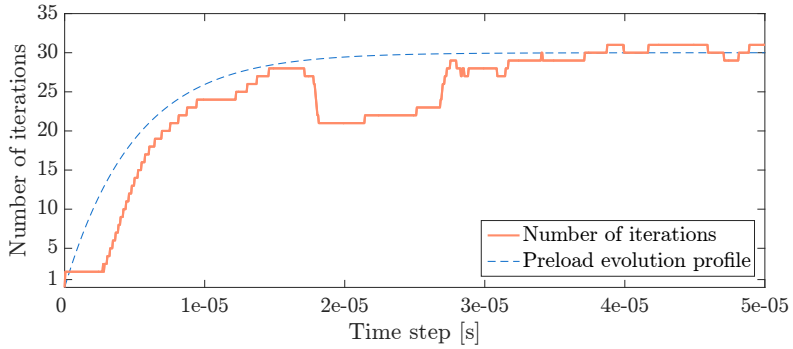

Figure 4.16 – Evolution of the iteration performed to reach the convergence assumed in Eq. (4.35).

Each iteration of the contact-friction force $\boldsymbol{p}_n$ requires the inversion of the mass matrix in order to complete the first operation (acceleration computation $\ddot{\boldsymbol{u}}_{n+1}$, Eq. (4.1)) in the function Evolution. This leads to time consuming simulations, indeed, in the current application, the blade has 39724 nodes that leads to finite element operators of size 119172×119172.

However, this operation could be deeply simplified using model reduction, indeed, using an orthogonal and mass-normalised reduction basis would provide a mass-diagonal $\tilde{\mathrm{M}}$, hence the mass inversion could be avoided. With this in mind, the next section investigates methodologies for the reduction of the current problem.

4.5 Reduction of the contact-friction problem

In the next sections, a reduction method is investigated for the time simulation of the blade. Indeed, time simulation can be used for the computation of the damping brought by the contact and friction for each assembled mode $\boldsymbol{\phi}_j$ of the system. Such simulations should consider the blade as statically loaded by $\boldsymbol{f}_{\text{pl.}}$ while the system initial position corresponds to the studied mode $\boldsymbol{\phi}_j$. Since the aim of these simulations is to study eigenmodes, the preload force $\boldsymbol{f}_{\text{pl.}}$ is the only external load applied on the system and is constant. The loss of energy due to contact and friction could then be numerically measured during the time-simulation.

The studied eigenmodes $\boldsymbol{\phi}_j$ are those of the assembled blade/hub. Those modes were computed for a linear model in chapter 3, with the assumption of exact interface perfect bonding. In the present chapter, the hub is assumed to be infinitely stiff. Consequently, the studied modes correspond to the blade eigenmodes with attached interface.

In [25] a reduction method for nonloinear problem structure dynamics problem is proposed. This method rely on use of the proper orthogonal decomposition (POD) [26] and allows to approximate the overall global response of a model fom a statistical point of view. Others applications of the POD methods for nonlinear problem can be found for metal forming in [27] or for problems with parameters variations [28]. In [29], the PGD method devellopped by [30] is used to solve contact-friction problems. This method searches the solution in a separable form reducing the computation cost.

In [31], Kim *et al.* proposed a reduction method based on the use of the assembled structure eigenmodes. In the present context this method seems convenient since the structure assembled eigennmodes can be easily computed thanks to the reduction method proposed in chapter 3. Whereas this method can be used to reduce non-smooth nonlinear problem and is applied on the Coulomb friction problem, it has not been tested on large finite element model. In [31] this method brings accurate results but is used to solve a friction problem with few hundreds of DoF only.

The use of nonlinear normal modes (NNM) [32] has been investigated for the reduction in [33]. An extension of the Craig-Bampton method using fixed interface nonlinear modes has been studied by Apiwattanalunggarn in [34]. More recently, an approach for the construction of nonlinear reduced order model in the frame of dynamic substructuring has been proposed by Kuether and Allen in [35]. This last approach has been applied on a finite element model carrying about ten thousand of DoF with large displacement nonlinearities.

In 2013, the reduction of the contact-friction problem has been tackled thanks to fuzzy logic based methods in [36]. This methods is referred to as the FL2C (Fuzzy Logic

Controller for frictional Contact) and used to solve the contact-friction problem. In the next sections, a reduction method for time simulation with contact-friction nonlinearities is proposed.

4.5.1 Motivations

The most time consuming operation of algorithm 4.4.3 is located in the "Evolution" function. More specifically, the "Computation of the acceleration $\ddot{\boldsymbol{u}}_n$" step is by far responsible of this slowness. This is due to the inversion of the mass matrix M (see Eq. (4.1)) in the physical space. The reduction is then targeted in order to speed up this operation.

Time simulation algorithm with model reduction

The convergence of algorithm 4.4.3 relies on the bipotential augmentation, thus a particular attention is given to the precision of this operation. As a consequence, the proposed method updates the contact-friction force $\boldsymbol{p}$ in the nodal (HFM) space.

Hence, in the frame of the contact-friction algorithm 4.4.3, the model reduction is targeted for the evaluation of the central difference scheme only. Thus, starting from the displacement $\boldsymbol{u}_n$ and force $\boldsymbol{p}_n$ the computation of these variables at t_{n+1} is made with respect to the procedure given in Fig. 4.17.

The construction of the reduction (that spans the reduced space) is detailed in sections 4.5.2 and 4.5.3. Note that the algorithm presented in Fig. 4.17 includes an enrichment of the reduction basis. This step is referred here to as an "on-line enrichment" and will be highlighted in section 4.5.4.

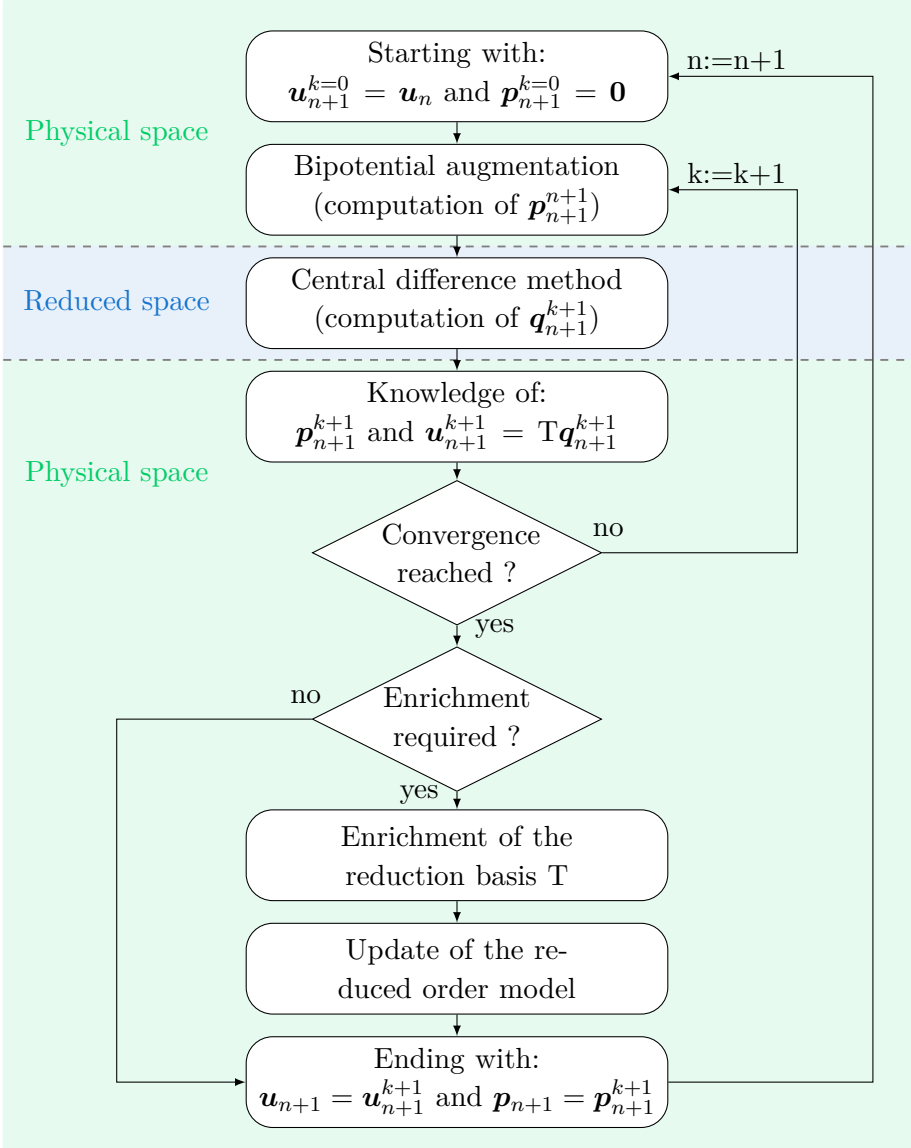

Figure 4.17 – Implementation of the proposed reduction method in the contact-friction resolution algorithm. The central difference scheme is evaluated in the reduced space, involving ROM.

Let us give a brief overview of the practical implementation of the procedure described in Fig. 4.17. The reduction basis T is now an input of the algorithm. The enrichment T is made after the convergence of the contact-friction force $\boldsymbol{p}_{n+1}$ and is described in section 4.5.4.

Algorithm 4.5.1: Central difference algorithm for the contact-friction problem

input : M, K, C, T, $\boldsymbol{u}_0$, $\dot{\boldsymbol{u}}_0$, $n = 0$

Model reduction

$\tilde{\mathrm{M}} = \mathrm{T}^\top \mathrm{M}\mathrm{T} \quad \tilde{\mathrm{C}} = \mathrm{T}^\top \mathrm{C}\mathrm{T} \quad \tilde{\mathrm{K}} = \mathrm{T}^\top \mathrm{K}\mathrm{T} \quad \boldsymbol{q}_0 = \mathrm{T}^\top \boldsymbol{u}_0 \quad \dot{\boldsymbol{q}}_0 = \mathrm{T}^\top \dot{\boldsymbol{u}}_0$

Initial acceleration computation $\ddot{\boldsymbol{q}}_0$

$\ddot{\boldsymbol{q}}_0 = \mathrm{M}^{-1}\left(\boldsymbol{f}_0 - \mathrm{C}\dot{\boldsymbol{q}}_0 - \mathrm{K}\boldsymbol{q}_0\right)$; *Eq. (4.1)*

Prediction of the velocity at $t_{\frac{1}{2}}$

$\dot{\boldsymbol{q}}_{n+\frac{1}{2}} = \dot{\boldsymbol{q}}_{\frac{1}{2}} = \dot{\boldsymbol{q}}_0 + \frac{1}{2}h\ddot{\boldsymbol{q}}_0$; $(+\frac{1}{2}h\ddot{\boldsymbol{q}}_1 = \boldsymbol{0})$ *Eq. (4.33)*

While end time of the simulation t_f is not reached

while $t_n < t_f$ **do**

Time incrementation to t_{n+1}

$t_{n+1} = t_n + h$;

First iteration on the contact-friction force $\boldsymbol{p}_n$

$\boldsymbol{p}_n^{k=0} = \boldsymbol{0}$; *Initialisation of $\boldsymbol{p}_n$*

$\left[\ddot{\boldsymbol{q}}_n^1, \dot{\boldsymbol{q}}_{n+\frac{1}{2}}^1, \boldsymbol{q}_{n+1}^1, \boldsymbol{p}_n^1\right] :=$ Evolution $\left(\dot{\boldsymbol{q}}_{n-\frac{1}{2}}, \boldsymbol{q}_n, \boldsymbol{p}_n^{k=0}\right)$;

While the value of $\boldsymbol{p}_n$ has not converged Eq. (4.35)

while $\|\boldsymbol{p}_n^{k+1} - \boldsymbol{p}_n^k\| > \varepsilon_{\boldsymbol{p}}$ **do**

Iteration on the contact-friction force $\boldsymbol{p}_n$

$k := k + 1$;

$\left[\ddot{\boldsymbol{q}}_n^{k+1}, \dot{\boldsymbol{q}}_{n+\frac{1}{2}}^{k+1}, \boldsymbol{q}_{n+1}^{k+1}, \boldsymbol{p}_n^{k+1}\right] :=$ Evolution $\left(\dot{\boldsymbol{q}}_{n-\frac{1}{2}}, \boldsymbol{q}_n, \boldsymbol{p}_n^k\right)$;

end

Save the converged solutions and reset k

$\ddot{\boldsymbol{q}}_n = \ddot{\boldsymbol{q}}_n^{k+1} \quad \dot{\boldsymbol{q}}_{n+\frac{1}{2}} = \dot{\boldsymbol{q}}_{n+\frac{1}{2}}^{k+1} \quad \boldsymbol{q}_{n+1} = \boldsymbol{q}_{n+1}^{k+1} \quad k = 0$;

Model enrichment (highlighted in section 4.5.4)

$\left[\tilde{\mathrm{M}}, \tilde{\mathrm{C}}, \tilde{\mathrm{K}}, \mathrm{T}, \ddot{\boldsymbol{q}}_n, \dot{\boldsymbol{q}}_{n+\frac{1}{2}}, \boldsymbol{q}_{n+1}\right] := \ldots$

OnLineEnrichment $\left(\tilde{\mathrm{M}}, \tilde{\mathrm{C}}, \tilde{\mathrm{K}}, \mathrm{T}, \ddot{\boldsymbol{q}}_n, \dot{\boldsymbol{q}}_{n-\frac{1}{2}}, \dot{\boldsymbol{q}}_{n+\frac{1}{2}}, \boldsymbol{q}_{n+1}, \boldsymbol{p}_{n+1}\right)$;

Time index incrementation

$n = n + 1$;

end

The function "Evolution" is also impacted by the use of the reduction. The modified "Evolution" function is given below.

Function Evolution($\dot{\boldsymbol{q}}_{n-\frac{1}{2}}, \boldsymbol{q}_n, \boldsymbol{p}_n^k$)

output: $\ddot{\boldsymbol{q}}_n, \dot{\boldsymbol{q}}_{n+\frac{1}{2}}, \boldsymbol{q}_{n+1}, \boldsymbol{p}_n^{k+1}$

Computation of the reduced acceleration $\ddot{\boldsymbol{q}}_n$

$$\ddot{\boldsymbol{q}}_n = \tilde{\mathrm{M}}^{-1}\left(\tilde{\boldsymbol{f}}_n + \mathrm{T}^\top \boldsymbol{p}_n^k - \tilde{\mathrm{C}}\dot{\boldsymbol{q}}_{n-\frac{1}{2}} - \tilde{\mathrm{K}}\boldsymbol{q}_n\right) ; \qquad \textit{Eq. (4.1)}$$

Estimation of the reduced velocity at $t_{n+\frac{1}{2}}$

$$\dot{\boldsymbol{q}}_{n+\frac{1}{2}} = \dot{\boldsymbol{q}}_{n-\frac{1}{2}} + h\ddot{\boldsymbol{q}}_n ; \qquad \textit{Eq. (4.32)}$$

Estimation of the position at t_{n+1}

$$\boldsymbol{q}_{n+1} = \boldsymbol{q}_n + h\dot{\boldsymbol{q}}_{n+\frac{1}{2}} ; \qquad \textit{Eq. (4.31)}$$

Lagrangian augmentation

$$\boldsymbol{p}_n^{k+1} = \mathrm{BipotentialAugmentation}\left(\mathrm{T}\dot{\boldsymbol{q}}_{n+\frac{1}{2}}, \mathrm{T}\boldsymbol{q}_{n+1}, \boldsymbol{p}_n^k\right); \qquad \textit{Eq. (4.34)}$$

Note that the practical implementation of the function "Evolution", the operation "BipotentialAugmentation" could be simplified. Indeed, in "Evolution" the input variables are defined on the whole system DoF while their restriction on the interface is sufficient for the bipotential augmentation.

Eventually, let us define briefly some DoF partitions that are helpful for the comprehension of the further reduction methodology. The whole degrees of freedom of the blade can be split into interior i, interface and force f DoF. The interface DoF are located on the contact interface Γ and undergo the contact-friction force $\boldsymbol{p}$. The force DoF refers to the DoF undergoing the external load $\boldsymbol{f}$. The interior partition i contains all the remaining DoF. The blade's DoF are sorted so that its displacement $\boldsymbol{u}$ can be decomposed as:

$$\boldsymbol{u} = \begin{bmatrix} \boldsymbol{u}_i \\ \boldsymbol{u}_\Gamma \\ \boldsymbol{u}_f \end{bmatrix} \tag{4.36}$$

In the next section, the hub is assumed to be infinitely stiff, thus, it has no motions and the DoF $\boldsymbol{u}$ corresponds to displacement of the blade only.

Features of the proposed reduction method

The Craig-Bampton method could be used for the reduction of the current contact-friction problem in algorithm 4.5.1. Indeed, this method involves the studied modes $\boldsymbol{\phi}_j$ since their interface are tied. In spite of this, the Craig-Bampton is not suited here due to the numerous DoF of the model interface. The use of this method would indeed produce large ROM.

An alternative to the Craig-Bampton method could be to use a small but inaccurate reduction basis that would be enriched during the time simulation. This last approach is referred here to as on-line enrichment. At first sight, on-line enrichment seems interesting as it allows to start the time simulation with compact ROM. Moreover, this approach enables to build reduction basis with high usefulness elements since the enrichment of the ROM is performed with regards to its error. However, such an enrichment requires the inversion of the system stiffness (see "Enrichment using harmonic solutions" in 3.1.3). Such an inversion has a high time cost and should therefore be avoided.

The method proposed in this section relies on the build a compact family of static responses Θ of the blade considering different interface loads. The construction of this basis is presented in section 4.5.2.

The numerous interface DoF of the blade prevent the use of a nodal basis for the description of the interface loads, otherwise Θ would be large. In order to bypass this issue, a method for the reduction of the interface DoF is proposed in section 4.5.3. More precisely, the proposed method involves a few static responses built from the combination of Θ. This combination is performed thanks to an estimation of the most significant contact-friction force before the simulation. In practice, for each studied mode $\boldsymbol{\phi}_j$, a compact reduction basis T_j is proposed.

Each proposed basis T_j is expected to be both accurate and compact. In order to make sure that the proposed reduction methodology is accurate, an on-line enrichment is implemented (see function "OnLineEnrichment"). Note that this static enrichment is performed when inaccuracy are detected and is expected to be seldom necessary. This enrichment is carried out by a function referred to as "OnLineEnrichment", detailed in section 4.5.4.

Therefore, the proposed method tries to provide a compact ROM whose on-line enrichment would be rarely needed. In summary, the reduction methodology for the evaluation of the damping associated to the mode $\boldsymbol{\phi}_j$ has three main steps:

- **a first off-line step:** (see section 4.5.2) computation of the static responses Θ for normal and tangent nodal solicitation of the interface.
- **a second off-line step:** (see section 4.5.3) combinations of the static and dynamic response with regards to the expected interface load $\boldsymbol{p}$. Construction of a reduction basis T_j for each studied mode $\boldsymbol{\phi}_j$.
- **an on-line step:** (see section 4.5.4) enrichment of the reduction basis T_j during the simulation, while studying the mode $\boldsymbol{\phi}_j$. This step is only performed when inaccuracy is detected and is expected to be seldom necessary.

Reduction of the internal DoF and external load representation

The proposed reduction method uses the eigenmodes ϕ_j of the system computed with the linear model for the description of the interior and force DoF. This is indeed convenient since a method for the computation of these modes has already been developed and validated in chapter 3. Moreover, since the modes ϕ_j are studied, thus their involvement in the reduction basis T_j seems pertinent.

The interface DoF of the modes ϕ_j are perfectly tied and no detachment or sliding are allowed. Indeed, in this chapter, the hub is assumed to be infinitely stiff, consequently, the modes Φ of the system with tied (no displacements) interface and force DoF:

$$\Phi = \begin{bmatrix} \boldsymbol{\phi}_1 & \boldsymbol{\phi}_2 & \dots \end{bmatrix} = \begin{bmatrix} \Psi_i \\ 0_\Gamma \\ 0_f \end{bmatrix} \quad \text{with} \quad \Big(-\Lambda_i \mathrm{M}_{ii} + \mathrm{K}_{ii} \Big) \Psi_i = 0. \tag{4.37}$$

Let $\boldsymbol{u}_{\text{pl.}}$ and $\boldsymbol{f}_{\text{pl.}}$ denote the displacement and contact-friction force when the blade is loaded. These vectors correspond to the initial position and the external supported load of the blade during the simulation. However, the reduction of the internal DoF using eigenmodes with bonded interface ($\boldsymbol{\phi}_j$) only is not sufficient to recover $\boldsymbol{u}_{\text{pl.}}$. In order to bypass this issue, $\boldsymbol{u}_{\text{pl.}}$ is included in the reduction basis T_j so that:

$$\mathrm{T}_j = \begin{bmatrix} \boldsymbol{\phi}_j & \boldsymbol{u}_{\text{pl.}} \end{bmatrix} \quad \text{with} \quad \mathrm{K}\boldsymbol{u}_{\text{pl.}} = \boldsymbol{f}_{\text{pl.}} + \boldsymbol{p}_{\text{pl.}}. \tag{4.38}$$

At this step, the reduction basis T_j is quite compact since it has only two vectors. Nevertheless, this basis T_j is not able to describe the interface motions, the next sections tackle this issue.

4.5.2 First off-line step: computation of static responses to interface loads

In order to describe the interface motions it is possible to enrich the reduction basis T_j (see Eq. (4.38)) with static responses Θ (see "Enrichment using harmonic solutions" in section 3.1.3) when unitary nodal loads are applied on the interface Γ. Whereas the contact-friction $\boldsymbol{p}$ force are computed with a high precision level in the nodal domain, the acceleration $\ddot{\boldsymbol{q}}$ (see operation "Computation of the acceleration $\ddot{\boldsymbol{u}}_n$") is performed in the reduced space. Thus, it is important that the reduction basis T_j can accurately describe how the force $\boldsymbol{p}$ impacts the acceleration $\ddot{\boldsymbol{q}}$. Static responses of the structures can bring such an information since they correspond to the structure displacement when undergoing a particular load. Therefore, such responses are used in the present method, they are computed for unitary loads applied on the interface Γ so that:

$$\Theta = \mathrm{K}^{-1} \begin{bmatrix} 0_i \\ \mathrm{I}_\Gamma \\ 0_f \end{bmatrix}. \tag{4.39}$$

In order to get the responses of the structure when undergoing unitary normal and tangential force on its interface, the vectors Θ are combined. Practically, these combinations lead to two set of vectors ($\Theta_{\vec{n}}$ and $\Theta_{\vec{t}}$) that are defined as follows:

$$\Theta_{\vec{n}} = \Theta \times \mathrm{diag}\Big(\begin{bmatrix} \vec{\boldsymbol{n}}_1{}^\top & \vec{\boldsymbol{n}}_2{}^\top & \dots & \vec{\boldsymbol{n}}_{n_\Gamma}{}^\top \end{bmatrix} \Big), \tag{4.40}$$

$$\Theta_{\vec{t}} = \Theta \times \mathrm{diag}\Big(\begin{bmatrix} \vec{\boldsymbol{t}}_1{}^\top & \vec{\boldsymbol{t}}_2{}^\top & \dots & \vec{\boldsymbol{t}}_{n_\Gamma}{}^\top \end{bmatrix} \Big). \tag{4.41}$$

4.5.3 Second off-line step: combination of the dynamic responses

Static responses ($\Theta_{\vec{n}}$ and $\Theta_{\vec{t}}$) have been computed in order to accurately represent the displacement induced by the contact-friction force. However, those responses are still numerous and their direct use would lead to large reduced order model. In order to increase the compactness of these ROM, a recombination of these vectors is proposed. This recombination is the central contribution of this work and is based on a prediction of the nodes which are most likely to slide and detach.

At the end of the preload simulation (see Fig. 4.13), the position of the blade corresponds to $\boldsymbol{u}_{\text{pl.}}$ while it undergoes the load $\boldsymbol{f}_{\text{pl.}}$. In such a state, the dynamic equation of the blade can be simply written as:

$$\mathrm{K}\boldsymbol{u}_{\text{pl.}} = \boldsymbol{f}_{\text{pl.}} + \boldsymbol{p}_{\text{pl.}}. \tag{4.42}$$

Note that this computation of the blade preload can be made thanks to algorithm 4.4.3 presented in section 4.4.3. During the time simulation the rise of the preload force is already completed and then $\boldsymbol{f}_{\text{pl.}}$ is constant. Let us assume that displacement brought to the contact and friction force are small in regard to oscillation of the structure around the studied mode $\boldsymbol{\phi}_j$. Under such an assumption, the displacement $\boldsymbol{u}$ can be approximated as the sum of the initial position $\boldsymbol{u}_{\text{pl.}}$ with the modal shape $\boldsymbol{\phi}_j q$. Hence, the dynamic equation of the blade can be written as:

$$\mathrm{M}\ddot{\boldsymbol{u}} + \mathrm{K}\boldsymbol{u} = \boldsymbol{f}_{\text{pl.}} + \boldsymbol{p} \quad \text{with} \quad \boldsymbol{u} \simeq \boldsymbol{u}_{\text{pl.}} + \boldsymbol{\phi}_j q. \tag{4.43}$$

Thanks to Eq. (4.42), the previous equation (Eq. (4.43)) can be rewritten as:

$$\mathrm{M}\boldsymbol{\phi}_j \ddot{q} + \mathrm{K}\boldsymbol{\phi}_j q \simeq \boldsymbol{p} - \boldsymbol{p}_{\text{pl.}} = \boldsymbol{r}. \tag{4.44}$$

The term $\boldsymbol{r}$ refers to a contact-friction force brought by the system oscillations. In this work, this force $\boldsymbol{r}$ is used to predict the interface state (stuck, sliding, contact or detachment) during the simulation. Under the assumption of sinusoidal displacements around the equilibrium position $\boldsymbol{u}_{\text{pl.}}$, the position and acceleration coordinates q and $\ddot{q}$ can be written as:

$$q = \alpha \cos(\omega_j t) \quad \text{and} \quad \ddot{q} = -\alpha \omega_j^2 \cos(\omega_j t). \tag{4.45}$$

Where ω_j corresponds to the natural frequency associated to $\boldsymbol{\phi}_j$. When the simulation for the evaluation of the damping starts, the blade's position corresponds to $\boldsymbol{u}_{\text{pl.}} + \alpha\boldsymbol{\phi}_j$.

During this simulation, the blade is expected to oscillate around its initial position $\boldsymbol{u}_{\text{pl.}}$ and to lose energy, consequently, the norm $\|\alpha\|$ is expected to decrease. Starting from Eq. (4.44), the forces $\boldsymbol{p}$ and $\boldsymbol{r}$ can be approximated as:

$$\boldsymbol{p} \simeq \mathrm{M}\boldsymbol{\phi}_j\ddot{q} + \mathrm{K}\boldsymbol{\phi}_j q + \boldsymbol{p}_{\text{pl.}} = \alpha(-\omega_j^2\mathrm{M} + \mathrm{K})\cos(\omega_j t)\boldsymbol{\phi}_j + \boldsymbol{p}_{\text{pl.}} \tag{4.46}$$

$$\text{thus: } \boldsymbol{r} \simeq \alpha(-\omega_j^2\mathrm{M} + \mathrm{K})\cos(\omega_j t)\boldsymbol{\phi}_j. \tag{4.47}$$

The contact-friction force $\boldsymbol{p}$ is expected to be maximal when the blade amplitude α is maximal. Let us study the force $\boldsymbol{r}$ in such a critical case. When facing the maximal amplitude of the blade's oscillation, the cosine term can be either equal to ± 1. This leads to the definition of two different critical contact-friction force denoted $\boldsymbol{r}_+$ and $\boldsymbol{r}_-$:

$$\boldsymbol{r}_+ = \alpha(-\omega_j^2\mathrm{M} + \mathrm{K})\boldsymbol{\phi}_j \quad \text{or} \quad \boldsymbol{r}_- = -\alpha(-\omega_j^2\mathrm{M} + \mathrm{K})\boldsymbol{\phi}_j. \tag{4.48}$$

The prediction of the contact-friction interface state is made from those two forces $\boldsymbol{r}_+$ and $\boldsymbol{r}_-$. Indeed, the load $\boldsymbol{r}$ rules the state of the interface nodes when the blade motion correspond to $\boldsymbol{\phi}_j q$. Before the simulation, the knowledge of $\boldsymbol{r}_+$ and $\boldsymbol{r}_-$ is used to estimate where the blade's oscillation $\boldsymbol{\phi}_j q$ is likely to generate detachment and sliding.

The goal of the dynamic responses ($\Theta_{\vec{n}}$ and $\Theta_{\vec{t}}$) is to describe the interface motions like sliding or detachment. With this aim, let us extract and study the normal and tangential contributions ($\boldsymbol{r}_{\vec{n}^+}$, $\boldsymbol{r}_{\vec{n}^-}$ and $\boldsymbol{r}_{\vec{t}}$) of the residual force $\boldsymbol{r}_+$ and $\boldsymbol{r}_-$ on the interface so that:

$$\boldsymbol{r}_{\vec{n}^+} = \begin{bmatrix} \boldsymbol{r}^1_{\vec{n}^+} \\ \boldsymbol{r}^2_{\vec{n}^+} \\ \vdots \\ \boldsymbol{r}^{n_\Gamma}_{\vec{n}^+} \end{bmatrix} = \begin{bmatrix} r^1_{\vec{n}^+}\vec{n}_1 \\ r^2_{\vec{n}^+}\vec{n}_2 \\ \vdots \\ r^{n_\Gamma}_{\vec{n}^+}\vec{n}_{n_\Gamma} \end{bmatrix} = \mathrm{B}_{\vec{n}}\boldsymbol{r}_+ \quad , \quad \boldsymbol{r}_{\vec{n}^-} = \begin{bmatrix} \boldsymbol{r}^1_{\vec{n}^-} \\ \boldsymbol{r}^2_{\vec{n}^-} \\ \vdots \\ \boldsymbol{r}^{n_\Gamma}_{\vec{n}^-} \end{bmatrix} = \begin{bmatrix} r^1_{\vec{n}^-}\vec{n}_1 \\ r^2_{\vec{n}^-}\vec{n}_2 \\ \vdots \\ r^{n_\Gamma}_{\vec{n}^-}\vec{n}_{n_\Gamma} \end{bmatrix} = \mathrm{B}_{\vec{n}}\boldsymbol{r}_-$$

$$\text{and} \quad \boldsymbol{r}_{\vec{t}} = \begin{bmatrix} \boldsymbol{r}^1_{\vec{t}} \\ \boldsymbol{r}^2_{\vec{t}} \\ \vdots \\ \boldsymbol{r}^{n_\Gamma}_{\vec{t}} \end{bmatrix} = \begin{bmatrix} r^1_{\vec{t}}\vec{t}_1 \\ r^2_{\vec{t}}\vec{t}_2 \\ \vdots \\ r^{n_\Gamma}_{\vec{t}}\vec{t}_{n_\Gamma} \end{bmatrix} = \mathrm{B}_{\vec{t}}\boldsymbol{r}_+.$$

In order to find the nodes on which sliding and detachment are most likely to occur the normal and tangential contributions ($\boldsymbol{r}_{\vec{n}^+}$, $\boldsymbol{r}_{\vec{n}^-}$ and $\boldsymbol{r}_{\vec{t}}$) are sorted by increasing values.

The detachment is expected to occur for large normal force $\boldsymbol{r}^+_{\vec{n}}$ and $\boldsymbol{r}^-_{\vec{n}}$. The sliding occurs when no detachment is detected and for large tangential forces. Hence sliding is expected for large tangential term $\|r_{\vec{t}}\|$ and small or negative normal terms contributions. Since the blade oscillate, the amplitudes and sign of $\boldsymbol{r}^+_{\vec{n}}$ and $\boldsymbol{r}^-_{\vec{n}}$ is expected to change during the time simulation. Consequently, the largest normal terms will become the smallest one after half an oscillation of the blade. From this, we deduce that the sliding is likely to occur where both normal and tangential amplitudes are large. The sliding is then expected for high values of $\|r_{\vec{t}}\| \times r_{\vec{n}^+}$ and $\|r_{\vec{t}}\| \times r_{\vec{n}^-}$.

The normalized cumulated sums of the variables $r_{\vec{n}+}$, $r_{\vec{n}-}$, $\|r_{\vec{t}}\| \times r_{\vec{n}+}$ and $\|r_{\vec{t}}\| \times r_{\vec{n}-}$ are plotted in Fig. 4.18. Such sums can be seen as integrals. The cumulated sums shown in Fig. 4.18 are used to regroup the studied variables into several set. The first set contains the indices i^{α} of the node whose normalized integral correspond to $\alpha\%$. The second set contains the indices i^{β} of the nodes that allow to recover $\beta\%$ of the remaining integral.

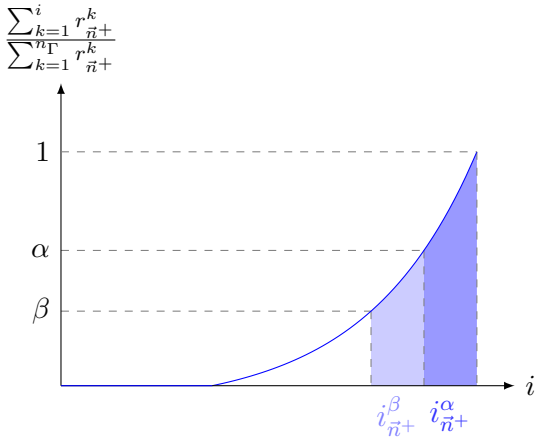

(a) Definition of the node sets $i^{\alpha}_{\vec{n}+}$ and $i^{\beta}_{\vec{n}+}$ associated to the amplitudes $r_{\vec{n}+}$.

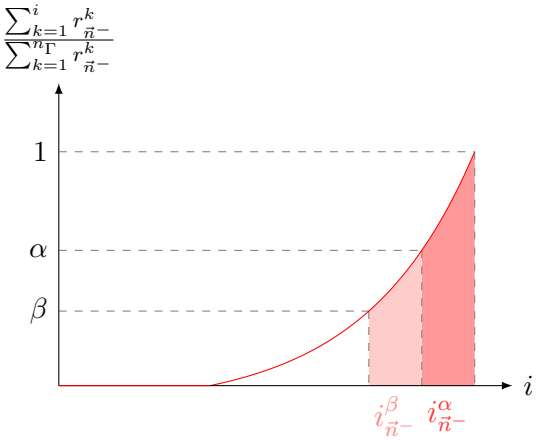

(b) Definition of the node sets $i^{\alpha}_{\vec{n}-}$ and $i^{\beta}_{\vec{n}-}$ associated to the amplitudes $r_{\vec{n}-}$.

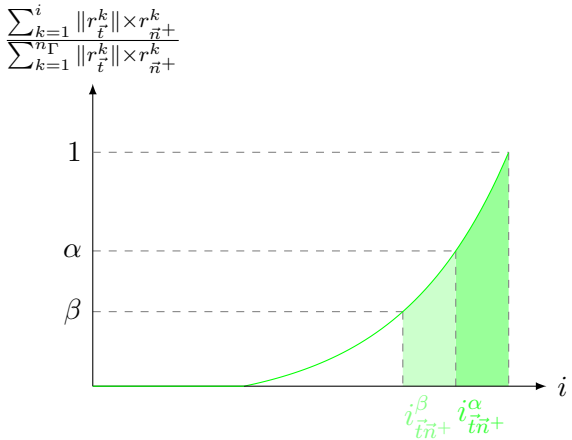

(c) Definition of the node sets $i^{\alpha}_{\vec{t}\vec{n}+}$ and $i^{\beta}_{\vec{t}\vec{n}+}$ associated to the amplitudes $r_{\vec{t}}$.

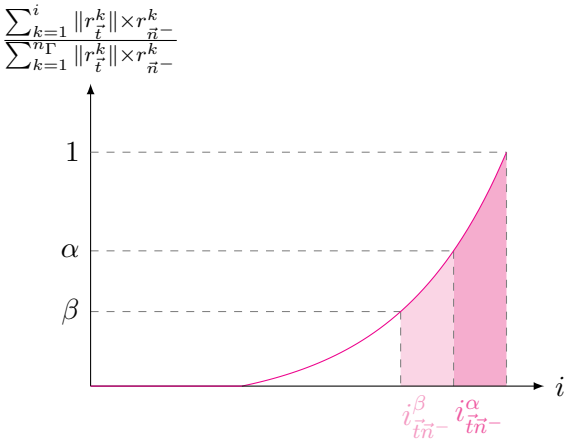

(d) Definition of the node sets $i^{\alpha}_{\vec{t}\vec{n}-}$ and $i^{\beta}_{\vec{t}\vec{n}-}$ associated to the amplitudes $r_{\vec{t}}$.

Figure 4.18 – Representation of the normalized cumulated sums of the different sorted amplitudes.

For each variable ($r_{\vec{n}+}$, $r_{\vec{n}-}$, $\|r_{\vec{t}}\| \times r_{\vec{n}+}$ and $\|r_{\vec{t}}\| \times r_{\vec{n}-}$), a node set i^{α} and i^{β} is defined. Note that more sets can be defined if needed. These node sets are used to determine the indices of the static responses that have to be combined. Hence, considering two node sets for each kind of amplitude, the reduction basis T_j (in Eq. (4.38)) is enriched with 8

vectors: 4 variables × 2 node sets:

$$\boldsymbol{\theta}^{\alpha}_{\vec{n}+} = \Theta_{\vec{n}} \times \boldsymbol{r}|_{i^{\alpha}_{\vec{n}+}}$$
$$\boldsymbol{\theta}^{\alpha}_{\vec{n}-} = \Theta_{\vec{n}} \times \boldsymbol{r}|_{i^{\alpha}_{\vec{n}-}}$$

$$\boldsymbol{\theta}^{\alpha}_{\vec{t}\vec{n}+} = \Theta_{\vec{n}} \times \boldsymbol{r}|_{i^{\alpha}_{\vec{t}\vec{n}+}}$$
$$\boldsymbol{\theta}^{\alpha}_{\vec{t}\vec{n}-} = \Theta_{\vec{n}} \times \boldsymbol{r}|_{i^{\alpha}_{\vec{t}\vec{n}-}}$$

$$\boldsymbol{\theta}^{\beta}_{\vec{n}+} = \Theta_{\vec{n}} \times \boldsymbol{r}|_{i^{\beta}_{\vec{n}+}}$$
$$\boldsymbol{\theta}^{\beta}_{\vec{n}-} = \Theta_{\vec{n}} \times \boldsymbol{r}|_{i^{\beta}_{\vec{n}-}}$$

$$\boldsymbol{\theta}^{\beta}_{\vec{t}\vec{n}+} = \Theta_{\vec{n}} \times \boldsymbol{r}|_{i^{\beta}_{\vec{t}\vec{n}+}}$$
$$\boldsymbol{\theta}^{\beta}_{\vec{t}\vec{n}-} = \Theta_{\vec{n}} \times \boldsymbol{r}|_{i^{\beta}_{\vec{t}\vec{n}-}}$$

For each amplitude and studied mode $\boldsymbol{\phi}_j$, different node sets i^{α} and i^{β} have to be computed. The reduction basis T_j used for the time simulation of the blade when studying the damping associated to the mode $\boldsymbol{\phi}_j$ uses the eight combined vectors as follows:

$$\mathrm{T}_j = \left[\boldsymbol{\phi}_j \;\; \boldsymbol{u}_{\text{pl.}} \;\; \boldsymbol{\theta}^{\alpha}_{\vec{n}+} \;\; \boldsymbol{\theta}^{\alpha}_{\vec{n}-} \;\; \boldsymbol{\theta}^{\alpha}_{\vec{t}\vec{n}+} \;\; \boldsymbol{\theta}^{\alpha}_{\vec{t}\vec{n}-} \;\; \boldsymbol{\theta}^{\beta}_{\vec{n}+} \;\; \boldsymbol{\theta}^{\beta}_{\vec{n}-} \;\; \boldsymbol{\theta}^{\beta}_{\vec{t}\vec{n}+} \;\; \boldsymbol{\theta}^{\beta}_{\vec{t}\vec{n}-} \;\; \right]. \tag{4.49}$$

In this presentation, the reduction basis has been enriched using two node sets i^{α} and i^{β}. It is however possible to use more sets, we expect that the more sets we use, the more the reduced order model is precise. Theoretically, in order to get very accurate results, the integral slices (see Fig. 4.18) should be as tight as possible.

4.5.4 On-line step: enrichment of the reduced order model

In the previous section, a method has been presented for the combination of dynamic responses in order to build compact reduction basis. Although the basis T_j (see Eq. (4.49)) proposed for the study of the mode $\boldsymbol{\phi}_j$ is expected to be accurate, an on-line enrichment procedure is added in the simulation algorithm.

The on-line enrichment step (function "OnLineEnrichment") occurs after the convergence of the contact-friction force $\boldsymbol{p}_n$ in 4.5.1. The enrichment is done here thanks to the use of static response (see Eq. (3.11)) computed from the dynamic residue $\boldsymbol{r}_{n+1}$:

$$\boldsymbol{r}_{n+1} = \mathrm{T}\Big(\tilde{\mathrm{M}}\ddot{\boldsymbol{q}}_{n+1} + \tilde{\mathrm{C}}\dot{\boldsymbol{q}}_{n+1} + \tilde{\mathrm{K}}\boldsymbol{q}_{n+1} - \tilde{\boldsymbol{f}}_{n+1}\Big) - \boldsymbol{p}_{n+1}. \tag{4.50}$$

Note that the acceleration $\ddot{\boldsymbol{u}}_{n+1}$ is only known at $n+2$. In order to bypass this issue and to evaluate the residue $\boldsymbol{r}_{n+1}$ (see Eq. (4.51)), the acceleration $\ddot{\boldsymbol{u}}_{n+1}$ is approximated as $\ddot{\boldsymbol{u}}_n$ during the enrichment procedure. Thus, the residue $\boldsymbol{r}_{n+1}$ is computed as

$$\boldsymbol{r}_{n+1} = \mathrm{T}\Big(\tilde{\mathrm{M}}\ddot{\boldsymbol{q}}_{n} + \tilde{\mathrm{C}}\dot{\boldsymbol{q}}_{n+1} + \tilde{\mathrm{K}}\boldsymbol{q}_{n+1} - \tilde{\boldsymbol{f}}_{n+1}\Big) - \boldsymbol{p}_{n+1}. \tag{4.51}$$

In practice, the enrichment becomes necessary when the residual load $\boldsymbol{r}_{n+1}$ is no more negligible compared to the external load $\boldsymbol{f}_{n+1}$ (here it corresponds to $\boldsymbol{f}_{\text{pl.}}$). Practically the enrichment procedure is started thanks to the use of a threshold ε, when:

$$\|\boldsymbol{r}_{n+1}\| > \varepsilon \|\boldsymbol{f}_{n+1}\|. \tag{4.52}$$

Function OnLineEnrichment($\tilde{\mathrm{M}}, \tilde{\mathrm{C}}, \tilde{\mathrm{K}}, \mathrm{T}, \ddot{\boldsymbol{q}}_n, \dot{\boldsymbol{q}}_{n-\frac{1}{2}}, \dot{\boldsymbol{q}}_{n+\frac{1}{2}}, \boldsymbol{q}_{n+1}, \boldsymbol{p}_{n+1}$)

output: $\tilde{\mathrm{M}}, \tilde{\mathrm{C}}, \tilde{\mathrm{K}}, \mathrm{T}, \ddot{\boldsymbol{q}}_n, \dot{\boldsymbol{q}}_{n+\frac{1}{2}}, \boldsymbol{q}_{n+1}$

Computation of the dynamic residue $\boldsymbol{r}_{n+1}$

$\boldsymbol{r}_{n+1} = \mathrm{T}\Big(\tilde{\mathrm{M}}\ddot{\boldsymbol{q}}_n + \frac{1}{2}\tilde{\mathrm{C}}(\dot{\boldsymbol{q}}_{n-\frac{1}{2}} + \dot{\boldsymbol{q}}_{n+\frac{1}{2}}) + \tilde{\mathrm{K}}\boldsymbol{q}_{n+1} - \tilde{\boldsymbol{f}}_{n+1}\Big) - \boldsymbol{p}_{n+1}$; *Eq. (4.51)*

If the residual load $\boldsymbol{r}_{n+1}$ is not negligible, then the model enrichment is performed

if $\|\boldsymbol{r}_{n+1}\| > \varepsilon \|\boldsymbol{f}_{n+1}\|$ **then**

Model enrichment

$\mathrm{T} := \begin{bmatrix} \mathrm{T} & \mathrm{K}^{-1}\boldsymbol{r}_{n+1} \end{bmatrix}$

Reduced order model update

$\tilde{\mathrm{M}} := \mathrm{T}^\top \mathrm{M}\mathrm{T} \quad \tilde{\mathrm{C}} := \mathrm{T}^\top \mathrm{C}\mathrm{T} \quad \tilde{\mathrm{K}} := \mathrm{T}^\top \mathrm{K}\mathrm{T};$

$\ddot{\boldsymbol{q}}_n := \begin{bmatrix} \ddot{\boldsymbol{q}}_n \\ 0 \end{bmatrix} \quad \dot{\boldsymbol{q}}_{n+\frac{1}{2}} := \begin{bmatrix} \dot{\boldsymbol{q}}_{n+\frac{1}{2}} \\ 0 \end{bmatrix} \quad \boldsymbol{q}_{n+1} := \begin{bmatrix} \boldsymbol{q}_{n+1} \\ 0 \end{bmatrix}$

end

Chapter conclusion

In the present chapter, bibliography of the contact-friction modelling and its resolution have been presented. Different formulations of the Signorini-Coulomb laws (see section 4.1) have been reminded and highlighted in section 4.2. The adopted formulation is referred to as the bipotential formulation and is classified as augmented Lagrangian formulation.

The resolution of the contact-friction problem in the time domain is studied in section 4.4. The central difference method and Uzawa iteration are conjointly used to solve the problem. The implementation of this method is given by algorithm 4.4.3. Eventually, this algorithm has been applied (section 4.4.3) to compute the response of the blade when undergoing the preload with the assumption of rigid hub.

In the last section, ideas for the reduction of the system in the frame of time simulation for the computation of the mode damping have been proposed. The proposed method relies on a combination of static responses in order to provide compact reduced order model. The proposed method consider the model enrichment during the simulation but has not been tested already. The application and improvement of this method is one of the main perspectives of the present work.

Bibliography

[1] F. Kuss, *Méthodes duales pour les problèmes de contact avec frottement.* PhD thesis, Université de Provence - Aix-Marseille I, 2008.

[2] D. J. Segalman, "A Four-Parameter Iwan Model for Lap-Type Joints," *Journal of Applied Mechanics*, vol. 72, no. 5, pp. 752–760, 2002.

[3] F. Renaud, *Etude de l'incidence des comportements dissipatifs dans les instabilités vibratoires des systèmes de freinage.* PhD thesis, Ecole Centrale Paris, 2011.

[4] C. Hammami, *Intégration de modèles de jonctions dissipatives dans la conception vibratoire de structures amorties.* PhD thesis, Ecole National Supérieure des Arts et Métiers - ENSAM, 2014.

[5] C. Duriez, *Contact frottant entre objets déformables dans des simulations temps-réel avec retour haptique.* PhD thesis, Université d'Evry, 2004.

[6] H. Festjens, G. Chevallier, and J.-L. Dion, "Nonlinear model order reduction of jointed structures for dynamic analysis," *Journal of Sound and Vibration*, vol. 333, no. 7, pp. 2100–2113, 2014.

[7] A. Signorini, "Sopra alcune questioni di statica dei sistemi continui.," *Annali della Scuola Normale Superiore di Pisa*, no. 2, pp. 231–251, 1933.

[8] T. Belytschko, W. K. Liu, B. Moran, and K. L. Elkhodary, *Nonlinear Finite Elements for Continua and Structures.* wiley ed., 2014.

[9] C. Coulomb, "Théorie des machines simples, en ayant égard au frottement de leurs parties, et à la raideur des cordages.," *Mémoires de mathématique et de physique de l'Académie Royale*, pp. 161 – 342, 1785.

[10] V. Acary and M. Jean, "Numerical simulation of monuments by the contact dynamics method," *Monument-98, Workshop on seismic perfomance of monuments*, pp. 69–78, 1998.

[11] G. Vermot Des Roches, É. Balmès, H. Ben Dhia, R. Lemaire, and T. Pasquet, "Compatibility measure and penalized contact resolution for incompatible interfaces," *European Journal of Computational Mechanics*, vol. 19, no. 3, pp. 317–328, 2010.

[12] J. Haslinger, "Least square method for solving contact problems with friction obeying the Coulomb law," *Aplikace matematiky*, vol. 29, no. 3, pp. 212–224, 1984.

[13] P. Alart and A. Curnier, "A mixed formulation for frictional contact problems prone to Newton like solution methods," *Computer Methods in Applied Mechanics and Engineering*, vol. 92, no. 3, pp. 353–375, 1991.

[14] G. De Saxcé and Z. Q. Feng, "The bipotential method: A constructive approach to design the complete contact law with friction and improved numerical algorithms," *Mathematical and Computer Modelling*, vol. 28, no. 4-8, pp. 225–245, 1998.

[15] P. Bussetta, D. Marceau, and J.-P. Ponthot, "The adapted augmented Lagrangian method: a new method for the resolution of the mechanical frictional contact problem," *Computational Mechanics*, vol. 49, no. 2, pp. 259–275, 2012.

[16] J. C. Simo, P. Wriggers, and R. L. Taylor, "A perturbed Lagrangian formulation for the finite element solution of contact problems," *Computer Methods in Applied Mechanics and Engineering*, vol. 50, no. 2, pp. 163–180, 1985.

[17] D. Chamoret, *Modélisation du contact : nouvelles approches numériques*. PhD thesis, École centrale de Lyon, 2002.

[18] D. Chamoret, P. Saillard, A. Rassineux, and J. M. Bergheau, "New smoothing procedures in contact mechanics," *Journal of Computational and Applied Mathematics*, vol. 168, no. 1, pp. 107–116, 2004.

[19] V. Acary, F. Cadoux, C. Lemaréchal, and J. Malick, "A formulation of the linear discrete Coulomb friction problem via convex optimization," *Zeitschrift für angewandte Mathematik und Mechanik*, vol. 91, no. 2, pp. 155–175, 2011.

[20] N. Talbi, *Résolution du contact frottant entre objets déformables en temps réel et avec retour haptique*. PhD thesis, Université d'Evry-Val d'Essonne, 2008.

[21] M. Jean, "The non-smooth contact dynamics method," *Computer Methods in Applied Mechanics and Engineering*, vol. 177, no. 3-4, pp. 235–257, 1999.

[22] V. Acary and B. Brogliato, *Numerical methods for nonsmooth dynamical systems: applications in mechanics and electronics*. 2008.

[23] M. Géradin and D. J. Rixen, *Mechanical Vibrations - Theory and Application to Structural Dynamics*. wiley ed., 1997.

[24] G. Vermot des Roches, *Frequency and time simulation of squeal instabilities. Application to the design of industrial automotive brakes*. PhD thesis, Ecole Centrale Paris, 2011.

[25] P. Krysl, S. Lall, and J. E. Marsden, "Dimensional Model Reduction in Non-linear Finite Element Dynamics of Solids and Structures," *International Journal for numerical methods in engineering*, vol. 51, no. 4, pp. 479–504, 2001.

[26] R. Pinnau, "Model Reduction via Proper Orthogonal Decomposition," *Model Order Reduction: Theory, Research Aspects and Applications*, vol. 13, pp. 95–109, 2008.

[27] F. E. Haddad, D. Ryckelynck, F. cois Bay, and L. Fourment, "Model order reduction applied to metal forming," in *12e Colloque national en calcul des structures (CSMA)*, 2015.

[28] L. Peng and K. Mohseni, "Nonlinear model reduction via a locally weighted POD method," *International Journal for Numerical Methods in Engineering*, vol. 106, no. 5, pp. 372–396, 2016.

[29] A. Giacoma, D. Dureisseix, A. Gravouil, and M. Rochette, "Toward an optimal a priori reduced basis strategy for frictional contact problems with LATIN solver," *Computer Methods in Applied Mechanics and Engineering*, vol. 283, pp. 1357–1381, 2015.

[30] P. Ladevèze and L. Chamoin, "No Title," *omputer Methods in Applied Mechanics and Engineering*, vol. 200, no. 23, pp. 2032–2047, 2011.

[31] J. Kim and T. D. Burton, "Reduction of nonlinear structural models having non-smooth nonlinearity," in *SPIE proceedings series*, Society of Photo-Optical Instrumentation Engineers, 2002.

[32] G. Kerschen, M. Peeters, J. C. Golinval, and A. F. Vakakis, "Nonlinear normal modes, Part I: A useful framework for the structural dynamicist," *Mechanical Systems and Signal Processing*, vol. 23, no. 1, pp. 170–194, 2009.

[33] W. Rhee, *Linear and nonlinear model reduction in structural dynamics with application to model updating*. PhD thesis, Texas Tech University, 2000.

[34] P. Apiwattanalunggarn, *Model reduction of nonlinear structural systems using nonlinear normal modes and component mode synthesis*. PhD thesis, Michigan State University in, 2003.

[35] R. Kuether and M. Allen, "Substructuring with nonlinear reduced order models and interface reduction with characteristic constraint modes," *55th AIAA/ASMe/ASCE/AHS/SC Structures, Structural Dynamics, and Materials Conference*, p. 1518, 2014.

[36] H. Q. Do, *Reduced model and uncertainty propagation for frictional contact and friction induced vibration problems*. PhD thesis, Université de Valenciennes, 2015.

Chapter 5

Conclusions & perspectives

The present work targets the design acceleration of the SAE's open rotor downstream stage (see Fig. 1.3) thanks to model reduction methodologies. These reductions aim at accelerating the modal analysis and time simulations of a CROR sector (see Fig. 2.1).

In order to provide methodologies adapted to the numerical studies performed by SAE and adapted to the system nature and design context, three research axis have been investigated:

- in chapter 2 the open rotor dynamics is presented and an appropriated finite element formulation (floating frame formulation) is highlighted.
- in chapter 3 the reduction of the open rotor is investigated for the modal analysis when the model is assumed to be linear.
- in chapter 4 the reduction of the open rotor is considered for time simulations with the assumption of contact and friction phenomenon.

Open rotor dynamics formulation

Chapter 2 gives a brief presentation of the CROR case study and its kinematics. This presentation justifies the coherency of the reduction methods proposed in chapter 3 and 4 with the multibody dynamics nature of the open rotor. Moreover, it draws the main issues of the searched reductions: the interface reduction and the consideration of contact-friction behaviour.

The open rotor dynamics matches with the definition of flexible multibody system, consequently, an appropriate formulation of the problem is presented. Indeed, the joints between the constitutive parts of the system allow rotations and translations (i.e. large displacements) that induce nonlinear dynamics. The formulation adopted is referred to

as floating frame formulation and is detailed in section 2.2.

Compared to a classical fixed frame approach, the floating frame formulation has several advantages. First of all, the number of nonlinear equations of the model is drastically reduced. Thus, even if some of finite element operators have to be frequently updated, they remain both small and few. Furthermore, the rigid and flexible motions are distinguished, that help the analysis of the system dynamics.

In order to reduce the time cost of the model update, assumptions and strategies have been proposed in section 2.2.4. This contribution leads to the conclusion that the six distinct mass finite element sub-operator can be split into three groups:

- 2 sub-operators (M_{xx} and M_{ff}) are invariant, they do not depend on the rigid coordinates and are only computed a single time.
- 2 sub-operators (M_{xf} and $\mathrm{M}_{x\theta}$) are parametrized and can then be easily recomputed thanks to matrix multiplications only.
- 2 sub-operators ($\mathrm{M}_{\theta\theta}$ and $\mathrm{M}_{\theta f}$) have to be entirely recomputed when the rigid coordinates ($\boldsymbol{u}_x$ and $\boldsymbol{u}_\theta$) change.

Chapter 2 ends with a meaningful comment about the blade-hub linkage. Indeed, whereas most of the joints between the component are pointwise, the interaction between the blade and the hub is spread over a large contact interface, meshed with lot of nodes. In the frame of the model reduction, the size of the interface between assembled components is a critical point that might lower the interest of a reduction approach. This issue is well illustrated in the application of the Craig-Bampton method (see section 3.5.4).

The present work aims at bypass this issue thanks to the interface reduction. Strategies for the interface reduction are then proposed in chapter 3, when the blade-hub linkage are bonded (formulation given in section 3.4) and in chapter 4, when contact and friction phenomenon are assumed between the blade and the hub (formulation given in section 4.2).

Interface reduction a of linear model

In chapter 3, a method is proposed for the reduction of linear assembled models. The perfect bonding of the model relies on linear holonomic constraints Eq. (3.31) and Eq. (3.32).

The proposed method couples dynamic substructuring principles and a reduction of the interface to provide accurate and compact reduced order models. The interface reduction involved in this method is the main contribution of the present work. This reduction relies on the assumption that the interface motions found in the component eigenmodes are

sufficient to accurately describe the interface kinematics when components are bonded. This assumption has been checked and verified on two different cases studies. The application proposed in section 3.5.4 has shown that the efficiency of the proposed approach is no more linked to its mesh but to its dynamics.

The application of the proposed method on the blade-hub assembly has led to the construction of a accurate and compact reduced order model. Whereas the proposed method is about equivalent to Craig-Bampton in terms of accuracy, it produces for more compact ROM (185 DoF for the proposed method and 1147 for Craig-Bampton). In a more general way, the accuracy of the proposed method can be considered as satisfying since it is equivalent to nowadays methods, the AMLS method. Nevertheless, it has to be noticed that the proposed ROM is less compact than the one produced by the AMLS method. Nevertheless, an improvement of the proposed method has been formulated in section 3.5.5 and increases the compactness of the proposed ROM.

The update of the reduced order model when one of the assembled component changes has been presented in section 3.5.3. This feature has however not been tested in the present work and its application then remains on of the perspective of this work.

To sum up, the proposed reduction method is an answer that responds to a reduction wish in a precise context with acceptable performance. This context is characterized by the following points:

- The interface is reduced using a basis built from component eigenmodes.
- The reduction targets the modal analysis in a redesign context.
- The method accuracy is about equivalent to the current state of the art and more compact the Craig-Bampton method.

Interface reduction with contact-friction phenomenon

Chapter 4 investigates the reduction of the interface when considering contact and friction phenomenon. The contact and friction are modelled thanks to the simple and widespread Signorini-Coulomb laws. The augmented-lagrangian is adopted for the formulation of those laws. More precisely, the bipotential formulation has been used (section 4.2.3) since it has proved its performance compared to simple potential formulations in publications. The integration scheme used for the finite element problem is the central difference method (section 4.4.3), based on the Newmark scheme. The built algorithm is then used to perform a time simulation of the blade preload.

Methods for the reduction nonlinear model can be found in the literature. Some of these

methods are based on the use of structures modes that can be very interesting in the present case since the computation of the structure mode is the main topic of chapter 3. However, the practical application of those methods have only been performed on models carrying at most ten thousands of DoF.

At the end of chapter 4, a reduction method is proposed. This method aims at speeding-up time simulation for the evaluation of the damping associated to the system eigenmodes. For each studied eigenmodes and amplitude level, a compact reduction basis is proposed. In order to provide compact reduced order models a combination of static and dynamic responses is made. This combination is made through an estimation of the contact-friction force. This method also involves an on-line enrichment in order to ensure a high quality of the ROM solution. However, this enrichment is expected to be time consuming but seldom necessary.

Perspectives of the present work

The accuracy and compactness of the method proposed for the reduction of the linear assembled model has been proven in section 3.5.3, however it has not been already tested in a design context. Thus, the efficiency of this method to provide quick updatable model has been studied by not practically observed. This point is then one of the main perspectives of the present work. Moreover, a CMS formulation of this method would be an interesting improvement. Indeed, such a formulation could have beneficial effects to consider a large number of assembled components.

The reduction method proposed in chapter 3 and 4 has been performed on constant flexible mass and stiffness matrix M_{ff} and K_{ff}. In chapter 2, it has been seen that these matrix can be obtained thanks to the floating frame formulation, so that the proposed reduction are coherent with the flexible multibody dynamics context of the open rotor. However, the way to link the reduced order model produced in our work with the rigid coordinates $\boldsymbol{u}_x$ and $\boldsymbol{u}_\theta$ has not been investigated.

Eventually, a fourth outlook of the present work is the application and validation of the reduction method assuming contact and friction, proposed in section 4.5.

Appendix A

Model reduction

A.1 Singular value decomposition

Let us give a quick presentation of the singular value decomposition and its properties. Let considering the matrix U as a set of vectors $\boldsymbol{u}$, referred to as snapshot, defined both on a discrete spatial domain $[\mathrm{x}_1, \mathrm{x}_2, \ldots, \mathrm{x}_n]^\top$ and the frequency ω (or time) domain so that:

$$\mathrm{U}(\mathrm{x}, \omega) = \begin{bmatrix} u(\mathrm{x}_1, \omega_1) & \ldots & u(\mathrm{x}_1, \omega_{n_\mathrm{u}}) \\ \vdots & \ddots & \vdots \\ u(\mathrm{x}_n, \omega_1) & \ldots & u(\mathrm{x}_n, \omega_{n_\mathrm{u}}) \end{bmatrix} = \begin{bmatrix} \boldsymbol{u}_1 & \boldsymbol{u}_2 & \ldots & \boldsymbol{u}_{n_\mathrm{u}} \end{bmatrix}_{n \times n_\mathrm{u}}$$

The Singular Value Decomposition can be seen as a generalisation of the eigen-decomposition problem for rectangular matrix. This method allows the decomposition of a rectangular matrix U as the product:

$$\mathrm{U} = \Phi \Sigma \Psi^\top \tag{A.1}$$

While Ψ is commonly referred to as the right singular vectors, the matrix Φ is the base that best spans the snapshots U. Mathematically, this basis is also the solution of the proper orthogonal decomposition (POD) problem:

$$\text{find} \quad \Phi = \begin{bmatrix} \boldsymbol{\varphi}_1 & \boldsymbol{\varphi}_2 & \ldots & \boldsymbol{\varphi}_n \end{bmatrix} \quad \text{so that} \quad \forall \boldsymbol{\varphi}_i \in \Phi \quad \max_{\boldsymbol{\varphi}_i} \frac{\left\langle (\mathrm{U} \mid \boldsymbol{\varphi}_i)^2 \right\rangle}{\|\boldsymbol{\varphi}_i\|^2} \tag{A.2}$$

The matrix Σ is diagonal and contains the singular values σ_i associated to each element $\boldsymbol{\varphi}_i$. The importance of each vector $\boldsymbol{\varphi}_i$ for the recovery of the snapshot basis U is expressed through the value σ_i. The vectors $\boldsymbol{\varphi}_i$ that best spans the snapshot are associated to the higher singular values σ_i.

The SVD based reduction methods are commonly referred to as *a posteriori* reduction methods as the construction of the reduction basis Φ relies on the knowledge of some snapshots $\mathrm{u}(\mathrm{x}, \omega)$ (i.e. HFM solutions).

A.2 Modal truncation augmentation

The philosophy of the modal truncation augmentation (MTA) is to split the exact solution $\boldsymbol{u}$ into a static $\mathrm{K}^{-1}\boldsymbol{f}$ and a dynamic part $\boldsymbol{u}_d$:

$$\boldsymbol{u} = \mathrm{K}^{-1}\boldsymbol{f} + \boldsymbol{u}_d \quad \text{, consequently:} \quad \ddot{\boldsymbol{u}} = \mathrm{K}^{-1}\ddot{\boldsymbol{f}} + \ddot{\boldsymbol{u}}_d \tag{A.3}$$

Replacing the expressions Eq. (A.3) into the frequency dynamic equation Eq. (2.9) leads to the expression of the dynamic term $\boldsymbol{u}_d$ as:

$$\mathrm{M}\ddot{\boldsymbol{u}} + \mathrm{K}\boldsymbol{u} = \mathrm{M}\left(\mathrm{K}^{-1}\ddot{\boldsymbol{f}} + \ddot{\boldsymbol{u}}_d\right) + \mathrm{K}\left(\mathrm{K}^{-1}\boldsymbol{f} + \boldsymbol{u}_d\right) = \boldsymbol{f} \tag{A.4}$$

$$\text{hence we deduce the relation:} \quad \mathrm{M}\ddot{\boldsymbol{u}}_d + \mathrm{K}\boldsymbol{u}_d = -\mathrm{M}\mathrm{K}^{-1}\ddot{\boldsymbol{f}} \tag{A.5}$$

The dynamic term $\boldsymbol{u}_d$ itself can be split into a quasi-static and a dynamic term $\boldsymbol{u}_{d^2}$. Analogously to the computation of the first static term $\mathrm{K}^{-1}\boldsymbol{f}$ in Eq. (A.3), the quasi-static term is defined as the solution of Eq. (A.5) when neglecting the acceleration so that:

$$\boldsymbol{u}_d = -\mathrm{K}^{-1}\mathrm{M}\mathrm{K}^{-1}\ddot{\boldsymbol{f}} + \boldsymbol{u}_{d^2} \quad \text{, consequently:} \quad \ddot{\boldsymbol{u}}_d = -\mathrm{K}^{-1}\mathrm{M}\mathrm{K}^{-1}\boldsymbol{f}^{(4)} + \ddot{\boldsymbol{u}}_{d^2}$$
$$\text{then anew dynamic relation is deduced:} \quad \mathrm{M}\ddot{\boldsymbol{u}}_d^2 + \mathrm{K}\boldsymbol{u}_d^2 = \mathrm{M}\mathrm{K}^{-1}\mathrm{M}\mathrm{K}^{-1}\boldsymbol{f}^{(4)}$$

Hence, repeating these operations leads to the expression of the displacement $\boldsymbol{u}$ as a sum of $p+1$ quasi-static terms $\boldsymbol{u}_{d^k}$ and the dynamic term $\boldsymbol{u}_{d^p}$:

$$\boldsymbol{u} = \sum_{k=0}^{p} \boldsymbol{u}_{d^k} = \sum_{k=0}^{p-1} \underbrace{\left(\left(-\mathrm{M}\mathrm{K}^{-1}\right)^k \mathrm{K}^{-1}\frac{\partial^{2k}\boldsymbol{f}}{\partial t^{2k}}\right)}_{\boldsymbol{u}_d^{k+1}} + \boldsymbol{u}_{d^{p+1}} \tag{A.6}$$

The last term $\boldsymbol{u}_{d^{p+1}}$ is approximated by the modal decomposition $\Phi\boldsymbol{q}$. Thus the approximation of the solution $\boldsymbol{u}$ is given by:

$$\boldsymbol{u} = \Phi\boldsymbol{q} + \sum_{k=0}^{p-1} \boldsymbol{u}_{d^k} \tag{A.7}$$

Since this method requires the inversion of the stiffness matrix K, this strategy is not suited for problem carrying rigid body motions.

A.3 Residual flexibility

In a general way, considering an orthogonal reduction basis Φ, the exact solution $\boldsymbol{u}$ can be express as the sum of the solution spanned by Φ and a displacement residue $\boldsymbol{r}$:

$$\boldsymbol{u} = \Phi\boldsymbol{q} + \boldsymbol{r} \tag{A.8}$$

Where $\boldsymbol{q}$ corresponds to purely modal coordinates. The residue $\boldsymbol{r}$ itself can be written as the multiplication of a matrix R called dynamic residual flexibility and the external force $\boldsymbol{f}$ for a given circular frequency ω. Starting from the HFM and ROM frequency equations it is possible to deduce the expression of $\boldsymbol{u}$ and $\Phi\boldsymbol{q}$:

$$\text{since } \begin{cases} \mathrm{Z}\boldsymbol{u} = \boldsymbol{f} \\ \tilde{\mathrm{Z}}\boldsymbol{q} = \Phi^\top \boldsymbol{f} \end{cases} \quad \text{then } \begin{cases} \boldsymbol{u} = \mathrm{Z}^{-1}\boldsymbol{f} \\ \Phi\boldsymbol{q} = \Phi\tilde{\mathrm{Z}}^{-1}\Phi^\top \boldsymbol{f} \end{cases} \quad \text{with } \begin{cases} \mathrm{Z} = -\omega^2\mathrm{M} + \mathrm{K} \\ \tilde{\mathrm{Z}} = \Phi^\top \mathrm{Z}\Phi \end{cases}$$

Knowing $\boldsymbol{u}$ and $\Phi\boldsymbol{q}$, it is then possible to express the residue $\boldsymbol{r}$ in the following way:

$$\boldsymbol{r} = \boldsymbol{u} - \Phi\boldsymbol{q} = \underbrace{\left(\mathrm{Z}^{-1} - \Phi\tilde{\mathrm{Z}}^{-1}\Phi^\top\right)}_{\mathrm{R}}\boldsymbol{f} \tag{A.9}$$

Another way to understand the dynamic residual matrix is to see it as the mechanical flexibility that is neglected by the truncation of the modal basis over the n_Φ first eigenmodes.

$$\mathrm{Z}^{-1} = \underbrace{\sum_{i=1}^{n_\Phi} \left(\boldsymbol{\phi}_i \left(-\omega^2 + \omega_i^2\right)^{-1} \boldsymbol{\phi}_i{}^\top\right)}_{\Phi\tilde{\mathrm{Z}}^{-1}\Phi^\top} + \underbrace{\sum_{i=n_\Phi+1}^{n} \left(\boldsymbol{\phi}_i \left(-\omega^2 + \omega_i^2\right)^{-1} \boldsymbol{\phi}_i{}^\top\right)}_{\mathrm{R}} \tag{A.10}$$

The residual displacement $\boldsymbol{r}$ is orthogonal to the solution spanned by the modal basis Φ. Let f denotes the DoF on which the external force $\boldsymbol{f}$ is applied and c the free DoF ($\boldsymbol{f}_c = \boldsymbol{0}$). The force $\boldsymbol{f}$ and the mechanical flexibility R can be split. It allows to express the residue $\boldsymbol{r}$ as:

$$\boldsymbol{r} = \mathrm{R}\boldsymbol{f} = \begin{bmatrix} \mathrm{R}_{cc} & \mathrm{R}_{cf} \\ \mathrm{R}_{fc} & \mathrm{R}_{ff} \end{bmatrix} \begin{bmatrix} \boldsymbol{0} \\ \boldsymbol{f}_f \end{bmatrix} = \begin{bmatrix} \mathrm{R}_c & \mathrm{R}_f \end{bmatrix} \begin{bmatrix} \boldsymbol{0} \\ \boldsymbol{f}_f \end{bmatrix} = \mathrm{R}_f \boldsymbol{f}_f$$

$$\text{with } \mathrm{R}_c = \begin{bmatrix} \mathrm{R}_{cc} \\ \mathrm{R}_{cf} \end{bmatrix} \quad \text{and } \mathrm{R}_f = \begin{bmatrix} \mathrm{R}_{fc} \\ \mathrm{R}_{ff} \end{bmatrix}$$

Hence, this enrichment leads to a reduction basis $\boldsymbol{u} = \Phi\boldsymbol{q} + \mathrm{R}_f\boldsymbol{f}_f$. Such a decomposition is notably exploited by the Craig-Martinez [1] (see appendix A.4) and Mac-Neal [2] (see appendix A.5) methods. Those methods involve a static residual flexibility and propose a reduction basis [3] for the statement given in Eq. (A.8).

A.4 Craig-Martinez method

The Craig-Martinez method assume that the displacement $\boldsymbol{u}$ of a structure can be spanned accurately by a truncated modal basis Φ and a residual flexibility R:

$$\boldsymbol{u} = \Phi\boldsymbol{q} + \mathrm{R}_f\boldsymbol{f}_f = \begin{bmatrix} \Phi_c & \mathrm{R}_{cf} \\ \Phi_f & \mathrm{R}_{ff} \end{bmatrix} \begin{Bmatrix} \boldsymbol{q} \\ \boldsymbol{f}_f \end{Bmatrix} = \begin{Bmatrix} \boldsymbol{u}_c \\ \boldsymbol{u}_f \end{Bmatrix} \tag{A.11}$$

The external load $\boldsymbol{f}$ can then be expressed as:

$$\boldsymbol{f}_f = \mathrm{R}_{ff}^{-1}\left(\boldsymbol{u}_f - \Phi_f\boldsymbol{q}\right) \tag{A.12}$$

This expression of the load allows to find the searched expression of $\boldsymbol{u}_c$ and then to define the transform matrix T of the Craig-Martinez method:

$$\text{since} \quad \boldsymbol{u}_i = \Phi_c\boldsymbol{q} + \mathrm{R}_{cf}\boldsymbol{f}_f = \Phi_c\boldsymbol{q} + \mathrm{R}_{cf}\mathrm{R}_{ff}^{-1}\left(\boldsymbol{u}_f - \Phi_f\boldsymbol{q}\right) \tag{A.13}$$

$$\text{then} \quad \begin{Bmatrix} \boldsymbol{u}_c \\ \boldsymbol{u}_f \end{Bmatrix} = \begin{bmatrix} \Phi_c - \mathrm{R}_{cf}\mathrm{R}_{ff}^{-1}\Phi_f & \mathrm{R}_{cf}\mathrm{R}_{ff}^{-1} \\ 0 & \mathrm{I}_f \end{bmatrix} \begin{Bmatrix} \boldsymbol{q} \\ \boldsymbol{u}_f \end{Bmatrix} = \mathrm{T} \begin{Bmatrix} \boldsymbol{q} \\ \boldsymbol{u}_f \end{Bmatrix} \tag{A.14}$$

This method is widely implemented in industrial codes and considers a static flexibility for the correction of the modal truncation effects [3].

A.5 Mac-Neal and Rubin's method

The Mac-Neal [2] and Rubin's [4] method use component free eigenmodes to describe the component behaviour and a dynamic residual flexibility R (see Eq. (3.16)) to correct the modal truncation. Hence, starting from Eq. (3.27), the displacement $\boldsymbol{u}_k$ of each substructure is given by:

$$\boldsymbol{u}_k = \Phi_k\boldsymbol{q}_k + \mathrm{R}_k(\boldsymbol{f}_k + \boldsymbol{p}_k) \quad \text{with} \quad \mathrm{R}_k = \mathrm{Z}_k^{-1} - \Phi_k\tilde{\mathrm{Z}}_k^{-1}\Phi_k^{\top} \tag{A.15}$$

Where Φ is the truncated basis of free component eigenmodes associated to the k^{th} substructure. Using Eq. (A.15) into the dynamic equation Eq. (3.27) and multiplying on the left by the transpose of the modal basis Φ_k leads to:

$$\Phi_k{}^{\top}\mathrm{Z}_k\Big(\Phi_k\boldsymbol{q}_k + \mathrm{R}_k(\boldsymbol{f}_k + \boldsymbol{p}_k)\Big) = \Phi_k{}^{\top}\Big(\boldsymbol{f}_k + \boldsymbol{p}_k\Big)$$

The orthogonality between the modal dynamics $\Phi\boldsymbol{q}$ and the flexible residual term (see section 3.1.3) allows a simplification of the previous equation as follow since $(\mathrm{R}_k(\boldsymbol{f}_k + \boldsymbol{p}_k)) \perp \Phi_k$:

$$\underbrace{\Phi_k{}^{\top}\mathrm{Z}_k\Phi_k}_{\tilde{\mathrm{Z}}_k}\boldsymbol{q}_k = \underbrace{\Phi_k{}^{\top}\boldsymbol{f}_k}_{\tilde{\boldsymbol{f}}_k} + \underbrace{\Phi_k{}^{\top}\boldsymbol{p}_k}_{\tilde{\boldsymbol{p}}_k}$$

Also the displacement compatibility equation Eq. (3.47) then becomes:

$$\begin{aligned}\boldsymbol{u}_{1,\Gamma} - \boldsymbol{u}_{2,\Gamma} &= \begin{bmatrix} 0 & \mathrm{I}_\Gamma & 0 & -\mathrm{I}_\Gamma \end{bmatrix} \begin{Bmatrix} \boldsymbol{u}_1 \\ \boldsymbol{u}_2 \end{Bmatrix} = \mathrm{B}\boldsymbol{q} \\ &= \begin{bmatrix} 0 & \mathrm{I}_\Gamma \end{bmatrix} \Big(\Phi_1 \boldsymbol{q}_1 + \mathrm{R}_1(\boldsymbol{f}_1 + \boldsymbol{p}_1) \Big) - \begin{bmatrix} 0 & \mathrm{I}_\Gamma \end{bmatrix} \Big(\Phi_2 \boldsymbol{q}_2 + \mathrm{R}_2(\boldsymbol{f}_2 + \boldsymbol{p}_2) \Big)\end{aligned}$$

Let us remind the expressions of the force $\boldsymbol{p}_1$ and $\boldsymbol{p}_2$ given in Eq. (3.54) and define two auxiliary variables W and $\boldsymbol{h}$:

$$\boldsymbol{p}_1 = \begin{Bmatrix} \mathbf{0} \\ \boldsymbol{p}_{1,\Gamma} \end{Bmatrix} = \begin{bmatrix} \mathbf{0} \\ -\mathrm{I}_\Gamma \end{bmatrix} \boldsymbol{p}_\Gamma \quad \text{and} \quad \boldsymbol{p}_2 = \begin{Bmatrix} \mathbf{0} \\ \boldsymbol{p}_{2,\Gamma} \end{Bmatrix} = \begin{bmatrix} \mathbf{0} \\ \mathrm{I}_\Gamma \end{bmatrix} \boldsymbol{p}_\Gamma$$

$$\mathrm{W} = -\Bigg(\begin{bmatrix} 0 & \mathrm{I}_\Gamma \end{bmatrix} \mathrm{R}_1 \begin{bmatrix} 0 \\ \mathrm{I}_\Gamma \end{bmatrix} + \begin{bmatrix} 0 & \mathrm{I}_\Gamma \end{bmatrix} \mathrm{R}_2 \begin{bmatrix} 0 \\ \mathrm{I}_\Gamma \end{bmatrix} \Bigg), \quad \boldsymbol{h} = -\Big(\begin{bmatrix} 0 & \mathrm{I}_\Gamma \end{bmatrix} \mathrm{R}_1 \boldsymbol{f}_1 + \begin{bmatrix} 0 & \mathrm{I}_\Gamma \end{bmatrix} \mathrm{R}_2 \boldsymbol{f}_2 \Big)$$

The Mac-Neal's reduced order model can be expressed a compact ways as follows:

$$\begin{bmatrix} \tilde{\mathrm{Z}} & \tilde{\mathrm{B}}^\top \\ \tilde{\mathrm{B}} & \mathrm{W} \end{bmatrix} \begin{Bmatrix} \boldsymbol{q} \\ \boldsymbol{p}_\Gamma \end{Bmatrix} = \begin{Bmatrix} \tilde{\boldsymbol{f}} \\ \boldsymbol{h} \end{Bmatrix}$$

In the case where the residual dynamic flexibility R is neglected, the dynamic substructuring is very sensitive to the modal truncation. The Mac-Neal method involve static residual flexibilities, so that R_1 and R_2 are computed for a null circular frequency (see their expression in Eq. (3.16)). Let n be the DoF number of a component, it has been seen in section 3.1.3 (see Eq. (A.10)) that any residual flexibility R can be expressed as the sum

$$\mathrm{R} = \sum_{i=n_\Phi+1}^{n} \Big(\boldsymbol{\phi}_i \Big(-\omega^2 + \omega_i^2 \Big)^{-1} {\boldsymbol{\phi}_i}^\top \Big) \tag{A.16}$$

When the circular frequency ω of the external loads are negligible with regards to the natural frequencies of the rejected modes then the use of a static residual flexibility is justified since:

$$\text{if } \ \omega^2 \ll \omega_i^2 \ \text{ then } \ \mathrm{R} \simeq \sum_{i=n_\Phi+1}^{n} \Big(\boldsymbol{\phi}_i \omega_i^{-2} {\boldsymbol{\phi}_i}^\top \Big) = \mathrm{R}(0) \tag{A.17}$$

The Rubin's method considers a second order approximation of the dynamic flexibilities W (using a Taylor expansion) around a null circular frequency [5]:

$$\mathrm{W} \simeq \mathrm{W}(0) + \left. \frac{\partial^2 \mathrm{W}}{\partial \omega^2} \right|_0 \omega^2$$

This last method is more accurate than the Mac-Neal. In practice, the use of residual loads is essential to obtain acceptable results.

A.6 AMLS method for modal analysis

In this section the AMLS method is only presented in the frame of the eigenproblem resolution as proposed by Gao *et al.* in [6]. Let us consider a structure Σ made of two distinct components, the matrix assembled in the physical domain is given by Eq. (3.52), and can be reordered in order to get the following topology:

$$\mathrm{K}_p = \begin{bmatrix} \mathrm{K}_{11} & 0 & \mathrm{K}_{13} \\ 0 & \mathrm{K}_{22} & \mathrm{K}_{23} \\ \mathrm{K}_{31} & \mathrm{K}_{32} & \mathrm{K}_{33} \end{bmatrix} \quad \text{and} \quad \mathrm{M}_p = \begin{bmatrix} \mathrm{M}_{11} & 0 & \mathrm{M}_{13} \\ 0 & \mathrm{M}_{22} & \mathrm{M}_{23} \\ \mathrm{M}_{31} & \mathrm{M}_{32} & \mathrm{M}_{33} \end{bmatrix} \tag{A.18}$$

Let consider now a structure partitioned into m substructures Fig. A.1a. Nowadays methods allow automatic partitioning or assembling structures. The characteristic matrix of those structures are then organised in a particular way so that their topologies follows an imbricated arrow shape [7].

From the topology of the reorganized finite element operators Eq. (A.18) it is possible to distinguish two kinds of DoF. The first partition of DoF, the bigger one, refers to substructure interior DoF. The second partition of DoF makes the junction of those interior DoF of the substructures. Those two partitions of DoF can be used to identify structures sub-meshes, as shown in Fig. A.1.

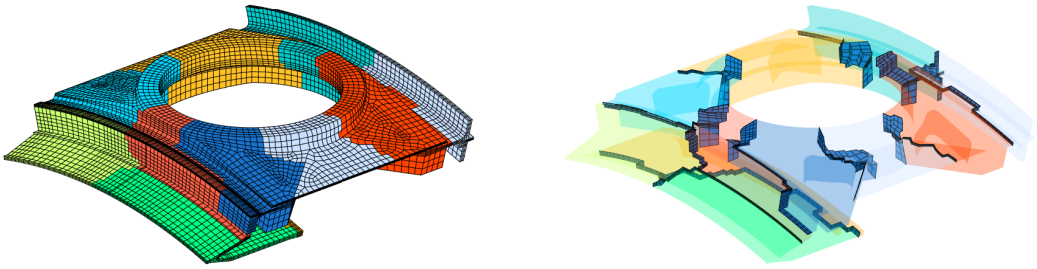

(a) Partitioning of the open rotor polygonal ring in 10 partitions, using the METIS library.

(b) The interface between the substructure are refereed to as separator.

Figure A.1 – The coloured substructures (a) are linked together through the separator interfaces (b). The METIS [8] based libraries allow partitioning mesh, combined with substructuring technique, this can be used to work on finite element model that are two large to be treated at a whole.

Since the stiffness matrix K_p is symmetric, it can be split using a Crout factorisation $\mathrm{LDL}^\top$. Knowing that the matrix L is a lower triangular matrix with a unitary diagonal and that the D is block diagonal, they can easily be identified for a structure split into

m substructure:

$$\mathrm{K}_p = \mathrm{L}\mathrm{D}\mathrm{L}^\top \quad \text{with} \quad \mathrm{L}_{ij} = \begin{cases} \mathrm{I}_i & \text{if} \quad i = j \\ \mathrm{K}_{ij}\mathrm{K}_{jj}^{-1} & \text{if} \quad i \neq j \end{cases} \quad \text{and} \quad \mathrm{D}_{ii} = \hat{\mathrm{K}}_{ii}$$

$$\text{knowing that} \quad \hat{\mathrm{K}}_{ii} = \begin{cases} \mathrm{K}_{ii} & \text{if } i \text{ refers to a substructure} \\ \mathrm{K}_{ii} - \sum_j \mathrm{K}_{ij}\mathrm{K}_{jj}^{-1}\mathrm{K}_{ji} & \text{if } i \text{ refers to a separator} \end{cases}$$

The separators term $\hat{\mathrm{K}}_{ii}$ are commonly referred to as Schur complements. The matrix $\hat{\mathrm{K}}$ and $\hat{\mathrm{M}}$, also called Craig-Bampton form, are defined as:

$$\hat{\mathrm{K}} = \mathrm{L}^{-1}\mathrm{K}_p\mathrm{L}^{-\top} \quad \text{and} \quad \hat{\mathrm{M}} = \mathrm{L}^{-1}\mathrm{M}_p\mathrm{L}^{-\top}$$

The matrix denoted $\hat{\mathrm{K}}$, $\hat{\mathrm{M}}$ can be seen as operator reduced in the space spanned by the vectors of the square matrix $\mathrm{L}^{-\top}$. It is possible to analytically identify all the matrix blocks of $\tilde{\mathrm{M}}$. Moreover, in order to speed up the computation it is possible to directly build $\tilde{\mathrm{M}}$ from its constitutive submmatrix $\hat{\mathrm{M}}_{ij}$.

$$\hat{\mathrm{M}}_{ij} = \begin{cases} \mathrm{M}_{ii} & \text{if } i = j \text{ and refers to substructures} \\ \mathrm{M}_{ji} - \mathrm{M}_{jj}\mathrm{K}_{jj}^{-1}\mathrm{K}_{ji} & \text{if } i \neq j \text{ and } i \text{ refers to separator} \\ \mathrm{M}_{ii} - \sum_{j\neq i} \Big(\mathrm{K}_{ij}\mathrm{K}_{jj}^{-1}\mathrm{M}_{ji} + \ldots & \\ \mathrm{M}_{ij}\mathrm{K}_{jj}^{-1}\mathrm{M}_{ji} - \mathrm{K}_{ij}\mathrm{K}_{jj}^{-1}\mathrm{M}_{jj}\mathrm{K}_{jj}^{-1}\mathrm{K}_{ji} \Big) & \text{if } i = j \text{ and refers to substructures} \end{cases}$$

In the space spanned by $\mathrm{L}^{-\top}$, the eigenmodes associated to the interior DoF and to the interface are used to reduce the dynamic stiffness matrix $\hat{\mathrm{Z}}$:

$$\tilde{\hat{\mathrm{Z}}} = \hat{\Phi}^\top \underbrace{\left(\mathrm{L}^{-1}\mathrm{Z}_p\mathrm{L}^{-\top}\right)}_{\hat{\mathrm{Z}}} \hat{\Phi} \quad \text{with} \quad \hat{\Phi} = \mathrm{diag}(\Phi_i)$$

The eigenmodes $\hat{\Phi}_i$ are respectively computed using the operator couples $(\tilde{\mathrm{K}}_{ii}, \tilde{\mathrm{M}}_{ii})$. Then, the eigensolutions $(\boldsymbol{\psi}_i, \mu_i)$ of the reduced problem are then computed and restitued into the initial nodal space:

$$\left(-\mu_i^2\tilde{\hat{\mathrm{M}}} + \tilde{\hat{\mathrm{K}}} \right)\boldsymbol{\psi}_i = \mathbf{0} \quad \text{then} \quad (\boldsymbol{\phi}_i,\ \omega_i) = \left(\mathrm{L}^{-\top}\hat{\Phi}\boldsymbol{\psi}_i,\ \mu_i \right)$$

The application of the AMLS method, presented above, is rather straightforward and described in algorithm A.6.1.

Algorithm A.6.1: AMLS method for eigenvalue problem

input : K_p, M_p

Reordering K_p *and* M_p

The assembled matrix K_p and M_p should be reordered in order to get arrow matrix, see Eq. (A.18).

Crout factorisation of K_p

Find L and D so that $\mathrm{K}_p = \mathrm{LDL}^\top$

Computation of the reduced operator $\hat{\mathrm{K}}$ *and* $\hat{\mathrm{M}}$

$\hat{\mathrm{K}} = \mathrm{L}^{-1}\mathrm{K}_p\mathrm{L}^{-\top}$ and $\hat{\mathrm{M}} = \mathrm{L}^{-1}\mathrm{M}_p\mathrm{L}^{-\top}$

Construction of the modal reduction matrix $\hat{\Phi}$

For each leave and root, compute the reduced eigenmodes $\hat{\Phi}_k$ using the operators $(\hat{\mathrm{K}}_{kk}, \hat{\mathrm{M}}_{kk})$. Then assemble $\hat{\Phi} = \mathrm{diag}\big(\hat{\Phi}_1,\ \hat{\Phi}_2\ \ldots\ \hat{\Phi}_n\big)$

Reduction of $\hat{\mathrm{K}}$ *and* $\hat{\mathrm{M}}$ *using* $\hat{\Phi}$

$\tilde{\hat{\mathrm{K}}} = \hat{\Phi}^\top\hat{\mathrm{K}}\hat{\Phi}$ and $\tilde{\hat{\mathrm{M}}} = \hat{\Phi}^\top\hat{\mathrm{M}}\hat{\Phi}$

Computation of the desired eigenvector in the reduced space $\mathrm{L}^{-\top}\hat{\Phi}$

Solve $\Big(-\mu_i^2\tilde{\hat{\mathrm{M}}} + \tilde{\hat{\mathrm{K}}}\Big)\boldsymbol{\psi}_i = \mathbf{0}$

Restitution of the eigensolution $(\boldsymbol{\psi}_i, \mu_i)$ *into the nodal space*

$\omega_i = \mu_i$ and $\boldsymbol{\phi}_i = \mathrm{L}^{-\top}\hat{\Phi}\boldsymbol{\psi}_i$

Although this method is rather fast, it provides results that are less accurate than those of the classical reduction method (according to Gao *et al.*). For some practical applications the accuracy of the AMLS solutions can not be tolerated, methods have been developed to improve the precision of the method but in detriment of its speed [6].

Bibliography

[1] D. Martinez, A. Miller, and T. Carne, "Combined experimental/analytical modeling of shell/payload structures." 1985.

[2] R. H. MacNeal, "A hybrid method of component mode synthesis," *Computers & Structures*, vol. 1, no. 4, pp. 581–601, 1971.

[3] A. Batailly and M. Legrand, "Technical note: another presentation of Craig-Martinez method." 2011.

[4] S. Rubin, "Improved component-mode representation for structural dynamic analysis," *AIAA Journal*, vol. 13, no. 8, pp. 995–1006, 1975.

[5] M. Corus, "Calcul modal par sous-structuration dynamique classique." 2011.

[6] W. Gao, X. S. Li, C. Yang, and Z. Bai, "An Implementation and Evaluation of the AMLS Method for Sparse Eigenvalue Problems," *ACM Transactions on Mathematical Software (TOMS)*, vol. 34, no. 4, p. 20, 2008.

[7] G. Vermot des Roches, *Frequency and time simulation of squeal instabilities. Application to the design of industrial automotive brakes*. PhD thesis, Ecole Centrale Paris, 2011.

[8] G. Karypis and V. Kumar, "A Fast and Highly Quality Multilevel Scheme for Partitioning Irregular Graphs," *SIAM Journal on Scientific Computing*, vol. 20, no. 1, pp. 359 – 392, 1998.

université PARIS-SACLAY

ÉCOLE DOCTORALE
Sciences mécaniques et énergétiques, matériaux et géosciences (SMEMAG)

Title : Methodoloy for the generation of dynamic and multi-physic reduced order models: application to open rotors

Keywords : interface reduction, modal analysis, contact-friction

Abstract : The mechanical design of a system involves numerous investigations, notably the validation of the system dynamics over its operating frequency range. This type of analysis can be performed numerically using the finite element method. However, in this context, the accuracy and level of detail required involve models whose significant sizes lead to time-consuming simulations. Moreover, the optimization process of such a system may demand numerous validation computations that considerably slow down the design process.

The linkage between the open rotor constitutive parts induce large translations and rotations that lead to non-linear dynamics. Those non-linearities can be efficiently managed thanks to appropriated flexible multibody formulations. The features of the floating frame approach are particularly suitable for the current case study and context.

The junction between the blade and the hub of the open rotor is spread over a large and rich contact interface. In the frame of the model reduction, the size of the interface between assembled components is a critical point that might lower the interest of a reduction approach. The present work aim at by pass this issue thanks to the interface reduction.

The interface reduction is first investigated when assuming the clamping of the blade and hub. Starting from the existing dynamic substructuring techniques, a reduction methodology has been proposed in the frame of the modal analysis. The interface reduction involved in this method is the main contribution of the present work. This reduction relies on the assumption that the interface deformation contained in the component eigenmodes are sufficient to describe the interface kinematic of the assembled components.

Lastly, the assumption of contact and friction between the blade and the hub is made. Indeed, such an assumption can be useful to estimate the damping of each mode due to the contact and friction. Such an estimation can be made through time simulation of the blade and hub. Recent methods have been presented in the literature for the reduction of non-linear problem, however those methods are only available for small models. Thus, a reduction method is proposed for time simulation with the assumption of contact-friction. This method relies on the reduction of the interface thanks to a prediction of the nominal contact and friction force.

Université Paris-Saclay
Espace Technologique / Immeuble Discovery
Route de l'Orme aux Merisiers RD 128 / 91190 Saint-Aubin, France

université PARIS-SACLAY

ÉCOLE DOCTORALE
Sciences mécaniques et énergétiques, matériaux et géosciences (SMEMAG)

Titre : Méthodologie pour génération de modèles réduits dynamiques multi-physiques : application aux open rotors

Keywords : réduction d'interface, analyse modale, contact frottant

Résumé : La conception mécanique d'un système requiert de nombreuses études, notamment afin de caractériser et de valider son comportement dynamique sur sa plage de fonctionnement. En pratique, ce type d'analyse peut être réalisée numériquement à l'aide de la méthode des éléments finis. Cependant, dans ce contexte, la précision et le niveau de détail requis mène à des modèles dont les tailles conséquentes et les temps de résolutions ralentissent significativement le processus de conception.

Les liaisons entre les composants de l'open rotor de SNECMA permettent de grands déplacements, ce qui donne un caractère non-linéaire à sa dynamique du système. La dynamique des multicorps flexible propose des formulations adaptées au traitement de ce type de non-linéarités. Dans ce contexte industriel précis, l'approche dite "référentiel mobile" possède des propriétés particulièrement intéressantes pour la formulation de la dynamique de l'open rotor.

Le contact entre la pale et son support s'effectue sur une importante surface. Dans le domaine de la réduction de modèle, de telles interfaces ont tendance à réduire l'efficacité des méthodes de réduction. C'est pourquoi, le travail présenté dans cette thèse s'attache principalement à la réduction de ces interfaces.

La réduction des interfaces de contact est dans un premier temps étudié en considérant ses composants encastrés sur une interface de contact. La méthode de réduction développée s'appuie sur les techniques de sous-structurations dynamiques déjà existantes. La stratégie de réduction des interfaces de contact, qui est exploitée par la méthode proposée est la principale contribution de ce travail. Cette réduction de l'interface se base sur l'hypothèse que les modes propres libres des composants contiennent suffisamment d'informations pour décrire la cinématique de cette interface lorsque les deux composants sont assemblés.

A la fin de ces travaux, le contact et la friction des deux composant est prise en compte. En effet, il est intéressant de pouvoir quantifier le niveau d'amortissement modal induit par la présence de ces phénomènes. Une telle estimation peut être réalisée à l'aide de simulation temporelles. Dans ce travail, le contact et la friction sont modélisés à l'aide des lois de Signorini et Coulomb. De récents travaux s'attaquent à la réduction de modèles non-lineaires cependant, les applications de ces travaux, sont encore restreint à des modèles de petites tailles. Ainsi, en dernière partie, une méthode de réduction est proposée pour des simulations en temps. Cette méthode implique la réduction de l'interface de contact à l'aide d'une prédiction des efforts de contact-friction.

Université Paris-Saclay
Espace Technologique / Immeuble Discovery
Route de l'Orme aux Merisiers RD 128 / 91190 Saint-Aubin, France

université PARIS-SACLAY

ÉCOLE DOCTORALE
Sciences mécaniques et énergétiques, matériaux et géosciences (SMEMAG)

Titre : Méthodologie pour génération de modèles réduits dynamiques multi-physiques : application aux open rotors

Mots clefs : réduction d'interface, analyse modale, contact frottant

Résumé : La conception d'un produit industriel requiert parfois des simulations afin de prédire le comportement du produit en question. En pratique ce type de simulations peut être réalisé en utilisant la méthode des éléments finis, cependant la précision et le niveau de détail souhaité génèrent des modèles difficiles à évaluer. En outre, le caractère itératif présent dans de nombreuses conceptions accentue le ralentissement induit par ces simulations couteuses en temps de calculs. Afin de pallier ce problème, une démarche de réduction de modèle est souhaitée par le partenaire industriel. Les grands axes de travail sur cette méthode sont : la recherche d'une haute compacité, la prise en compte de non-linéarités de grands déplacements et l'évaluation de l'amortissement dans les liaisons du système due au phénomène de contact-friction.

Title : Methodoloy for the generation of dynamic and multi-physic reduced order models: application to open rotors

Keywords : interface reduction, modal analysis, contact-friction

Abstract : The mechanical design of a system involves many investigations, notably the validation of its structural behaviour over its operating frequency range. This kind of analysis can be numerically performed using the finite element method, however in such a context, the required accuracy and detail level imply models whose significant sizes lead to time consuming simulations. Moreover, the optimization process of such a system may request numerous validation computations that turn out extremely slow the design process. In the framework of this PhD we target a reduction methodology whose main features are: being compact, dealing with non-linear displacement and recovering the damping effects of the model joint due to the contact-friction phenomenon.

Université Paris-Saclay
Espace Technologique / Immeuble Discovery
Route de l'Orme aux Merisiers RD 128 / 91190 Saint-Aubin, France